Ministry of Education and Science of the Russian Federation
Saint Petersburg National Research University of Information
Technologies, Mechanics, and Optics

NANOSYSTEMS:

PHYSICS, CHEMISTRY, MATHEMATICS

2018, volume 9(6)

Наносистемы: физика, химия, математика

2018, том 9, № 6

NANOSYSTEMS:

PHYSICS, CHEMISTRY, MATHEMATICS

ADVISORY BOARD MEMBERS

Chairman: V.N. Vasiliev *(St. Petersburg, Russia)*,
V.M. Buznik *(Moscow, Russia)*; V.M. Ievlev *(Voronezh, Russia)*, P.S. Kop'ev*(St. Petersburg, Russia)*, N.F. Morozov *(St. Petersburg, Russia)*, V.N. Parmon *(Novosibirsk, Russia)*, A.I. Rusanov *(St. Petersburg, Russia)*,

EDITORIAL BOARD

Editor-in-Chief: I.Yu. Popov *(St. Petersburg, Russia)*

Section Co-Editors:
Physics – V.M. Uzdin *(St. Petersburg, Russia)*,
Chemistry, material science –V.V. Gusarov *(St. Petersburg, Russia)*,
Mathematics – I.Yu. Popov *(St. Petersburg, Russia)*.

Editorial Board Members:
V.M. Adamyan *(Odessa, Ukraine)*; O.V. Al'myasheva *(St. Petersburg, Russia)*; A.P. Alodjants *(Vladimir, Russia)*; S. Bechta *(Stockholm, Sweden)*; J. Behrndt *(Graz, Austria)*; M.B. Belonenko *(Volgograd, Russia)*; J. Brasche *(Clausthal, Germany)*; A. Chatterjee (*Hyderabad, India)*; S.A. Chivilikhin *(St. Petersburg, Russia)*; A.V. Chizhov *(Dubna, Russia)*; A.N. Enyashin *(Ekaterinburg, Russia)*, P.P. Fedorov *(Moscow, Russia)*; E.A. Gudilin *(Moscow, Russia)*; V.K. Ivanov *(Moscow, Russia)*, H. Jónsson *(Reykjavik, Iceland)*; A.A. Kiselev *(Durham, USA)*; Yu.S. Kivshar *(Canberra, Australia)*; S.A. Kozlov *(St. Petersburg, Russia)*; P.A. Kurasov *(Stockholm, Sweden)*; A.V. Lukashin *(Moscow, Russia)*; V.A. Margulis *(Saransk, Russia)*; I.V. Melikhov *(Moscow, Russia)*; G.P. Miroshnichenko *(St. Petersburg, Russia)*; I.Ya. Mittova *(Voronezh, Russia)*; H. Neidhardt *(Berlin, Germany)*; V.V. Pankov *(Minsk, Belagus)*; K. Pankrashkin *(Orsay, France)*; A.V. Ragulya *(Kiev, Ukraine)*; V. Rajendran *(Tamil Nadu, India)*; A.A. Rempel *(Ekaterinburg, Russia)*; V.Ya. Rudyak *(Novosibirsk, Russia)*; D Shoikhet *(Karmiel, Israel)*; P Stovicek *(Prague, Czech Republic)*; V.M. Talanov *(Novocherkassk, Russia)*; A.Ya. Vul' *(St. Petersburg, Russia)*; A.V. Yakimansky (*St. Petersburg, Russia*), V.A. Zagrebnov *(Marseille, France)*.

Editors:
I.V. Blinova; A.I. Popov; A.I. Trifanov; E.S. Trifanova *(St. Petersburg, Russia)*,
R. Simoneaux *(Philadelphia, Pennsylvania, USA)*.

Address: University ITMO, Kronverkskiy pr., 49, St. Petersburg 197101, Russia.
Phone: +7(812)312-61-31, **Journal site:** http://nanojournal.ifmo.ru/,
E-mail: popov1955@gmail.com

AIM AND SCOPE

The scope of the journal includes all areas of nano-sciences. Papers devoted to basic problems of physics, chemistry, material science and mathematics inspired by nanosystems investigations are welcomed. Both theoretical and experimental works concerning the properties and behavior of nanosystems, problems of its creation and application, mathematical methods of nanosystem studies are considered.

The journal publishes scientific reviews (up to 30 journal pages), research papers (up to 15 pages) and letters (up to 5 pages). All manuscripts are peer-reviewed. Authors are informed about the referee opinion and the Editorial decision.

CONTENT

MATHEMATICS

PHYSICS

CHEMISTRY AND MATERIAL SCIENCE

NANOSYSTEMS: PHYSICS, CHEMISTRY, MATHEMATICS, 2018, 9 (6), P. 703–710

Scattering on a chain of zero-range potentials with internal structure in the stochastic magnetic field

A. E. Ryzhkov

ITMO University, Kronverkskiy, 49, St. Petersburg, 197101, Russia

verdad60@mail.ru

PACS 02.30.Tb **DOI 10.17586/2220-8054-2018-9-6-703-710**

Scattering problem on an infinite chain of zero-range potentials with internal structure in the stochastic magnetic field is investigated. Model operator is constructed using the perturbation theory for the self-adjoint operators. The relations with the scattering problem without stochasticity are investigated.

Keywords: operator extension, stochastic magnetic field, scattering problem.

Received: 1 October 2018

Revised: 20 November 2018

1. Introduction

Nanostructures having the form of chains of short-range potentials are widely used in nanotechnologies. Berezin and Faddeev (see [1]) showed that the Hamiltonian with zero-range Fermi type potential is just an extension of a suitable defined symmetric operator. Later, it has been shown by Pavlov [2], that the structure of the standard point interaction models can be enriched substantially when the self-adjoint extensions are constructed in a wider Hilbert space. This idea yields various models of zero-range interaction with an additional internal structure (see, e.g., [3–5]). In papers [6, 7] this method has been used to construct and investigate explicitly solvable models of the scattering of the neutron on a point nucleus, whose internal structure depends on a stochastic magnetic field, and of the scattering of acoustic waves on a stochastic point defect with an internal structure.

In the present paper, an exactly solvable model of the neutron scattering on the one-dimensional infinite chain embedded into the three dimensional configuration space $\mathbb{R}^3$. We will suppose that the chain is inserted into the stochastic magnetic field. The nuclei in the chain are assumed to be equivalent with the internal structure dependent on the magnetic field. This model corresponds to the case, when the whole chain belongs to one magnetic domain. In the absence of the stochasticity, such model was investigated by Albeverio, Gesztesy, Hoegh-Krohn, Holden [8], Karpeshina [9], Subramanian [10], Kurasov and Pavlov [11]. It was shown that the spectrum of the related operator is purely continuous and consists of two branches:

1) Scattered waves branch σ_s; corresponding eigenfunctions are defined by free waves reflected by the lattice. This branch coincides with the spectrum of the free Laplacian $-\Delta$ in $L_2\left(\mathbb{R}^3\right)$.

2) Waveguide branch σ_w; corresponding eigenfunctions are localized in a vicinity of the lattice. In the discussing periodic case these functions are of the Bloch type.

It will be shown that the spectral properties of the problem with the stochastic filed are related to the properties of the problems without any stochasticity.

2. Model operator

This section is devoted to the construction of the model operator describing scattering in the stochastic magnetic field. Let $L_2\left(\mathbb{R}^3\right)$ be an external space and free Laplacian $-\Delta$ defined on $W_2^2\left(\mathbb{R}^3\right)$ be an unperturbed operator, simulating the Hamiltonian of the free neutron. Let $E^{int} = \oplus\Sigma_n E_n$ be an orthogonal sum of unitary equivalent finite-dimensional Hilbert spaces. We will restrict our consideration to the simplest case, $E_n = \mathbb{C}^2$, $n \in \mathbb{Z}$. Let A_n be selfadjoint operators in E_n which are mutually unitary equivalent. We will consider, as in the paper [6]:

$$A_n = A\left(H\left(\tau\right)\right) \equiv \operatorname{diag}\left\{\lambda_0, \lambda_1\right\} + \sigma_3 H\left(\tau\right), \quad H\left(\tau\right) = \pm e_z, \tag{1}$$

Where λ_0, λ_1 are the “levels” of the nucleus, $\sigma_3 = \begin{pmatrix} q & 0 \\ 0 & -q \end{pmatrix}$ is Pauli matrix corresponding to the direction of the stochastic magnetic field $H\left(\tau\right)$ parallel to the z-axis. Let $A^{int} = \oplus\Sigma_n A_n$ then the nonperturbed operator is defined as a direct sum $\mathcal{L} = (-\Delta) \oplus A^{int}$ in the space $L_2\left(\mathbb{R}^3\right) \oplus E^{int}$ of the kinetic energy operator $(-\Delta)$

and the "inner" operator A^{int}. The restriction $-\Delta \Rightarrow -\Delta_0$ on the linear set D_0^{ext} of all W_2^2-smooth functions in $\mathbb{R}^3 \setminus \{x_n\}_{n\in\mathbb{Z}}$ which have the following asymptotic:

$$u(x) \underset{x\to x_n}{\sim} \frac{u^{n-}}{4\pi\,|x-x_n|} + u^{n_0} + o\,(1)\,, \tag{2}$$

creates the boundary form:

$$J_{ext}\,(u,v) = \langle -\Delta_0^* u, v\rangle - \langle u, -\Delta_0^* v\rangle = -\sum_{n\in\mathbb{Z}} \left(u^{n-}\overline{v^{n_0}} - u^{n_0}\overline{v^{n-}}\right). \tag{3}$$

Here, $x_n = n\overrightarrow{e}$ are the positions of nuclei of the lattice.

The restriction of the inner operator $A^{int} \to A_0^{int}$ to the linear set D_0^{int} described in [2, 6] also leads to nontrivial boundary form:

$$J_{int}\,(\eta,\xi) = -\sum_{n\in\mathbb{Z}} \left(\eta^{n-}\overline{\xi^{n_0}} - \eta^{n_0}\overline{\xi^{n-}}\right), \tag{4}$$

where $\eta, \xi \in E^{int}$. We consider here the infinite vectors $\{u^{n-}\}$, $\{u^{n_0}\}$, $\{v^{n-}\}$, $\{u^{n_0}\}$, etc., to be elements from ℓ^2. It is obvious that the restricted operators $-\Delta_0$ and A_0^{int} have infinite deficiency indices (∞,∞). The boundary form $J_{ext}\,(u,v) + J_{int}\,(\eta,\xi)$ vanishes on the Lagrange planes given by the translation-invariant boundary conditions described in [11]:

$$\begin{pmatrix} u^{n-} \\ \eta^{n-} \end{pmatrix} = \sum_{m\in\mathbb{Z}} \mathbf{\Gamma}_{n-m} \begin{pmatrix} u^{n_0} \\ \eta^{n_0} \end{pmatrix}, \quad \mathbf{\Gamma}_{-n} = \mathbf{\Gamma}_n^*, \;\; |n| > N \to \mathbf{\Gamma}_n = \mathbf{0};$$

or

$$\begin{pmatrix} u^{n-} \\ -\eta^{n_0} \end{pmatrix} = \sum_{m\in\mathbb{Z}} \mathbf{B}_{n-m} \begin{pmatrix} u^{n_0} \\ \eta^{n-} \end{pmatrix}, \quad \mathbf{B}_{-n} = \mathbf{B}_n^*, \;\; |n| > N \to \mathbf{B}_n = \mathbf{0}. \tag{5}$$

Interaction between the nearest neighbors is introduced by these boundary conditions. We restrict our consideration to the case $N = 0$, $\mathbf{\Gamma}_0 = \begin{pmatrix} 0 & \alpha \\ \alpha & 0 \end{pmatrix}$:

$$\begin{pmatrix} u^{n-} \\ \eta^{n-} \end{pmatrix} = \begin{pmatrix} 0 & \alpha \\ \alpha & 0 \end{pmatrix} \cdot \begin{pmatrix} u^{n_0} \\ \eta^{n_0} \end{pmatrix}, \quad \Im\mathrm{m}\alpha = 0. \tag{6}$$

A self adjoint extension $\mathcal{L}\left(\overrightarrow{H}\,(\tau)\right)$ of the operator $-\Delta_0 \oplus A_0^{int}$ specified by the boundary conditions (6) simulates the Hamiltonian of the "neutron-lattice" system. Since $\overrightarrow{H} = \overrightarrow{H}\,(\tau)$, this Hamiltonian is time-dependent. We consider $\overrightarrow{H}\,(\tau)$ to be a Markovian stochastic process with two stochastic states. The corresponding evolution operator $U\,(t)$, restricted to a fixed trajectory of the process $\overrightarrow{H}\,(t)$, is the solution of the Cauchy problem:

$$\frac{1}{i}\cdot\frac{\partial U}{\partial \tau} = \mathcal{L}\left(\overrightarrow{H}\,(\tau)\right) U, \quad U|_{\tau=0} = I_q \equiv I_e \oplus I_i, \tag{7}$$

where I_e and I_i are the identity operators in the external and internal spaces respectively.

Together with the stochastic evolution described by equation (7), we will consider the "deterministic" evolutions corresponding to the Hamiltonians $\mathcal{L}\,(+H)$ and $\mathcal{L}\,(-H)$, in which the magnetic field is fixed in up-state $\overrightarrow{H} = H\overrightarrow{e}_z$ or in the down state $\overrightarrow{H} = -H\overrightarrow{e}_z$. On the intervals where $\overrightarrow{H}\,(\tau)$ is constant, the evolution equation (7) can be solved by the time-ordered exponentials corresponding to the operators $\mathcal{L}\,(+H)$ and $\mathcal{L}\,(-H)$ respectively. On each trajectory of magnetic momentum, the evolution operator (7) is the T-product of the corresponding exponentials (see [6]).

Starting with the equation for the transition probabilities whose resolvent matrix $\mathcal{P}$ represents a solution of the following equation:

$$\frac{d\mathcal{P}}{d\tau} = \chi \begin{pmatrix} -1 & 1 \\ 1 & -1 \end{pmatrix} \mathcal{P}, \quad \mathcal{P}\,(0) = \begin{pmatrix} 1 & 0 \\ 0 & 1 \end{pmatrix}, \tag{8}$$

we introduce the measure on the space of trajectories according to the paper [6]. The probability of the beam of trajectories which are in the states $\alpha_s = \pm H$ at the moments $t = s\delta$, $s = 0, 1, 2, \ldots, n$ can be defined by the following formula:

$$P_{\alpha_n,\alpha_{n-1},\ldots,\alpha_1} = \prod_{s=1}^{n} \left\{ \exp\left[\chi \begin{pmatrix} -1 & 1 \\ 1 & -1 \end{pmatrix}\right] \delta \right\}_{\alpha_n,\alpha_{n-1}}.$$

The averaged evolution operator can be calculated by the Trotter formula. By the same method as in [6] the following theorem can be proven:

Theorem 1. *The quantum evolution operator, averaged over the set of trajectories of magnetic field starting in the stochastic state β at $\tau = 0$ and ending in the stochastic state α at $\tau = T$ coincides with the element $\overline{U}_{\alpha\beta}(T)$ of the operator matrix, which satisfies the differential equation*

$$\frac{1}{i} \cdot \frac{\partial}{\partial \tau}\overline{U} = \hat{\mathcal{L}}_{\chi}\overline{U}, \qquad \overline{U}|_{t=0} = \begin{pmatrix} I_q & 0 \\ 0 & I_q \end{pmatrix}. \tag{9}$$

Here, the generator $\hat{\mathcal{L}}_{\chi}$ of the averaged semigroup $\overline{U}(\tau)$ is given by the following expression:

$$\hat{\mathcal{L}}_{\chi} = \begin{pmatrix} \mathcal{L}(+H) & 0 \\ 0 & \mathcal{L}(-H) \end{pmatrix} + i\chi \begin{pmatrix} I_q & 0 \\ 0 & I_q \end{pmatrix}. \tag{10}$$

It acts in the quantum-stochastic space $\hat{\mathcal{L}}_{\chi} = \left[L_2\left(\mathbb{R}^3 \oplus E^{int}\right)\right] \otimes \mathbb{R}^2$ which is the tensor product of the quantum space $\mathcal{H}_q = L_2\left(\mathbb{R}^3\right) \oplus E^{int}$ by the stochastic space $\mathbb{R}^2$, $\mathcal{H} = \mathcal{H}_q \oplus \mathcal{H}_q$.

3. Spectral analysis of the averaged operator

We will consider the perturbed $\hat{\mathcal{L}}_{\chi}$ and the unperturbed operator $\hat{\mathcal{L}}_{\chi}^0$ together. The unperturbed operator corresponds to the case when the quantum operator can be presented as the orthogonal sum of the operators in the external and internal spaces. It corresponds to the coupling constant α equal to zero. The external and internal parts of the unperturbed operator are:

$$-\hat{\Delta} = \begin{pmatrix} -\Delta & 0 \\ 0 & -\Delta \end{pmatrix} + i\chi \begin{pmatrix} I_q & -I_q \\ -I_q & I_q \end{pmatrix}$$

$$\hat{A}^{int} = \begin{pmatrix} A_{int}^u & 0 \\ 0 & A_{int}^d \end{pmatrix} + i\chi \begin{pmatrix} I_i & -I_i \\ -I_i & I_i \end{pmatrix}, \tag{11}$$

where $A_{int}^{u,d} = \oplus \sum\limits_n A^{u,d}$; $A^u = A(+H)$, $A^d = A(-H)$.

The unperturbed operator $\hat{\mathcal{L}}_{\chi}^0 = -\hat{\Delta} \oplus \hat{A}^{int}$ is normal and its spectral characteristics can be calculated explicitly. For example, the spectrum of this operator is the sum of the spectrum of the operator $-\hat{\Delta}$ (whose spectrum is purely continuous and consists of the two branches: $\lambda = k^2$ and $\lambda = k^2 + 2\imath\chi$, $\Im\mathrm{m}k = 0$) and the spectrum of the operator $\hat{A}^{int}$, which consists of four eigenvalues of infinite multiplicity:

$$\lambda_{1,2}\left(\hat{A}^{int}\right) = \lambda_0 + i\chi \pm \sqrt{H^2 - \chi^2}$$

$$\lambda_{3,4}\left(\hat{A}^{int}\right) = \lambda_1 + i\chi \pm \sqrt{H^2 - \chi^2}. \tag{12}$$

Calculating the resolvent of operator $\hat{\mathcal{L}}_{\chi}$ one can obtain, that the spectrum of $\hat{\mathcal{L}}_{\chi}$ is purely continuous and consists of the following branches:

1) $\mathbb{R}^+$ and $\mathbb{R}^+ + 2\imath\chi$, which coincide with the spectrum of the operator $\hat{\mathcal{L}}_{\chi}^0$

2) four branches, or bands, each corresponding to one of the eigenvalues of operator $\hat{\mathcal{L}}_{\chi}^0$. These branches can be calculated by solving the following equations:

$$\lambda - \lambda_n\left(\hat{\mathcal{L}}_{\chi}^0\right) = \pm\frac{\alpha_i^2}{32\pi}\frac{F_n(\lambda, t)}{\sqrt{h^2 - \chi^2}} + o(\alpha^2). \tag{13}$$

This formula is valid for the small values of the coupling constant α only. Sign “-” in the rhs of (13) corresponds to $n = 1, 3$, “+ ” to $n = 2, 4$. Function $F_n(\lambda, t)$ defined by the following expression:

$$F_n(\lambda, t) = (B_n^+ B_n^-)^{-1}\left\{B_n^+\left(C_n^- \Delta_u^n + i\chi_u^n\right) + B_n^-\left(C_n^+ \Delta_d^n + i\chi_d^n\right)\right\}, \tag{14}$$

$$\Delta_{u,d}^n = R^+(\lambda) D_n^{\pm} B_n^{\mp} - i\chi R^-(\lambda) B_n^{\pm} A_n^{\mp}, n = 0, 1; \tag{15}$$

$$\nabla_{u,d}^n = R^-(\lambda) D_n^{\mp} B_n^{\pm} - i\chi R^+(\lambda) B_n^{\mp} A_n^{\pm}, n = 0, 1;$$

$$R^{\pm}(\lambda) = \hat{B}\left(\sqrt{\lambda}, t\right) \pm \hat{B}\left(\sqrt{\lambda - 2i\chi}, t\right), \tag{16}$$

where $A_n^{\pm}, B_n^{\pm}, D_n^{\pm}$ are defined as in [6]:

$$A_0^{\pm} = \lambda_0 \pm H, \quad A_1^{\pm} = \lambda_1 \mp H,$$

$$B_n^{\pm} = A_n^{\pm} - i, \quad D_n^{\pm} = (i\chi - \lambda)\, A_n^{\pm} - i.$$

Parameter t in the formulas (13), (14), (16) is the quasimomentum and it belongs to the interval $[-\pi, \pi]$. The function $\hat{B}(\sqrt{\lambda}, t)$ is the lattice sum for the linear infinite chain:

$$\hat{B}\left(\sqrt{\lambda}, t\right) = ik + \sum_{n \in Z} \frac{\exp\left(i\sqrt{\lambda}|n|\right)}{4\pi|n|} \exp(-itn) = \ln\left(\frac{1}{2(\cos\sqrt{-(\lambda_0 + H_0)} - \cos t)}\right), \tag{17}$$

which was calculated first by Subramanian [10]. The branch of the logarithm is fixed by the condition of analytical continuability of $\hat{B}\left(\sqrt{\lambda}, t\right)$ into the complex spectral plane λ and vanishing of the imaginary part of the logarithm on the negative semi-axis. The properties of the function $\hat{B}\left(\sqrt{\lambda}, t\right)$ were described in [11].

Analysis of the equation (13) can be carried out for the small values of the coupling constant $a \ll 1$ and of the stochastic evolution parameter $\chi \ll 1$. In this case the resonant bands correspond to the negative eigenvalues of the operators $A^u = \begin{pmatrix} \lambda_0 + H & 0 \\ 0 & \lambda_1 - H \end{pmatrix}$ and $A^d = \begin{pmatrix} \lambda_0 - H & 0 \\ 0 & \lambda_1 + H \end{pmatrix}$. For example, let λ_0 be negative. Then the corresponding eigenvalue of the operator $\hat{\mathcal{L}}_\chi^0$ is given by the following asymptotic expression:

$$\lambda_1\left(\hat{\mathcal{L}}_\chi^0\right) \lambda_0 + H + i\chi + o(\chi), \tag{18}$$

and corresponding band by the expression:

$$\lambda_1(t) = \lambda_1\left(\hat{\mathcal{L}}_\chi^0\right) - \frac{\alpha^2 i}{8\pi} H\left[(\lambda_0 + H)^2 + 1\right] \ln \frac{1}{2\left(\cos\sqrt{-(\lambda_0 + H)} - \cos t\right)} + o(\alpha^2, \chi), \tag{19}$$

where $\ln$ is defined as a function of the real variable. The right edge of the band coincides with $\lambda(\pi)$ and the left one with $\lambda(0)$. The function $\hat{B}\left(\sqrt{\lambda}, t\right)$ is an even function of the variable t, hence the multiplicity of the spectrum is two (see Fig. 1).

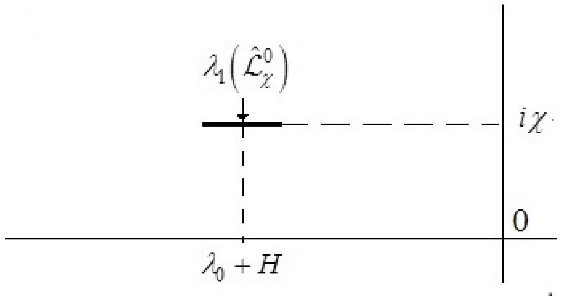

FIG. 1. Spectral band formed by the negative eigenvalue. The right edge of the band coincides with $\lambda_1(\pi)$ and the left one with $\lambda_1(0)$, where the argument t of the function $\lambda_1(t)$ is the quasimomentum (see formula (19) describing the band)

The structure of the band spectrum corresponding to the positive eigenvalues of the operators A^u, A^d is more complicated. Analysis of the equation (13) shows that the bands corresponding to each positive eigenvalue of $\hat{\mathcal{L}}_\chi^0$ have a gap (see Fig. 2). Let, for example, $\sqrt{\lambda_0 + H}$ be from the interval $[0, \pi]$. Then, the band has a gap near $\lambda_1\left(\hat{\mathcal{L}}_\chi^0\right)$. The second band of solutions of the equation (13) is situated exactly under this band, but it does not correspond to the spectrum of the operator. The first band transforms into the stationary (waveguide) band with the gap near $\lambda_0 + H$ when the parameter χ tends to zero. The second band transforms into the resonant gap (see Fig. 2 – Spectral band formed by the positive eigenvalue). The first band corresponds to the values of λ, that are less than $|t|^2$, the second - to $\lambda : |\lambda| > |t|^2$. When $\sqrt{\lambda_0 + H}$ is greater than π, no stationary band appears.

Thus, the spectrum of the operator $\hat{\mathcal{L}}_\chi$ consists of two scattered waves branches $\mathbb{R}^+$ and $\mathrm{R}^+ + 2i\chi$ and not more than four stationary bands (see Fig. 3). The Bloch waves corresponding to the resonant bands are increasing at infinity functions and are not eigenfunctions of the operator. We are going to prove that the generator $\hat{\mathcal{L}}_\chi$ is a dissipative operator with complex branches of the continuous spectrum. The corresponding eigenfunctions can be calculated (see the following papers [6, 11]). The eigenfunctions corresponding to the branches $\mathbb{R}^+$ and $\mathrm{R}^+ + 2i\chi$

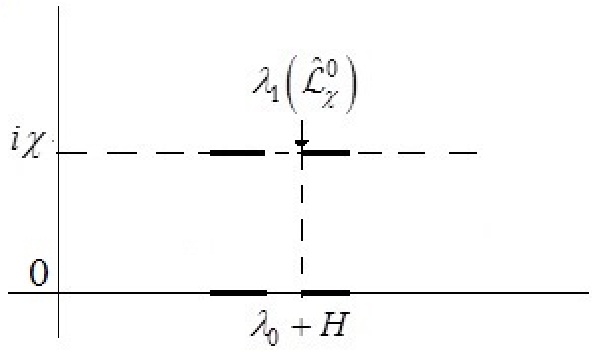

FIG. 2. Spectral band formed by the positive eigenvalue. Analysis of the equation (13) shows that when $\sqrt{\lambda_0 + H}$ is from the interval $[0, \pi]$, this band have a gap. When $\sqrt{\lambda_0 + H}$ is greater than π, no stationary band appears

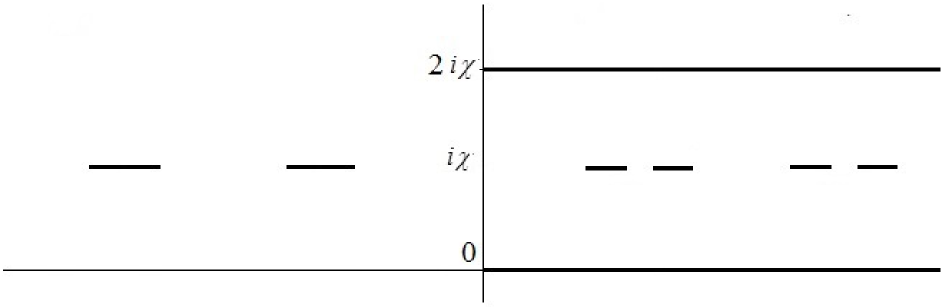

FIG. 3. Spectrum of the averaged operator. It consists of two branches $\mathbb{R}^+$ and $\mathbb{R}^+ + 2i\chi$, eigenfunctions corresponding to which have a form of scattered waves, and not more than four stationary bands

have a form of scattered waves. The initial plane wave is symmetric with respect to the stochastic variables for the branch $\mathbb{R}^+$ (or stable branch) of the spectrum:

$$\Psi_s(\lambda, \boldsymbol{\nu}) = \left\{ \begin{array}{c} \psi_s^{ext}(\mathbf{x}, \lambda, \boldsymbol{\nu}) \\ \psi_s^{int}(\lambda, nu) \end{array} \right., \ \lambda = k^2, \ k \geq 0, \ \boldsymbol{\nu} \in S^2, \tag{20}$$

$$\psi_s^{ext}(\mathbf{x}, \lambda, \boldsymbol{\nu}) = \exp\left\{-i\sqrt{\lambda}\langle \boldsymbol{\nu}, \mathbf{x}\rangle\right\} \cdot \left(\begin{array}{c} 1 \\ 1 \end{array}\right) + \left[f_{00}(\lambda, \boldsymbol{\nu}) \sum_{n\in\mathbb{Z}} \frac{\exp(ik|\mathbf{x} - \mathbf{x}_n|)}{4\pi|\mathbf{x} - \mathbf{x}_n|} \left(\begin{array}{c} 1 \\ 1 \end{array}\right) + \right.$$

$$\left. + f_{10}(\lambda, \boldsymbol{\nu}) \sum_{n\in\mathbb{Z}} \frac{\exp\left(i\sqrt{\lambda - 2i\chi}\,|\mathbf{x} - \mathbf{x}_n|\right)}{4\pi|\mathbf{x} - \mathbf{x}_n|} \cdot \left(\begin{array}{c} 1 \\ -1 \end{array}\right)\right] \exp\left(-i\sqrt{\lambda}\langle \boldsymbol{\nu}, \mathbf{x}_n\rangle\right), \tag{21}$$

$$\left(\psi_s^{int}(\lambda, \boldsymbol{\nu})\right)_n = \left(\begin{array}{c} \eta_u^0 \\ \eta_d^0 \end{array}\right)(\lambda, \boldsymbol{\nu}) \exp\left(-i\sqrt{\lambda}\langle \boldsymbol{\nu}, \mathbf{x}_n\rangle\right), \ \mathbf{x}_n = n\mathbf{e}.$$

The initial plane wave corresponding to the relaxation branch $\mathbb{R}^+ + 2i\chi$ is antisymmetric with respect to the stochastic variables:

$$\Psi_{as}(\lambda, \boldsymbol{\nu}) = \left\{ \begin{array}{c} \psi_{as}^{ext}(\mathbf{x}, \lambda, \boldsymbol{\nu}) \\ \psi_{as}^{int}(\lambda, nu) \end{array} \right., \ \lambda = k^2 + 2i\chi, \ k \geq 0, \ \boldsymbol{\nu} \in S^2, \tag{22}$$

$$\psi_{as}^{ext}(\mathbf{x}, \lambda, \boldsymbol{\nu}) = \exp\left\{-\imath\sqrt{\lambda - 2i\chi}\langle \boldsymbol{\nu}, \mathbf{x}\rangle\right\} \cdot \left(\begin{array}{c} 1 \\ -1 \end{array}\right) + \left[f_{01}(\lambda, \boldsymbol{\nu}) \sum_{n\in\mathbb{Z}} \frac{\exp(ik|\mathbf{x} - \mathbf{x}_n|)}{4\pi|\mathbf{x} - \mathbf{x}_n|} \cdot \left(\begin{array}{c} 1 \\ 1 \end{array}\right) + \right.$$

$$f_{11}(\lambda,\boldsymbol{\nu})\sum_{n\in\mathbb{Z}}\frac{\exp\left(i\sqrt{\lambda-2i\chi}\,|\mathbf{x}-\mathbf{x}_n|\right)}{4\pi\,|\mathbf{x}-\mathbf{x}_n|}\cdot\begin{pmatrix}1\\-1\end{pmatrix}\Bigg]\exp\left(-i\sqrt{\lambda-2i\chi}\,\langle\boldsymbol{\nu},\mathbf{x}_n\rangle\right), \tag{23}$$

$$\left(\psi_{as}^{int}(\lambda,\boldsymbol{\nu})\right)_n=\begin{pmatrix}\eta_u^0\\\eta_d^0\end{pmatrix}(\lambda,\boldsymbol{\nu})\exp\left(-i\sqrt{\lambda-2i\chi}\,\langle\boldsymbol{\nu},\mathbf{x}_n\rangle\right),\quad \mathbf{x}_n=n\mathbf{e}.$$

One can see, that the functions $\psi_s^{ext},\psi_{as}^{ext}$ satisfy Bloch conditions. For example:

$$\psi_s^{ext}(\mathbf{x}+m\tilde{\mathbf{e}},\lambda,\boldsymbol{\nu})=\psi_s^{ext}(\mathbf{x},\lambda,nu)\cdot\exp\left(-i\sqrt{\lambda}\langle\boldsymbol{\nu},m\vec{\mathbf{e}}\rangle\right),\quad m\in\mathbb{Z} \tag{24}$$

Explicit expressions for the amplitudes $f_{mn}(\lambda,\boldsymbol{\nu})$ in (21), (23) can be calculated by substitution of the considering ansatz (21), (23) for the scattered waves into the boundary conditions (6). For example, the amplitude $f_{00}(\lambda,\boldsymbol{\nu})$ is:

$$f_{00}(\lambda,\boldsymbol{\nu})=\frac{\alpha^2}{4}\sum_{n,m=0}^{1}\frac{\left(\lambda_n-(-1)^{n+m}H-\lambda\right)\left(\lambda_n+(-1)^{n+m}H-i\right)+2\imath\chi\left(\lambda_n-i\right)}{\left[(\lambda_n-i)^2-H^2\right]\left[(\lambda_n+i\chi-\lambda)^2-\left(H^2-\chi^2-F_k\left(\sqrt{\lambda},k_{\|}\right)\right)\right]}Z_n^m+o\left(\alpha^2\right), \tag{25}$$

where the following notations were used:

$$k_{\|}=k\,\langle\boldsymbol{\nu},\mathbf{e}\rangle;\quad k=\sqrt{\lambda};\quad Z_m^0=Z_m^+,Z_m^1=Z_m^-;\quad Z_m^{\pm}=i\chi B_m^{\pm}A_m^{\pm}-D_m^{\pm}B_m^{\pm} \tag{26}$$

The eigenfunctions corresponding to the stationary band can be calculated in the same way

$$\Psi_j(t)=\begin{cases}\psi_j^{ext}(\mathbf{x},t)\\\psi_j^{int}(t)\end{cases}. \tag{27}$$

Let us denote by $\lambda_j(t)$ the corresponding solution of the equation (13). Then the components of the eigenfunction are:

$$\psi_j^{ext}(\mathbf{x},t)=\frac{1}{2}\sum_{n\in\mathbb{Z}}\left[C_0\frac{\exp\left(i\cdot\sqrt{\lambda_j(t)}\,|\mathbf{x}-\mathbf{x}_n|\right)}{4\pi\,|\mathbf{x}-\mathbf{x}_n|}\begin{pmatrix}1\\1\end{pmatrix}+\right.$$

$$\left.+C_\chi\frac{\exp\left(i\cdot\sqrt{\lambda_j(t)-2i\chi}\,|\mathbf{x}-\mathbf{x}_n|\right)}{4\pi\,|\mathbf{x}-\mathbf{x}_n|}\begin{pmatrix}1\\-1\end{pmatrix}\right]\cdot\exp(-int),$$

$$\psi_j^{int}(t)=\begin{pmatrix}\eta_u^0\\\eta_d^0\end{pmatrix}(j,t)\exp(-int), \tag{28}$$

where the following notations were used:

$$C_{0,\chi}=\mathrm{const}\cdot\alpha\left(C_m^-B_m^+\pm i\chi B_m^-\right)+o\left(\alpha^2\right);$$

$$m=0\ \text{ for }\ j=1,2\ \text{ and }\ m=1\ \text{ for }\ j=3,4;$$

$$C_m^{\pm}\left(\lambda_j(t)\right)=A_m^{\pm}+i\chi-\lambda_j(t). \tag{29}$$

4. Eigenfunction-expansion theorem

We will restrict our consideration to the case of the initial data with the trivial “internal” component, i.e. we will consider functions:

$$\hat{f}\begin{pmatrix}f_u & \xi_u\\ f_d & \xi_d\end{pmatrix},\quad \xi_u=\xi_d=0. \tag{30}$$

The external part of the function can be defined as follows:

$$[\hat{f}]^{ext}(\mathbf{x})=\begin{pmatrix}f_u\\f_d\end{pmatrix}(\mathbf{x})\equiv f(\mathbf{x}),\quad f_u,f_d\in L_2(\mathbb{R}^3). \tag{31}$$

The following assertion can be proven:

Theorem 2. *Let the vector $\hat{f}$ from the quantum-stochastic space $\mathcal{H}$ has the form (30), then the following representation holds almost everywhere in the Lebesque measure sense:*

$$f(\mathbf{x})=\sum_{j=1}^{4}K_i\int\limits_{\Delta_j}dt\int\limits_{\mathbb{R}^3}d\mathbf{y}\,\psi_j^{ext}(\mathbf{x},t)\,\overline{\phi_j^{ext}(\mathbf{y},t)}f(\mathbf{y})+$$

$$+\frac{1}{16\pi^3}\int\limits_{\mathbb{R}^+} k^2dk\int\limits_{S^2} d\boldsymbol{\nu}\int\limits_{\mathrm{R}^3} d\mathbf{y}\left\{\psi_s^{ext}\left(\mathbf{x},k,\boldsymbol{\nu}\right)\overline{\phi_s^{ext}\left(\mathbf{y},t\right)}+\psi_{as}^{ext}\left(\mathbf{x},k,\boldsymbol{\nu}\right)\overline{\phi_{as}^{ext}\left(\mathbf{y},t\right)}\right\}f\left(\mathbf{y}\right). \tag{32}$$

Vector-valued functions $\phi_i\left(\mathbf{y},t\right)$, $\phi_{s,as}\left(\mathbf{y},k,\boldsymbol{\nu}\right)$ are externals parts of the eigenfunctions of the adjoint operator $\hat{\mathcal{L}}_\chi^*$ corresponding to the stationary bands and branches of the continuous spectrum $\mathbb{R}^+$ and $\mathbb{R}^+ + 2i\chi$ respectively. The intervals $\Delta_j = [-\alpha_j,-\beta_j]\cup[\beta_j,\alpha_j]$ are introduced in such a way, that the spectral parameter $\lambda_j\left(t\right)$ covers the stationary band twice, when the quasimomentum varies on the interval Δ_j.

This theorem can be proved by integrating by parts the bilinear form of the resolvent of the operator $\hat{\mathcal{L}}_\chi$ around the spectrum. This theorem allows us to calculate the averaged evolution operator $\overline{U}$, which will be used to derive the scattering operator:

$$\left[\overline{U}(\tau)\hat{f}\right]^{ext}(x)=\left[\exp i\hat{\mathcal{L}}_\chi\tau\hat{f}^{ext}\right](\mathbf{x})=$$

$$\sum_{j=1}^{4}K_j\int\limits_{\Delta_j}dt\cdot\exp\left(i\lambda_j\left(t\right)\tau\right)\int\limits_{\mathbb{R}^3}d\mathbf{y}\cdot\psi_j^{ext}\left(\mathbf{x},t\right)\overline{\phi_j^{ext}\left(\mathbf{y},t\right)}f\left(\mathbf{y}\right)+$$

$$+\frac{1}{16\pi^3}\int\limits_{\mathbb{R}^+}\exp\left(ik^2\tau\right)k^2dk\int\limits_{S^2}d\boldsymbol{\nu}\int\limits_{\mathbb{R}^3}d\mathbf{y}\cdot\psi_s^{ext}\left(\mathbf{x},k,\boldsymbol{\nu}\right)\overline{\phi_s^{ext}\left(\mathbf{y},t\right)}f\left(\mathbf{y}\right)+$$

$$+\frac{1}{16\pi^3}\int\limits_{\mathbb{R}^+}\exp\left(i\left(k^2+2i\chi\right)\tau\right)k^2dk\int\limits_{S^2}d\boldsymbol{\nu}\int\limits_{\mathbb{R}^3}d\mathbf{y}\cdot\psi_{as}^{ext}\left(\mathbf{x},k,\boldsymbol{\nu}\right)\overline{\phi_{as}^{ext}\left(\mathbf{y},t\right)}f\left(\mathbf{y}\right). \tag{33}$$

5. Scattering operator

The averaging of the quantum evolution leads to the evolution operator semigroup with the generator $\hat{\mathcal{L}}_\chi$:

$$\overline{U}(\tau)=\exp\left(i\hat{\mathcal{L}}_\chi\tau\right),\quad \tau>0,$$

which acts in the quantum-stochastic space $\mathcal{H}$. Formula (33) shows that the contribution of the nonreal part of the spectrum tends to zero for large $\tau\to\infty$. As a result, only the real branch of spectrum $\mathbb{R}^+$ contributes to the scattering process. We will define the unperturbed operator for the scattering problem as the restriction of the operator $-\hat{\Delta}$ to the stable invariant subspace corresponding to the real branch of the continuous spectrum $\mathbb{R}^+$. The corresponding operator will be denoted by $\hat{L}_0$. It is unitarily equivalent to the nonperturbed Laplacian defined on the domain $W_2^2\left(\mathbb{R}^3\right)$. The identification operator $J=J_0$ is the projector on the set H_s of the functions which are symmetric with respect to the stochastic variables. In this way we eliminate the relaxation branch and the scattering matrix can be defined as follows:

$$\overline{S}_\chi(\alpha,\hat{L}_0)=s-\lim_{\tau\to\infty}\exp\left(-i\hat{L}_0\tau\right)J_0\exp\left(2i\hat{\mathcal{L}_\chi}\tau\right)J_0^*\exp\left(-i\hat{L}_0\tau\right). \tag{34}$$

Using the unitary operator $\Sigma : H_s\to L_2\left(\mathbb{R}^3\right)$:

$$\Sigma:\hat{f}=\begin{pmatrix} f\\ f\end{pmatrix}\to\frac{1}{2}(f+f)=f,$$

the averaged scattering operator from $L_2\left(\mathbb{R}^3\right)$ to $L_2\left(\mathbb{R}^3\right)$ can be written in the following form:

$$\overline{S}_\chi(\alpha)=s-\lim_{\tau\to\infty}\exp\left(i\Delta\tau\right)\Sigma J_0\overline{U}(2\tau)J_0^*\Sigma^*\exp\left(i\Delta\tau\right). \tag{35}$$

Then the averaged scattering matrix can be calculated:

$$\overline{S}_\chi\left(\mathbf{p},\mathbf{p}'\right)=\delta\left(\mathbf{p}-\mathbf{p}'\right)-\frac{1}{4\pi^2}\delta\left(\mathbf{p^2}-(\mathbf{p}')^\mathbf{2}\right)\cdot f_{00}\left(|\mathbf{p}|,-\frac{\mathbf{p}}{|\mathbf{p}|}\right)\sum_{n\in\mathbb{Z}}\delta\left(2\pi n+\langle\mathbf{p}-\mathbf{p}',\mathbf{e}\rangle\right), \tag{36}$$

Thus the scattering amplitude $f\left(\boldsymbol{\omega},\boldsymbol{\nu},k\right)$ has the following form:

$$f\left(\boldsymbol{\omega},\boldsymbol{\nu},k\right)=-f_{00}\left(k,\boldsymbol{\nu}\right)\cdot\sum_{n\in\mathbb{Z}}\delta\left(2\pi n+k\langle\boldsymbol{\nu}+\boldsymbol{\omega},\mathrm{e}\rangle\right), \tag{37}$$

where $f_{00}\left(k,\boldsymbol{\nu}\right)$ depends on the direction of the initial plane wave trough the projection of the vector $k\boldsymbol{\nu}$ on the lattice vector $\tilde{\mathbf{e}}$:

$$k_{\|}=k\left\langle\boldsymbol{\nu},\mathbf{e}\right\rangle.$$

The scattering amplitude has Laue singularities.

It is important to discuss the limit of the scattering amplitude when the stochastic parameter tends to zero. We will denote by $f^{\pm}(\boldsymbol{\omega}, \boldsymbol{\nu}, k)$ the scattering amplitudes corresponding to the operators with the fixed stochastic states: $\mathcal{L}(+H)$ and $\mathcal{L}(-H)$. Then the following formula can be derived:

$$\lim_{\chi \to 0} f(\boldsymbol{\omega}, \boldsymbol{\nu}, k) = \frac{1}{2}\left[f^{+}(\boldsymbol{\omega}, \boldsymbol{\nu}, k) + f^{-}(\boldsymbol{\omega}, \boldsymbol{\nu}, k)\right]. \tag{38}$$

This formula shows that the limit amplitude is equal to the arithmetic average of the amplitudes corresponding to the deterministic processes.

Acknowledgement

This work was initiated by my professor B. S. Pavlov, an outstanding mathematician of the St. Petersburg mathematical school who passed away more than two years ago.

The author wants to thank professor P. B. Kurasov for the scientific support in solving the problem under consideration.

References

[1] Berezin F.A., Faddeev L.D. Remark on the Schrödinger equation with singular potential. *Dokl. Akad. Nauk SSSR*, 1961, **137**(5), P. 1011–1014 (in Russian).

[2] Pavlov B.S. Model of a zero-range potential with internal structure. *Theoret. and Math. Phys.*, 1984, **59**(3), P. 544–550.

[3] Pavlov B.S., The theory of extensions and explicitly-soluble models. *Russian Math. Surveys*, 1987, **42**(6), P. 127–168.

[4] Albeverio S. and Kurasov P. Singular perturbations of differential operators. *Solvable Schrodinger type operators*. London Mathematical Society Lecture Notes 271, Cambridge Univ. Press, Cambridge 2000, 444 p.

[5] Boitsev A.A., Neidhardt H., Popov I.Y. Dirac operator coupled to bosons. *Nanosystems: Physics, Chemistry, Mathematics*, 2016, **7**(2), P. 332–339.

[6] Pavlov B.S., Ryzhkov A.E. Scattering on a random point potential, in P.Exner, P.Seba *Applications of Self-Adjoint Extensions in Quantum Physics*, Lecture Notes in Physics no 324, Springer-Verlag, Berlin-Heidelberg-New York, 1989, P. 100–114.

[7] Ryzhkov A.E. Scattering of the acoustic waves on a Markovian point defect, in P. Exner, P. Seba. *Schroedinger Operators, Standard and Nonstandard*, World Scientific, Singapore, 1989, P. 407–409.

[8] Albeverio S., Gesztesy F., Hoegh-Krohn R. and Holden H., with an appendix by P. Exner. *Solvable Models in Quantum Mechanics*, 2-nd ed., American Mathematical Society, Providence, Rhode Island, 2005, 488 p.

[9] Karpeshina Yu.E. Eigenfunction-expansion theorem of scattering problems on one-dimensional periodic supports of the chain type in three-dimensional space. *Problemy Mat. Fiz.*, 1983, **10**, P. 137–163 (in Russian).

[10] Subramanian R. *Some applications of the method of zero-range potentials in quantum mechanics*. Author's Abstract of Candidate's Dissertation, Leningrad State University, 1986 (in Russian).

[11] Kurasov P.B., Pavlov B.S. Electron in a homogeneous crystal of point atoms with internal structure. II. *Theoret. and Math. Phys.*, 1988, **74**(1), P. 58–66.

NANOSYSTEMS: PHYSICS, CHEMISTRY, MATHEMATICS, 2018, 9 (6), P. 711–715

Models of the energy landscape for an element of shakti spin ice

U. B. Arnalds[1], S. Y. Liashko[1,2], P. F. Bessarab[1,2], V. M. Uzdin[2,3], H. Jónsson[1,4,5]
[1]Science Institute, University of Iceland, 107 Reykjavík, Iceland
[2]ITMO University, Kronverkskiy, 49, St. Petersburg, 197101, Russia
[3]St. Petersburg State University, St. Petersburg, 198504, Russia
[4]Faculty of Physical Sciences, University of Iceland, 107 Reykjavík, Iceland
[5]Dept. of Applied Physics, Aalto University, Espoo, FI-00076, Finland
v_uzdin@mail.ru

PACS 75.75.-c, 75.75.Jn, 75.60.Jk **DOI 10.17586/2220-8054-2018-9-6-711-715**

Micromagnetic calculations are compared with faster model calculations of interacting nanoscopic magnetic islands representing an element of a shakti spin ice lattice. Several pathways for transitions between equivalent ground states are studied. The model calculations describe the interaction between the islands either with the point dipole approximation, or with a dumbbell approximation where the distance between the two poles is optimized to match the micromagnetic results. The closest agreement in the energy of both local minima as well as transition state configurations where one macrospin has rotated by 90° is obtained with a dumbbell model where the distance between the poles is ca. 20 % smaller than the island length.

Keywords: magnetic islands, activation energy, micromagnetics, dipole interaction, dumbbell, spin ice.

Received: 11 November 2018

Revised: 18 November 2018

1. Introduction

Artificial spin systems have made it possible to study magnetic ordering phenomena and thermal dynamics at macroscopic length scales in extended spin arrays. These systems consist of lithographically patterned magnetic islands arranged in various ways. Initially, the arrangements were chosen to mimic pyrochlore spin ice [1] but the vast capabilities available within nanostructuring have allowed new research into a multitude of different types of systems [2–5]. The interaction between the islands affects the properties of the artificial spin ice systems controlling their ground state magnetic ordering and affecting the energy barriers for transitions between various possible orientations of the magnetization of the islands. The arrangement of the islands, therefore, directly affects the energetics of the system.

The shakti lattice is a recent addition to the catalog of artificial spin ice systems. Extended systems of this geometry have been studied both theoretically [6, 7] as well as experimentally [9, 10]. Interestingly, the shakti geometry falls into a category of pentagonal tilings but is often described as a decimation of a square tiling. A closer analogy would be that of a Cairo pentagonal tiling or a Panama weave tiling as the system is composed of islands of two different lengths [6]. The different island lengths give rise to different energy barriers for reversing their magnetization direction creating an energy scale hierarchy affecting the energy landscape and ordering of the system [10].

Studies of finite arrays of islands representing a part of an extended system have been important for gaining an understanding of the physical properties of artificial spin ice systems. The magnetic ordering of kagome spin ice building blocks has been extensively studied both for demagnetized states [8] and thermally relaxed ground state ordering [11] as well as thermally induced dynamics [12]. For square ice building blocks, thermal effects have been directly measured through their stray field [13, 14]. Studies of the energy landscape and ordering of shakti lattice building blocks containing elements of two different island sizes have previously not been reported in the literature.

Several different methodologies have been applied to model artificial spin ice to gain an understanding of the energetics and underlying physics. Micromagnetics is the most accurate approach but it requires significant computational effort even for systems consisting of only a few islands. Calculations involving magnetization dynamics and incorporation of thermal effects in extended spin ice systems are computationally too demanding at this level of theory. Simpler models such as the point dipole or dumbbell representations of each island have therefore been used to calculate ground state ordering, thermal dynamics and long range interaction between islands. In the point dipole model, a magnetic dipole is placed at the center of each island and the dipole-dipole interaction between islands evaluated, while for the dumbbell approximation, two magnetic charges, separated by some fixed distance, are placed on each island [15–17].

The mechanism of thermally assisted transitions in such systems can be evaluated using the geodesic nudged elastic band (GNEB) method [18] where the activation energy is obtained as the energy rise along the minimum energy path for the transition. The pre-exponential in the Arrhenius rate expression can be estimated from harmonic transition state theory [19–21] as has been demonstrated for isolated islands [22] as well as elements of kagome spin ice [23]. When the islands are not too large, the magnetization can be in a single domain state and described by a single vector, the macrospin. The GNEB and harmonic transition state theory (HTST) methodology can, however, also be used to describe more general transition mechanisms where the internal structure of the island is taken into account [24].

In this article, the energetics of a shakti spin ice element consisting of eight small islands and one large island is studied. Two reversal pathways between equivalent, low energy states are studied. The point dipole model and dumbbell model with adjustable distance between the magnetic charges are compared with micromagnetic calculations for both local energy minima and configurations representing transition states.

2. Models and methodology

The system investigated in this study can be considered as a building block of the shakti lattice comprising one long island and eight surrounding short islands, as shown in Fig. 1. The islands are stadium shaped, 150 nm wide of 3 nm thickness and with a length of 450 nm (short islands) or 1050 nm (long islands). The lattice constant, defined as shown in Fig. 1, is taken to be 600 nm. The islands are assumed to be composed of a soft magnetic material with magnetization of $M = 200$ kA/m. The dimensions of the islands and materials parameters used for the modeling are similar to those previously reported in the literature.

2.1. Micromagnetic modelling

The energetics of the system are modeled by micromagnetic calculations performed using the software mumax3 [25]. The exchange constant is taken to be $A = 13 \times 10^{-12}$ J/m and the magnetization value given above. No magnetocrystalline anisotropy is included for the magnetic material composing the islands. The total magnetic moment of the islands comes out to be $4.05 \times 10^6\ \mu_{\rm B}$ for the small islands and $10.5 \times 10^6\ \mu_{\rm B}$ for the large ones.

The energy associated with the macrospin of each island includes a shape anisotropy term, $E_a = K\cos(\theta)^2$, where θ is the angle between the magnetization and the long axis, in addition to the total sum of magnetostatic interaction with all the other macrospins in the system. The micromagnetic model is used to evaluate this anisotropy term which is added to the dipole and dumbbell models. The anisotropy parameter K is determined by calculating the energy increase when the macrospin of an island is rotated from the low energy state with the magnetization pointing along the long axis of the island to the elevated energy state where the magnetization is pointing perpendicular to the long axis. In both cases, the macrospin vector is in the plane of the island. This shape anisotropy term corresponds to $K = 0.69$ eV and 1.78 eV for the short and long islands, respectively.

2.2. Point dipole model

In the point dipole model, the energy of the system is approximated as

$$E_{d-d} \;=\; E_a \;-\; M^2 \sum_i \sum_{j>i} V_i V_j \left(\frac{\vec{m}_i \cdot \vec{m}_j}{|\vec{r}_{ij}|^3} - \frac{3\ \vec{m}_i \cdot \vec{r}_{ji}\ \vec{m}_j \cdot \vec{r}_{ij}}{|\vec{r}_{ij}|^5} \right) \tag{1}$$

where V_i is the volume of island i, M is the magnetization per volume, m_i a unit vector giving the direction of the magnetic moment of island i, $\vec{r}_i$ is the location of the center of island i and $\vec{r}_{ij} = \vec{r}_j - \vec{r}_i$.

2.2.1. Dumbbell model. In the dumbbell model, the energy of the system is approximated as

$$E_{db} \;=\; E_a \;- M^2 \sum_i \sum_{j>i} \frac{V_i V_j}{d_i d_j} \left(\frac{1}{|\vec{r}_{p_i} - \vec{r}_{p_j}|} - \frac{1}{|\vec{r}_{p_i} - \vec{r}_{n_j}|} - \frac{1}{|\vec{r}_{n_i} - \vec{r}_{p_j}|} + \frac{1}{|\vec{r}_{n_i} - \vec{r}_{n_j}|} \right) \tag{2}$$

where $\vec{r}_{p_i}$ and $\vec{r}_{n_i}$ are the locations of the positive and negative charges associated with island i, placed symmetrically along the long axis of the island, and d_i is the distance between them. We introduce here an adjustable parameter in the dumbbell model, namely the ratio of the distance and the length of the island, d/L. Traditionally, d has been assumed to be equal the length of the island, i.e. the magnetic charges are placed at opposite ends of the islands. As we demonstrate below, this leads to an overestimation of the interaction. The scaling parameter d/L is thus introduced to adjust the strength of the interaction and match the results of the micromagnetic calculations. The same ratio is used for the small and the large islands. For a small distance between the two magnetic charges,

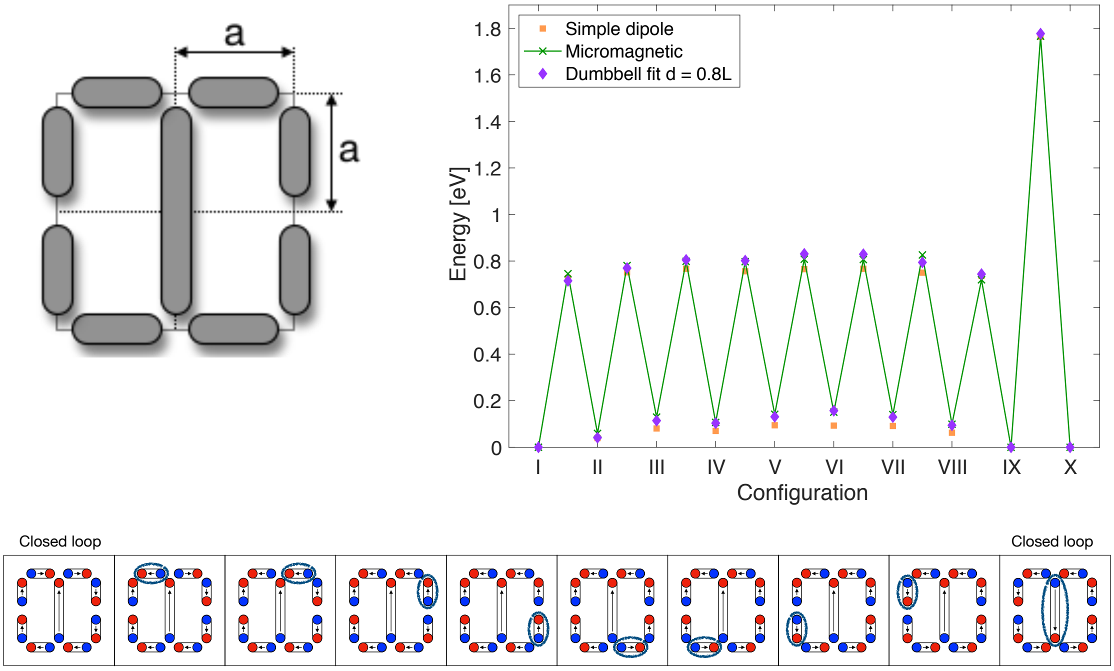

FIG. 1. **Top left:** An illustration of the shakti lattice building block studied here showing the definition of the lattice parameter, a. The long island has the same nearest neighbor distance as the shorter islands. **Top right:** Comparison of micromagnetic, dipole and scaled dumbbell model calculations of the energy along a transition path from one low energy, closed loop state to another equivalent one with opposite orientation of the magnetic moments. The point dipole model underestimates while the dumbbell model overestimates the interaction energy. By reducing the distance between the two magnetic charges to 0.8 of the island length, $d = 0.8L$, close agreement is obtained between the dumbbell and micromagnetic results. **Bottom:** Schematic illustration of the arrangement of the magnetic moments along the transition path between the two closed loop ground states. The island where the macrospin has been reversed in going from left to right is circled.

$d/L < 0.1$, the dumbbell model gives results that are close to those of the point dipole model. For larger distances, the dumbbell model includes the effect of higher order multipoles in the multipole expansion of the magnetic field of an island. As a result, the dumbbell model gives stronger interaction between the islands than the point dipole model.

3. Results

The calculations of the shakti element are started with each macrospin pointing along the long axis of the corresponding island, forming either in a closed loop configuration, where the macrospins of all the short islands are arranged head to tail (shown in Fig. 1) or in a so-called onion configuration (shown in Fig. 2). The orientation of the macrospins is then allowed to change in order to minimize the energy of the system. This relaxation turns out to result in only a minor change in the orientation of the macrospins and the energy of the system. In the micromagnetic calculations, the closed loop state is found to be slightly lower in energy than the onion state, by 0.05 eV.

The GNEB method is used in combination with the point dipole model to find an optimal transition path between the two closed loop states as well as an optimal transition path between the two onion states. The resulting paths determined from these calculations are shown in Fig. 1,2. For each island, there are two possibilities for rotating the macrospin, either inward or outward. Depending on the arrangement of the macrospins of the neighboring island, one could have a lower energy barrier than the other. The figure shows the energy for the rotation direction that corresponds to the lower energy barrier, but in all cases the difference is small. The energy along these paths is then evaluated using also the micromagnetic and the dumbbell models.

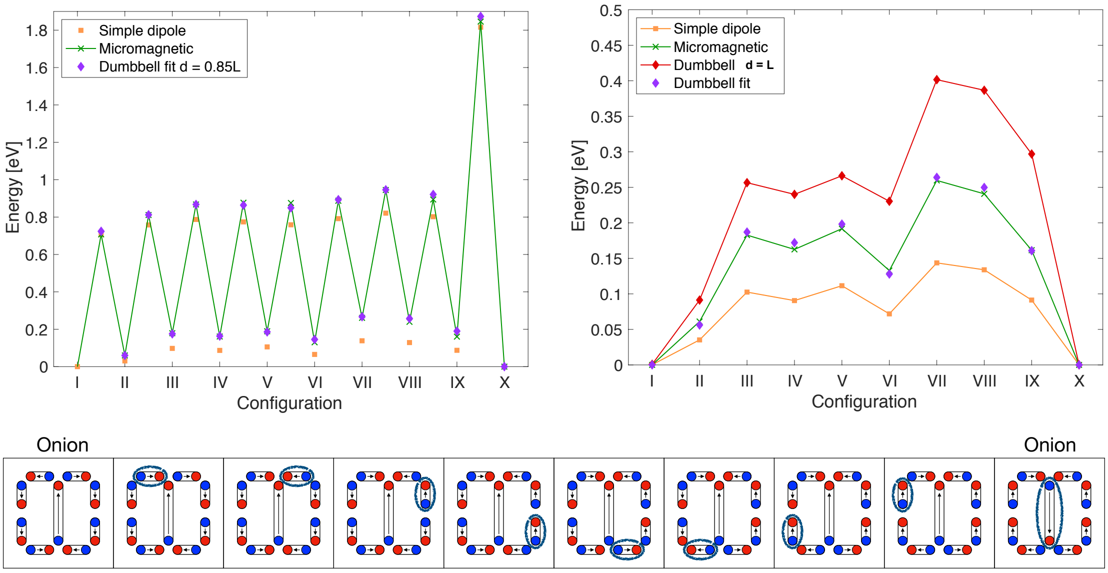

FIG. 2. **Top left:** Comparison of micromagnetic, dipole and scaled dumbbell model calculations of the energy along a transition path from one onion state to another equivalent one with opposite orientation of the magnetic moments. The point dipole model underestimates while the dumbbell model overestimates the interaction energy. By reducing the distance between the two magnetic charges, $d = 0.85L$, close agreement is obtained between the dumbbell and micromagnetic results. **Top right:** A zoom in on the energy of the local minima, same as on the graph to the left. The overestimate of the interaction energy when the magnetic charges are placed at the end of the islands, $d = L$, is about as large as the underestimation by the point dipole model. **Bottom:** Schematic illustration of the arrangement of the magnetic moments along the transition path between the two onion states. The island where the macrospin has been reversed in going from left to right is circled.

Figures 1, 2 show the calculated results for the transition paths between the two closed loop states (see Fig. 1) and between the two onion states (see Fig. 2). Both the energy of the various states as well as the estimated activation energy for macrospin rotations are shown. The activation energy for the rotation of the large island macrospin occurs last in these paths and is clearly much larger than the activation energy for the small islands. The point dipole model is found to underestimate the interaction energy. Both the energy of the various local energy minima and the estimates of the energy barriers are lower than the micromagnetic predictions. The dumbbell model, however, overestimates the interaction energy by a similar amount (see results for $d = L$ in the top right of Fig. 2). However, by bringing the magnetic charges closer by about 20 %, the dumbbell model can reproduce the micromagnetic results quite well, both the energy minima and the energy barriers.

4. Conclusions

The calculated results presented here show that the point dipole model can underestimate the interaction between islands in spin ice systems, while the dumbbell model gives an overestimation. A modified dumbbell model where the distance between the magnetic poles in an island is smaller than the length of the island, in this case by ca. 20 %, can however reproduce the results of micromagnetic calculations quite closely. Not only is the energy of the various states reproduced well, but also the energy barriers for transitions. The same parameter value was used for the large and small islands in the shakti lattice element studied here, but it remains to be seen how general the optimal value of this parameter is for the large variety of islands used in spin ice systems.

In order to simulate the long time scale evolution of spin ice systems, it is important to have a model for the energetics that does not require excessive computational effort. The modified dumbbell model with a scaled distance parameter appears to provide a good choice. The mechanism and rate of transitions can then be calculated using saddle point searches with the adaptation of the minimum mode following method to magnetic systems [26] and long time scale evolution simulated with the adaptive kinetic Monte Carlo method [27, 28].

5. Acknowledgments

This work was funded by Icelandic Research Fund (grants no. 152483-051, 185405-051, 163048-053 and 184949-051), University of Iceland Research Fund and Russian Foundation of Basic Research (grant RFBR 18-02-00267 A). The calculations were performed on resources provided by the Icelandic High Performance Computing Centre at the University of Iceland.

References

[1] Wang R.F., Nisoli C., Freitas R.S., Li J., McConville W., Cooley B.J., Lund M.S., Samarth N., Leighton C., Crespi V.H. and Schiffer P. Artificial 'spin ice' in a geometrically frustrated lattice of nanoscale ferromagnetic islands. *Nature*, 2006, **439**, P. 303–306.

[2] Nisoli C., Moessner R. and Schffer P. *Colloquium*: Artificial spin ice: Designing and imaging magnetic frustration. *Rev. Mod. Phys.*, 2013, **85**, P. 1473–1490.

[3] Kapaklis V., Arnalds U.B., Farhan A., Chopdekar R.V., Balan A., Scholl A., Heyderman L.J. and Hjörvarsson B. Thermal fluctuations in artificial spin ice. *Nat. Nanotech.*, 2014, **9**, P. 514–519.

[4] Farhan A., Scholl A., Petersen C.F., Anghinolfi L., Wuth C., Dhuey S., Chopdekar R.V., Mellado P., Alava M.J. and van Dijken S. Thermodynamics of emergent magnetic charge screening in artificial spin ice. *Nat. Commun.*, 2016, **7**, P. 12635 (6 pp).

[5] Arnalds U.B., Chico J., Stopfel H., Kapaklis V., Bärenbold O., Verschuuren M.A., Wolff U., Neu V., Bergman A. and Hjörvarsson B. A new look on the two-dimensional Ising model: thermal artificial spins. *New J. Phys.*, 2016, **18**, P. 023008 (8 pp).

[6] Chern G.-W., Morrison M.J. and Nisoli C. Degeneracy and Criticality from Emergent Frustration in Artificial Spin Ice. *Phys. Rev. Lett.*, 2013, **111**, P. 177201 (5 pp).

[7] Morrison M.J., Nelson T.R. and Nisoli C. Unhappy vertices in artificial spin ice: New degeneracies from vertex frustration. *New J. Phys.*, 2013, **15**, P. 045009 (23 pp).

[8] Mengotti E., Heyderman L.J., Rodríguez F., Bisig A., Le Guyader L., Nolting F. and Braun H.-B. Building blocks of an artificial kagome spin ice: Photoemission electron microscopy of arrays of ferromagnetic islands. *Phys. Rev. B*, 2008, **78**, P. 144402 (7 pp).

[9] Gilbert I., Chern G.-W., Zhang S., O'Brien L., Fore B., Nisoli C. and Schiffer P. Emergent ice rule and magnetic charge screening from vertex frustration in artificial spin ice. *Nat. Phys.*, 2014, **10**, P. 670–675.

[10] Stopfel H., Östman E., Chioar I.-A., Greving D., Arnalds U.B., Hase T.P.A, Stein A., Hjörvarsson B. and Kapaklis V. Magnetic order and energy-scale hierarchy in artificial spin-ice structures. *Phys. Rev. B*, 2018, **98**, P. 014435 (8 pp).

[11] Arnalds U.B., Farhan A., Chopdekar R.V., Kapaklis V., Balan A., Papaioannou E.T. Ahlberg M., Nolting F., Heyderman L.J. and Hjörvarsson B. Thermalized ground state of artificial kagome spin ice building blocks. *Appl. Phys. Lett.*, 2012, **101**, P. 112404 (4 pp).

[12] Farhan A., Derlet P.M., Kleibert A., Balan A., Chopdekar R.V., Wyss M., Anghinolfi L., Nolting F. and Heyderman L.J. Exploring hyper-cubic energy landscapes in thermally active finite artificial spin-ice systems. *Nat. Phys.*, 2013, **9**, P. 375–382.

[13] Pohlit M., Porrati F., Huth M., Ohno Y., Ohno H. and Müller J. Nanocluster building blocks of artificial square spin ice: Stray-field studies of thermal dynamics. *J. Appl. Phys.*, 2015, **117**(17), P. 17C746.

[14] Pohlit M., Porrati F., Huth M., Ohno Y., Ohno H., and Müller J., Magnetic stray-field studies of a single Cobalt nanoelement as a component of the building blocks of artificial square spin ice. *J. Magn. Magn. Mater.*, 2016, **400**, P. 206–212.

[15] Chern G.-W., Mellado P. and Tchernyshyov O., Two-Stage Ordering of Spins in Dipolar Spin Ice on the Kagome Lattice. *Phys. Rev. Lett.*, 2011, **106**, P. 207202 (4 pp).

[16] Castelnovo C., Moessner R., and Sondhi S.L. Magnetic monopoles in spin ice. *Nature*, 2008, **451**, P. 42–45.

[17] Möller G. and Moessner R. Magnetic multipole analysis of kagome and artificial spin-ice dipolar arrays. *Phys. Rev. B*, 2009, **80**, P. 140409 (4 pp).

[18] Bessarab P.F., Uzdin V.M. and Jónsson H. Method for finding mechanism and activation energy of magnetic transitions, applied to skyrmion and antivortex annihilation. *Comp. Phys. Commun.*, 2015, **196**, P. 335–347.

[19] Bessarab P.F., Uzdin V.M. and Jónsson H. Harmonic transition state theory of thermal spin transitions. *Phys. Rev. B*, 2012, **85**, P. 184409 (4 pp).

[20] Bessarab P.F., Uzdin V.M. and Jónsson H. Potential energy surfaces and rates of spin transitions. *Z. Phys. Chem.*, 2013, **227**, P. 1543–1557.

[21] Liashko S.Y., Uzdin V.M., Jónsson H. Thermal stability of magnetic states in submicron magnetic islands. *Nanosystems: Physics, Chemistry, Mathematics*, 2017, **8**(5), P. 572–578.

[22] Liashko S.Y., Jónsson H., Uzdin V.M. Calculations of switching field and energy barrier for magnetic islands with perpendicular anisotropy. *Nanosystems: Physics, Chemistry, Mathematics*, 2017, **8**(6), P. 701–708.

[23] Liashko S.Y., Jónsson H., Uzdin V.M. The effect of temperature and external field on transitions in elements of kagome spin ice. *New J. Phys.*, 2017, **19**, P. 113008 (8 pp).

[24] Bessarab P.F., Uzdin V.M. Jónsson H. Size and shape dependence of thermal spin transitions in nanoislands. *Phys. Rev. Lett.*, 2013, **110**(2), P. 020604 (5 pp).

[25] Vansteenkiste A., Leliaert J., Dvornik M., Helsen M., Garcia-Sanchez F. and Van Waeyenberge B. The design and verification of MuMax3. *AIP Advances*, 2014, **4**, P. 107133 (22 pp).

[26] Müller G., Bessarab P.F., Vlasov S.M., Lux F., Kiselev N.S., Blügel S., Uzdin V.M. and Jónsson H. Duplication, collapse and escape of magnetic skyrmions revealed using a systematic saddle point search method. *Phys. Rev. Lett.*, 2018, **121**, P. 197202 (5 pp).

[27] Henkelman G. and Jónsson H. Long time scale kinetic Monte Carlo simulations without lattice approximation and predefined event table. *J. Chem. Phys.*, 2001, **115**, P. 9657–9666.

[28] Chill S.T., Welborn M., Terrell R., Zhang L., Berthet J.-C., Pedersen A., Jónsson H., and Henkelman G. EON: Software for long time simulations of atomic scale systems. *Modelling Simul. Mater. Sci. Eng.*, 2014, **22**, P. 055002 (16 pp).

NANOSYSTEMS: PHYSICS, CHEMISTRY, MATHEMATICS, 2018, 9 (6), P. 716–723

Edge states in coupled periodic dielectric waveguides induced by long-range interaction

R. S. Savelev
ITMO University, St. Petersburg 197101, Russia
r.savelev@metalab.ifmo.ru

PACS 42.79.Gn, 42.82.Et **DOI 10.17586/2220-8054-2018-9-6-716-723**

We study the properties of coupled periodic dielectric nanowaveguides and reveal that finite arrays of equally spaced waveguides with certain parameters support edge modes, which originate due to the presence of the long-range interactions between the waveguides. We provide a simple model of the coupled waveguides with next-to-nearest neighbors interaction that captures the main properties of the considered system including the formation of the edge states. The predicted results suggest that the arrays of periodic dielectric nanowaveguides may serve as a fruitful system for studying the discrete coupled systems with long-range interaction and realizing optical metasurfaces with novel functionalities for guiding surface waves.

Keywords: periodic waveguides, coupled discrete systems, edge states, long-range interaction.

Received: 19 November 2018

Revised: 6 December 2018

1. Introduction

Recently, arrays of coupled dielectric and plasmonic waveguides have been studied in a vast amount of theoretical and experimental works and have been proven to serve as a very convenient platform to study various optical effects such as discrete diffraction [1], observation of topologically protected photonic edge states [2–4] and formation of optical solitons [5, 6]. The properties of the waveguide arrays usually can be determined very accurately within the tight-binding approximation, which allows one to employ such discrete systems for emulation and direct observation of optical analogues of many effects from solid state physics such as Bloch oscillations [7–9], Zener tunneling [10, 11], Anderson localization [12–14] etc [15].

The flexibility of the waveguide arrays in terms of their modulation in transverse or longitudinal direction provides additional versatility to these systems [16]. Such modulation, typically achieved by bending the waveguides or by changing the refractive index in the direction of the waveguide axis changes their propagation constants or interaction constants between the waveguides and leads to such phenomena as dynamic localization and subdiffractive propagation of light [16]. The extreme case of longitudinal refractive index modulation corresponds to the formation of a periodic waveguide that consists of separate parts [17–19]. Such waveguides, composed of individual dielectric nanoparticles with high refractive index, such as silicon, were proposed and theoretically studied few years ago and experimentally realized only recently [20]. The dispersion properties of such nanowaveguides are mostly determined by the optical response of their constituent elements, i.e. dielectric nanoparticles. Extensive studies in this field in the last several years have provided multiple experimental observations of the efficient geometrical tuning of the high-index dielectric nanoparticles [21], which consequently suggests a wide potential in controlling the properties of the nanoparticle waveguides [22].

The presence of the periodicity in a waveguide might bring additional features in the properties of the coupled waveguides system due to several reasons. First, the electromagnetic fields in the nanoparticle waveguides become highly confined, and, therefore, their vectorial nature has to be taken into account. Second, as compared to an array of homogeneous waveguides, where the only parameter is the distance between the waveguides, periodic waveguides can also be shifted relative to each other along their axis. Such a shift results in the formation of a different system with potentially different properties similar to the modulated optical lattices.

In a conventional scenario, the edge modes in coupled discrete systems appear as a result of a perturbation at the boundary of the structure or propagation constant shift in nonlinear regime [23]. However, in systems with complex geometry surface states can exist even without any perturbation. For instance, in an array of curved waveguides, the surface states can appear due to transverse modulation of the waveguides axes, which induces "virtual" perturbation at the boundary of the array [24]. Here, we show that an array of equally spaced alternating nanoparticle waveguides of two types, as schematically shown in Fig. 1, may possess nontrivial eigenmode structure. In particular, we demonstrate that the specially designed array of nanocylinder chains shifted relative to each other by half of the period possesses a gap in the spectrum of the eigenstates, which is accompanied by the formation of the edge states in the finite size array, despite the absence of any edge perturbation. We show that the presence of the spectral gap cannot be understood within the conventional tight-binding approximation and requires taking into account at least the next-to-nearest neighbor's interaction.

2. Polarization properties of individual nanoparticle waveguides

As a first step, we consider the polarization properties of the eigenmodes of the individual nanoparticle waveguides. Dispersion properties of such waveguides are discussed in details, e.g. in the Ref. [19]. Here, in Figs. 2(a,b) we show the schematic representation of the magnetic field polarization that can be understood within the framework of the dipole model. In this approximation all particles are modelled as point magnetic dipoles [19], with their instantaneous directions indicated by the arrows inside the circles at points "O". Such approximation can be justified for particles that possess only magnetic dipole resonant response, which is often the case, e.g. for silicon nanoparticles with typical linear size ≈ 100-300 nm in visible and near infrared frequency range [25]. Although, the resonant frequencies of high-index dielectric nanoparticles depend on their shapes and in some specific cases high-order multipoles should be taken into account [26], there is a wide range of parameters when the frequency of the fundamental magnetic dipole resonance is well separated from the higher-order ones, which in turn can be neglected. For instance, such approximation can be considered as relatively accurate even in the simplest case of spherical particles. In the dipole model two modes polarized in $x-y$ plane can be distinguished: x-polarized mode corresponds to the oscillation of magnetic dipoles along the waveguide axis and y-polarized mode correspond to the transverse oscillations of the dipoles. In what follows, we consider the waveguide modes close to the edge of the Brillouin zone, i.e. with Bloch wavenumber in x direction close to $\beta_x = \pi$. In this case the fields in neighbor particles (or the neighboring dipoles) oscillate out-of-phase.

If we want to establish the polarization of the magnetic field at the points "B" or "B′", which are shifted along the y axis from the center of the particle (point "O"), we need to add the contributions from all dipoles in the chain. In general, all dipoles except the nearest one numbered as $j = 0$ induce both x and y components of the magnetic field at the points "B" and "B′". However, the contributions of the y (x) component from the pair of dipoles with number $+j$ and $-j$ cancel each other in the case of x-polarized (y-polarized) eigenmodes, respectively, because they oscillate in phase. Therefore, at these points magnetic field of the x-polarized (y) mode oscillates in x (y) direction. To estimate the phase of the magnetic field we recall that the full field produced by a dipole is given by the dyadic Green's function [27]. Since it decreases with the distance, in the zeroth approximation we can assume

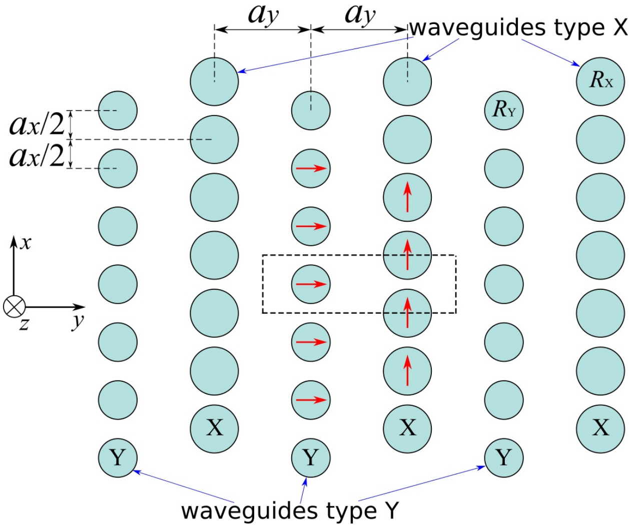

FIG. 1. A scheme of the array of periodic waveguides composed of dielectric nanoparticles with every other waveguide shifted in x direction by $a_x/2$. The distance between the waveguides is a_y. Waveguides denoted by "X" ("Y") are composed of dielectric cylinders with radius R_X (R_Y) and height H (dimension along z direction) placed with the period a_x. Polarization of the waveguide modes are determined by the magnetic field in the center of the cylinders. In the waveguides "X" ("Y") eigenmodes are polarized in x (y) direction, which is indicated by the red arrows

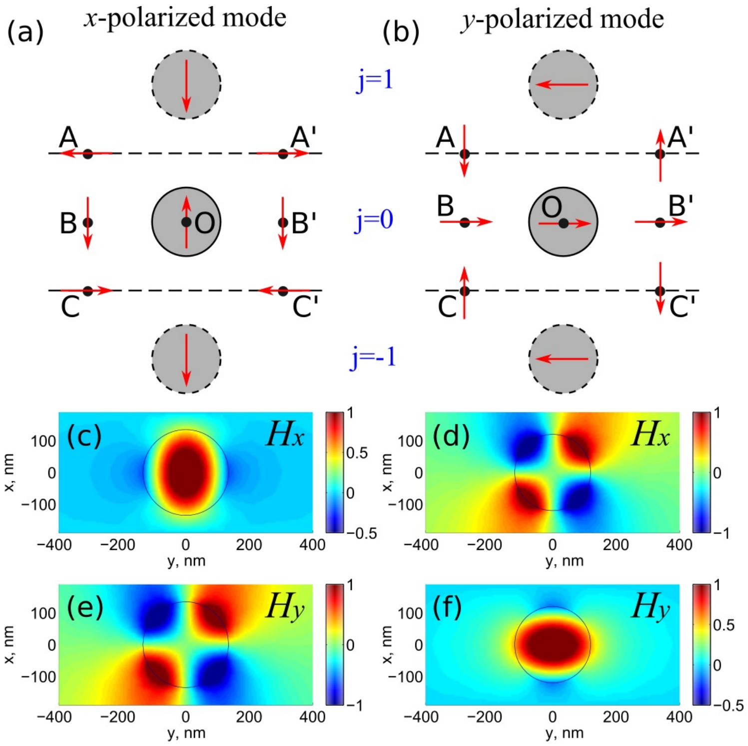

FIG. 2. (a,b) Schemes of the polarization of x- and y-polarized modes, respectively. Red arrows indicate the direction of magnetic field. (c,d) Instantaneous H_x and (e,f) H_y components of the magnetic field distribution in chains of cylinders with (c,e) radius R_X that exhibit x-polarized mode, and (d,f) radius R_Y that exhibit y-polarized mode. Parameters of the waveguides are given in the text

that the largest contribution to the total field comes only from the nearest dipole. Further, we take into account only the near-field part of Green's function, which is $\propto 2/r^3$ in the case of x polarization and $\propto -1/r^3$ in the case of y polarization. This provides a qualitative explanation of why there is a zero phase difference between the magnetic field at points "B","B$'$" and the dipole oscillations (indicated by the arrow at point "O") in Fig. 2(b), while for x-polarized mode in Fig. 2(a) the corresponding phase difference is equal to π.

The direction of the fields at points "A", "A$'$" and "C", "C$'$" can be analyzed in the same way. Now, the x (y) component is cancelled for the x (y) polarized mode. For instance, at the point "A" in Fig. 2(a) the x component is cancelled because the dipole with numbers j and $-j+1$ (e.g. 0 and 1) oscillate out-of-phase. Due to electric mirror symmetry with respect to $x-z$ plane we can immediately say that in Fig. 2(a) the field at the point "A$'$" ("C$'$") should by oriented opposite to that at the point "A" ("C"). The same consideration applies to the y-polarized mode in Fig. 2(b) due to magnetic mirror symmetry.

To prove that this analysis is relevant to realistic systems, in Figs. 2(c-f) we show the numerically calculated magnetic field distribution of the eigenmodes of the chain of dielectric cylinders that correspond to Figs. 2(a,b). In Figs. 2(c,e) we show the field distribution in the chain of cylinders (one unit cell) with radius $R_X = 135$ nm and height $H = 240$ nm (dimension along z direction) made from dielectric with permittivity $\varepsilon = 13$ and placed with the period $a_x = 380$ nm. The individual chain of such particles possesses x-polarized mode at the frequency $\omega_0 \approx 2\pi \cdot 290$ rad/s with wavenumber $\beta_x = \pi$. Cylinders in Figs. 2(d,f) have slightly smaller radius $R_Y = 120$ nm, so the chain of such cylinders supports y-polarized at approximately the same frequency ω_0. We observe that the dipole model provides us with an adequate picture of the modes polarization for realistic parameters.

The conducted analysis and numerical calculations provide an intuitive picture of the coupling between the neighboring chains of nanoparticles. When there is no shift between the waveguides along x direction, there is an interaction only between the waveguides of the same type, i.e. that support eigenmodes with the same polarization. When there is a non-zero shift, both x and y polarized waveguide modes can couple to each other, provided they have close eigenfrequencies. In the special case, when the waveguides are shifted by half of the period, the polarization in the points of the interest is rotated by $\pi/2$ in the $x-y$ plane, as compared to the direction of oscillation of the field in the centers of particles. Therefore, there is an interaction only between the waveguide modes with different polarization.

3. Couple mode theory for nanoparticle waveguides

From the analysis of the polarization properties of the individual nanoparticle waveguide eigenmodes we can develop a simple model for the eigenmodes of the coupled array of the nanoparticle waveguides. If we assume that the waveguides are coupled only to their nearest neighbors, the system of equation appears as follows:

$$\begin{cases}(\omega_0-\omega)Y+(J_1+J_2e^{-i\beta_y})X=0,\\(\omega_0-\omega)X+(J_1+J_2e^{i\beta_y})Y=0,\end{cases} \tag{1}$$

where ω_0 is the frequency of the eigenmodes of individual chains, ω is the frequency of the eigenmodes of the array of coupled waveguides, β_y is the Bloch wavenumber along the y axis, and coupling constants J_1 and J_2 are assumed to be real-valued, since there is no phase delay between the field at points "O" and "A","C" in Figs. 2(a,b). In general, the system (1) is the celebrated SSH model [28, 29], which is known to possess two bands separated by the bandgap when the coupling constants J_1 and J_2 are different. In this work, we restrict ourselves with the case when the distance between the waveguides is the same. As a consequence the coupling constants J_1, J_2 have the same magnitude and only differ in sign. Therefore, from the simple tight-binding model one cannot expect the formation of the gap in the spectrum of the array of equally spaced waveguides.

However, it is known that at the points close to the edge of the Brillouin zone, where the group velocity is small, coupling not only to the nearest neighbors might become substantial [30]. To estimate the effect caused by the long-range interaction we consider the model that takes into account also the coupling between next-to-nearest neighbors. Since the analysis of the eigenmodes polarization in Figs. 2(a,b) is valid for arbitrary x coordinates of the points "A-C", we can expect that the waveguides X (Y) will couple not only to the nearest neighbor waveguides Y (X) but also to next-to-nearest neighbor waveguides X (Y) with a certain coupling constant J_X (J_Y). Due to difference in the phase shift between the points "O" and "B" for different polarizations (see previous section) we expect coupling constants J_X and J_Y to have different signs. The values of J_X and J_Y in realistic systems may differ substantially from those expected from Figs. 2(c,f) mainly because we are interersted in fields at larger distances in y direction. However, as we will see further, the main feature, which is the non-zero difference $|J_X-J_Y|$, remains unaffected.

The model that includes the interaction between the next-to-nearest neighbors appears as follows [31]:

$$\begin{cases}(\omega_0-\omega+2J_X\cos\beta_y)X+(J_1+J_2e^{i\beta_y})Y=0,\\(\omega_0-\omega+2J_Y\cos\beta_y)Y+(J_1+J_2e^{-i\beta_y})X=0.\end{cases} \tag{2}$$

Solution of the system (2) given the dispersion $\omega(\beta_y)$:

$$\begin{gathered}\omega=\omega_0+(J_X+J_Y)\cos\beta_y\pm\\ \sqrt{(J_X-J_Y)^2\cos^2\beta_y+J_1^2+J_2^2+2J_1J_2\cos\beta_y}.\end{gathered} \tag{3}$$

Now, even when $|J_1|=|J_2|$ and there is no gap in the nearest neighbor approximation, the long-range interaction indeed induces the gap for non-equal constants J_X and J_Y. For $\beta_y=0$ the spectral gap is given by $\Delta\omega_c=2\sqrt{(J_X-J_Y)^2+(J_1+J_2)^2}$, and for $\beta_y=\pi$: $\Delta\omega_e=2\sqrt{(J_X-J_Y)^2+(J_1-J_2)^2}$. From that we can deduce that the system is gapped whenever the difference $|J_X-J_Y|$ is non-zero, which is exactly the case for the considered system. In a particular case when $J_1=-J_2=J$ we have $\Delta\omega_c=2|J_X-J_Y|$ and $\Delta\omega_e=2\sqrt{(J_X-J_Y)^2+4J^2}$.

As an example, in Fig. 3(a) we plot the dispersion for the two cases: $J_X=J_Y=0$ (solid black curves) and $J_X=-J_Y=0.4$ (dashed blue curves); other parameters are following: $\omega_0=0$, $J_1=-J_2=1$. We observe that the long-range interaction between the waveguides induces the gap in the eigenmodes spectrum.

It can be shown, that along with the existence of the gap in the infinite system for non-zero values of $|J_X-J_Y|$, in the finite size system one can also expect the formation of the edge states. The frequencies of these states ω_{e1} and ω_{e2} for the termination at "Y" or "X" site, respectively, can be estimated analytically as follows:

$$\begin{aligned}\omega_{e1}&\approx\omega_0+2J_Y[1-J_Y^2/(J^2+J_Y^2-J_XJ_Y)],\\ \omega_{e2}&\approx\omega_0+2J_X[1-J_X^2/(J^2+J_X^2-J_XJ_Y)].\end{aligned} \tag{4}$$

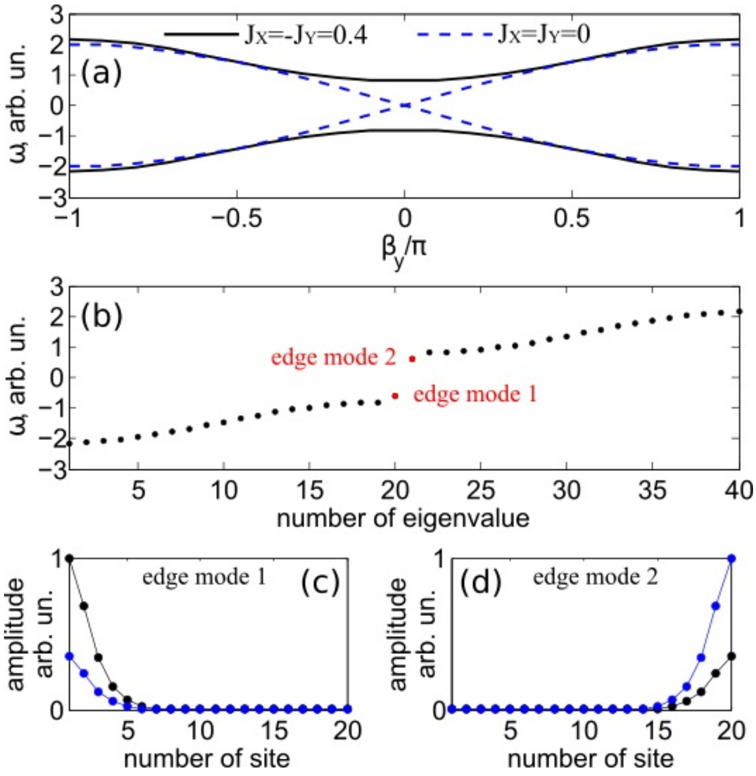

FIG. 3. (a) Spectrum of the eigenmodes calculated with equation (3) for the following parameters: $\omega_0 = 0$, $J_1 = -J_2 = 1$, $J_X = J_Y = 0$ (dashed blue curves), $J_X = -J_Y = 0.4$ (solid black curves). (b) Eigenfrequencies of the finite size array consisting of 50 coupled chains for the parameters corresponding to solid black curves in (a). (c-d) Amplitudes of the edge modes marked in (b) as a function of the number of site; blue dots correspond to the amplitudes in sublattice X and black dots — in sublattice Y

The amplitudes in two sublattices are related as $X/Y = J_X/J$ for the "X" edge termination and $X/Y = J_Y/J$ for "Y" edge termination. Further, since ratios $|J_{X,Y}/J|$ are assumed to be small we may simplify (4) as follows:

$$\begin{aligned} \omega_{e1} - \omega_0 &= 2J_X(1 - J_X^2/J^2), \\ \omega_{e2} - \omega_0 &= 2J_Y(1 - J_Y^2/J^2). \end{aligned} \tag{5}$$

To verify our estimations, in Fig. 3(b) we plot the spectrum of the finite system consisted of the 20 unit cells (started with "A" on the right edge) for the same parameters as in Fig. 3(a) and $J_X = -J_Y = 0.4$. We can observe that the finite array possesses two edge states symmetric with respect to ω_0 (due to equality of the magnitudes of J_X and J_Y) with the localization length that is determined by the proximity of the corresponding frequency to the central frequency ω_0. The profiles of these states, shown in Fig. 3(c,d), also confirm the predicted ratios between the amplitude on the two sites within the unit cell.

4. Results of numerical simulation of realistic systems

Next, we study whether the long-range interaction is relevant in realistic systems. For that, we perform full-wave numerical simulations of the array of the cylinders with z-oriented axis in CST Microwave Studio software, which numerically solves Maxwell's equations for given geometrical and material parameters of the structure and boundary conditions. The parameters of the system were the same as in calculations in Fig. 2: for the sublattice X — $R_X = 135$ nm, for the sublattice Y — $R_Y = 120$ nm; height $H = 240$ nm, $a_x = 380$ nm, $a_y = 450$ nm.

First, we calculate the spectrum of eigenmodes of the array infinite in both x and y directions. In this case periodic boundary conditions were employed in x and y directions, while in z direction the electric walls were placed at the distance $\approx \lambda/2$ from the array. Although, the system is not open in z direction, this almost does not affect the modes that are localized near the array, due to exponential decay of the fields along z. Wavenumber in x direction is fixed as $\beta_x = \pi$. In Fig. 4 we plot the eigenfrequency as a function of the wavenumber in y direction β_y. These calculations qualitatively agree with those predicted in the next-to-nearest neighbors approximation:

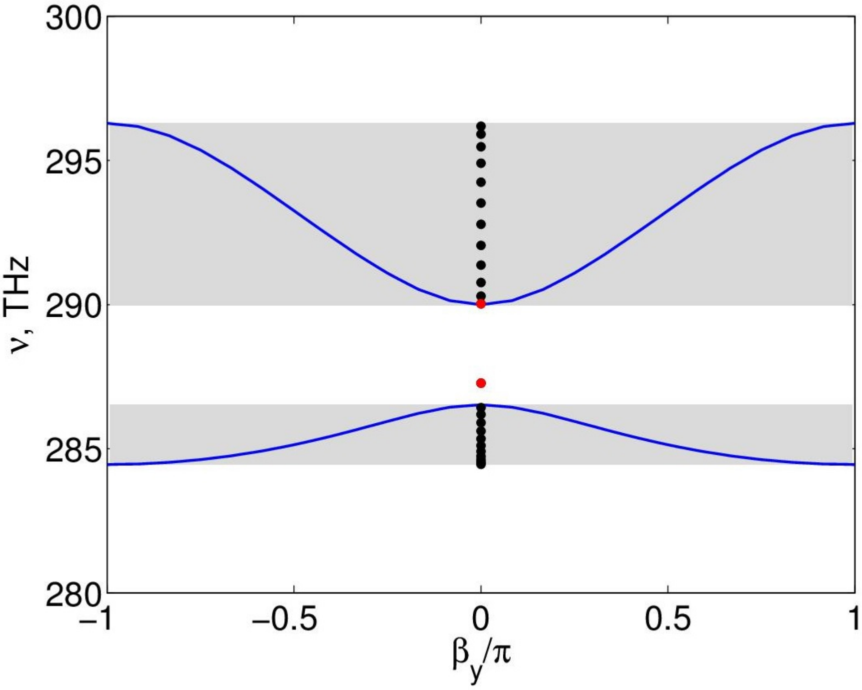

FIG. 4. Spectrum of the numerically calculated eigenmodes of an array of cylinders infinite in both x and y directions (solid blue curves) and infinite in x direction and finite (12 periods) in y direction (black and red dots). Wavenumber in x direction is fixed as $\beta_x = \pi$. Red dots indicate the edge modes that fall in the gap region between the two bands (shaded gray areas)

there is a gap between two branches, and the difference between the frequencies of upper and lower branches is increasing when β_y changes from 0 to π. We conclude that such system indeed can be described by taking into account at least next-to-nearest neighbor interaction, and therefore the finite size array should possess localized edge states.

To verify the existence of the edge states, we calculate the eigenmodes of the system in the strip geometry. More precisely, the system is infinite in x direction with fixed $\beta_x = \pi$ and has N periods in y direction (see Fig. 1). Eigenfrequencies of the system with $N = 12$ are shown in Fig. 5 with black and red dots. Black dots indicate the volume modes and are contained within the bands of the infinite structure, while red dots indicate the edge modes that fall within the gap. Note that the edge mode with higher frequency lies very close to the allowed band. This indicates that one of the interaction constants J_X or J_Y (in this case it is J_X) is in fact close to zero.

The magnetic field distribution of the edge modes within one unit cell in x direction are shown in Figs. 5(a,b). The x component of magnetic field at the centers of X cylinders and y component of magnetic field at the centers of Y cylinders are shown in Fig. 5(c) with blue, magenta and black, red curves, respectively. We observe, that the localization strength and the ratio of the amplitudes in two sublattices is in well agreement with the predictions made in the previous section. Note that since the polarization of both sublattices is parallel to the plane of the array, the potential substrate inevitable in experiments would affect the properties of each chain in approximately the same way. Therefore, only slight adjustment of the geometrical parameters of the system would be necessary in the case when a substrate is present.

5. Summary

In summary, we have studied the properties of an array of coupled nanoparticle waveguides. We have shown that such structures may possess a spectral gap, the presence of which can be explained only by taking into account long range interaction between the waveguides. The appearance of the gap is accompanied by the formation of the defect-free edge modes in the finite size array. Our findings reveal the rich potential of the arrays of nanoparticle waveguides in realization of optical metasurfaces for guiding surface waves with complex functionalities and studying discrete systems beyond the tight-binding approximation.

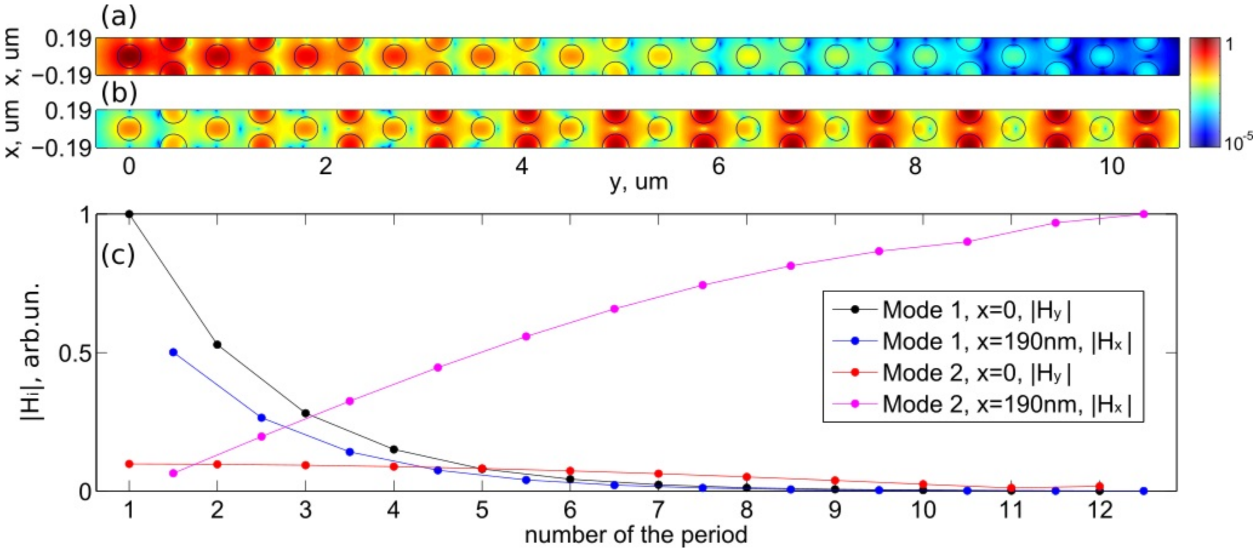

FIG. 5. (a,b) Magnetic field distribution $|H|$ of the two modes marked with red circles in Fig. 4 in the plane $z = 0$ in logarithmic scale. The structure is periodic in x direction; one unit cell is shown. (c) Amplitude of the y component (black and red curves) and x component (blue and magenta curves) of the magnetic field in the center of each cylinder; black and blue dots correspond to the edge mode in (a), red and magenta – in (b).

Acknowledgements

This work was supported by the Russian Foundation for Basic Research, according to the research project No. 16-37-60092 mol_a_dk, and the Grant from the President of the Russian Federation (MK-381.2017.2).

References

[1] Christodoulides D., Lederer F., Silberberg Y. Discretizing light behaviour in linear and nonlinear waveguide lattices. *Nature*, 2003, **424**, P. 817–823.

[2] Malkova N., Hromada I., Wang X., Bryant G., Chen Z. Transition between Tamm-like and Shockleylike surface states in optically induced photonic superlattices. *Phys. Rev. A.*, 2009, **80**, P. 043806.

[3] Blanco-Redondo A., Andonegui I., Collins M.J., Harari G., Lumer Y., Rechtsman M.C., Eggleton B.J., Segev M. Topological Optical Waveguiding in Silicon and the Transition between Topological and Trivial Defect States. *Phys. Rev. Lett.* 2016, **116**, P. 163901.

[4] Kraus Y.E., Lahini Y., Ringel Z., Verbin M., Zilberberg O. Topological States and Adiabatic Pumping in Quasicrystals. *Phys. Rev. Lett.*, 2012, **109**, P. 106402.

[5] Sukhorukov A.A., Kivshar Y.S., Eisenberg H.S., Silberberg Y. Spatial optical solitons in waveguide arrays. *IEEE Journal of Quantum Electronics*, 2003, **39**, P. 31–50.

[6] Fleischer J.W., Bartal G., Cohen O., Schwartz T., Manela O., Freedman B., Segev M., Buljan H., Efremidis N.K. Spatial photonics in nonlinear waveguide arrays. *Opt. Express*, 2005, **13**, P. 1780–1796.

[7] Peschel U., Pertsch T., Lederer F. Optical Bloch oscillations in waveguide arrays. *Opt. Lett.*, 1998, **23**, P. 1701–1703.

[8] Pertsch T., Dannberg P., Elflein W., Bräuer A., Lederer F. Optical Bloch Oscillations in Temperature Tuned Waveguide Arrays. *Phys. Rev. Lett.*, 1999, **83**, P. 4752–4755.

[9] Morandotti R., Peschel U., Aitchison J.S., Eisenberg H.S., Silberberg Y. Experimental Observation of Linear and Nonlinear Optical Bloch Oscillations. *Phys. Rev. Lett.*, 1999, **83**, P. 4756–4759.

[10] Longhi S. Optical Zener-Bloch oscillations in binary waveguide arrays. *EPL (Europhysics Letters)*, 2006, **76**, P. 416.

[11] Trompeter H., Krolikowski W., Neshev D.N., Desyatnikov A.S., Sukhorukov A.A., Kivshar Y.S., Pertsch T., Peschel U., Lederer F. Bloch Oscillations and Zener Tunneling in Two-Dimensional Photonic Lattices. *Phys. Rev. Lett.*, 2006, **96**, P. 053903.

[12] Lahini Y., Avidan A., Pozzi F., Sorel M., Morandotti R., Christodoulides D.N., Silberberg Y. Anderson Localization and Nonlinearity in One-Dimensional Disordered Photonic Lattices. *Phys. Rev. Lett.*, 2008, **100**, P. 013906.

[13] Martin L., Giuseppe G.D., Perez-Leija A., Keil R., Dreisow F., Heinrich M., Nolte S., Szameit A., Abouraddy A.F., Christodoulides D.N., Saleh B.E.A. Anderson localization in optical waveguide arrays with off-diagonal coupling disorder. *Opt. Express*, 2011, **19**, P. 13636–13646.

[14] Cherpakova Z., Bleckmann F., Vogler T., Linden S. Transverse Anderson localization of surface plasmon polaritons. *Opt. Lett.*, 2017, **42**, P. 2165–2168.

[15] Longhi S. Quantum-optical analogies using photonic structures. *Laser and Photonics Reviews*, 2009, **3**(3), P. 243–261.

[16] Garanovich I.L., Longhi S., Sukhorukov A.A., Kivshar Y.S. Light propagation and localization in modulated photonic lattices and waveguides. *Phys. Rep.*, 2012, **518**, P. 1–79.

[17] Fan S., Winn J.N., Devenyi A., Chen J.C., Meade R.D., Joannopoulos J.D. Guided and defect modes in periodic dielectric waveguides. *J. Opt. Soc. Am. B.*, 1995, **12**, P. 1267–1272.

[18] Du J., Liu S., Lin Z., Zi J., Chui S.T. Dielectric-based extremely-low-loss subwavelength-light transport at the nanoscale: An alternative to surface-plasmon-mediated waveguiding. *Phys. Rev. A*, 2011, **83**, P. 035803.

[19] Savelev R.S., Slobozhanyuk A.P., Miroshnichenko A.E., Kivshar Y.S., Belov P.A. Subwavelength waveguides composed of dielectric nanoparticles. *Phys. Rev. B*, 2014, **89**, P. 035435.

[20] Bakker R.M., Yu Y.F., Paniagua-Domínguez R., Luk'yanchuk B., Kuznetsov A.I. Resonant Light Guiding Along a Chain of Silicon Nanoparticles. *Nano Lett.*, 2017, **17**, P. 3458–3464.

[21] Kuznetsov A.I., Miroshnichenko A.E., Brongersma M.L., Kivshar Y.S., Luk'yanchuk B. Optically resonant dielectric nanostructures. *Science*, 2016, **354**.

[22] Savelev R.S., Filonov D.S., Kapitanova P.V., Krasnok A.E., Miroshnichenko A.E., Belov P.A., Kivshar Y.S. Bending of electromagnetic waves in all-dielectric particle array waveguides. *Appl. Phys. Lett.*, 2014, **105**, P. 181116.

[23] Kivshar Y.S. Nonlinear Tamm states and surface effects in periodic photonic structures. *Laser Phys. Lett.*, 2008, **5**, P. 703.

[24] Garanovich I.L., Sukhorukov A.A., Kivshar Y.S. Defect-Free Surface States in Modulated Photonic Lattices. *Phys. Rev. Lett.*, 2008, **100**, P. 203904.

[25] Evlyukhin A.B., Reinhardt C., Seidel A., Luk'yanchuk B.S., Chichkov B.N. Optical response features of Si-nanoparticle arrays. *Phys. Rev. B*, 2010, **82**, P. 045404.

[26] Evlyukhin A., Reinhardt C., Chichkov B. Multipole light scattering by nonspherical nanoparticles in the discrete dipole approximation. *Phys. Rev. B*, 2011, **23**, P. 235429.

[27] Novotny L., Hecht B. *Principles of Nano-optics*. Cambridge University Press, New York, 2006.

[28] Su W.P., Schrieffer J.R., Heeger A.J. Solitons in Polyacetylene. *Phys. Rev. Lett.*, 1979, **42**, P. 1698–1701.

[29] Gorlach M., Slobozhanyuk A. Nonlinear topological states in the Su-Schrieffer-Heeger model. *Nanosystems: Physics, Chemistry, Mathematics*, 2017, **8**, P. 695–700.

[30] Plotnik Y., Rechtsman M.C., Song D., Heinrich M., Zeuner J.M., Nolte S., Lumer Y., Malkova N., Xu J., Szameit A., Chen Z., Segev M. Observation of unconventional edge states in "photonic graphene". *Nature Mater.*, 2013, **13**, P. 57–62.

[31] Li L., Xu Z., Chen S. Topological phases of generalized Su-Schrieffer-Heeger models. *Phys. Rev. B*, 2014, **89**, P. 085111.

NANOSYSTEMS: PHYSICS, CHEMISTRY, MATHEMATICS, 2018, 9 (6), P. 724–734

A comparative analysis of the observed effects of 2D tunneling bifurcations for quasi-one-dimensional and quasi-two-dimensional Au–QD systems in an external electric field

M. B. Semenov[1], V. D. Krevchik[1], O. N. Gorshkov[2], D. O. Filatov[2], Y. Dakhnovsky[3], A. V. Nikolaev[4], A. P. Shkurinov[4], V. Yu. Timoshenko[4], P. V. Krevchik[1], A. K. Malik[5], Y. H. Wang[6], T. R. Li[6], Y. Zhu[7], S. Zhuang[7], R. V. Zaytsev[1], I. S. Antonov[1], I. M. Semenov[1], A. K. Aringazin[8], A. V. Shorokhov[9]

[1]Department of Physics, Penza State University, Penza 440026, Russia

[2]Department of Physics, Lobachevsky State University of Nizhny Novgorod,
Nizhny Novgorod 603950, Russia

[3] Department of Physics and Astronomy, University of Wyoming, WY 82071 Laramie, USA

[4]Moscow State University, Moscow 119991, Russia

[5]Department of Physics, Multanimal Modi College Modinagar, Uttar Prasesh 201204, India

[6] Institute of Functional and Environmental Materials, Lanzhou University, Lanzhou, China

[7]University of Shanghai for Science and Technology, Shanghai 200093, China

[8] Institute for Basic Research, Eurasian National University, Astana 010008, Kazakhstan

[9]Institute of Physics and Chemistry, National Research Mordovia State University, Saransk 430005, Russia

misha29.02@gmail.com, alex.shorokhov@mail.ru

PACS 73.40.Gk, 03.65.Xp **DOI 10.17586/2220-8054-2018-9-6-724-734**

The effects of 2D tunneling bifurcations for quasi-one-dimensional and quasi-two-dimensional Au-quantum dot (QD) arrays in thin dielectric films in an external electric field have been studied theoretically and experimentally by Conductive Atomic Force Microscopy (CAFM). In the case of quasi-one-dimensional Au–QD structures (with the QD size $\sim$ 5 nm), in a dielectric film, a single break under positive bias polarity, corresponding to the effect of 2D tunneling bifurcation, previously predicted theoretically by our team [1], has been detected in experimental I—V curves of the CAFM probe-to-sample contact. A convincing qualitative agreement between the obtained experimental I—V curves and the theoretical field dependence for the 2D-dissipative tunneling probability in the model 2D-oscillator potential has been obtained for the case of parallel tunneling in the weak-dissipation limit at a finite temperature in an external electric field. In the case of quasi-two-dimensional structures with Au QD (with the QD sizes of 2 to 5 nm), possessing metamaterial properties, a pair of kinks corresponding to the double effect of 2D-tunneling bifurcations has been detected on the experimental I—V curves. A qualitative agreement between the experimental I—V curves and the theoretical field dependence for the 2D-dissipative tunneling probability has been obtained for a situation with an effectively "negative" permittivity of the heat bath.

Keywords: quantum tunneling with dissipation, quantum dots, two-dimensional bifurcations.

Received: 27 October 2018

1. Introduction

The first mention of the 2D-tunneling bifurcations effect was in the work of Yu. N. Ovchinnikov and B. I. Ivlev [2] under consideration of two-dimensional systems with interacting Josephson junctions. The authors assumed that this effect can be observed in the form of a characteristic break in the corresponding tunnel I–V curves, but its observation proved difficult due to the washout of this feature by current noise in the vicinity of the bifurcation point. The unstable effect of 2D-bifurcations for the case of antiparallel tunneling transport turned out to be observable in the form of a kink on the temperature dependence of the chemical reaction rate of the interacting protons transfer in a porphyrin- type system. A theory of the 2D-tunneling bifurcations effect in 2D potentials with different topologies was developed in the works by V. A. Bendersky and co-authors [3].

The effect of 2D-tunneling bifurcations for the parallel transfer of interacting particles in the weak-dissipation limit with allowance for the quantum beat regime in the vicinity of the bifurcation point, predicted by us in an earlier work [1], has been observed experimentally in a quasi-one-dimensional Au–QD array in an external electric field by Conductive Atomic Force Microscopy (CAFM). A description of the relevant experiment is presented in Section 2 of this article [4].

Section 3 is devoted to the recently performed author's experiment on measuring the tunnel I–V curves of the quasi-two-dimensional Au–QD arrays, which could potentially manifest the metamaterial properties (particularly, a negative refractive index) at certain values of spacing between the Au–QDs in the periodic 2D-arrays [5–7]. In Sections 4 and 5 we give a theoretical calculation of the 2D-dissipative tunneling probability with allowance for 2D-bifurcation modes in the model 2D-oscillator potential at a finite temperature in an external electric field in the weak dissipation limit for both the dielectric matrix case (Section 4) and the case of 2D-structures (dielectric matrix + Au–QDs), which have the properties of a metamaterial (Section 5). In general, the dielectric matrix itself can possess the properties of a metamaterial, but for this it must have a periodic modulation of the refractive index in space, for example, a multilayer structure. However, in this case we often speak of quantum dots in microresonators. Section 6 gives the qualitative comparison of the obtained experimental and theoretical results and compares the effects of 2D tunnel bifurcations both for quasi-one-dimensional and quasi-two-dimensional structures with Au–QDs.

A qualitative conclusion is drawn that it is possible to experimentally confirm the theoretically predicted effect of 2D-tunneling bifurcations for the investigated nanostructures.

2. Experimental I—V characteristics for quasi-one-dimensional Au–QD structures

In the work by Yu. N. Ovchinnikov [8], it has been shown that the conductivity of granular metallic films is related to the tunneling processes between neighboring granules and that the interaction with the heat bath, ensuring a real transition to states localized in the "neighboring" cluster, is rather small. Thus, the characteristics of the tunnel current in the systems under study can be considered in the limit of comparatively "weak" dissipation, but sufficient to ensure the "decay" of the double-well oscillator potential used in the proposed model. In addition, an appreciable contribution to the tunneling current can be provided by the tunneling probability, estimated to within a pre-exponential factor in Ref. [9].

Figure 1 presents the experimental scheme of the studies and a typical current-voltage (I—V) curves obtained by the experimental group (O. N. Gorshkov, D. O. Filatov, D. A. Antonov) in Research and Educational Center for Physics of Solid State Nanstructures at Lobachevskii State University of Nizhni Novgorod (Russia) [4]. When measuring the tunnel current from the CAFM probe tip to the nearest Au nanocluster (QD), it is quite possible that, due to some inhomogeneities (protrusions) on the tip apex, parallel closely spaced channels of the tunnel current can take place (so called nulti-tip effect). If the sizes of the protrusions are less than the nanocluster (QD) ones, then at a negative bias voltage the asymmetry of the potential along the transfer coordinate changes, and the system becomes a two-dimensional one essentially. Depending on the magnitude of the external electric field strength, as well as on temperature and on relative permittivity of the heat bath, in the parallel synchronous transfer of Coulomb-interacting particles, either stable synchronous or asynchronous transfer takes place. The switching from one mode to another corresponds to a bifurcation point, which will be theoretically described briefly in Section 4.

One of the characteristic features of the I–V curves, shown in Fig. 1b, is a sharp break observed at positive bias voltages, which is assumed to be due to a change in the tunneling regime along parallel channels in an asymmetric 2D potential or by the presence of a bifurcation point described in [1]. Near this point, a small transition region with a separate feature was observed on the current-voltage curves, which probably can correspond to the quantum beat regime predicted in [1].

Finally, in the negative voltage region, we observed a characteristic single peak, which, as described in Ref. [9], is related to the singularity of the pre-exponential factor under conditions when the model potential becomes symmetric with the change of the external electric field that affects the magnitude of the potential asymmetry parameter.

This set of the theoretically and experimentally studied effects allows us to conclude that it is possible to experimentally observe stable 2D tunneling bifurcations with dissipation, which is one of the main results of this work.

3. Experimental I—V characteristics for quasi-two-dimensional Au–QD structures

In the framework of the experimental scheme described in Section 2, a situation was realized where the tunnel current was not formed through a single Au–QD (quasi-one-dimensional case), but through two neighboring Au–QDs (quasi-two-dimensional case, Fig. 2). The following tunneling current-voltage characteristics were obtained (Fig. 3), having two "smoothed" kinks. It is assumed that such quasi-two-dimensional structures may have the properties of a metamaterial.

On the experimental curve of Fig. 3b, in addition to the "smoothed" double kinks, the quantum beat regime was also observed in the neighborhood of the points of 2D bifurcations.

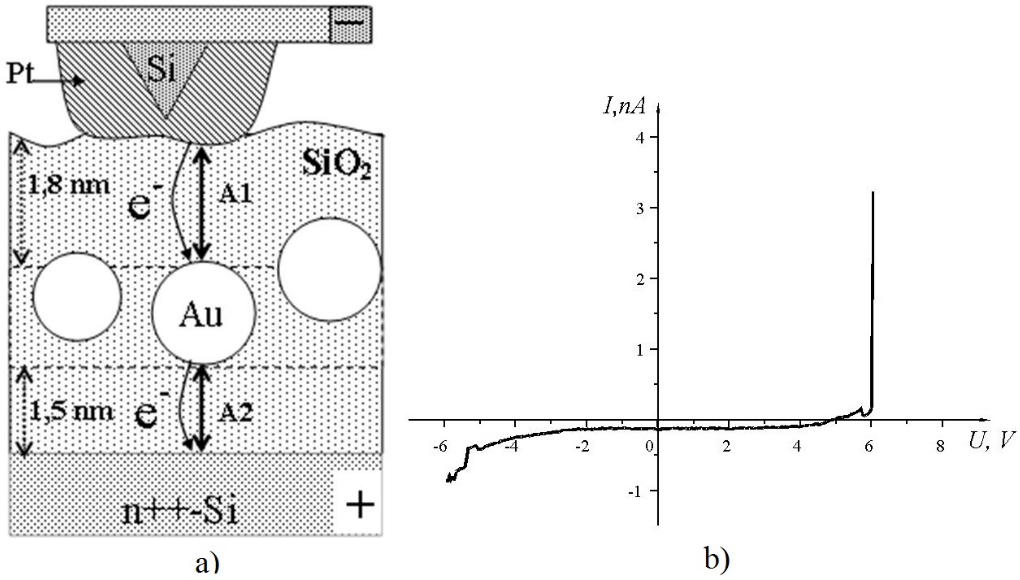

a) b)

FIG. 1. (a) Schematic representation of the experimental setup for studying the dissipative electron tunneling via an individual Au nanoclusters embedded into a tunnel-transparent SiO_2 film on n^+-Si substrate by CAFM. $A1$ is the tunnel-transparent probe-cluster potential barrier, $A2$ is the cluster-substrate one. (b) An example of I—V curve of a CAFM probe contact to the nanocomposite SiO_2(1.5 nm)/SiO_2:nc-Au(1.6 nm)/SiO_2(1.8 nm)/n^+-Si(100) stack film

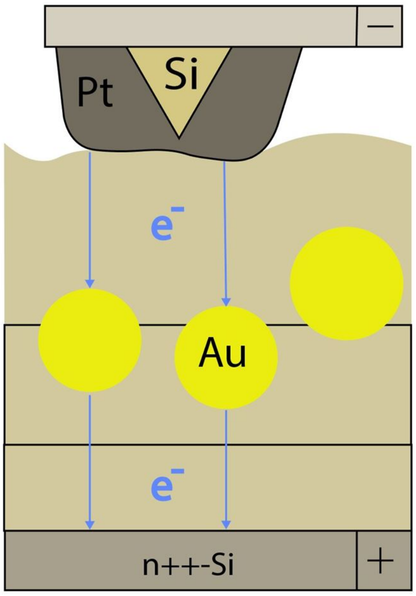

FIG. 2. Schematic representation of the experimental setup for studying the dissipative electron tunneling via double Au-QDs embedded into a tunnel-transparent SiO_2 film on n^+-Si substrate by CAFM. This case corresponds to the quasi-two-dimensional structures, which may have the properties of a metamaterial

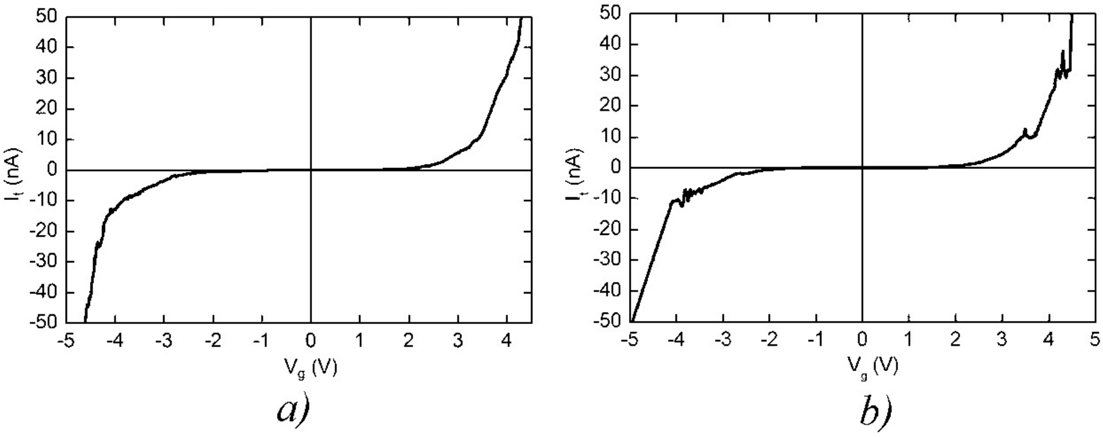

FIG. 3. An example I—V curves of a CAFM probe contact to the nanocomposite SiO_2(1.5 nm)/SiO_2: double nc-Au(1.6 nm)/SiO_2(1.8 nm)/n^+-Si stack film (Fig. 2): with "smoothed" double kinks + (b, with) and – (a, without) the quantum beat regime

In Section 4, a qualitative comparison of the tunneling current-voltage characteristics given in Fig. 3a and Fig. 3b with the field dependence of the 2D-dissipative parallel tunneling probability in case of the quasi-two-dimensional structure with properties of a metamaterial, will be presented.

4. Theoretical calculation of the 2D bifurcation regime in the model 2D oscillator potential at a finite temperature in an external electric field in the weak dissipation limit for the case of a dielectric matrix

The influence of the electric field E on the asymmetric two-well oscillator potential gives the following expression for $\tilde{U}(q)$

$$\tilde{U}(q) = \frac{\omega_0^2}{2}(q-b_0)^2\theta(q) + \left[\frac{\omega_0^2}{2}(q+a_0)^2 - \Delta I\right]\theta(-q) - |e|\,Eq, \tag{1}$$

where the parameter $\Delta I = \frac{\omega_0^2}{2}(a_0^2 - b_0^2)$ determines the initial asymmetry of the potential in the absence of the field, and, as it is known, leads to a change in the asymmetry parameter proportional to the electric field magnitude.

In order to use the standard model to determine the probability of 2D-dissipative tunneling, we use the following notation for the renormalized two-well oscillator potential in an external electric field: $b = b_0 + \frac{|e|E}{\omega_0^2}$, $a = a_0 - \frac{|e|E}{\omega_0^2}$.

For the case of parallel tunneling particles, we select the potential energy $U_1(R_1,\, R_2)$ in the following form (see [4, 14] as also Fig. 4):

$$U_1(R_1,\, R_2) = \frac{\omega^2(R_1+a)^2}{2}\theta(-R_1) + \left[-\Delta\mathrm{I} + \frac{\omega^2(R_1-b)^2}{2}\right]\theta(R_1) + \\ + \frac{\omega^2(R_2+a)^2}{2}\theta(-R_2) + \left[-\Delta\mathrm{I} + \frac{\omega^2(R_2-b)^2}{2}\right]\theta(R_2) - \frac{\alpha(R_1-R_2)^2}{2}, \tag{2}$$

where $\Delta I = \frac{1}{2}\omega^2\left(b^2 - a^2\right)$ is the "reaction heat" or the asymmetry parameter of the potential; α ($\alpha > 0$) is the coefficient of interaction between particles, which in the dipole-dipole approximation depends on the magnitude of the relative dielectric constant of the heat-bath (or dielectric matrix), $R_{1,2}$ are the parallel coordinates of the tunneling.

Taking into account the interaction of particles tunneling through parallel channels, the potential reconstruction becomes essentially two-dimensional (see Fig. 5).

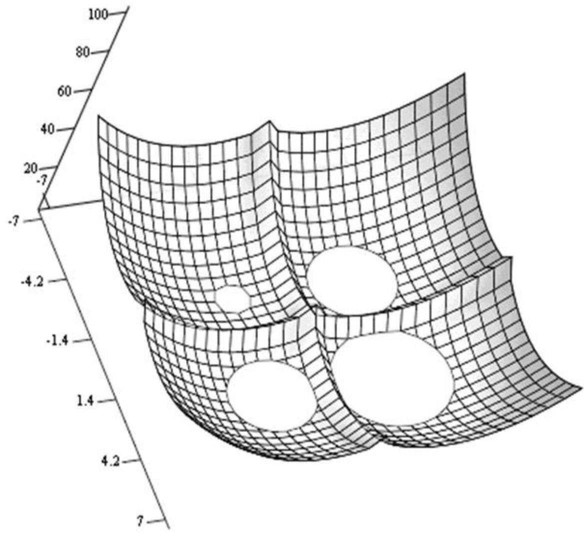

FIG. 4. Surface of the potential energy Eq. (2), (after "switching on" the interaction between particles), as a function of the reaction coordinates for particles moving in parallel coordinates (from catilever needle to the nearest Au–QD),($a = 2$; $b = 2.5$; $\alpha^* = 2\alpha/\omega^2 = 0.0001$)

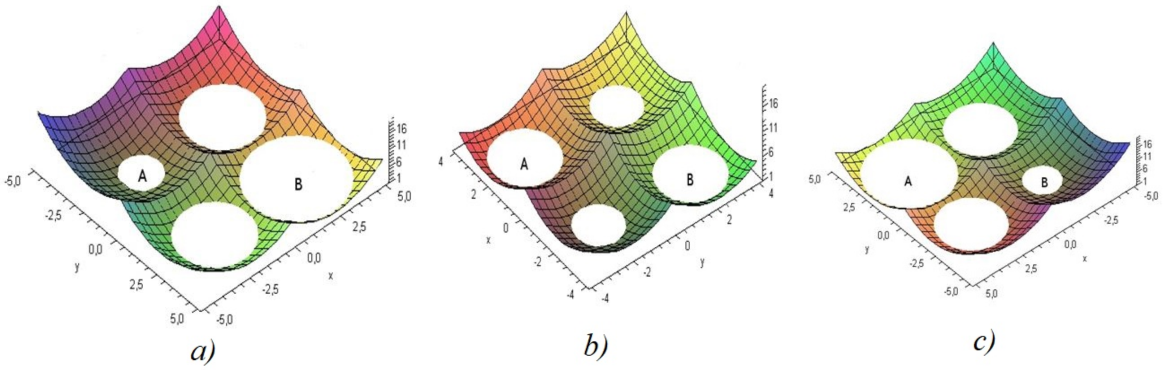

a) *b)* *c)*

FIG. 5. Change in the asymmetry of the potential energy surface for parallel transport of particles in an external electric field (with negative applied voltage). At a certain value of the applied voltage, the potential becomes symmetrical (b)

In the framework of the standard 2D-model of dissipative tunneling in the weak dissipation limit [1], we obtain

$$S\{R_1, R_2\} = \int\limits_{-\beta/2}^{\beta/2} d\tau \left\{ \frac{\dot{R_1}^2}{2} + \frac{\dot{R_2}^2}{2} + V(R_1, R_2) + \frac{1}{2} \int\limits_{-\beta/2}^{\beta/2} d\tau' \, D(\tau - \tau') \, [R_1(\tau) + R_2(\tau)] \, [R_1(\tau') + R_2(\tau')] \right\}, \quad (3)$$

where

$$D(\tau) = \frac{1}{\beta} \sum_{n=-\infty}^{\infty} D(\nu_n) \, e^{i\nu_n \tau}, \quad (4)$$

$\beta = \hbar/k_B T$ is the inverse temperature, ($\hbar$, k_B and the particle masses, as before, are assumed to be equal to 1); $\nu_n = 2\pi n/\beta$ is the Matsubara frequency; and, finally, $D(\tau)$ is the Green's function of phonons.

A two-dimensional quasiclassical trajectory (instanton), that minimizes the action functional, is determined from the equations of motion

$$\frac{\delta S}{\delta R_1} = 0, \quad \frac{\delta S}{\delta R_2} = 0. \tag{5}$$

We seek a solution of the system of these equations in the following form:

$$R_1(\tau) = \frac{1}{\beta}\sum_{n=-\infty}^{\infty} R_n{}^{(1)}\, e^{i\nu_n\tau}, \quad R_2(\tau) = \frac{1}{\beta}\sum_{n=-\infty}^{\infty} R_n{}^{(2)}\, e^{i\nu_n\tau}. \tag{6}$$

It should be mentioned that the solutions of the equations system (5) are under the assumption of simultaneous start of tunneling particles. The times τ_1 and τ_2 correspond to the moments of passage for the tops of the barriers by the particles along the corresponding reaction coordinates, and can be found from the following equations:

$$R_1(\tau_1) = 0, \quad R_2(\tau_2) = 0. \tag{7}$$

In the case of parallel motion of tunneling particles (potential energy $U_1(R_1, R_2)$ (Eq. 2), the action S as a function of the parameters τ_1 and τ_2 takes the form:

$$S = 2a(b+a)(\tau_1+\tau_2)\,\omega^2 - \frac{\omega^2(a+b)^2(\tau_1+\tau_2)^2}{\beta} - \frac{\omega^4(a+b)^2(\tau_1-\tau_2)^2}{(\omega^2-2\alpha)\,\beta} - \\ - \frac{2\omega^4(a+b)^2}{\beta}\sum_{n=1}^{\infty}\left\{\frac{(\sin\nu_n\tau_1+\sin\nu_n\tau_2)^2}{\nu_n{}^2(\nu_n{}^2+\omega^2+\xi_n)} + \frac{(\sin\nu_n\tau_1-\sin\nu_n\tau_2)^2}{\nu_n{}^2(\nu_n{}^2+\omega^2-2\alpha)}\right\}, \tag{8}$$

where ξ_n can be assumed to be 0, if we neglect the interaction with the oscillators of the medium.

We introduce the notations: $\varepsilon = \varepsilon^*\omega = (\tau_1-\tau_2)\,\omega$; $\tau = 2\tau^*\omega = (\tau_1+\tau_2)\,\omega$; $\beta^* = \beta\omega/2$; $\alpha^* = 2\alpha/\omega^2$; $b^* = b/a$, $b \geq a$.

If we neglect interaction with phonons (medium oscillators), then $\xi_n = 0$, and the action S (8) as a function of the parameters ε and τ takes the form

$$S = (a+b)\,\omega\tau\left(2a - \frac{a+b}{2}\left[1+\frac{1}{1-\alpha^*}\right]\right) + \frac{\omega(a+b)^2}{2}(\tau-|\varepsilon|)\frac{\alpha^*}{1-\alpha^*} - \\ - \frac{\omega(a+b)^2}{2}\left\{-\coth\beta^* + \frac{1}{\sinh\beta^*}\left[\cosh(\beta^*-\tau)\,\cosh\varepsilon + \cosh(\beta^*-\tau) - \cosh(\beta^*-|\varepsilon|)\right]\right\} - \\ - \frac{\omega(a+b)^2}{2(1-\alpha^*)^{3/2}}\left\{\coth\left(\beta^*\sqrt{1-\alpha^*}\right) + \frac{1}{\sinh\left(\beta^*\sqrt{1-\alpha^*}\right)}\left[\cosh\left((\beta^*-\tau)\sqrt{1-\alpha^*}\right)\times\right.\right. \\ \left.\left.\times\cosh\left(\varepsilon\sqrt{1-\alpha^*}\right) - \cosh\left((\beta^*-\tau)\sqrt{1-\alpha^*}\right) + \cosh\left((\beta^*-|\varepsilon|)\sqrt{1-\alpha^*}\right)\right]\right\}. \tag{9}$$

We will write expressions ((7)) in the form

$$\sinh\varepsilon\left[\cosh\tau\coth\beta^* - \sinh\tau - \coth\beta^*\right] + \frac{1}{1-\alpha^*}\sinh\left(\varepsilon\sqrt{1-\alpha^*}\right)\times \\ \times\left[\cosh\left(\tau\sqrt{1-\alpha^*}\right)\coth\left(\beta^*\sqrt{1-\alpha^*}\right) - \sinh\left(\tau\sqrt{1-\alpha^*}\right) + \coth\left(\beta^*\sqrt{1-\alpha^*}\right)\right] = 0, \tag{10}$$

$$3 - \frac{4}{1+b^*} - \frac{1}{1-\alpha^*} + \cosh\varepsilon\left[\sinh\tau\coth\beta^* - \cosh\tau - 1\right] + \sinh\tau\coth\beta^* - \\ - \cosh\tau + \frac{1}{1-\alpha^*}\cosh\left(\varepsilon\sqrt{1-\alpha^*}\right)\left[\sinh\left(\tau\sqrt{1-\alpha^*}\right)\coth\left(\beta^*\sqrt{1-\alpha^*}\right) - \cosh\left(\tau\sqrt{1-\alpha^*}\right) + 1\right] - \\ - \frac{1}{1-\alpha^*}\left[\sinh\left(\tau\sqrt{1-\alpha^*}\right)\coth\left(\beta^*\sqrt{1-\alpha^*}\right) - \coth\left(\tau\sqrt{1-\alpha^*}\right)\right] = 0. \tag{11}$$

In addition to the always existing solution $\tau_1 = \tau_2$, additional solutions appear in Fig. 6b and 6c, (with increasing of β-parameter or decreasing temperature). Fig. 6b shows the moment (bifurcation) of the appearance of an additional solution, more preferable in magnitude of the quasiclassical action. In Fig. 6c, there are already two such additional solutions, but only one of them is preferable in the magnitude of the action (in the case when these solutions are close, the quantum beat regime is realized).

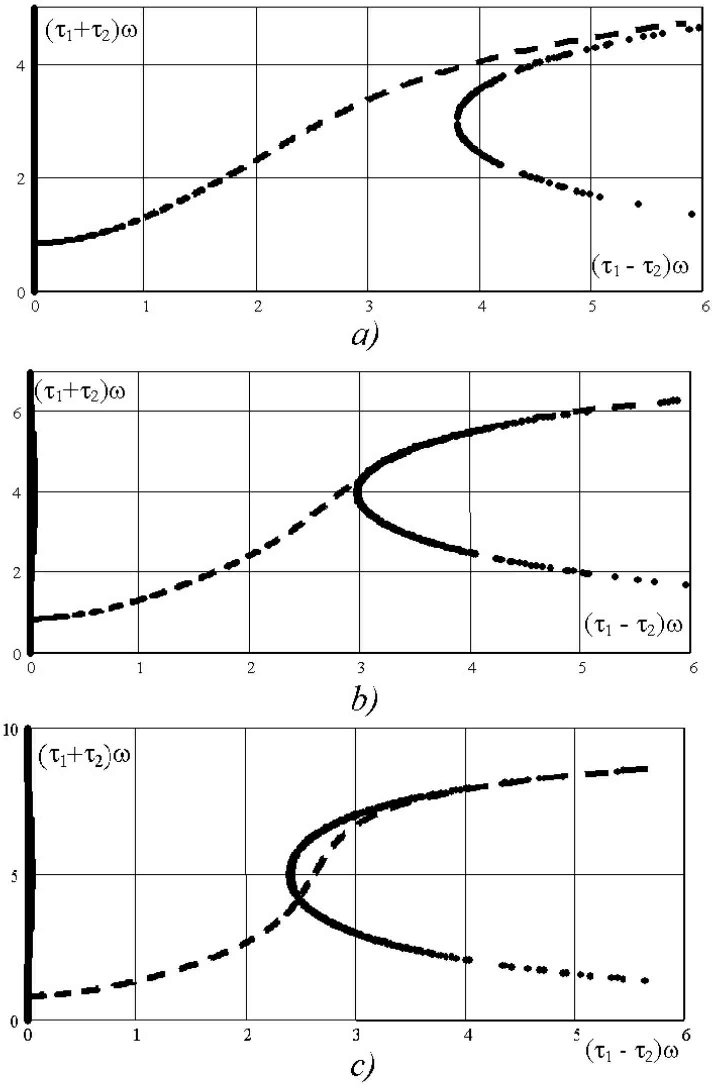

FIG. 6. Results of a numerical solution of a system of transcendental equations (10–11)

5. Theoretical calculation of 2D bifurcation modes in the model 2D-oscillator potential at a finite temperature in an external electric field in the weak dissipation limit for a matrix, possessing metamaterial properties

In case of the quasi-two-dimensional Au–QD structures under investigation, we are dealing with a situation where these structures can have the properties of a metamaterial, i.e. the relative permittivity of the heat-bath effectively becomes "negative", and with it the coefficient of interaction of the tunneling particles in the dipole-dipole approximation also becomes negative ($\alpha < 0$). As in the numerical analysis of the equations system (10–11), it is possible to identify a bifurcation-tunnel trajectories for certain values of temperature, either the asymmetry parameter of the potential (associated with the magnitude of the external electric field) or the interaction coefficient α ($\alpha < 0$), which depends on the relative permittivity, negative for metamaterials. Numerical analysis of the system (10–11) also makes it possible to reveal a fine structure of the transition in the vicinity of the bifurcation point, i.e. the quantum beat regime for parallel transport of tunneling particles (in addition to the trivial solution (10–11), an additional solution appears).

The result of this numerical analysis is shown in Fig. 7 (and, as is easy to see, differs from the analogous result presented in Fig. 6).

Dependence of the tunneling probability on the electric field strength magnitude is shown in Fig. 8. Realization of the stable 2D bifurcations region has been revealed in Fig. 8b. Fig. 8a shows the beginning of this region.

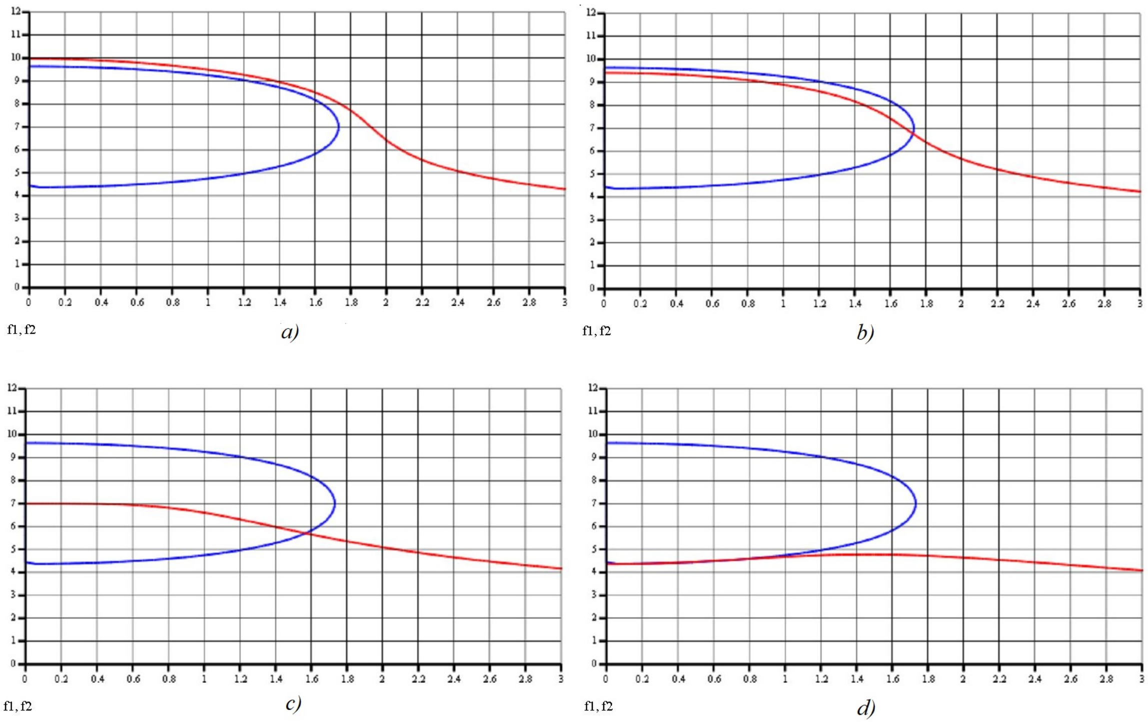

FIG. 7. Numerical solution of the transcendental equations system (10–11) for the case $\alpha < 0$. The transition from figure $a)$ to figure $d)$ is accompanied by an increase in the strength of the electric field (or the asymmetry parameter of the oscillator potential)

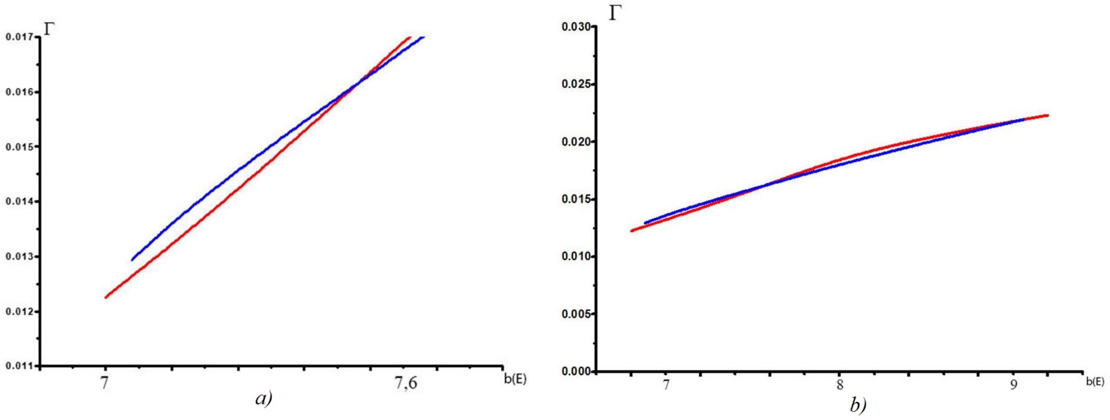

FIG. 8. Dependence of the tunneling probability on the magnitude of the electric field strength

In the vicinity of this point (as in the vicinity of the end point of the stable regime of 2D bifurcations, Fig. 8a and Fig. 8b), the quantum beats mechanism is realized, where the mechanisms of synchronous and asynchronous transfer of tunneling particles compete. Regions for realization of the 2D bifurcations stable effect are identified and the corresponding boundaries for the existence of 2D bifurcations are numerically analyzed when the control parameters (the reciprocal temperature β, the relative permittivity of the heat-bath ε, and the asymmetry parameter for 2D-potential of the system b, which weakly nonlinearly dependent on the strength value of the external electric field) are changed. The corresponding dependence of the field strength range at which stable 2D bifurcations are realized, depending on the magnitude of the inverse temperature, is shown in Fig. 9.

Fig. 10 presents the "phase diagram" for realization of the stable 2D-bifurcations regime for tunneling current (in case of quasi-two-dimensional Au–QD structure) in a matrix of metamaterial depending on the control parameters: the reciprocal temperature, magnitude of the electric field strength (or the asymmetry parameter of

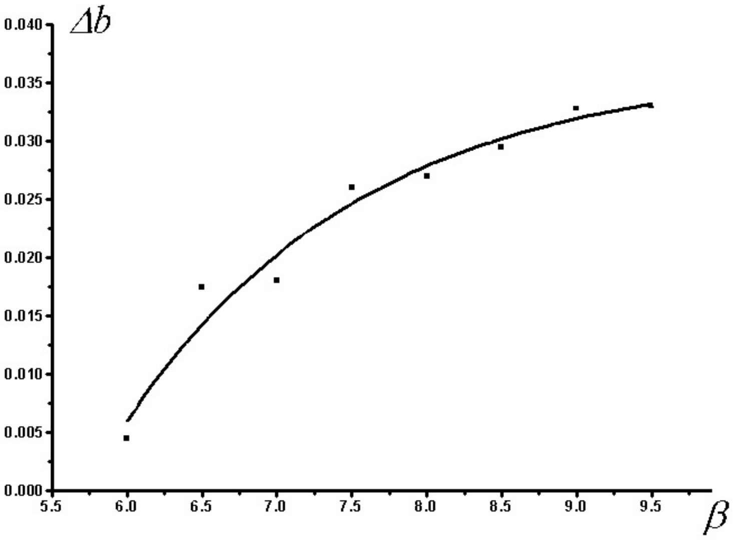

FIG. 9. Dependence of the field strength range at which stable 2D bifurcations are realized, depending on the inverse temperature

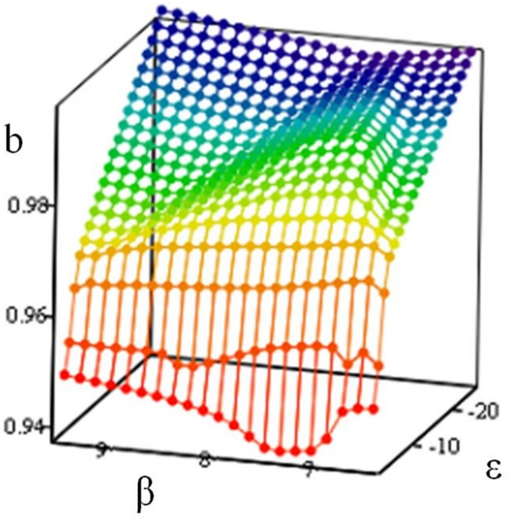

FIG. 10. The phase diagram for realization of the stable 2D-tunneling current bifurcations in a matrix of metamaterial depending on the control parameters: the inverse temperature, the electric field strength (or the potential asymmetry parameter), and the value of the (negative) relative permittivity for the heat-bath matrix

the potential), and the value (negative) of the relative dielectric permeability in the heat-bath matrix, in which the metamaterial is used.

Thus, dependence of the field strength, at which stable 2D bifurcations are realized, on the magnitude of the reciprocal temperature is investigated. In contrast to conventional dielectric matrices, in the case of a metamaterial, the region of stable 2D bifurcations significantly narrows, which is probably due to the inversion of the sign of the tunneling particles interaction.

6. A qualitative comparison of the obtained experimental and theoretical results, as well as a comparative analysis of the 2D-tunneling bifurcations effects both for the case of quasi-one-dimensional and quasi-two-dimensional structures with Au–QD

As noted in Section 4, solution of the transcendental equations system (10–11) allows us to identify the bifurcation of 2D-tunnel trajectories, at a certain value of the temperature β^*, or the potential asymmetry parameter

$b^* = b/a$ associated with the magnitude of the applied electric field, or the interaction coefficient $\alpha^* = 2\alpha/\omega^2$, (where $\alpha = e^2/\varepsilon\varepsilon_0 R_0^3$, in particular, depends on the relative dielectric constant of the heat-bath; the problem of studying 2D bifurcations with dissipation when changing the parameter ε may be of separate interest). Numerical analysis of the system (10–11) also makes it possible to reveal a fine structure of the transition in the neighborhood of the bifurcation point, namely, the quantum beat regime for parallel transport of tunneling particles. As a result, the probability of 2D tunneling with exponential accuracy is defined as $\Gamma = \exp(-S)$, where S is given by expression (9), taking into account the solution of system (10–11). Since we are interested in a qualitative comparison with the existing tunnel VAC for the system "cantilever needle – gold nanoclusters (quasi-one-dimensional Au–QD structures" (see Section 2), we are interested in the dependence Γ on the asymmetry parameter $b^* = b/a$. The result of a comparison of this theoretical curve with the experimental I—V characteristic is shown below in Fig. 11. But it must be taken into account that we consider two regions of the electric field change: under positive voltage with the realization of the 2D-bifurcation regime; and at a negative voltage with the attainment of a symmetric potential, which in the case of synchronous tunnel transport along parallel coordinates gives, in the doubled pre-exponential factor, a singularity of the single peak type in this case.

The conditions for the model applicability under consideration are due to the approach of a rarefied gas of pairs "instanton-anti-instanton" and have been discussed in [1–4, 8–14]. In the model under consideration, the Coulomb effects can be suppressed if the starting energy of a particle in a QD substantially exceeds the energy of the Coulomb repulsion: $U_0 \gg \frac{e^2}{a_0+b_0}$.

Thus, generalizing the results of Refs. [1, 9], we have obtained a qualitative comparison of the theoretical curves for the dissipative 2D-tunneling probability as a function of the applied electric field, taking into account the bifurcation point (at positive voltage) and the presence of a single peak in the case of a symmetric potential (with negative voltage) with separate experimental I—V characteristics for the "platinized cantilever needle – quantum dot (gold nanoclusters)" system, obtained by a group of co-authors from Nizhny Novgorod State University, named by N. I. Lobachevsky. These results are shown in Fig. 11.

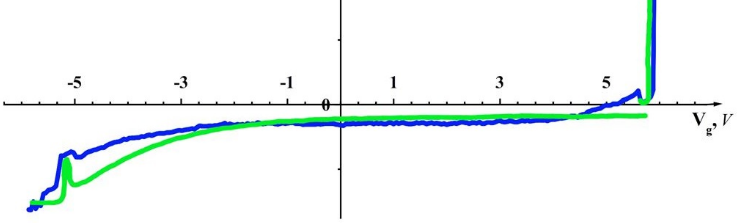

FIG. 11. Comparison of the theoretical curve (green curve) for the 2D-dissipative parallel tunneling probability with the experimental I—V characteristic given in Fig. 1b (blue curve)

In addition to the fairly good qualitative agreement between the theoretical and experimental dependences (with the exception of small transition regions), the result of this work allows us to conclude that the stable 2D bifurcation (changing the tunneling mode from synchronous to asynchronous) predicted in Ref. [1] have been found experimentally. Near this point (a sharp break in the VAC), the small local minimum may be a consequence of the quantum beat regime also described in [1], and which were taken into account in the numerical analysis presented in Fig. 11.

In the case of quasi-two-dimensional Au–QD structures possessing metamaterial properties (see Section 3), as noted in Section 5, we obtain on the field dependence of the 2D-dissipative tunneling probabilities not one, but two characteristic breaks. The result of comparing for this field dependence with the experimental I—V characteristic (see Fig. 3) is shown in Fig. 12.

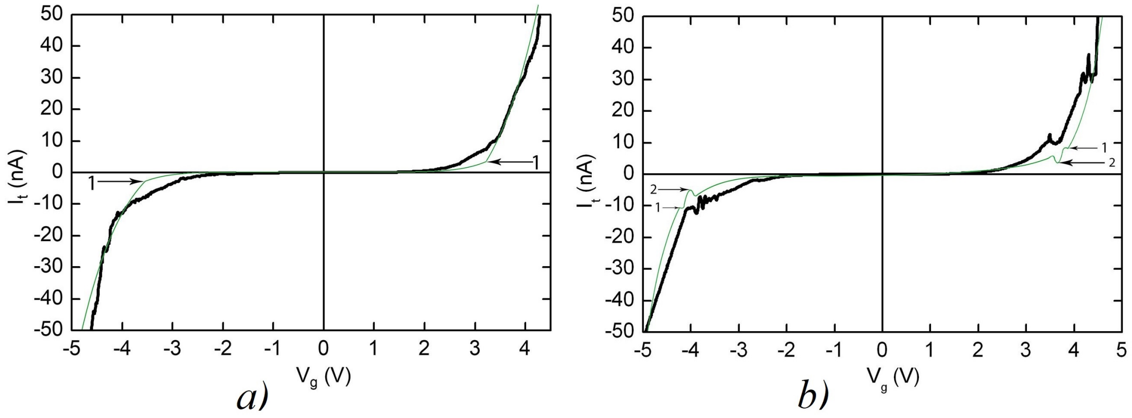

FIG. 12. Comparison of the experimental VAC (black curve) for quasi-two-dimensional Au–QD structures possessing the metamaterial properties (Figs. 2 and 3, with the field dependence of the 2D-dissipative tunneling probability (green curve) calculated in Section 4 in the weak-dissipation limit. Case *a*) corresponds to the "smoothed" double kinks or 2D-bifurcations without quantum beats regime. In case *b*) in addition to the "smoothed" double kinks (or double 2D-bifurcations regime), the quantum beat regime was also observed in the vicinity of the points of 2D bifurcations

7. Conclusion

The science of the quantum tunneling with dissipation has been developed in the works of A. J. Leggett, I. Affleck, P. Wolynes, A. I. Larkin, Yu. N. Ovchinnikov and other authors [1–3, 8, 10–12, 14]. Earlier in his review [10] A. J. Leggett posed the "supertask" of experimental observation for the macroscopic quantum effects of dissipative tunneling. The possibilities and development of the modern nanostructures technology brought the realization of this task closer. We hope that with this work we make our modest contribution to its solution.

Acknowledgements

Authors thank Prof. A. J. Leggett and Prof. Yu. N. Ovchinnikov (who for the first time together with B. I. Ivlev predicted the 2D-tunneling bifurcations effect) for useful discussions. This work was supported by the Ministry of Education and Science of the Russian Federation (Project No. 3.6321.2017/8.9).

References

[1] Aringazin A. K., Dahnovsky Yu. I., Krevchik V. D., Semenov M. B., Ovchinnikov A. A., Yamamoto K. Two-dimensional tunnel correlations with dissipation. *Phys. Rev. B*, 2003, **68**, P. 155426(1–12).

[2] Ivlev B. I., Ovchinnikov Yu. N. Decay of metastable states in a situation with close-lying tunneling trajectories. *JETP*, 1987, **66**, P. 378–383.

[3] Benderskii V. A., Vetoshkin E. V., Kats E. I., Trommsdorff H. P. Competing tunneling trajectories in a two-dimensional potential with variable topology as a model for quantum bifurcations. *Phys. Rev. E*, 2003, **67**, P. 026102(1–10).

[4] Zhukovskii V. Ch., Dakhnovskii Yu. I., Gorshkov O. N., Krevchik V. D., Semenov M. B., Smirnov Yu. G., Chuprunov E. V. Rudin V. A., Skibitskaya N. Yu., Krevchik P. V., Filatov D. O., Antonov D. A., Lapshina M. A., Yamomoto K., Shenina M. E. Observed two-dimensional tunnel bifurcations in an external electric field. *Moscow University Physics Bulletin*, 2009, **64**, P. 475–479.

[5] Engheta N. (edt.), Ziolkowski R. W. (edt.) *Metamaterials: Physics and Engineering Explorations*. John Wiley & Sons & IEEE Press, 2006, 440 p.

[6] Valentine J., Zhang S., Zentgraf T., Ulin-Avila E., Genov D. A., Bartal G., Zhang X. Three-dimensional optical metamaterial with a negative refractive index. *Nature*, 2008, **455**(7211), P. 376–379.

[7] *National Science Review*. Special issue "Metamaterials Collection", 2018, **5**.

[8] Ovchinnikov Yu. N. Conductivity of granulated metallic films. *JETP*, 2007, **131**, P. 286–290.

[9] Zhukovsky V. Ch., Gorshkov O. N., Krevchik V. D., Semenov M. B., Groznaya E. V., Filatov D. O., Antonov D. A. Controlled dissipative tunneling in an external electric field. *Moscow University Physics Bulletin*, 2009, **64**, P. 27–32.

[10] Caldeira A. O., Leggett A. J. Quantum tunnelling in a dissipative system. *Ann. of Phys*, 1983, **149**, P. 374–456.

[11] Larkin A. I., Ovchinnikov Yu. N. Decay of the supercurrent in tunnel junctions. *Phys. Rev. B*, 1983, **28**, P. 6281–6285.

[12] Leggett A. J., Ovchinnikov Yu. N., Krevchik V. D., Semenov M. B., Shorokhov A. V. et. al. *Transfer Processes in Low-dimensional systems*. UT Research Press, Tokyo, 2005, 690 p.

[13] Filatov D., Guseinov D., Antonov I., Kasatkin A. Gorshkov O. Imaging and spectroscopy of Au nanoclusters in yttria-stabilized zirconia films using ballistic electron/hole emission microscopy. *RSC Advances*, 2014, **4**, P. 57337–57342.

[14] Leggett A. J., Ovchinnikov Yu. N., Krevchik V. D., Semenov M. B., Yamamoto K., Filatov D. O. *Controllable dissipative tunneling. Tunnel transport in low-dimensional systems*. Fizmatlit, Moscow, 2011–2012, 600 p.

NANOSYSTEMS: PHYSICS, CHEMISTRY, MATHEMATICS, 2018, 9 (6), P. 735–740

Orientational order parameter of liquid crystalline mixtures – A birefringence study

Shahina[1], C. M. Subhan[2], S. Rangappa[3], K. Fakruddin[1*]

[1]Department of Physics, Ghousia College of Engineering, Ramanagara., Karnataka, India
[2]Department of Physics, Shri Shirdi Sai Institute of Science and Engineering, Vadiyampeta,
Anantapurmu, Andhra Pradesh, India
[3]Department of Physics, BIT, Bangalore, Karnataka, India

*drfakruddin2008@gmail.com

PACS 42.70.Df, 61.30.Gd,42.81.Gs,78.20.Ci **DOI 10.17586/2220-8054-2018-9-6-735-740**

The orientational order parameter is one of the most important material parameters of nematic phase. In the present work, the phase transition temperatures of the mesogenic mixtures are measured by using a polarizing optical microscope. The birefringence in nematic phase is estimated by measuring ordinary and extraordinary refractive indices. The birefringence is also measured by measuring the diameter of Newton's rings at various temperatures in nematic phase. The orientational order parameter is evaluated by using the birefringence data obtained in the above two methods. The orientation order parameter can be enhanced by the dispersion of different nanoparticles in the liquid crystal matrix.

Keywords: Liquid crystalline mesogens, orientational order parameter, birefringence, refractive index, Newtons rings.

Received: 17 August 2018

Revised: 27 October 2018

1. Introduction

Liquid crystals are self-assembled dynamic functional soft materials which posses both order and mobility at molecular, supramolecular and microscopic levels [1, 2]. Liquid crystals have received much attention in the recent years because they exhibit anisotropy in their mechanical, electrical and optical properties, behaving like solid crystals nevertheless they have no ability to support shearing and thus they flow like ordinary isotropic solution. This dual nature of the materials is important in technological applications such as displays and optical switches. With technological advances the LC display (LCD) is currently expected to achieve high electro optical performance as well as to be of low power consumption [3]. Instead of synthesizing a number of LC compounds as constituents, either a suitable mixtures can be used or by doping nano materials into LCs can be used. By mixing two nematogens, one can often obtain a lower melting point. Usually two nematogens exhibit the property of continuous miscibility without crossing any line [4]. Binary mixtures offer the advantage of frequently exhibiting eutectic behavior in their solid mesophase transition and in mesophase isotropic transition. The temperature varies linearly with composition further for the technological use of LC; the liquid crystalline materials of specific molecular design and synthesis are viable but expensive to influence the properties of mesophases. The desired properties can be obtained by mixing compounds of various molecular shapes rather than by looking for pure compounds [5, 6] or by the incorporation of metal nanoparticles into LCs, which makes it easier to obtain a better profile of display parameters [7]. The metal nanoparicles embedded in LCs have attracted much interest not only in the field of magnetic recording media but also in the area of medical care including hyperthermia, photomagnetics, magnetic resonance imaging, cancer therapy, sensors and high frequency applications [8–12].

The amino methyl hydroxyl phenoxycarbonitrile and amino phenyl benzoates are the exciting class of new LC compounds with different spacer, end and terminal groups having fascinating structural variations. In the present work, the following homologous series of compounds are selected and their mixtures are taken in equal ratio. The molecular structure of the liquid crystal compounds in the present work is shown in Fig. 1. The optical studies were carried out; using the data obtained and the orientational order parameter by birefringence methods is evaluated.

2. Experimental

2.1. Refractive index method to measure birefringence

The refractive indices of the liquid crystalline compounds were measured with wedge shaped glass cell similar to the one used to obtain birefringence by Haller et al. [13, 14] and modified spectrometer. A wedge shaped glass cell was prepared with two optical flats of rectangular glass plates (50 mm × 25 mm) sandwiched with glass slide of 0.05 mm thick which acted as a wedge spacer. The cell is filled with the liquid crystal material. The liquid

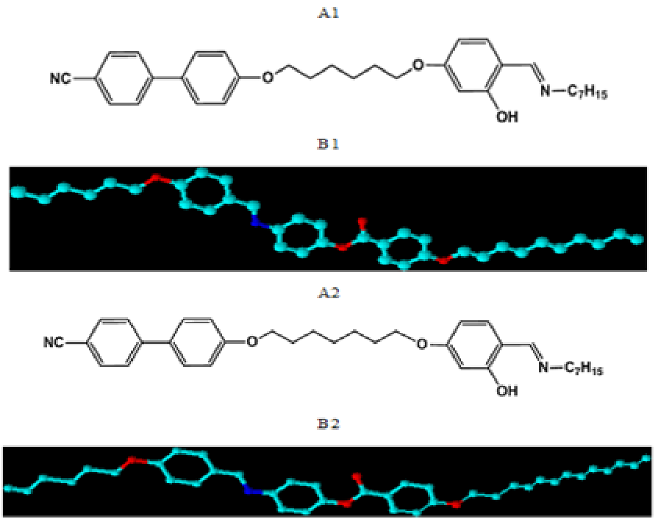

FIG. 1. Molecular structure of the LC compounds C1=A1+B1 & C2=A2+B2
A1: 41-(6-(4-(heptylamino)methyl)-3-hydroxyphenoxy)hexyloxy)biphenyl-4-carbonitrile[$C_{33}H_{40}N_2O_3$]
B1: 4-((4-(hexyloxy)benzylidene)amino)phenyl4-(decycloxy)benzoate[$C_{36}H_{47}N_1O_4$]
A2: 41-(7-(4-(pentylamino)methyl)-3-hydroxyphenoxy)heptyloxy)biphenyl-4-carbonitrile[$C_{34}H_{42}N_2O_3$]
B2: 4-((4-(hexyloxy)benzylidene)amino)phenyl4-(tridecycloxy)benzoate[$C_{39}H_{53}N_1O_4$]

crystal material in the cell acts as a uniaxial crystal with its optic axis parallel to the edge of the spacer glass plate. The same technique is also used by several authors [15–17].

2.2. Newton's ring method to measure birefringence

The experimental setup consists of Plano convex lens of small radius of curvature (13 mm) and plane glass plate which is being placed in hot stage connected to specially designed microcontroller based temperature and image capturing device. The LC sample whose birefringence is to be measured is placed between the lens and plate. Systems of concentric rings were observed in nematic phase. The optical path difference between e-ray and o-ray is given by y, δn which corresponds to ring number k and wavelength λ for a bright fringe is given by:

$$\delta n = \frac{k\lambda}{y}, \tag{1}$$

$$y = \frac{x^2}{2R}. \tag{2}$$

From Eqns. (1) and (2),

$$\delta n = \frac{(2R\lambda)\,k}{x^2}. \tag{3}$$

Since $2R\lambda = C$, cell constant for the given wavelength of light:

$$\delta n = \frac{Ck}{x^2}, \tag{4}$$

where x is the radius of the ring and R is the radius of curvature of the lens used. Thus, δn can be measured with great accuracy by taking the slope of the straight line drawn between x^2 versus the ring number, k. We can obtain the same result by considering the dark rings also; as the temperature decreases, birefringence δn increases. The method adopted for the estimation of orientational order parameter from δn given by Kuczynski et al. [18, 19].

2.3. Estimation of order parameter from birefringence (δn)

For the determination of order parameter S from the birefringence measurements δn without considering the local field experienced by the molecule in a LC phase were used by many authors [20–22]. The birefringence δn, which is a function of temperature, is fitted to the following equation:

$$\delta n = \Delta n \left(1 - \frac{T}{T^*}\right)^{\beta}, \tag{5}$$

TABLE 1. The phase variants and transition temperatures and thermal ranges of mesogenic mixtures

Sl.	Compound	Transition Temperature °C				Thermal range	
No.		I–N	N–SmA	SmA–SmB	Crystal	ΔN	ΔSmA
1	C1 = 50% A1 + 50% B1	184.6	169	160	85.6	15.6	9
2	C2 = 50% A2 + 50% B2	137.8	126.4	109	67.1	11.4	17.4

where T the absolute temperature, T^* and β are constants, $T^* = T + X$, where X is varied from 0.0001 to 4 K and the exponent β is close to 0.17 – 0.22. This procedure enables one to extrapolate δn to the absolute zero temperature. In practice, the three adjustable parameters T, Δn and β were obtained by fitting the experimental data for δn to the following equation written in the logarithmic form:

$$\log \delta n = \log \Delta n + \beta \log \left(\frac{T^* - T}{T^*} \right). \tag{6}$$

In these investigations, the values $\log \Delta n$ and β are estimated by the linear regression method. The parameter T^* is adjusted to get best correlation coefficient of the linear regression (T^* is higher than the clearing temperature and is adjusted up to 4 K to obtain the best correlation regression coefficient of linear regression). Further, in evaluating Δn, only the nematic range is considered. Thus, S is given by:

$$S = \frac{\delta n}{\Delta n}. \tag{7}$$

3. Results and discussion

The phase variants and transition temperatures of the above mesogenic mixtures are measured by using polarizing thermal microscope and depicted in Table 1. The refractive indices of the mesogenic mixtures are measured at various temperatures by using modified spectrometer attached with small angled prism which houses the LC sample. Anisotropy is an inherent property of liquid crystals therefore it exhibits birefringence. When the temperature dependence of refractive index (R.I) is measured, the R.I remains constant in isotropic phase. With the decrease of temperature from I–N phase, the isotropic R.I value splits into two, extraordinary R.I ($n_e > n_{iso}$) and ordinary R.I ($n_o < n_{iso}$) respectively. This splitting is clearly observed in the telescope of spectrometer at an angle of minimum deviation. When the temperature decreases, ne increases while the no decreases. With the further decrease of temperature in the deep nematic region the R.I value of both ne and no attains deep saturation which is shown in Fig. 2. It is also observed that the refractive indices could not be measured in smectic phases as the splitting has hazy appearance.

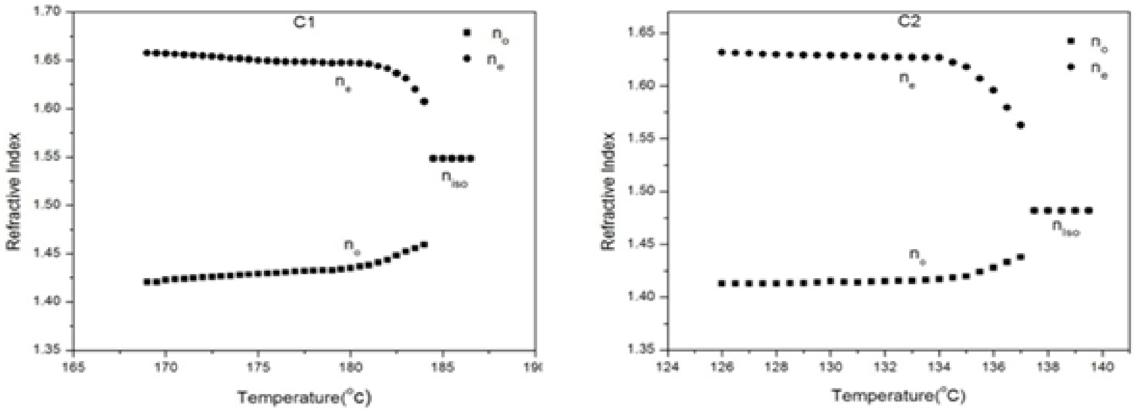

FIG. 2. The temperature variation of Refractive index in C1 & C2 mixtures

While evaluating the S by refractive indices and Newton's rings methods the parameter T^* is adjusted to $T_C + (1.5 - 2.2\ \text{K})$. The birefringence in perfect order and β values obtained are represented in Table 2.

TABLE 2. The birefringence of compounds in perfect order and β values

Sl. No.	Compound	Birefringence in perfect order		β (values)	
		RI method	Newton rings method	RI method	Newton rings method
1	C1	0.42	0.420	0.19	0.189
2	C2	0.40	0.417	0.22	0.200

In the liquid crystalline phase both Brownian and crystalline fields are acting, which results the decrease of potential on the electron system,thus contributing to more polarization. Hence the birefringence increases with decrease of temperature. As $\log(1 - T/T^*)$ decreases $\log(\delta n)$ increases as shown in Fig. 3.

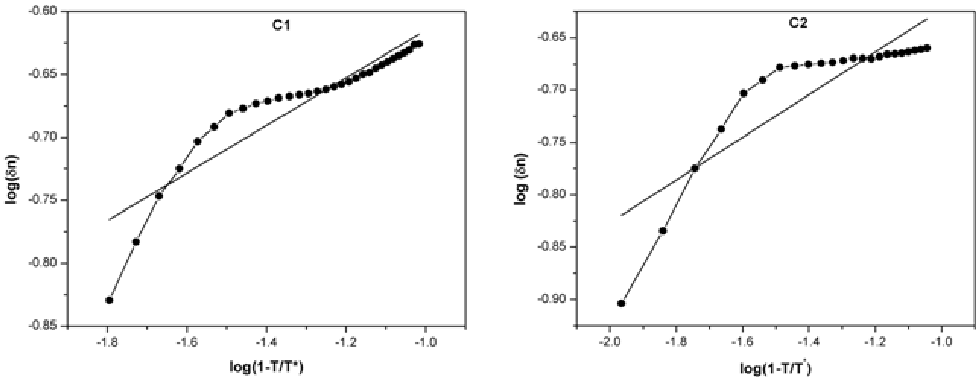

FIG. 3. The $\log(\delta n)$ vs $\log(1 - T/T^*)$ by RI method for C1 & C2

The diameter of Newton's rings is directly proportional to square root of natural numbers. The birefringence δn is measured by Newton's rings method by measuring the radius of the Newton's rings at various temperatures. The slope of the straight line is estimated by plotting the graph between the square of the radius of the ring vs. the ring number at 518 nm for I–N temperatures. It is observed that as the temperature increases the slope increases and birefringence decreases. This variation is represented in the Fig. 4 for C1 and C2 mixtures.

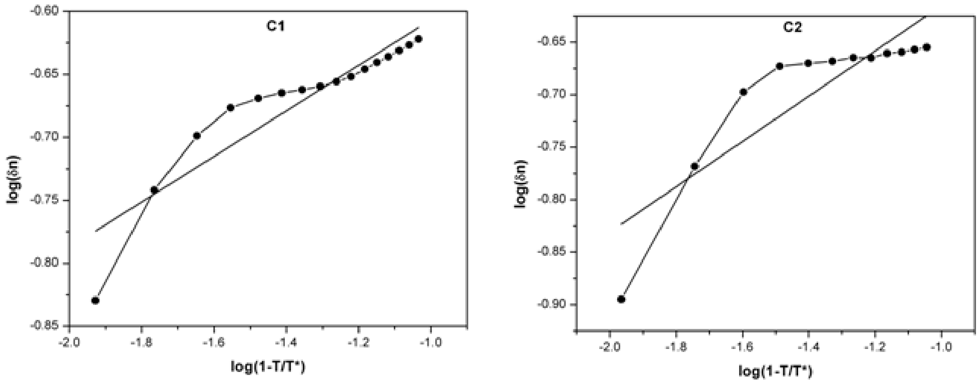

FIG. 4. The $\log(\delta n)$ vs $\log(1 - T/T^*)$ in newton rings method of C1 & C2

As the LC transitions takes place from I–N, the packing of the molecules occurs with positional as well as translational order, hence order parameter (S) increases with decrease of temperature. The OOP obtained by birefringence methods are in the range of 0.3 – 0.7 for the above LC mixtures. The S values obtained from δn by refractive index and Newton rings method are in good agreement with each other. The comparison of the S by the two optical methods is shown in the Fig. 6.

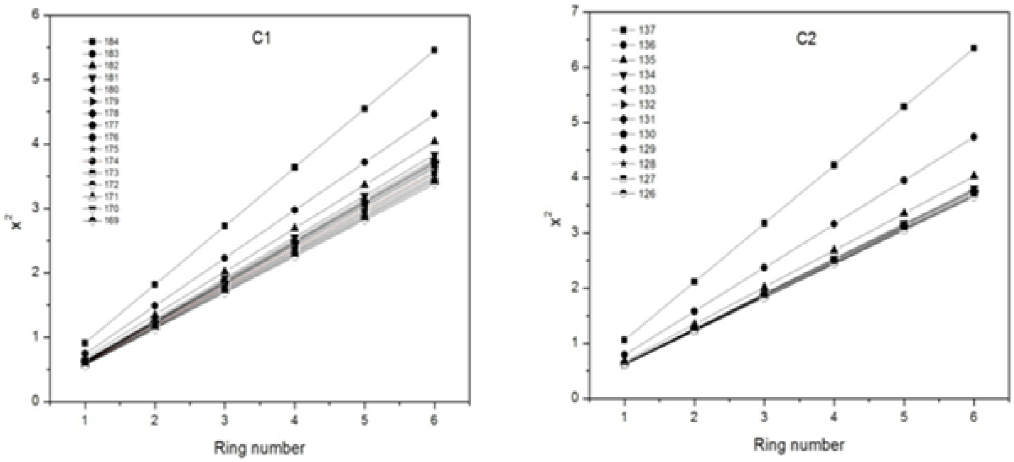

FIG. 5. The variation of ring number and square of radius in C1 & C2 compounds

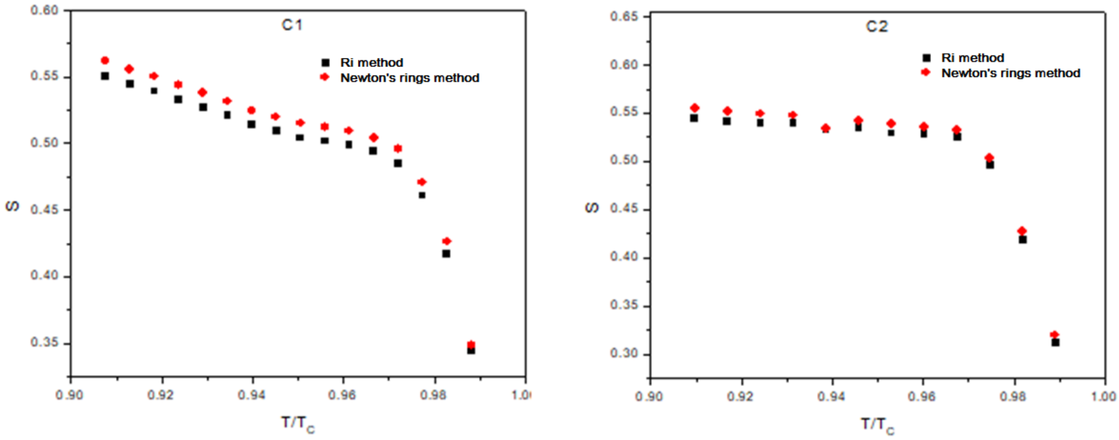

FIG. 6. The variation of S with reduced temperature in C1 & C2 mixtures

4. Summary

The use of Newton's rings technique is a precise method for the determination of birefringence of different liquid crystalline phases using simple approximations. This method can also be applied to study the order parameter in smectic phases, as no local field is involved. The order parameter obtained by Newton's rings method is compared with that of refractive indices method. The liquid crystals, being anisotropic media, hence provide good support for the self assembly of nano materials into large organizing structures in multiple dimensions. Therefore, dispersion of nano particles into liquid crystals has emerged as fascinating area of research from an application point of view. Nano objects (guests) that are embedded in the liquid crystals (hosts) can trap the ion concentration, electrical conductivity and improve electro optic response of the host materials. Hence, by the dispersion of nanoparticles into liquid crystals, one can improve the orientation order parameter, an important display property.

Acknowledgements

Authors express their thanks to the Department of Physics, Ghousia College of Engineering, Ramanagaram for providing laboratory facilities. The authors are thankful to Dr. C. M. Yellamagad and Dr. D. S. ShankarRao for providing liquid crystalline compounds to carry out the present studies. The financial support rendered by the VTU Belgaum under VTU research grant scheme for the research project [No. VTU/Aca/2011-12/A-9/750] is gratefully acknowledged.

References

[1] Kato T., Mizoshita N., Kishimoto K. Functional liquid-crystalline assemblies: self-organized soft materials. *Angew Chem. Int. Ed. Engl.*, 2005, **45** (1), P. 38–68.

[2] Goodby J.W., Saez I.M., et al. Transmission and amplification of information and properties in nanostructured liquid crystal. *Angew Chem. Int. Ed. Engl.*, 2008, **47** (15), P. 2754–2787.

[3] Shiraishi Y., Toshima N., et al. Frequency modulation response of a liquid-crystal electro-optic device doped with nanoparticles. *Appl. Phys. Lett.*, 2002, **81** (15), P. 2845–2847.

[4] de Gennes P.G., Prost J. *The Physics of Liquid Crystals*, Clarendon Press, Oxford, 1998.

[5] Obadovic D.Z., Stojanovic M., et al. Study of Binary Cholesteric Liquid Crystalline Mixtures Doped with Some Chiral Nonmesogenic Estradiol Derivatives. *Mol. Cryst. Liq. Cryst.,* 2011, **547**, P. 1736–1743.

[6] Eren San S., Mustafa Okutan, Oguz Koysal, Yusuf Yerli. Carbon Nanoparticles in Nematic Liquid Crystals. *Chin. Phys. Lett.*, 2008, **25** (1), P. 212–215.

[7] Goel P., Arora M., Biradar A.M. Electro-optic switching in iron oxide nanoparticle embedded paramagnetic chiral liquid crystal via magneto-electric coupling. *J. App. Phy.,* 2014, **115**, P. 124905.

[8] Silva J.B., Brito W.D., Mohallem N.D.S. Influence of heat treatment on cobalt ferrite ceramic powders. *Material Sci. Eng. B*, 2004, **112**, P. 182–187.

[9] Sun S., Murray C.B., et al. Monodisperse FePt Nanoparticles and Ferromagnetic FePt Nano Crystal Superlattices. *Science*, 2000, **287**, P. 1989–1992.

[10] Pankhurst Q.A., Connolly J., Jones S.K., Dobson J. Applications of magnetic nanoparticles in biomedicine. *J. Phys. D: Appl. Phys.*, 2003, **36**, P. 167–181.

[11] Ito A., Shinkai M., Honda H., Kobayashi T. Medical application of functionalized magnetic nanoparticles. *J. Bio. Sci Bio. Eng.*, 2005, **100** (1), P. 1–11.

[12] Meng X., Li H., et al. Mossbauer study of cobalt ferrite nanocrystals substituted with rare-earth Y^{3+} ions. *J. Magn. Magn. Meter.*, 2009, **321**, P. 1155–1158.

[13] Toh C.L., Xu J., He C. Synthesis and characterisation of main-chain hydrogen-bonded supramolecular liquid crystalline complexes formed by azo-containing compounds. *Liq. Cryst.*, 2008, **35** (3), P. 241–251.

[14] Haller I., Huggins H.A., Lilienthal H.R., McGuire T.R. Order – Related Properties of Some Nematic Liquids. *J. Phys. Chem.*, 1973, **77** (7), P. 950–954.

[15] Fakruddin K., JeevanKumar R., DattaPrasad P.V., Pisipati V.G.K.M. Orientational Order Parameter – 1 A Birefringence Study. *Mol. Cryst. Liq. Cryst.,* 2009, **511**, P. 133–145.

[16] Subhan C.M., Jeevan Kumar R., et al. An Optical Study to Estimate Orientational Order Parameter on Some Benzylidene amino phenyl benzoate Liquid Crystals. *Acta Physica Polonica A,* 2016, **129** (3), P. 284–288.

[17] Narasimhamurthy G.K., Subhan C.M., et al. Orientational order parameter of some CBOnO.m liquid crystalline compounds – an optical study. *Mol. Cryst. Liq. Cryst.*, 2016, **641**, P. 25–36.

[18] Kuczynski W., Zywucki B., Malecki J. Determination of Orientational Order Parameter in Various Liquid-Crystalline Phases. *Mol. Cryst. Liq. Cryst.*, 2002, **381**, P. 1–19.

[19] Zywucki B.J., Kuczynski W. The Orientational Order in Nematic Liquid Crystals From Birefringence Measurements. *Dielectr. Electr. Insul.,* 2001, **8** (3), P. 512–515.

[20] Ramakrishna Nanchara Rao M., Datta Prasad P. V., Pisipati V.G.K.M., MadhaviLatha D. An Optical study on Orientational order parameter and Molecular Polarizability in Benzylidene Anilines. *Solid State Phenomena*, 2012, **181–182**, P. 102–105.

[21] Subramhanyam H.S., Krishnamurti D. Polarization Field and Molecular Order in Nematic Liquid Crystals. *Mol. Cryst. Liq. Cryst.*, 1973, **22**, P. 239–248.

[22] Pardhasaradhi P., Datta Prasad P.V., et al. Orientational order parameter studies in two symmetric dimeric liquid crystals – an optical study. *Phase Transitions*, 2012, **85** (12), P. 1031–1044.

NANOSYSTEMS: PHYSICS, CHEMISTRY, MATHEMATICS, 2018, 9 (6), P. 741–745

X-ray structural studies of the Pd–In–Ru system using synchrotron radiation

O. V. Akimova[1], A. A. Veligzhanin[2]
[1]Moscow State University,Moscow, 119991 Russia
[2]National Researches Centre “Kurchatov Institute”, Moscow, 123098 Russia
akimova@physics.msu.ru

PACS 61.10.-i, 64.60.Cn, 61.82.Bg **DOI 10.17586/2220-8054-2018-9-6-741-745**

The paper presents X-ray diffraction studies of diffusion filters-membranes based on palladium. Information on the structural state of membranes was obtained using synchrotron radiation (SR) of Kurchatov Synchrotron Radiation Source. A comparison was made between states of the prolonged membrane relaxation after hydrogenation and that exposed to additional applied load by the method of electrolytic hydrogenation (EH). In addition to the structural maxima determining the face-centered lattice of the alloy matrix, reflections were revealed on the diffraction patterns, indicating the presence of long-range ordering in the structure.

Keywords: X-ray diffraction, synchrotron radiation, superstructure, palladium-based alloys.

Received: 15 October 2018

Revised: 27 October 2018

1. Introduction

When metal filters are used in the diffusion of high purity hydrogen production [1–4], the problems of reliability and duration of the membrane operation arise during interaction with hydrogen [4, 5]. These issues are related to changes in the structure of metals and alloys as a result of their hydrogenation [5–8]. Therefore, X-ray structural studies for analysis of the kinetics of structural defects in diffusion filters after hydrogenation are needed for the development of safe industrial technologies for production [1,4], storage and transfer of high-purity hydrogen [2, 3].

Atoms of alloying elements added to palladium in order to improve the mechanical characteristics and reliability of membrane operation in an aggressive gaseous medium [4]. The additives usually form point defects in the lattice of the metal-solvent that can be ordered to some degree. As a rule, hydrogenation is associated with strong plastic deformation for membranes, which is accompanied by the appearance and development of order-disorder processes in the distribution of metal atoms [9, 10]. Hydrogenation enhances diffusion processes [8, 11] and initiates phase transformations [12–14], generating a high concentration of vacancies, especially for various chemical interactions or affinity of elements with hydrogen [8, 15, 16]. Phase transformations in hydrogenated systems occur over a period of time [13] and affect on many of the structure-sensitive properties of membranes [1,4,5].

There are several advantages for synchrotron radiation (SR) in comparison with X-ray tube radiation, including: brightness, high photon flux, level of monochromatization, easily adjusted X-ray wavelength, a high degree of polarization and collimation provide a new level of X-ray analysis as well as the quality of information acquisition [17–19]. Therefore, the aim of this study was to perform an X-ray diffraction study of membranes using SR with special attention to the region of small angles where order-disorder phase transitions occur in the Pd–In–Ru system after hydrogenation can be observed.

The X-ray experiment was carried out using the equipment of the “Structural Material Science” station of Kurchatov Synchrotron Radiation Source [20].

2. Experimental and calculation details

2.1. The object of research

Foils Pd-6 wt.% In-0.5 wt.% Ru were developed and prepared by the research group of the Institute of Metallurgy and Material Science of the Russian Academy of Sciences (IMET RAN) [4]. The membranes of given composition possess high hydrogen permeability, good corrosion resistance, high plasticity and strength during maintenance in hydrogen containing gas mixtures. Nevertheless, there are some problems with their reliability that can be related with structural changes in membranes occurring during their operation in hydrogen.

Foils of 50 μm thickness were fabricated from high purity materials ($\approx$99.9 %) by electric arc melting and cold rolling of blanks on a four-roll rolling mill with intermediate vacuum annealing at a temperature of 900 °C for 1 hour [4]. Further, the foils were used as a filter in the plant for the determination of hydrogen permeability [19].

Then, the membranes, denoted as foil 1 and foil 2, were cooled slowly to the room temperature and stored under normal conditions (room temperature and pressure) for a year.

Further, foil 2 was electrolytically saturated by hydrogen (electrolyte-4% aqueous solution Na–F) during 0.5 hour at a current density of 10 mA/cm^2. X-ray diffraction (XRD) patterns were obtained using Cu-Kα_1 radiation upon the Bragg–Brentano geometry [13, 14]. X-ray diffractograms were measured over a narrow angular range near the structural maxima corresponding to the "main" phase of the foil. Only the upper 6 μm-thick layer of the foil contributed to the diffraction maxima.

2.2. X-ray experiment using synchrotron radiation (SR)

The X-ray diffraction with synchrotron radiation source was carried out in the Debye transmission geometry. A beam of SR was monochromatized using a silicon 111 channel-cut monochromator with energy resolution of 2×10^{-4} keV. The beam size was determined using motorized slits and was equal to (250×250) μm^2. The diffraction patterns of the samples were obtained at 0.6199 Å and 0.4573 Å, corresponding to the energies 20 keV and 24 keV. The samples were oriented perpendicularly to the beam. The scattering radiation was recorded by a two-coordinate detector Mar CCd165. During measurement, the samples performed an oscillatory motion perpendicular to the beam SR in two directions: within a range of 4 mm in the horizontal direction and 1 mm in the vertical direction, thus improving the averaging over crystallites orientations. To determine the distance and non-orthogonality of the detector to the beam, a standard sample of CeO$_2$ was used. Two dimensional X-ray diffraction patterns were integrated to one-dimensional I(2θ) curves by Fit2D software [21]. Analysis of diffraction profiles was carried out using the software package "Fityk" [22].

The phase diagram of the Pd-In-Ru system is not available in the literature. Since the concentration of Ru in the samples is small, and the difference between the atomic radii of Pd and Ru is about 2% (1.37 Å and 1.34 Å respectively) the system was considered binary. The Pd–In phase diagram [23] shows that solid solution Pd-6 wt.% In at room temperature is in single-phase region (Fig. 1). Indium concentration in observed phases was determined from lattice parameters according to Vegard law.

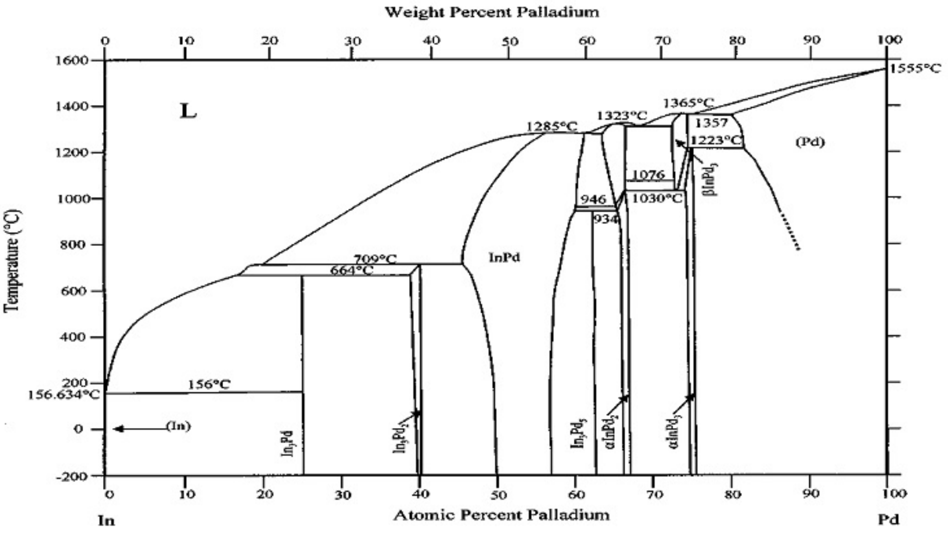

FIG. 1. Phase diagram of Pd–In system [23]

3. Results and discussion

Diffraction patterns of foil 1 and foil 2 obtained at the radiation energy 20 keV are shown onto Fig. 2. The angular positions of intense diffraction maxima corresponding to the main phase of foil 1 have determined a face-centered cubic lattice with a period a_0= 3.9031±0.0019 Å. The concentration of In was estimated to be 4.87±0.04 at. %. For foil 2, a face-centered cubic lattice with a period a_0= 3.9043 ± 0.0012 at. % has determined similarly, which corresponds to the In concentration of about 5.32±0.02 at.%.

Differences in the intensity of near orders reflections of coherent scattering regions (CSR) with Miller indices 111 and 100, in further CSR (111) and CSR (100), at identical relation of intensities for the far order reflections both foils may be showing the increasing effect of extinction upon the crystallographic direction [111].

In addition to the maxima corresponding to the main phase of the membranes, diffraction peaks of low intensity were found. The phenomenon of such reflections on diffraction patterns indicated in the membranes the presence of areas with concentrations of In significantly different from the alloy matrix. As one can see from the diffractograms in Fig. 2, the diffraction maxima of such phases were found in diffractograms of both foils and had a similar shape.

For foil 1, the diffraction peak isolated near the main maximum for CSR (110) (Fig. 2(a)) has corresponded to the phase with the lattice parameter 4.0868±0.0012 Å. Near it there is maximum that has corresponded for the basis phase with the lattice parameter 3.9059±0.0004 Å. That result corresponded to a concentration 5.9±0.1 at. % In.

For foil 2, a similar diffraction peak near the main maximum for CSR (110) (Fig. 2(b)) has allowed to identify three phases with lattice parameters 4.0731±0.0008 Å, 4.0826±0.0011 Å, 4.0912±0.0009 Å. Also for foil 2, a small fraction phase with lattice parameter 3.9577±0.0004 Å, the In content is 25.3±0.1 at. %, was determined for CSR (111).

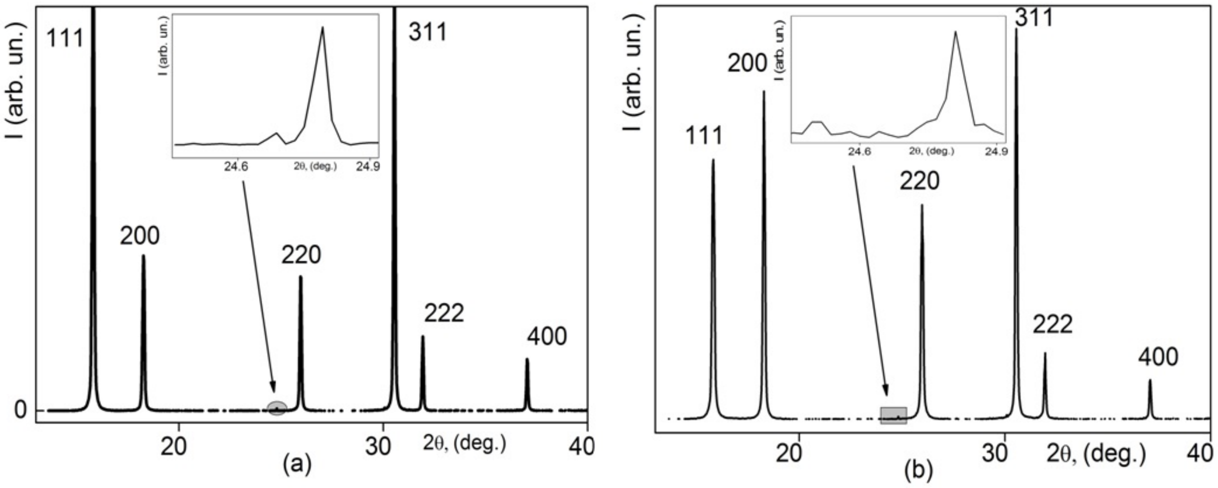

FIG. 2. Diffraction patterns foils at a beam energy of SR 20 keV: (a) – for foil 1; (b) – for foil 2

In order to investigate the possible superstructure nature of these phases, the diffraction spectra of foils were obtained at a beam energy of SR 24 keV (Fig. 3).

Structural reflections for the base (main) phase have revealed a cubic face-centered lattice for both foils with the same parameters as specified above.

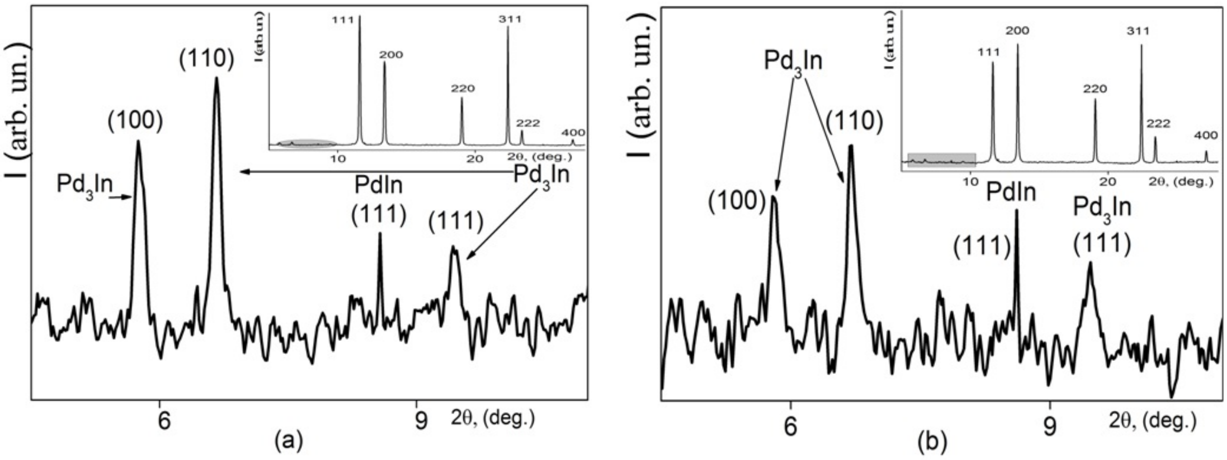

FIG. 3. Diffraction patterns foils at a beam energy of SR 24 keV, the definition superstructure regions: (a) – for foil 1; (b) – for foil 2

Finding reflections with prohibited interference indices for a face-centered cubic cell have indicated the presence of long-range ordering regions in both foils [24, 25]. Marked on Fig. 3, the diffraction peaks of low intensity correspond to the first order reflections for CSR (100), CSR (111) and CSR (110).

The results of the research show that the beginning of the process of regularization is likely upon the first hydrogenation of foils in IMET [4]. Differences in the shape of profiles similar superstructural maxima indicate that electrolytic hydrogenation can make some adjustments into the distribution of the components of the superstructural inclusions.

The angular positions of the superstructural peaks show phases corresponding to two groups with the formulas Pd_3In and PdIn. The results obtained are in agreement with the phase diagram data (Fig. 1).

The analysis of the angular positions of diffraction maxima corresponding to the phase Pd_3In revealed that the phase has a face-centered lattice. That is, the ordering process in the arrangement of atoms has passed with the preservation the structure of the metal-solvent lattice.

According to [25], the physical reason for the formation of such ordered regions is a decrease in the free energy of the system in the formation of segments with an increased concentration of atoms of one class. Such areas can increase as a result of ascending diffusion [25, 26]. As is shown by the description of alloys near the stoichiometric composition corresponding to the formula AB_3 [25], the most fully investigated in this area are alloys of the AuCu system near the composition of $AuCu_3$. The ordered phase in such systems exists in the range of concentrations from 17 at. % up to 37 at. %, which was also revealed for both Pd–In–Ru foils. In atoms in such ordered regions, occupying three times fewer positions, can be located at the vertices of cubic cells, and palladium atoms in the centers of faces.

It should be noted that alloys having a face-centered cubic lattice in an unordered state, upon formation of areas with content of components approaching 50% composition, can have an ordered state structure of the type AuCu [25]. Atoms of each kind in this type of ordering are arranged in alternating atomic planes and the crystal lattice becomes tetragonal during the ordering. In the experiment, this type of ordering corresponds superstructural phase PdIn.

Exceptional characteristics of SR [17–19] allowed us to identify fluctuations in the arrangement of atoms in superstructural phases. The presence of domains of different degree ordering in the alloy matrix has led to a nontrivial form of diffraction profiles.

4. Conclusions

X-ray structural studies of diffusion filters using SR revealed the existence of long-range ordering regions in both foils.

The facts presented in this paper show the quasistability of superstructural inclusions in membranes in the hydrogenation process.

Analysis of angular positions of the diffraction peaks corresponding to superstructural phases showed that the phases they determine fell into two large structural groups. One of them, the Pd_3In composition, has a face-centered lattice in both foils, similar to the structure of $AuCu_3$. Another group is the regions of the PdIn composition with an AuCu type structure.

The exceptional characteristics of the SR made it possible to obtain for the first time in the experimental work the results reflecting the continuum of domains of transition concentrations and fluctuations in the distribution of metal atoms by concentration in the ordering regions.

The work was presented as a plenary (oral) speech at the International Conference "Solid State Chemistry and Functional Materials" (12th International Symposium "Thermodynamics and Materials Science"), held at Ioffe Institute (May 21–27, 2018).

Acknowledgement

The synchrotron diffraction measurements were performed at unique scientific equipment Kurchatov Synchrotron Radiation source at NRC Kurchatov institute, which partially financially supported by Science and Education Ministry of Russian Federation by the State program "Investigation and development of priority directions of development of Russian scientific and technological complex in 2014–2020", agreement 14.619.21.0007, project RFMEFI61917X0007.

References

[1] Grashoff G.J., Pelkington C.E., Corty C.W. The purification of Hydrogen. *Platinum Metals Review*, 1983, **27**(4), P. 157–169.

[2] Stiller C., Schmidt P., Michalski J. Storage of Renewable Electricity through Hydrogen Production. World Renewable Energy Congress. *Linköping University Electronic Press.* 2011, **15**, P. 4202–4208.

[3] Tereshchuk V.S. Hydrogen Generator Based on Reduced Solid Fuel. *Russian Engineering Research*, 2011, **31**(12), P. 1205–1212.

[4] Burkhanov G.S. , Gorina N.B., Kolchugina N.B., Roshan N.R., Slovetsky D.I., Chistov E.M. Palladium-Based Alloy Membranes for Separation of High Purity Hydrogen from Hydrogen-Containing Gas Mixtures. *Platinum Metals Review*, 2011, **55**(1), P. 3–12.

[5] Knyaginichev A.V., Khan KhaSok, Avdyukhina V.M., Katsnel'son A.A., Revkevich G.P. Physics of the evolution of structure and elastic stresses in Pd-Mo alloys saturated with hydrogen. *Physics of the Solid State*, 2001, **43**(2), P. 207–213.

[6] Fukai Y., Okuma N. Formation of Superabundant Vacancies in Pd Hydride under High Hydrogen Pressures. *Physical Review Letters*, 1994, **73**(12), P. 1640–1668.

[7] Dos Santos D.S., Tavares S.M., Miraglia S., Fruchart D., dos Santos D.R. Analysis of the nanopores produced in nickel and palladium by high hydrogen pressure. *Journal of Alloys and Compounds*, 2003, **356–357**, P. 258–262.

[8] Alefeld G., Felkl I. Hydrogen in metals. M.: Mir, 1981, 430 p.

[9] Tawancy H.M. Correlation between disorder-order transformations in a Ni-based alloy and its mechanical properties. *Materials Science and Engineering: A*, 2018, **719**, P. 93–103.

[10] Straumal B.B., Kilmametov A.R., Lopez G.A., Lopez-Ferreno I., No M.L., San Juan J. Hahn H., Batretzky B. High-b pressure torsion driven phase transformations in Cu–Al–Ni shape memory alloys. *Acta Materialia*, 2017, **125**, P. 274–285.

[11] Avdyukhina V.M., Akimova O.V., Levin I.S., and Revkevich G.P. Nonmonotonic Redistribution of Indium Atoms in Pd–In–Ru Alloy Foils after Electrolytic Hydrogenation. *Russian Metallurgy (Metally)*, 2011, **7**, P. 646–651.

[12] Avdyukhina V.M., Akimova O.V., Levin I.S., and Revkevich G.P. The Influence of Hydrogenation on the Redistribution of Indium in a Pd–In–Ru Alloy in the Course of Relaxation. *Moscow University Physics Bulletin*, 2011, **66**(1), P. 33–38.

[13] Avdyukhina V.M., Akimova O.V., Levin I.S., and Revkevich G.P. Changes in the Phase Structure State of Pd–In–Ru Alloy Foils after Hydrogenation and Prolonged Relaxation. *Moscow University Physics Bulletin*, 2014, **69**(4), P. 349–356.

[14] Jamieson H.C., Weatherly G.C., Manchester F.D. The Transformation in Palladium–Hydrogen Alloys. *J. Less. Comon. Metals*, 1976, **50**, P. 85–102.

[15] Avdyukhina V.M., Revkevich G.P., Katsnel'son A.A. Special role of vacancies during structural transformation of Pd–H and Pd–M–H system. *J. Alter. Energ. Ecolog.*, 2005, **7**, P. 20–28 .

[16] Akimova O.V., Avdyukhina V.M., Shchetinin I.V. Role of vacancies in the relaxation of Pd-5.3 at. % In-0.5at. % Ru alloy foil after hydrogen desorption. *The Physics of Metal and Metallography*, 2016, **117**(2), P. 130–134.

[17] Koval'chuk M.V., Kvardakov V.V., Korchuganov V.N., KISR-yesterday, today, tomorrow. *Priroda*, 2013, **12**, P. 25–36.

[18] Zubavichus Y.V., Slovokhotov Y.L. X-ray Synchrotron Radiation in physico-chemical studies. *Chemical success*, 2001, **70**(5), P. 429–463.

[19] Akimova O.V., Veligzhanin A.A. Structural Diagnostics of Metal Alloys-New Possibilities in the Use of Synchrotron Radiation. *Journal of Surface Investigation: X-ray, Synchrotron and Neutron Techniques*, 2018, **12**(1), P. 111–115.

[20] Chernyshov A.A., Veligzhanin A.A., Zubavichus Y.V. Structural Materials Science end-station at the Kurchatov Synchrotron Radiation Source: Recent instrumentation upgrades and experimental results. *Nucl. Instrum. Methods Phys. Res. A*, 2009, **603**(1-2), P. 95–98.

[21] Hammersley A.P. FIT2D: a multi-purpose data reduction, analysis and visualization program. *J. Appl. Crystallogr.*, 2016, **49**(2), P. 646–652.

[22] Wojdyr M. Fityk: a general-purpose peak fitting program. *J.Appl. Cryst.*, 2010, **43**, P. 1126–1128.

[23] Lyakishev N.I. State diagrams of double metal systems. *M.: Mechanical Engineering*, 2001, **3**(1), 872 p.

[24] Iveronova V.I., Revkevich G.P. *Theory of X-ray scattering*. Moscow, 1978, 278 p.

[25] Krivoglaz M.A., Smirnov A.A. *Theory of ordering alloys*. Moscow, 1958, 388 p.

[26] Revkevich G.P., Mitkova M.K., Katsnel'son A.A. Phenomenon of upward diffusion in hydrogen-saturated alloys palladium-samarium. *Vestnik Mosk. Univ.*, 1997, **38**(2), P. 30–33.

NANOSYSTEMS: PHYSICS, CHEMISTRY, MATHEMATICS, 2018, 9 (6), P. 746–753

Influence of thermal treatment of nanometer-sized titanate and barium orthotitanate precursors on the electrorheological effect

K. V. Ivanov[1], A. V. Agafonov[1], A. E. Baranchikov[2], V. K. Ivanov[2], S. A. Kozyukhin[2],
E. V. Fatyushina[2], V. V. Kozik[3]

[1]G. A. Krestov Institute of Solution Chemistry, RAS, Ivanovo, Russia
[2]Kurnakov Institute of General and Inorganic Chemistry, RAS, Moscow, Russia
[3]National Research Tomsk State University, Tomsk, Russia

ava@isc-ras.ru

PACS 61.46.+w, 77.22.-d, 82.45.Vp, 82.80.-d **DOI 10.17586/2220-8054-2018-9-6-746-753**

The results for the sol-gel synthesis of acylate gels are reported in the titanium tetra-n-butoxide – barium hydroxide – acetic acid system at a molar ratio of Ba:Ti components of 1:1 and 2:1. The thermal decomposition of these gels over temperatures ranging from 85 –1200 °C was investigated using thermal analysis methods, XRD, FTIR spectroscopy, electron microscopy, and dielectrometry at frequencies from 25 – 106 Hz. The electrorheological effect in suspensions of powders synthesized at different temperatures with a stoichiometric Ba:Ti ratio = 1:1 and 2:1, in polydimethylsiloxane was studied. The influence of thermal gel treatment was analyzed on their dielectric properties as fillers of electrorheological fluids and on the magnitude of the electrorheological effect.

Keywords: sol-gel synthesis, barium titanate, electrorheological fluids, dielectric liquids, nanometer-sized, thermal treatment.

Received: 29 June 2018

Revised: 11 October 2018

1. Introduction

Electrorheological (ER) fluids are suspensions of polarizable semiconductor particles in dielectric liquids. The viscoplastic properties of ER fluids depend on the strength of the applied electric field up to the total loss of fluidity [1, 2]. The loss of fluidity of the ER fluid in an electric field occurs due to polarization interactions, leading to structuring of the dispersed phase. The formation of chain or pillar structures from separate particles and closing of the interelectrode gap occurs within milliseconds. The presence of a limiting value of the electric field strength is typical for the electrorheological effect, after which the structure formation takes place and the fluid enhances its viscoplastic properties.

The magnitude of the ER effect is significantly affected by such factors as polarization, dielectric constant, conductivity, the applied electric field strength, the size, shape and structure of particles [3–9]. Another important factor affecting the properties of ER fluids is the water content in the dispersed phase [10]. Obviously, the aggregate functional properties of an ER fluid are determined by the composition and nature of the components.

The barium titanyl acylates complexes are considered promising among other fillers of ER fluids [11–14]. The yield strength of an ER fluid based on barium titanyl oxalate, with the surface of nanoparticles covered by adsorption layer of urea molecules, can exceed 100 kPa in a 4 kV/mm field [15–17]. At the same time, the yield strength of barium titanate suspension obtained by calcination of acylate complexes in an electric field of 4 kV/mm does not exceed 1 kPa [18]. Thus, the ER efficiency of the acylate complexes is significantly reduced during calcination. Apparently, this occurs as a result of polar organic group elimination from the material, leading to a decrease in the polarizability of the filler particles.

This work aims to reveal the influence of thermal treatment of acylate gels – the precursors of barium titanate and orthotitanate, used as ER fluid fillers, on the magnitude of the ER effect.

2. Experimental section

Barium hydroxide $Ba(OH)_2 \cdot 8H_2O$, glacial acetic acid CH_3COOH and 99 % pure titanium tetra-n-butoxide $Ti[O(CH_2)_3CH_3]_4$ were used as starting materials. All reagents were purchased from SIGMA-Aldrich.

The following sol-gel synthesis of nanometer-sized barium titanyl acylate powders at stoichiometric Ba:Ti ratios of 1:1 and 2:1 was applied: 10 g of barium hydroxide octahydrate was dissolved in 17.31 g of glacial acetic acid at constant stirring until a clear solution was obtained, followed by dropwise addition of 10.8 g (or 5.4 g) of titanium tetra-n-butoxide via a syringe. The contents of the reaction flask were stirred for an hour, then the temperature of the solution was raised to 85 °C. After a short period of time, the solution changed into a transparent, durable gel. Drying the gel in air at 85 °C to a constant weight afforded white powders. According to elemental analysis, the content of organic phase in samples of dry gel powders with stoichiometric Ba:Ti ratios = 1:1 and 2:1 amounted to some 35 and 17 % (with an accuracy of 1 %). The resulting powders were calcined for an hour in air at temperatures of 200, 400, 600, 800 and 1200 °C and used for subsequent analysis and for the preparation of ER fluids.

3. Thermal evolution characterization of the obtained materials

Transmission electron microscopy (electron microscope 2MB-100L) was used to study the shape and particle size of the powders obtained. According to electron microscopy, when the Ba:Ti molar ratio in the synthesis is 1:1, the 50 – 200 nm polydisperse particles are formed, while an initial 2:1 Ba:Ti ratio affords 50 – 80 nm polydisperse particles (Fig. 1). From the electron microscopic images it can be seen that the particles have a rounded shape.

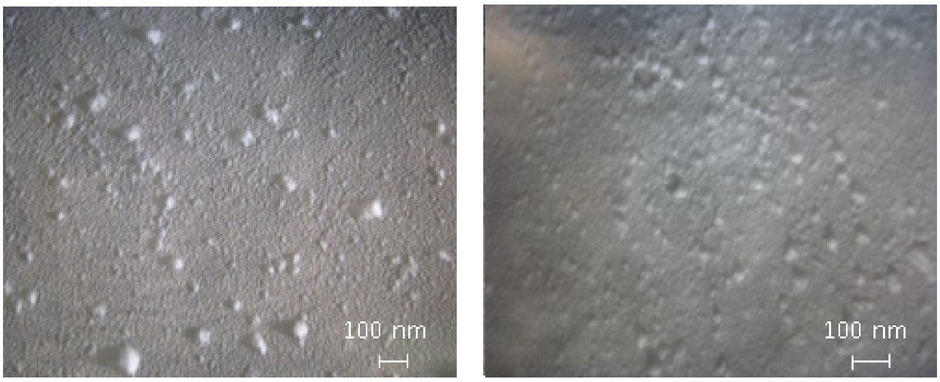

(a) (b)

FIG. 1. TEM images of dried at 85 °C acylate gels obtained at Ba:Ti 1:1 (a) and 2:1 (b) molar ratios

The analysis of phase composition was performed on a DRON-2 diffractometer using Cu-Kα radiation. According to the results of X-ray diffraction, when the initial stoichiometric Ba:Ti ratio is 1:1 (Fig. 2(a)), the formation of barium titanate starts at 600 °C and terminates at 800 °C. When the initial Ba:Ti molar ratio of components is 2:1 (Fig. 2(b)), the reflexes corresponding to barium titanate and barium orthotitanate are observed at 400 °C. With an increase of temperature to 1200 °C, the reflexes of $BaTiO_3$ and Ba_2TiO_4 are observed.

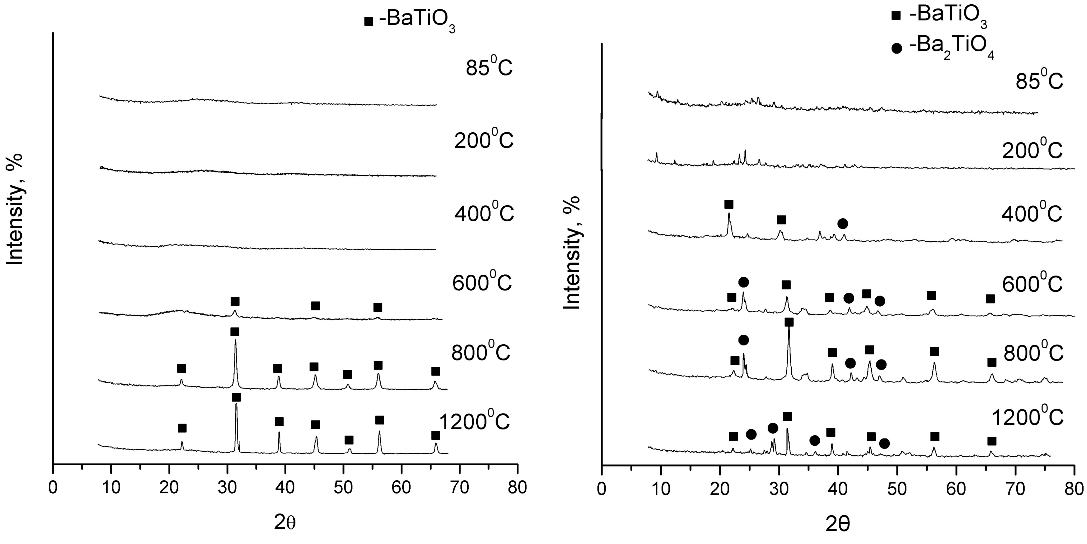

(a) (b)

FIG. 2. X-ray phase analysis of barium-titanium acylate complexes obtained at Ba:Ti 1:1 (a) and 2:1 (b) molar ratios and their calcination products at various temperatures

The IR spectra of the synthesized compounds were recorded in a potassium bromide matrix on a VERTEX 80v FT-IR spectrometer. IR spectra of synthesized ultradispersed materials (Fig. 3) contain absorption bands characteristic for barium acetate, titanium dioxide and its hydroxy-forms, butoxy groups, as well as titanium butoxide and water molecules: Ba–OH 1459, 1420 and 1379 cm^{-1}; titanium butoxide 1458, 1429, 1371 and 1362 cm^{-1}. The band at 1125 cm^{-1} can be attributed to the vibrations of the Ti–O–C bond, the band at 948 cm^{-1} – to Ti–OH vibrations, and the band at 3390 cm^{-1} may correspond to the stretching of OH groups. The CO_3^{2-} ion has a characteristic absorption maximum at 1540 cm^{-1}, and the band at 1461 cm^{-1} characterizes asymmetric oscillations in the stretching of the C–O bond. For the acetate ion, depending on the type of coordination, absorption maxima for symmetric (νS) and antisymmetric (νA) C–O vibrations are observed at different positions [19] for monodentate ($\nu S = 1295$ cm^{-1}, $\nu A = 1720$ cm^{-1}), bridged bidentate ($\nu S = 1430$ cm^{-1}, $\nu A = 1590$ cm^{-1}) and chelate bidentate complexes ($\nu S = 1470$ cm^{-1}, $\nu A = 1550$ cm^{-1}). An intense absorption band at 650 cm^{-1} characterizes the vibrations of the Ti–O–Ti bond. The Ba–O oscillations correspond to the band at 474 cm^{-1}. As the samples are thermally processed, the IR spectra begin to correspond to the spectra of the corresponding titanates.

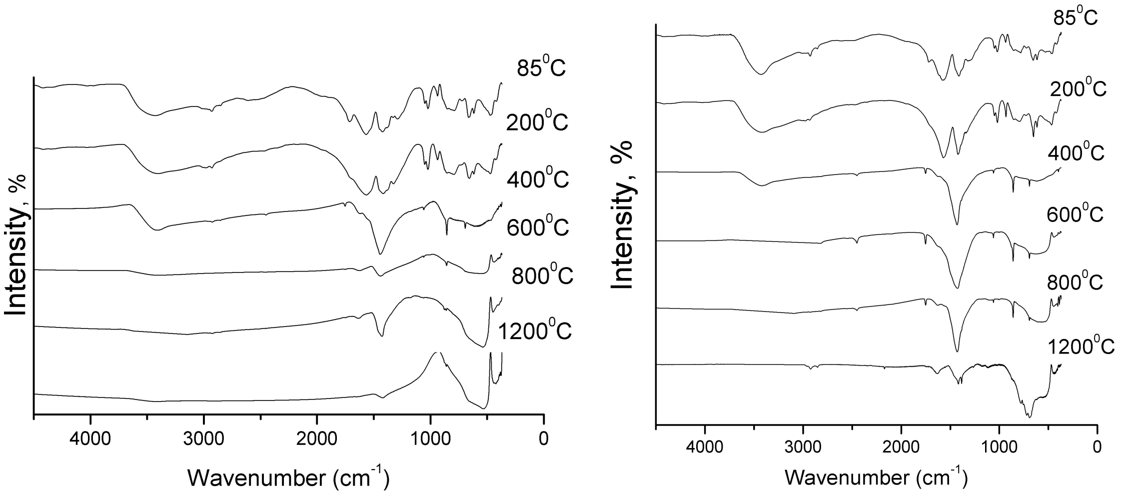

(a) (b)

FIG. 3. IR spectra of acylate complexes powders with Ba:Ti 1:1 (a) and 2:1 (b) molar ratios and their calcination products at different temperature

The thermal analysis of the synthesized powders was performed on a 1000D Paulik–Paulik–Erdei derivatograph at a heating rate of 5 °C/min. One can distinguish three ranges associated with a change in the mass of the sample on the thermograms of synthesized materials (Fig. 4). The first range (50 – 150 °C) might be associated with the removal of acetic acid and the adsorbed water. The second range (150 – 450 °C) corresponds to the decomposition of titanium butoxide complexes with acetate ions to titanium dioxide. At temperatures of 500 – 750 °C the thermal decomposition of barium carbonate, which is present as an impurity in the material, is likely to occur with the formation of barium titanate. The total weight loss for each of the samples does not exceed 45 %.

The analysis of materials calcined at 1200 °C with differential scanning calorimetry (DSC) was performed on a DSC 204 F1 Phoenix calorimeter with the μ-sensor. The maxima on the heat capacity-temperature curves, which indicate a phase transition, are observed at temperatures ranging from 0 – 200 °C for both materials with 1:1 and 2:1 Ba:Ti molar ratio. For the system with a stoichiometric 1:1 Ba:Ti molar ratio, the phase transition temperature is 119 °C and for the system with a 2:1 Ba:Ti ratio, the phase transition temperature is 122 °C (Fig. 5).

The dielectric spectra of 30 % suspensions of the resulting powders in silicone oil PMS-20 were measured in a cylindrical cell of the condenser type at $T = 293$ K using an E7-20 immittance meter in the frequency range from 25 to 1×106 Hz. Fig. 6 shows the dependences of ε and $\tan\delta$ on the frequency of the electric current.

The $\tan\delta$ frequency dependences of suspensions indicate the relaxation character of the dielectric spectra. As it follows from Fig. 6(a), a suspension of the initial powder is characterized by the presence of a relaxation maximum, which disappears after calcination. As is evident from the Fig. 6(b), the position of relaxation maximum for the suspension of the initial powder with the 2:1 Ba:Ti ratio is at lower frequency in comparison to the powder with the 1:1 Ba:Ti ratio. In that regard, the relaxation shape of the dielectric spectrum persists for suspensions with filler particles calcined at 200 and 400 °C. An increase in the temperature of heat treatment of fillers with

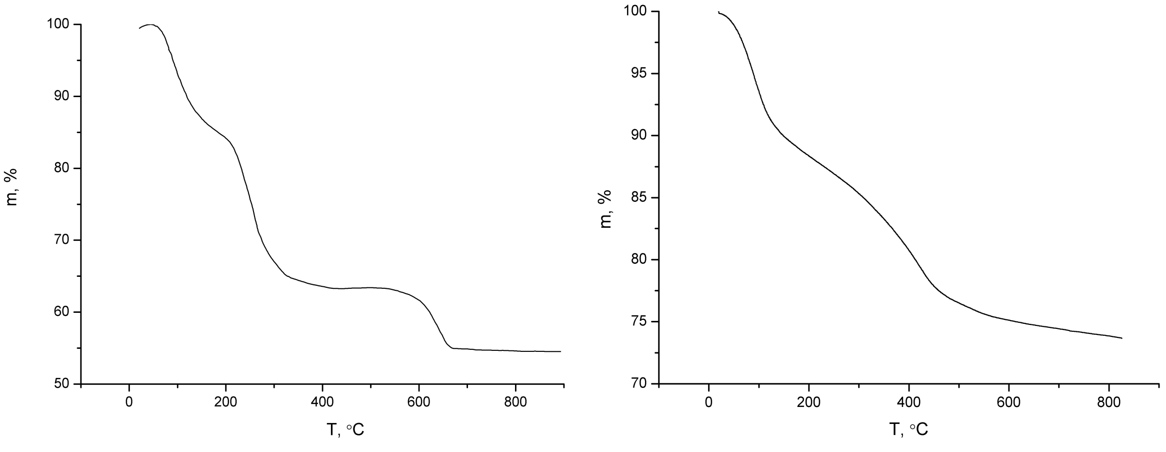

(a) (b)

FIG. 4. Thermal analysis of acylate complexes powders with Ba:Ti 1:1 (a) and 2:1 (b) molar ratios

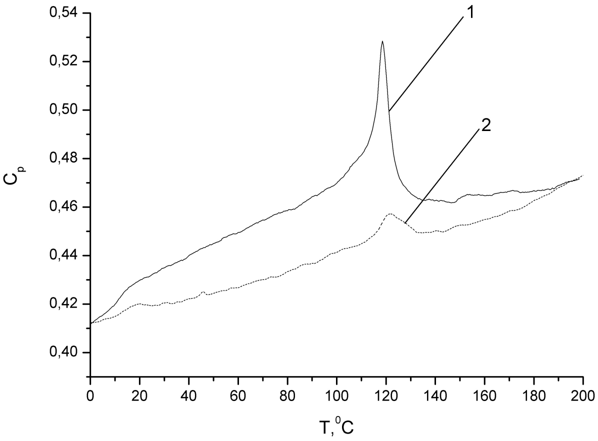

FIG. 5. DSC of materials obtained by calcination at 1200 °C with Ba:Ti 1:1 (1) and 2:1 (2) molar ratios

BaO:TiO_2 ratios of 1:1 and 2:1 results in a similar shape of ε and $\tan\delta$ frequency dependences for these systems and an absence of relaxation maxima in them.

4. Results and discussion

The obtained complex of data characterizing the phase composition of the obtained materials at different temperatures allows us to make assumptions about the patterns of structure formation during its thermal treatment.

The interaction of titanium tetra-n-butoxide with glacial acetic acid results in the gelation due to the formation of polynuclear complexes in which bidentate acetate ions act as ligands (Fig.7) [20]. When barium hydroxide is dissolved in glacial acetic acid, barium acetate forms, which, apparently, can be incorporated into the structure of the titanium acylate complex [21] or form clathrate complexes [22].

The thermal treatment of the obtained powders with a different ratio of reagents in the mixture leads to their decomposition. Thermal decomposition of the acylate polynuclear complex of titanium tetra-n-butoxide in an oxidizing atmosphere is accompanied by the removal of volatile organic components, oxidation of acetate and butoxide groups. In parallel, the decomposition of barium acetate occurs, which is accompanied by successive transformations [21]:

$$Ba(OOCCH_3)_2 \rightarrow BaCO_3 + CO \rightarrow BaO + CO_2.$$

In general, thermal transformations of materials obtained from precursors with the 1:1 and 2:1 Ba:Ti ratios involve the same processes, however, product formation proceeds according to different schemes. To a considerable degree, this is determined by both the reactivity of barium orthotitanate and by the various molar ratios of water and titanium butoxide in the synthesis of Ba_2TiO_4 and $BaTiO_3$. As follows from Figs. 2(a), 3(a) and 4(1), in a

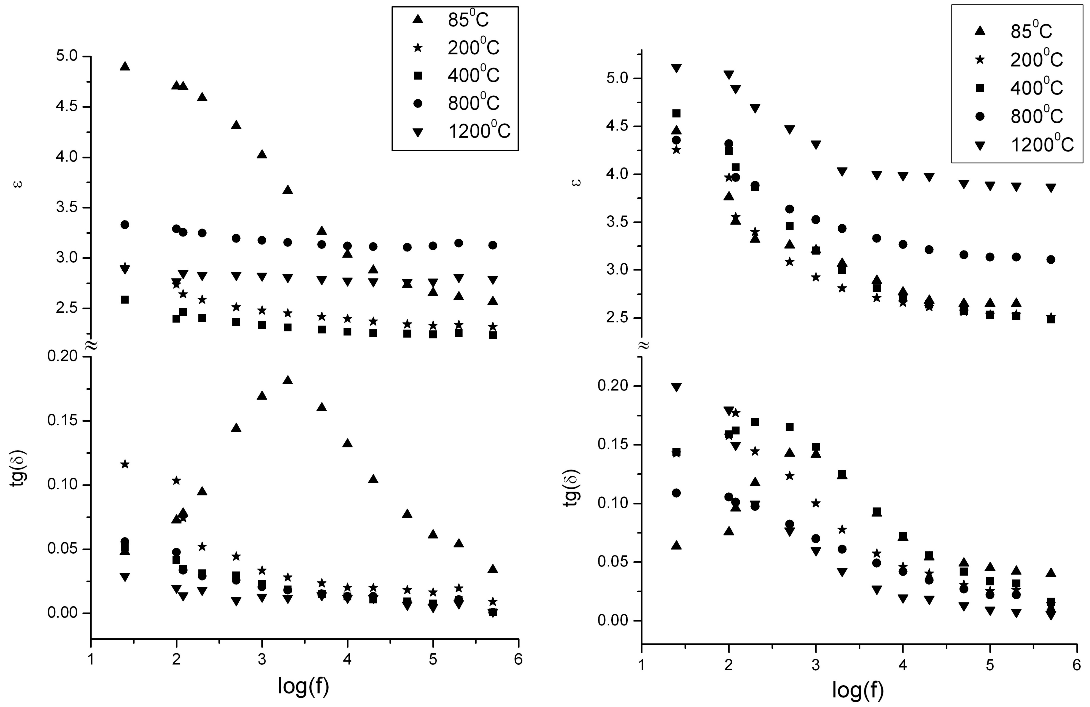

(a) (b)

FIG. 6. Dielectric parameters of 30 % suspensions of samples with Ba:Ti 1:1 (a) and 2:1 (b) stoichiometric ratio in silicone oil at 25 °C

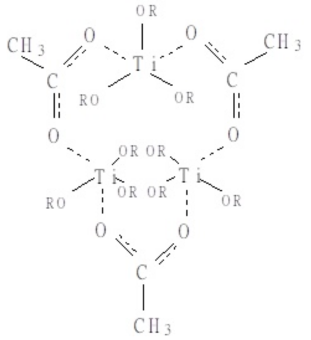

FIG. 7. Polynuclear acylate complex of titanium tetrabutoxide ([20])

system containing Ba and Ti in a ratio of 1:1 at 200 and 400 °C, the formation of X-ray amorphous products containing organic residues occurs as well as hydroxy compounds of these metals. At that the formation of $BaTiO_3$ phase begins at 600 °C. This process is accompanied by the decomposition of barium carbonate: $BaCO_3 \to BaO + CO_2$ and the reaction $BaO + TiO_2 \to BaTiO_3$. At 1200 °C, $BaTiO_3$ is present in the system as well as traces of BaO.

The thermal evolution of the product obtained from starting material with 2:1 Ba:Ti ratio proceeds according to a different scheme. As follows from Figs. 2(b), 3(b) and 4(2), calcination at 200 °C does not lead to significant changes in the physicochemical characteristics of the material.

The phases of $BaTiO_3$ and Ba_2TiO_4 start to form at 400 °C. This is 200 °C below the temperature of the $BaTiO_3$ phase formation in the synthesis with the 1:1 Ba:Ti ratio. We explain such differences by different ratios of Ba:Ti and H_2O:Ti in the reaction mixtures. Calcination at 600, 800 and 1200 °C favors an increase in the phase content of $BaTiO_3$ and Ba_2TiO_4. The product calcined at 1200 °C is a mixture of Ba_2TiO_4 and $BaTiO_3$ phases in a ratio of 30 % and 70 %.

The Ba_2TiO_4 and $BaTiO_3$ phases have different Ba:Ti stoichiometric ratios. This affects the packing density of ions in the Ba_2TiO_4 and $BaTiO_3$ lattices and determines the polarization parameters of the materials. Barium titanate with a tetragonal structure at room temperature (~ 25 °C) has a dielectric constant of about 1500, and barium orthotitanate with an orthorhombic structure of about 20 °C has a dielectric constant of about 1500 [19].

The described transformations of the acylate complexes obtained at different Ba:Ti ratios are reflected in the corresponding dielectric spectra of the powder suspensions in silicone oil PMS-20.

The influecne of thermal treatment of powders on the ER effect was determined from the change in shear stress, as a function of the applied DC electric field in the range 0 – 7 kV/mm. For the investigation, 30 % suspensions of the obtained materials in polydimethylsiloxane (PMS-20 Penta Silicones) were prepared. The required amount of powder was triturated in polydimethylsiloxane until a homogeneous suspension was formed. The measurements were carried out on a modified Brookfield DV-II viscosimeter at various shear rates and DC electric field strengths applied to a 1 mm parallel plane gap between the electrodes.

The ER effect theoretical models, based on the electrostatic theory of dipole-dipole interactions, describe the attractive force between the particles in an electric field according to the following equation [23]:

$$F = \frac{24a^6\varepsilon_0 E^2}{R^4}\frac{K_f(K_p - K_f)^2}{(K_p + 2K_f)^2}, \tag{1}$$

where a – is radius of the filler particle, R – interparticle distance, ε_0 – dielectric constant of vacuum, E – the electric field strength, K_f – dielectric permittivity of a liquid dielectric (dispersion medium), K_p – dielectric constant of the filler particle material.

This equation emphasizes the role of the differences in the dielectric parameters of the dispersion medium and the dispersed phase in the formation of the ER effect and justifies the quadratic dependence of the electrorheological effect on the electric field strength.

The dependence of the shear stress on the electric field strength at various shear rates for suspensions of acylate complexes with the 1:1 and 2:1 Ba:Ti ratio of components dried at 85 °C are presented in Fig. 8. The results demonstrated in Fig. 8(b) obey the equation 1, while the results in Fig. 8(a) do not obey. A direct proportion of the shear stress on the field strength is characteristic for acylate complexes with a Ba:Ti ratio of 1:1 after saturation is achieved after $E = 4.5$ kV/mm starting from a field strength of 0.5 kV/mm. This may be due to presence of the adsorbed acetic acid on the surface of particles, which leads to the effects reported in [24].

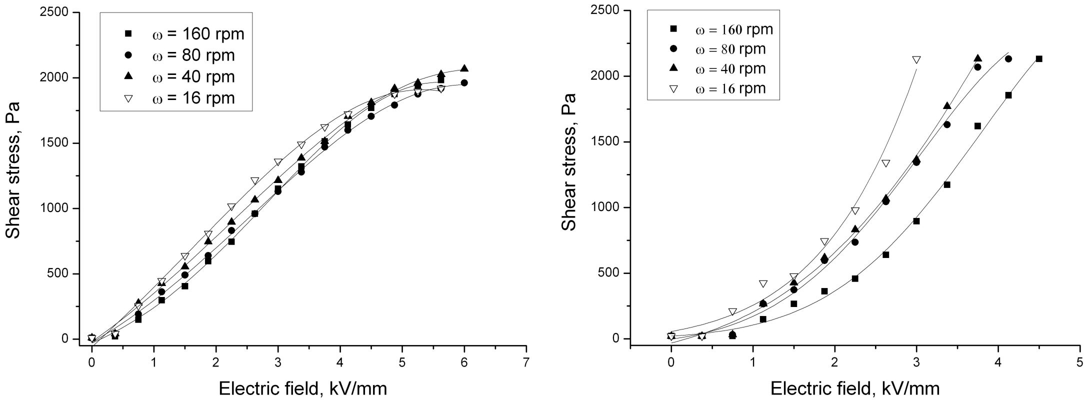

(a) (b)

FIG. 8. The dependence of shear stress on the electric field strength at different shear rates for 30 % suspensions of acylate complexes powders dried at 85 °C. 1:1 (a) and 2:1 (b) Ba:Ti ratios

The influence of the filler calcination temperature on the magnitude of the ER effect at a shear rate of 160 rpm is shown in Fig. 9. One can note that the ER effect regularities associated with the use of filler materials subjected to different thermal treatments can be explained from the standpoint of the classic electrostatic theory of the dipole-dipole interactions. As follows from Fig. 6, the permittivity of the suspensions is successively decreased with the increasing calcination temperature. In accordance with equation 1, this leads to a decrease in the attractive force between the filler particles and to a decrease in the ER effect, which is observed (Fig. 9).

In the process of ER fluids structuring in electric fields with increasing field strength the distance between particles decreases (a decrease in the thickness of the dielectric liquid interlayer between the particles, the appearance of tight contacts), leading to an increase in conductivity. In this case, the conductivity increases proportionally to the number of formed contacts between the filler particles. The voltammetric parameters for 30 % suspensions of materials with 1:1 and 2:1 Ba:Ti ratios calcined at different temperatures at a shear rate of 160 rpm are significantly

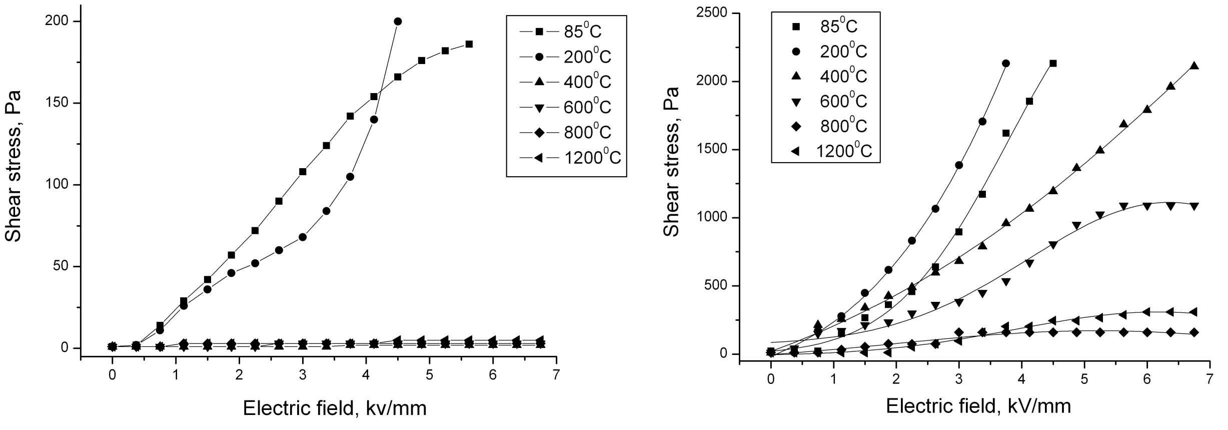

(a) (b)

FIG. 9. Dependence of the shear stress of 30 % suspensions of acylate complexes with the 1:1 (a) and 2:1 (b) Ba:Ti ratios calcined at different temperatures on the electric field strength at a shear rate of 160 rpm

different (Fig. 10). For 30 % suspensions of materials with 1:1 Ba:Ti ratio, an increase in the calcination temperature leads to a consistent decrease in the current flowing through the suspension at an equal applied voltage. This may be due to the fact that molecules of acetic acid and polar acetate groups are present on the surface of filler particles that determine the value of the conductivity. As the organic components are removed, the conductivity of the suspensions decreases. For 30 % suspensions of materials with 2:1 Ba:Ti ratio (Fig. 1(b)), an increase in the calcination temperature of the filler material leads to an increase in the electrical conductivity of the suspensions. From Fig. 6, one can see that the value of the dielectric loss tangent for such suspensions is higher than for the systems with the 1:1 Ba:Ti ratio.

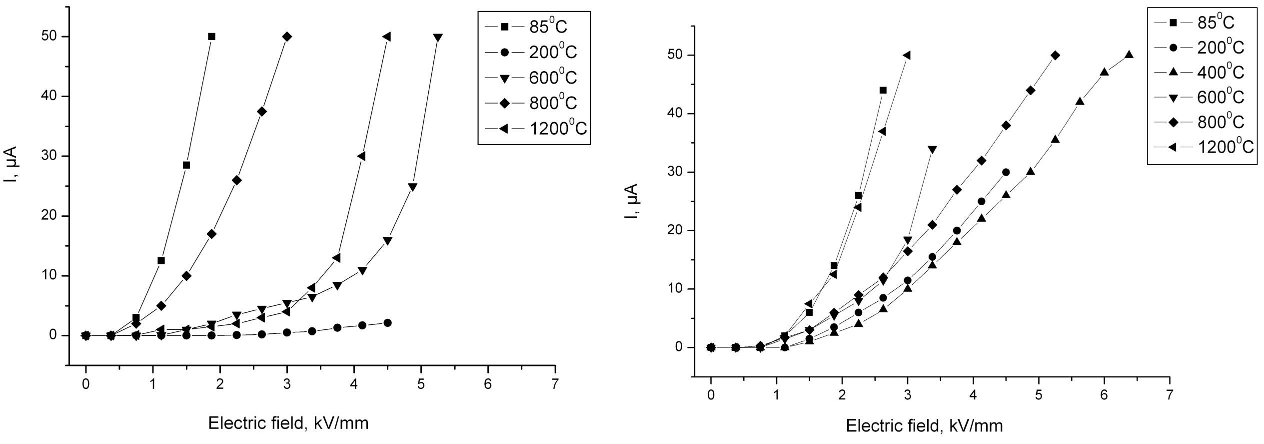

(a) (b)

FIG. 10. Voltammetric parameters for 30 % suspensions of acylate complexes with the 1:1 (a) and 2:1 (b) Ba:Ti ratios calcined at different temperatures at a shear rate of 160 rpm

5. Conclusions

The acylate gels were obtained via a sol-gel method in the titanium tetra-n-butoxide-barium hydroxide-acetic acid system in excess of acetic acid with a molar ratio of Ba:Ti components of 1:1 and 2:1. The regularities for the formation of Ba_2TiO_4 and $BaTiO_3$ phases during calcination of the obtained gels at 200, 400, 600, 800 and 1200 °C were investigated. A detailed study of phase transformations for the obtained materials was performed using thermogravimetric analysis, differential scanning calorimetry, X-ray phase analysis, FTIR spectroscopy, and electron microscopy. It was established that the thermolysis of acylate complexes with 1:1 Ba:Ti ratio at 200 and 400 °C affords X-ray amorphous products with a low organic phase content and significant metal hydroxy compounds content. The formation of the $BaTiO_3$ phase begins at 600 °C, and at 1200 °C, $BaTiO_3$ is present in the system with traces of BaO. The decomposition of the acylate complexes with the 2:1 Ba:Ti ratio leads to the formation of $BaTiO_3$ and Ba_2TiO_4 phases as low as at 400 °C. This is 200 °C lower than the temperature of $BaTiO_3$ phase formation in the synthesis with 1:1 Ba:Ti ratio. Calcination at 600, 800 and 1200 °C leads to a gradual increase of the Ba_2TiO_4 and $BaTiO_3$ phase content in the product. The product calcined at 1200 °C is a mixture of the Ba_2TiO_4 and $BaTiO_3$ phases in a ratio of 30 % and 70 %, respectively. For the first time, data was obtained on the influence of thermal treatment temperature on the magnitude of the ER effect in suspensions based on these materials. It was established that the regularities of the ER effect magnitude variation can be explained from the standpoint of the classical electrostatic theory of the dipole-dipole interactions in electric fields.

References

[1] Agafonov A.V., Zakharov A.G. Electrorheological fluids. *Russ. J. Gen. Chem.*, 2010, **80**, P. 567–575.

[2] Liu Y.D., Choi H.J. Electrorheological fluids: smart soft matter and characteristics. *Soft Matter*, 2012, **8**, P. 11961–11978.

[3] Wen W., Huang X., Sheng P. Electrorheological fluids: structures and mechanisms. *Soft Matter*, 2008, **4**, P. 200–210.

[4] Wu C.W., Conrad H. Dielectric and conduction effects in non-Ohmic electrorheological fluids *Phys. Rev. E*, 1997, **56** (5), P. 5789–5797.

[5] Whitte M., Bullough W.A., Peel D.J., et al. Dependence of electrorhrologycal response on conductivity and polarization time. *Phys. Rev. E*, 1994, **49** (6), P. 5249–5283.

[6] Agafonov V., Kraev A.S., et al. Comparative study of the electrorheological effect in suspensions of needle-like and isotropic cerium dioxide nanoparticles. *Rheol Acta*, 2018, **57**, P. 307–315.

[7] Agafonov A.V., Kraev A.S., et al. Properties of electrorheological fluids based on nanocrystalline cerium dioxide. *Russ. J. Inorg. Chem.*, 2017, **62**, P. 625–632.

[8] Agafonov A.V., Krayev A.S., et al. Nanocrystalline ceria: a novel material for electrorheological fluids. *RSC Adv.*, 2016, **6**, P. 88851–88858.

[9] Parthasarathy M., Klingenberg D.G. Electrorheology: mechanisms and models. *Mater. Sci. Eng.*, 1996, **17**, P. 57–103.

[10] Ivanov K.V., Ivanova O.S., Agafonov A.V., Kozyukhin S.A. The dielectric properties and flow of electrorheological fluids based on polymer-coated nanodispersed barium tetraacetate titanyl particles upon a dynamic shear in electric fields. *Colloid Journal*, 2017, **79** (2), P. 204–211.

[11] Xufeng Dong, Ning Ma, et al. The contribution of friction to electrorheological properties of a chrysanthemum-like particle suspension. *RSC Adv.*, 2015, **5**, P. 74656–74663.

[12] Wu J., Song Z., et al. Giant electrorheological fluids with ultrahigh electrorheological efficiency based on a micro/nano hybrid calcium titanyl oxalate composite. *NPG Asia Materials*, 2016, **8**, P. 322.

[13] Liu Y., Guan J., et al. Chromium doped barium titanyl oxalate nano-sandwich particles: A facile synthesis and structure enhanced electrorheological properties. *Materials Chemistry and Physics*, 2010, **122**, P. 73–78.

[14] Jiang W., Jiang C., Gong X., Zhang Z. Structure and electrorheological properties of nanoporous $BaTiO_3$ crystalline powders prepared by solgel method. *J. Sol-Gel Sci. Technol.*, 2009, **52**, P. 8–14.

[15] Wen W., Huang X., et al. The giant electrorheological effect in suspensions of nanoparticles. *J. Nature Materials*, 2003, **2**, P. 727–730.

[16] Bose H., Trendler A. Comparison of rheological and electric properties of ER fluids based on different materials. *Int. J. Mod. Phys. B*, 2001, **15** (6–7), P. 626–633.

[17] Rankin P.J., Klingenberg D.J. The electrorheology of barium titanate suspensions. *J. Rheol.*, 1998, **42** (3), P. 639–656.

[18] Ahmad T., Ganguli A.K. Synthesis of nanometer-sized particles of barium orthotitanate prepared through a modified reverse micellar route: Structural characterization, phase stability and dielectric properties. *J. Mater. Res.*, 2004, **19** (10), P. 2905–2912.

[19] Schubert U. Organically modified transition metal alkoxides: Chemical problems and structural issues on the way to materials syntheses. *Acc. Chem. Res.*, 2007, **40**, P. 730–737.

[20] Wang L., Liu L., et al. Wet routes of high purity $BaTiO_3$ nanopowders. *Journal of Alloys and Compounds*, 2007, **440**, P. 78–83.

[21] Hwang U.Y., Park H.S., Koo K.K. Behavior of barium acetate and titanium isopropoxide during the formation of crystalline barium titanate. *Ind. Eng. Chem. Res.*, 2004, **43**, P. 728–734.

[22] Hao T. Electrorheological fluids: The non-aqueous suspensions. *Cambridge Massachusetts USA*, 2005, **22**, 553 p.

[23] Shen R., Wang X., et al. Polar-molecule-dominated electrorheological fluids featuring high yield stresses. *Adv. Mater.*, 2009, **21**, P. 4631–4635.

[24] Agafonov A.V., Davydova O.I., et al. Unexpected effects of activator molecules' polarity on the electroreological activity of titanium dioxide nanopowders. *J. Phys. Chem. B*, 2017, **121** (27), P. 6732–6738.

NANOSYSTEMS: PHYSICS, CHEMISTRY, MATHEMATICS, 2018, 9 (6), P. 754–762

Impact of nano-sized cerium oxide on physico-mechanical characteristics and thermal properties of the bacterial cellulose films

I. V. Gofman[1], A. L. Nikolaeva[1], A. K. Khripunov[1], A. V. Yakimansky[1,2], E. M. Ivan'kova[1],
D. P. Romanov[3], O. S. Ivanova[4], M. A. Teplonogova[4], V. K. Ivanov[4]

[1]Institute of Macromolecular Compounds, Russian Academy of Sciences, 199004, Bolshoi prospect 31,
Saint Petersburg, Russia
[2]Saint Petersburg State University, Institute of Chemistry, 198504, Universitetskii prospect 26,
Peterhof, Saint Petersburg, Russia
[3]Institute of Silicate Chemistry, Russian Academy of Sciences, 199034, Adm. Makarova emb., 2,
Saint Petersburg, Russia
[4]Kurnakov Institute of General and Inorganic Chemistry, Russian Academy of Sciences, 119991,
Leninsky prospect 31, Moscow, Russia

gofman@imc.macro.ru, alexandra.l.nikolaeva@gmail.com, diadora3@mail.ru, yakimansky@yahoo.com,
ivelen@mail.ru, dprom@mail.ru, runetta05@mail.ru, m.teplonogova@gmail.com, van@igic.ras.ru

DOI 10.17586/2220-8054-2018-9-6-754-762

A set of nanocomposite film materials based on bacterial cellulose containing nanoparticles of cerium dioxide was prepared. An investigation into the structural and morphological characteristics of the films has been performed, their thermal, mechanical and tribological properties were determined. A protocol of the nanocomposite materials formation used in the work was shown to provide a homogeneous distribution of ceria nanoparticles in the matrix polymer volume in addition to the presence of certain amount of broadly size-dispersed cerium oxide aggregates in the bulk film. The increase of nanoparticles concentration in the composite provokes a progressive growth of the Young's modulus and strength of the film material. Introduction of nanoparticles into the polymer causes the stabilization of sliding friction processes in the tribocontact with steel as well as the decrease of intensity in the wear rate of the film. An increase of the nanoparticles concentration results in a decrease of the material thermal stability.

Keywords: polymer-inorganic nanocomposites, bacterial cellulose, ceria, electron microscopy, mechanical properties, thermal stability, tribologic properties.

Received: 5 December 2018

Revised: 8 December 2018

1. Introduction

In recent years, so-called natural or "green" polymeric materials, especially cellulose and its derivatives, have attracted much attention from researchers [1]. Materials based on bacterial cellulose (BC) are of special interest [2]. These materials are the products of life activity of Acetobacter bacteria in the nutrient solutions. This type of cellulose is a material of high purity with an enhanced complex of properties [3–6] against those of cellulose of other types.

Interesting prospects are associated with processing of different BC-based compositions filled with inorganic and organic components [7–10], in particular, with various nanoparticles. This approach is widely used for obtaining new materials based on a variety of polymers.

At present, nanoscale fillers are commonly used for modification of the properties of polymeric materials. Oxide nanoparticles are among the most promising. A number of properties of matrix polymer materials can be substantially improved by the introduction of these nanoparticles, namely, the mechanical characteristics, electrical and transport properties, *etc.* [11–14]. Using metal oxide nanoparticles as an active filler of BC, one can obtain a deep variation the complex of the cellulosic material properties.

One promising group of oxide nanofillers, which draws attention of researchers, is ceria nanoparticles. By using them, one can obtain polymer-based composite materials demonstrating the effect of screening of electromagnetic irradiation, possessing catalytic activity, new materials with modified acoustic characteristics, and bioactive materials [15–20]. Of especial interest are ceria-containing nanocomposites based on BC, particularly as the materials for biomedical applications. In the context of interesting potential possibilities of practical application of such materials, it is sensible to comprehensively characterize them, both *per se* and in juxtaposition with their unmodified polymer matrices.

In the present communication, we present and analyze systematic information on the effect of cerium dioxide nanoparticles on the complex of properties of the film materials based on BC.

2. Experimental

BC or so-called Acetobacter xylinum was grown by using VKM-880 strain in aqueous solutions containing 2 wt. % of glucose, 0.3 wt. % of yeast extract and 2 wt. % of ethanol at 30 °C in cylindrical glass vessels for 14 – 21 days as described in detail in [21]. The as-prepared BC samples being gel-like pellicles with up to 25 mm thickness were partially dehydrated by pressing on a hand press, BC content in the pressed BC being about 14 wt. %.

To obtain both the BC and nanocomposite films, the pressed BC was disintegrated in a high-speed blender (15000 rpm, 15 min) in aqueous media (300 ml of water per 1 g of dry BC). In the case of nanocomposites, definite amounts of aqueous dispersion of cerium dioxide nanoparticles (ceria concentration – 1.5 wt.%) were poured into the preliminary prepared BC aqueous suspension, and then, the mixtures obtained were homogenized in a blender (15000 rpm, 1 min). In both cases, layers of equal thickness of resulting homogeneous suspensions were formed on a glass substrates and dried to constant weight at 160 °C. The final concentrations of CeO_2 nanoparticles in the samples were 0, 1, 3, 5, and 10 wt. %. Cerium dioxide nanoparticles with sizes $\sim$ 3.5 nm used in our experiments were synthesized by hydrothermal method [22].

XDR analysis of BC and composite films was carried out by X-ray diffractometer DRON-3M (CuKα-irradiation). The registration of X-ray beam diffraction was performed according to the Bragg–Brentano scheme [23].

SEM micrographs of films' surfaces were obtained by scanning electron microscope SUPRA-55VP (Carl Zeiss, Germany) using a secondary electron detector as well as a detector of back-scattered electrons. The samples were fixed with special glue on the microscope holders and sputtered by thin layer of platinum. Maps of the elements distribution were collected using a detector of energy dispersive X-ray analysis X-max 80 mm^2 (Oxford Instruments, United Kingdom).

Thermogravimetric analysis (TGA) of BC and composite samples was performed using a DTG-60 thermal analyser (Shimadzu, Japan). Specimens ($\sim$ 5 mg) were heated in air up to 600 °C with the rate of 5 °C /min. The TGA curves obtained were used to determine the thermal stability indices of the materials under study, τ_5 and τ_{10} (the temperature values at which a polymer or a composite loses 5 % and 10 % of its initial weight, respectively, due to the thermal destruction processes).

The mechanical tests of the films under investigation were carried out in the uniaxial extension mode at room temperature using an AG-100kNX Plus universal mechanical test system (Shimadzu, Japan). Strip-like samples 2×30 mm were stretched at a rate of 10 mm/min, according to ASTM D638 requirements. The Young's modulus E, the break stress σ_b and the ultimate deformation ε_b were determined.

Tribological characteristics of the films (friction coefficients and wear rates) were studied by an AG-100kNX Plus universal mechanical test system (Shimadzu, Japan) with a tribological tests accessory [24] in the dry friction mode at room temperature. The speed of linear shuttle motion of the counterbodies against the polymer surfaces was as high as 1000 mm/min.

3. Results and discussion

First, it should be noted, that the aforementioned technique provides a means for obtaining dense homogeneous films. XRD analysis of their compositions has demonstrated the presence of CeO_2 inclusions (Fig. 1): X-ray diffraction patterns of the composite films contain the reflexes corresponding to BC and those at $2\Theta = 28.5$, 33.7 and 47.4 deg., corresponding to cubic phase of crystalline CeO_2. The intensity of these reflexes increases along with the increase of the nanoparticles concentration in the cellulose matrix. A considerable broadening of the reflexes in comparison with those in the diffractogram of pure cerium dioxide (Fig. 1, curve 4) points out the very small dimensions of domains of the composite material in which the diffraction takes place.

The microscopic images of the studied samples are presented in Fig. 2. Fig. 2(a) presents the nanoparticles of CeO_2. One can see that in a dried state this material consists of broad aggregates of individual ceria nanoparticles. This tendency to the agglomeration processes is inherent to this nanofiller. So some special cares were provided during the formation of the nanocomposite films to insure the distribution of ceria in the BC volume as uniform as possible (see the "Materials and methods' section).

A sample of pure bacterial cellulose (Fig. 1(b)) consists of fibrils with a diameter of 30 nm. The samples filled with CeO_2 nanoparticles (Fig.1 c-e) were studied using a back-scattered electron detector capable of detecting the so-called Z-contrast having an atomic-number (Z) sensitive nature, i.e. the higher the atomic number of the element, the brighter it appears in the microscopic image. In this particular case, CeO_2 particles should look

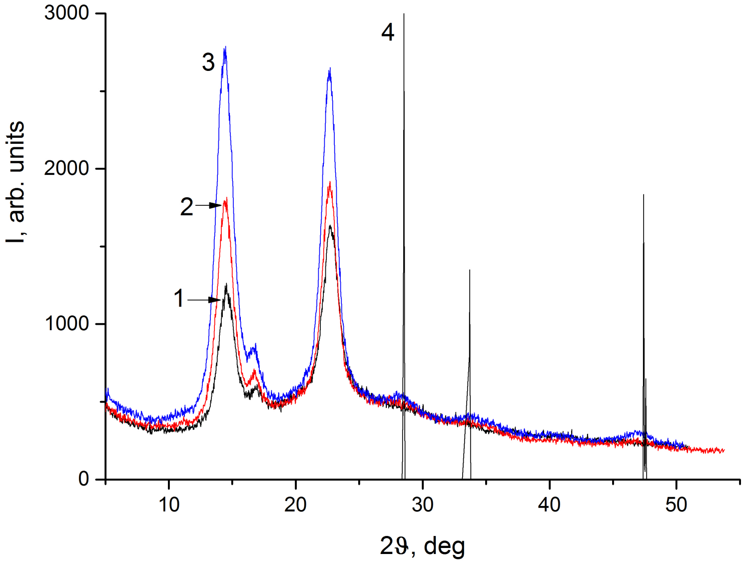

FIG. 1. Diffractograms of the films: BC (1), nanocomposites with 3 and 10 wt. %, (2 and 3, respectively); X-ray diffraction pattern of crystalline cerium dioxide, cubic phase (4)

most bright. This figure clearly shows that CeO_2 nanoparticles are not well-dispersed in the matrix of bacterial cellulose. CeO_2 aggregates of various sizes are observed. In this case, we can conclude that the higher the content of nanofiller particles in the composite material, the larger the sizes of the detected CeO_2 aggregates.

The following figure (Fig. 3) shows the results of energy dispersive X-ray analysis (EDX) of the nanocomposite films tested (Fig. 3(c, e, g)). This research method allows one to collect maps of the elements distribution. All the EDX data obtained clearly revealed the presence of cerium (indicated in yellow) in the test samples on the same parts of the samples, which are also shown in SEM micrographs on the left side (Fig. 3(b, d, f)). Moreover, its content corresponds to the calculated one.

The obtained cerium distribution maps for different samples confirm the SEM results discussed above, i.e. the higher the content of introduced CeO_2 nanoparticles, the higher the probability of detecting large agglomerates containing cerium. At the same time, there is a certain proportion of nanoparticles that is uniformly distributed in the samples.

Cerium dioxide is known to act as a catalyst in the destructive processes of organic compounds and to significantly affect the redox processes in the latter [25]. It was interesting to verify the effect of CeO_2 nanofiller on the thermal destruction of BC in the air atmosphere. The curves of BC and BC-CeO_2 nanocomposite films weight losses *vs.* temperature in the said conditions are shown in Fig. 4. The TGA curves obtained are typical for cellulose thermal destruction. The first region of weight losses (2 – 2.5 wt. %) observed at temperatures up to 100 °C is related to evaporation of water and low-molecular compounds, which are adsorbed on the cellulose surface. At temperatures 190 – 350 °C (depending on CeO_2 content) all of the samples undergo thermo-oxidative decomposition. Finally, at the terminal phase (at the highest temperatures) the carbonaceous residue interacts with atmospheric oxygen bringing to formation of CO and CO_2. As a result, an organic part of the sample was completely destroyed in the oxidative atmosphere (coke residue weigh is 0). The analysis of TGA curves reveals that the doping of BC matrix with CeO_2 nanoparticles as well as increasing of their content leads to a gradual temperature decrease of all of the aforementioned processes. This, obviously, confirms a noticeable catalytic activity of nano-sized cerium dioxide in the thermal oxidative destruction of cellulose. Indeed, embedment of these nanoparticles in concentrations 5 and 10 wt. % results in a decrease in thermal stability index, τ_5, by 29 and 45 degrees, respectively (See Table 1).

The results of mechanical tests of the films (Table 2) demonstrate an increase in stiffness of matrix polymer upon introduction of CeO_2 nanoparticles therein. Due to the hyperbranched system of hydrogen bonds, BC is a quite rigid, high-modulus polymer material [26]. In our study, we have observed a gradual augment of Young's moduli of the films as CeO_2 content was increased (Table 2). In fact, Young's moduli of the nanocomposite films with 5 and 10 wt. % of cerium dioxide are increased 1.25 and 1.63 fold, relative to that of a pristine BC film. A simultaneous increase of material tensile strength was also registered. On the other hand the composite film with even the highest concentration of CeO_2 nanoparticles exhibits no deterioration of elongation at break value. The

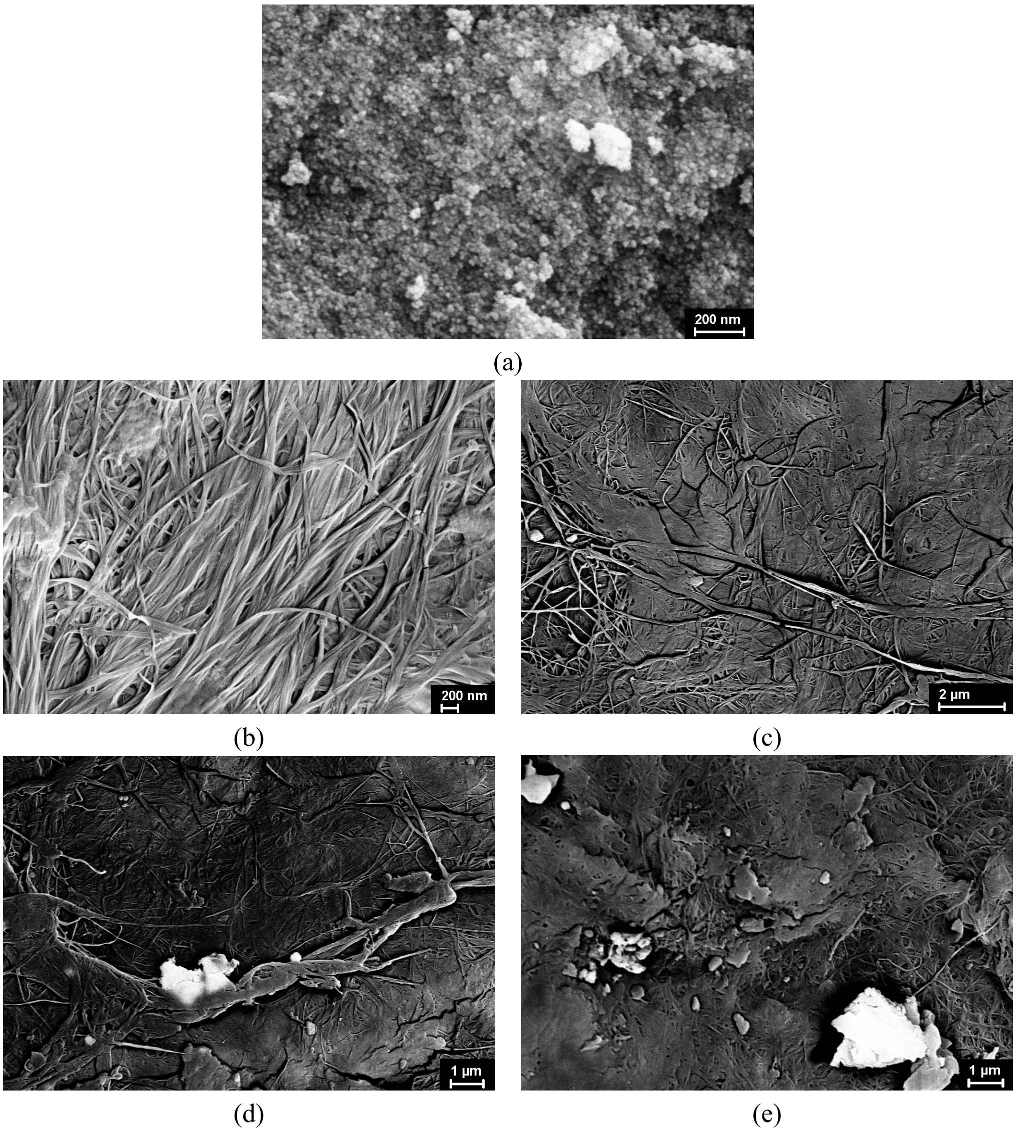

(a) (b) (c) (d) (e)

FIG. 2. SEM micrographs of the investigated samples: (a) – CeO_2 nanoparticles; (b) – pure BC; (c–d) – BC-ceria nanocomposite films containing 3, 5, and 10 wt. % CeO_2; respectively

TABLE 1. Indices of thermal stability of BC and BC-ceria nanocomposite films

Sample	τ_1, °C	τ_5, °C	τ_{10}, °C
BC	258	288	302
Composite, 1 wt.% of CeO_2	241	284	299
Composite, 3 wt.% of CeO_2	202	272	290
Composite, 5 wt.% of CeO_2	194	259	282
Composite, 10 wt.% of CeO_2	181	243	274

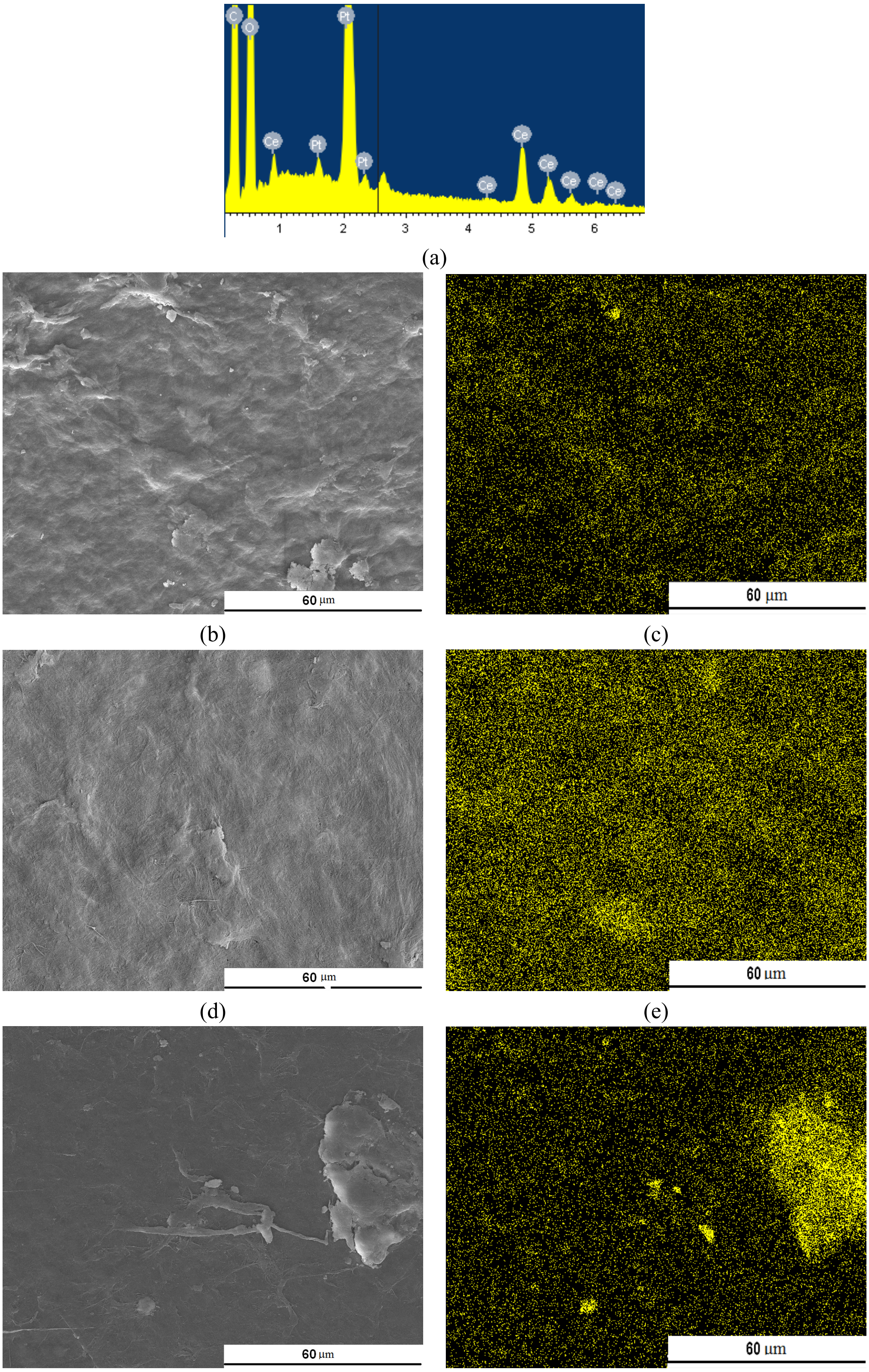

(a)

(b) (c)

(d) (e)

(f) (g)

FIG. 3. (a) – An example of EXD spectra obtained for investigated samples. SEM micrographs (left side) and EXD maps of cerium distribution (right side) of the nanocomposite samples containing: (b, c) – 3 wt. % CeO_2; (d, e) – 5 wt. % CeO_2; (f, g) – 10 wt. % CeO_2

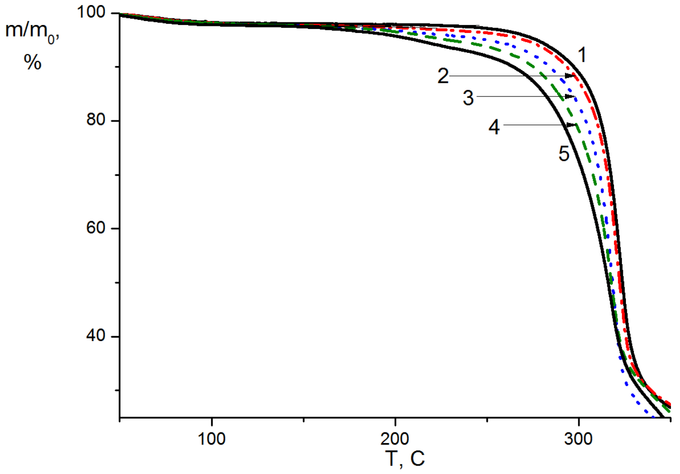

FIG. 4. TGA curves of (1) BC and (2–5) BC-ceria nanocomposite films. CeO_2 concentrations in the materials are (2) – 1 %, (3) – 3 %, (4) – 5 % and (5) – 10 %

TABLE 2. Mechanical characteristics of BC film and BC-ceria nanocomposite ones

No.	Sample	E, GPa	σ_b, MPa	ε_b, %
0	BC	6.41 ± 0.56	96 ± 6	3.9 ± 0.4
1	Composite, 1 wt.% of CeO_2	6.46 ± 0.42	94 ± 3	4.0 ± 0.5
2	Composite, 3 wt.% of CeO_2	6.75 ± 0.43	98 ± 7	3.9 ± 0.4
3	Composite, 5 wt.% of CeO_2	8.02 ± 0.56	108 ± 5	4.1 ± 0.5
4	Composite, 10 wt.% of CeO_2	10.45 ± 0.36	132 ± 6	4.4 ± 0.5

latter fact is quite interesting given that a wide range of polymers show the opposite behavior when doped with nanoparticles [27].

The significant increase in the material stiffness that we recorded, caused by the introduction of cerium dioxide into the polymer matrix, can hardly be explained by the well-known physical effect of reinforcement observed when nanoparticles such as carbon nanotubes, nanofibers, and graphene are introduced into different polymeric materials [27]. Indeed, unlike all the said and a number of other nanoscale fillers, characterized by a pronounced geometrical anisotropy with high aspect ratio values, cerium dioxide nanoparticles have a spherical or quasi-spherical shape, that is, they are characterized by an aspect ratio close to 1. With the introduction of fillers of such types with poor aspect ratios into the bulk of the polymer material, reinforcement effects can be expected at their much higher concentrations than those implemented in the composites we studied [28].

It should be assumed that the introduction of cerium dioxide in BC leads to profound changes in the structure of the intermolecular bonds in this material, to a steady increase in their number (as the concentration of nanoparticles increases). This effect can explain the changes in the stiffness and strength of the material, observed when cerium dioxide is introduced into the BC.

Such behavior of nanocomposite material can find room in a number of practical uses, e.g., for the tailoring of various materials for biomedical applications, primarily for materials for surgery, to which the presence of cerium oxide in BC will procure bactericidal properties and enhance healing of lesions [29, 30].

Another mode of work of polymeric materials under the long-term action of mechanical stresses, which is interesting and important from the viewpoint of the possible practical use of the materials, is their behavior in the friction couples, for example in the couples with metals. Lately a potential possibility of the polymer materials to be used as components of the friction units became the subject of close interest of the researchers. Albeit, in general, the nanosized fillers can improve the tribologic properties of different polymer materials [31, 32], ceria particles are known to be widely used as abrasive materials [33,34]. In line with this circumstance we have tackled clarifying the effect of the ceria nanoparticles on the tribologic behavior of the BC films in the friction couple with the stainless steel.

At the first stage of these experiments, we have determined the k value of the matrix BC in the couple with steel (Fig. 5). The results obtained are typical for cellulose materials – $\sim$ 0.36 – 0.42 depending upon the normal load F_z.

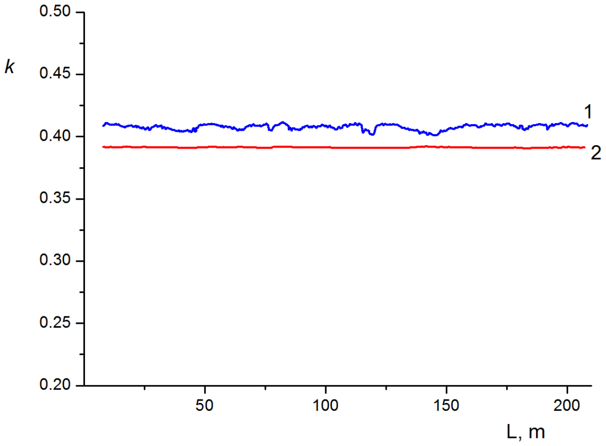

FIG. 5. Friction curves of (1) BC/steel and (2) BC-ceria/steel couples. The ceria concentration is 3 wt. %, the mean normal pressure – 10 MPa

The experiments carried out at the next step of the investigation (Fig. 5) have shown that introduction of ceria nanoparticles into the polymer at a concentration of 3 wt. % does not provoke any significant change of the polymer/steel friction coefficient: the k value of the composite film is 0.391, while that of the unfilled polymer film – 0.407 (at the mean value of normal stress 10 MPa). However, another positive effect of the ceria nanoparticles introduction was observed: the friction process becomes more stable against that in the BC/steel friction couple (Fig. 5), practically no noticeable changes or fluctuations, no wobbles in the k value were registered during the friction experiment.

A more pronounced positive effect of the ceria introduction into the polymer, registered in the tribologic tests, is a decrease of the wear rate of the nanocomposite material as compared to that of the unfilled BC film. The mass wear rate W was determined as:

$$W = \frac{\Delta m}{L \times \rho \times F_z},$$

where Δm denotes the mass loss during the test, L is the running distance during the test, ρ – the density of the polymer tested, and F_z – the normal contact load.

The W value of unfilled BC film was found to be as high as 4×10^{-3} mm^3/Nm (the average roughness Ra of the steel surface was about 1.0 μm). The BC-ceria nanocomposite film is characterized by a substantial depression of the wear rate down to 7×10^{-4} mm^3/Nm. This positive effect can be attributed to stabilization of the friction process provided by the nanoparticles inserted in the BC volume (Fig. 5).

4. Conclusions

The protocol of film formation from mixtures of aqueous suspensions of disintegrated BC and ceria nanoparticles elaborated in the present work provides an algorithm of preparation of the stiff and non-brittle nanocomposite films. During the film preparation a partial aggregation of ceria takes place, the phenomenon presumably occurring at the stage of the film drying. In accordance with the data obtained in the XRD and SEM examinations of the films, a substantial portion of the ceria nanoparticles is distributed uniformly in the volume of the material. This situation takes place up to the maximal concentration of ceria used in our work: 10 wt. %.

The mechanical tests of the films demonstrate the progressive increase of both the Young's modulus and the ultimate stress values along with the increase of the nanofiller's concentration in the material without any depression of the ultimate deformation. These facts indicate possible formation of certain system of interactions between BC macrochains and ceria nanoparticles in the nanocomposite materials obtained.

The tribologic tests of both BC and composite films in the friction couples with steel have given evidence for the substantial stabilization of the friction process caused by introduction of ceria into BC bulk along with the significant decrease of the mass wear rate of the material.

A substantial successive decrease of the thermal stability of the films provoked by the increase in the ceria concentration was registered in the thermogravimetric tests in air, the fact testifying catalytic action of ceria during thermo-oxidative destruction of BC. However, this specific feature of the nanocomposite materials studied does not appear to be a hindrance for the practical use of these materials in the biomedical applications.

Acknowledgements

The work was financially supported by the Russian Science Foundation (grant No. 18-13-00305).

References

[1] *Cellulose Chemistry and Properties: Fibers, Nanocelluloses and Advanced Materials*. Ed. O. J. Rojas. Springer International Publishing, Switzerland, 2016.

[2] Esa F., Tasirin S.M., Rahman N.A. Overview of Bacterial Cellulose Production and Application. *Agriculture and Agricultural Science Procedia*, 2014, **2**, P. 113–119.

[3] Mitrofanov R.Y., Budaeva V.V., Sakovich G.V. Preparation and Properties of Bacterial Cellulose Gel Films. *Chemistry for Sustainable Development*, 2010, **18**, P. 503–508.

[4] Gromovykh T.I., Sadykova V.S., et al. Bacterial cellulose synthesized by Gluconacetobacter hansenii for medical applications. *Applied Biochemistry and Microbiology*, 2017, **53**, P. 60–67.

[5] Backdahl H., Helenius G., et al. Mechanical properties of bacterial cellulose and interactions with smooth muscle cells. *Biomaterials*, 2006, **27**, P. 2141–2149.

[6] Feng X., Ullah N., et al. Characterization of Bacterial Cellulose by Gluconacetobacter hansenii CGMCC 3917. *Journal of Food Science*, 2015, **80** (10), E2217–27.

[7] Shah N., Ul-Islam M., Khattak W.A., Park J.K. Overview of bacterial cellulose composites: A multipurpose advanced material. *Carbohydrate Polymers*, 2013, **98**, P. 1585–1598.

[8] Nainggolan H., Gea S., et al. Mechanical and thermal properties of bacterial-cellulose-fibre-reinforced Mater-Bi bionanocomposite. *Beilstein J. Nanotechnol.*, 2013, **4**, P. 325–329.

[9] Buyanov A.L., Gofman I.V., et al. Anisotropic swelling and mechanical behavior of composite bacterial cellulose-(polyacrylamide or polyacrylamide-sodium polyacrylate) hydrogels. *Journal of the mechanical behaviour of biomedical materials*, 2010, **3**, P. 102–111.

[10] Smyslov R.Yu., Ezdakova K.V.,et al. Morphological structure of Gluconacetobacter xylinus cellulose and cellulose-based organic-inorganic composite materials. *Journal of Physics: Conference Series*, 2017, **848**, P. 012017–012028.

[11] Shah P., Pandey K. Advancement in packaging film using microcrystalline cellulose and TiO_2. *American Journal of Polymer Science and Technology*, 2017, **3**, P. 97–102.

[12] Bouadjela S., Abdoune F.Z., et al. Effect of titanium dioxide nanoparticles on polymer network formation. *Spectroscopy Letters*, 2017, **50**, P. 522–527.

[13] Tamayo L., Azocar M., et al. Copper-polymer nanocomposites: An excellent and cost-effective biocide for use on antibacterial surfaces. Review. *Materials Science and Engineering C*, 2016, **69**, P. 1391–1409.

[14] Mallakpour S., Darvishzadeh M. Ultrasonic treatment as recent and environmentally friendly route for the synthesis and characterization of polymer nanocomposite having PVA and biosafe BSA modified ZnO nanoparticles. *Polymers for Advanced Technologies*, 2018, **29**, P. 2174–2183.

[15] Lu Z., Mao C., et al. Fabrication of CeO_2 nanoparticle-modified silk for UV protection and antibacterial applications. *Journal of Colloid and Interface Science*, 2014, **435**, P. 8–14.

[16] Liu K.-Q., Kuang C.-X., et al. Synthesis, characterization and UV-shielding property of polystyrene-embedded CeO_2 nanoparticles. *Optical Materials*, 2013, **35**, P. 2710–2715.

[17] Mullins D.R. The surface chemistry of cerium oxide. *Surface Science Reports*, 2015, **70**, P. 42–85.

[18] Tiefensee F., Becker-Willinger C., et al. Nanocomposite cerium oxide polymer matching layers with adjustable acoustic impedance between 4 MRayl and 7 MRayl. *Ultrasonics*, 2010, **50**, P. 363–366.

[19] Jia R.-P., Wang C.-F., et al. Preparation, characterization, and properties of CeO_2/thermoplastic polyurethane nanocomposites. *Journal of Reinforced Plastics and Composites*, 2015, **34**, P. 1090–1098.

[20] Shang Z., Lu C., Lu X., Gao L. Studies on syntheses and properties of novel CeO_2/polyimide nanocomposite films from $Ce(Phen)_3$ complex. *Polymer*, 2007, **48**, P. 4041–4046.

[21] Buyanov A.L., Revel'skaya L.G., Kuznetzov Yu.P., Shestakova A.S. Cellulose-poly(acrylamide or acrylic acid) interpenetrating polymer membranes for the pervaporation of water-ethanol mixtures. *J. Appl. Polym. Sci.*, 1998, **69**, P. 761–768.

[22] Ivanov V.K., Polezhaeva O.S., et al. Synthesis and thermal stability of nanocrystalline ceria sols stabilized by citric and polyacrylic acids. *Russian Journal of Inorganic Chemistry*, 2010, **55** (3), P. 328–332.

[23] Kriegner D., Matej Z., Kuzel R., Holý V. Powder diffraction in Bragg–Brentano geometry with straight linear detectors. *J. Appl. Cryst.*, 2015, **48**, P. 613–618.

[24] Gofman I., Larin S., Liulin S., Falkovich S. The device for the determination of coefficient of sliding friction. Patent of Russian Federation No. 150882, Published 10.03.2015. Inventions. Useful models. 2015. No 7.

[25] Mullins D.R. The surface chemistry of cerium oxide. *Surface Science Reports*, 2015, **70**, P. 42–85.

[26] Kannam S.K., Oehme D.P., et al. Hydrogen bonds and twist in cellulose microfibrils. *Carbohydrate Polymers*, 2017, **175**, P. 433–439.

[27] Valenkov A.M., Gofman I.V., et al. Polymeric Composite Systems Modifi ed with Allotropic Forms of Carbon (Review). *Russian Journal of Applied Chemistry*, 2011, **84** (5), P. 735–750.

[28] Garboczi E.J., Snyder K.A., Douglas J.F., Thorpe M.F. Geometrical percolation threshold of overlapping ellipsoids. *Phys. Review. E*, 1995, **52** (1), P. 819–828.

[29] Rajeshkumar S., Naik P. Synthesis and biomedical applications of Cerium oxide nanoparticles – A Review. *Biotechnology Reports*, 2018, **17**, P. 1–5.

[30] Popov A.L., Ermakov A.M., et al. Biosafety and effect of nanoparticles of CeO_2 on metabolic and proliferative activity of human mesenchymal stem cells *In Vitro*. *Int. J. Nanomech. Sci. Tech.*, 2016, **7**, P. 165–175.

[31] Aly A., Zeidan E., et al. Friction and Wear of Polymer Composites Filled by Nano-Particles: A Review. *World Journal of Nano Science and Engineering*, 2012, **2**, P. 32–39.

[32] Chamnipan R., Chutima S., Uthaisangsuk V. Processing and characterization of nano filler containing friction materials. *Materials Today: Proceedings*, 2018, **5**, P. 9467–9475.

[33] Shin C., Choi J., et al. Trace metals optimization in ceria abrasive for material removal rate enhancement during ILD CMP. *ECS J. Solid State Sci. Technol.*, 2017, **6**, P. 687–690.

[34] Suda S. Nanocomposite glass abrasives. *Journal of the Ceramic Society of Japan*, 2014, **122**, P. 244–249.

NANOSYSTEMS: PHYSICS, CHEMISTRY, MATHEMATICS, 2018, 9 (6), P. 763–769

Solid-phase interaction in ZrO_2–Fe_2O_3 nanocrystalline system

S. A. Kirillova[1], O. V. Almjasheva[1], V. V. Panchuk[2], V. G. Semenov[2]

[1]St. Petersburg State Electrotechnical University “LETI”, ul. Professora Popova, 5, St. Petersburg, 197376, Russia
[2]St. Petersburg State University, Universitetskaya nab., 7–9, St. Petersburg, 199034, Russia
refractory-sveta@mail.ru, almjasheva@mail.ru, vitpan@mail.ru, val_sem@mail.ru

PACS 64.75.+g; 76.20.+q **DOI 10.17586/2220-8054-2018-9-6-763-769**

Based on the results of X-ray phase analysis and Mössbauer spectroscopy, it was demonstrated that in the ZrO_2–Fe_2O_3 system, represented by the mechanical mixture of m–ZrO_2 (14 ± 2 nm) and α-Fe_2O_3 (43 ± 2 nm) nanoparticles, being heated above the temperature corresponding to the melting temperature of the two-dimensional nonautonomous phase, transformation of α-Fe_2O_3 occurs resulting in appearing of the X-ray amorphous magnetically disordered state localized on the surface of ZrO_2 nanoparticles in the form of a thin layer. Transformation pattern in ZrO_2–Fe_2O_3 nanocrystalline system has been introduced.

Keywords: nanostructures, iron-zirconia, surface, X-ray diffraction, Mössbauer spectroscopy.

Received: 2 October 2018

Revised: 24 November 2018

1. Introduction

Interest in systems containing zirconium dioxide is caused by high refractory properties, strength, crack resistance, chemical inertness, superionic oxygen conductivity, biocompatibility, catalytic activity and other important characteristics of the materials, based on this substance [1, 2]. Ceramic and composite materials, based on ZrO_2–Fe_2O_3 system, are widely used as catalysts or catalyst carriers for hydrocarbons isomerization, carbon monoxide hydrogenization, selective hydrogenation (Fischer–Tropsch reaction) and ammonia synthesis [3, 4], as well as the magnetic materials [5, 6].

Different contradictory data, published in the scientific literature, are pertinent to possibilities and ranges of solid solutions formation in ZrO_2–Fe_2O_3 system. The study of phase formation processes in the considered system is connected with definite methodological difficulties, related to the behavior of the studied system components [7–16].

While extremely localized areas of the iron oxide-based solid solutions in zirconium dioxide may exist for the macroscopic particles, as it follows from data [17–26] (which is most pronounced for the low-temperature range), more wide solubility range of iron oxide in ZrO_2-based nanocrystals was detected, which is shown by data [27–36], in case of nano-scale particles. In this case, the possibility and the ranges of solid solutions existence in this system to a great degree are determined by the synthesis method of considered compositions.

Composition synthesis and subsequent study of their behavior during heating for ZrO_2–Fe_2O_3 system are generally realized with application of sol-gel synthesis followed by the annealing-quenching heat treatment of received precursors [16, 22–24, 31–33]; hydrothermal synthesis [5]; thermal decomposition of iron (III) and zirconium salts [27]; ZrO_2 impregnating with aqueous solution of ferric (III) nitrate and subsequent drying and incineration [3, 4]; solid-phase synthesis method [25, 37]; reaction media burning method (solid-phase flame method, solution burning) [26, 38, 39], etc. [6, 34–36].

Inconsistencies pertinent to ranges of solid solutions areas, a state of ZrO_2 surface and iron ions location in different positions still exist and may be found almost in any new paper devoted to this system. Therefore, it is of interest to study the behavior of ZrO_2 and Fe_2O_3 nano-scale particles during their thermal treatment.

2. Experimental procedures

In order to study the solid-phase interaction of the components, ZrO_2 and Fe_2O_3 nano-scale powders, which have been obtained by hydrothermal treatment method (refer to [40]), were mixed in ethyl alcohol. Specimens were formed by pressing under pressure of 5 MPa, after which these specimens were heat treated in the air following the annealing-quenching mode with exposure during 30 minutes at temperatures of 800, 900, 1000 and 1100 °C.

The phase composition of the specimens was studied by X-ray phase analysis using XRD-7000 Shimadzu diffractometer (CuK_α-radiation). The X-ray diffraction pattern peak identification was performed using the PDWin 4.0 software solution and Crystallographica Search-Match package. Based on the data analysis pertinent to X-ray diffraction pattern peak tailing, the average crystalline particle size has been calculated. Calculation was performed using the Sherrer equation [41].

The specimens' elemental composition was determined by electron probe microanalysis using Hitachi S-570 scanning electron microscope, equipped with Bruker Quantax 200 microprobe system.

Exposure of Mössbauer spectra was realized using WISSEL spectrometer operating in the constant acceleration mode, at the room temperature and at the liquid nitrogen boiling point. ^{57}Co in Rh-matrix, characterized by the radioactivity of 30 mC, was used as the source. Mathematical treatment of the experimental spectra was performed using the MOSSFIT software package [42]. The spectrometer velocity scale was calibrated using α-Fe foil at the room temperature. The chemical shift values were presented relative α-Fe.

3. Results and their discussion

Results of X-ray phase analysis of specimens, containing 6.4 ± 0.3 and 9.0 ± 0.6 mol.% $FeO_{1.5}$, which have been annealed at a temperature of 800, 900, 1000 and 1100 °C over 30 minutes, are presented in Figs. 1(*a*) and 2(*a*). Initial specimens were represented by the mechanical mixture of preliminary received nano-scale powders of ZrO_2 (monoclinic and tetragonal modification groups) and Fe_2O_3 [hematite, (104) peak, I – 100 %]. After heating at a temperature of 800 – 900 °C, a decrease in the intensity of the t-ZrO_2 peaks was observed, and after heating at a temperature above 900 °C, diffractograms contained only those reflections, which corresponded to monoclinic modification group of ZrO_2. For the specimen containing 6.4 ± 0.3 mol.% $FeO_{1.5}$, which was annealed at 800 and 900 °C, a peak on diffractograms, corresponding to α-Fe_2O_3, disappeared. During further increase of the thermal treatment temperature, (104) peak on diffractograms appeared again, however, its intensity was substantially less as compared with the initial composition. For the specimen, containing 9.0 ± 0.6 mol.% $FeO_{1.5}$, which has been annealed at a temperature of 800 – 900 °C, the relative intensity of (104) peak on diffractograms decreased as compared with the initial composition, while at a temperature of 1000 – 1100 °C the integral intensity of this peak has increased, becoming comparable with the initial composition.

It should be noted that sizes of m-ZrO_2 crystallites during heating up to a temperature of 900 °C have changed only slightly both for the specimen, containing 6.4 ± 0.3 mol.% $FeO_{1.5}$ (Fig. 3), as well as for the specimen, containing 9.0 ± 0.6 mol.% $FeO_{1.5}$. Analysis of m-ZrO_2 unit cell parameters dependence on temperature has demonstrated their invariability within the measurement accuracy (Fig. 4). Absence of variation of ZrO_2 unit cell parameters may be indicative of the fact that heat treatment during 30 minutes at a temperature of up to 1000 and 1100 °C did result in m-ZrO_2-based solid solution formation.

Mössbauer spectra for initial compositions of specimens, containing 6.4 ± 0.3 and 9.0 ± 0.6 mol.% $FeO_{1.5}$, as well as for specimens, annealed at 800, 900, 1000 and 1100 °C, are presented in Figs. 1(b) and 2(b), respectively. The results of experimental spectra analysis with detection of sextet and doublet components, corresponding to iron atoms in magnetically ordered and magnetically disordered phases, are also presented in Figs. 1(b) and 2(b). Mössbauer parameters for sextet and doublet components of the iron-containing phases are presented in Table 1. The quantitative estimation of the iron relative content in different phases was performed with precision determined by difference in values of f_M Mössbauer factor (probability of resonance absorption in each phase).

For the initial specimens, which were represented by the mechanical mixture of the preliminary produced t-, m-ZrO_2 and α-Fe_2O_3 nano-scale powders, the Mössbauer spectrum was characterized by sextet, parameters of which have corresponded to the sextet parameters for α-Fe_2O_3 [43].

For the specimens being thermally treated at 800 °C, the Mössbauer spectrum was characterized by doublet (6.4 ± 0.3 mol.% $FeO_{1.5}$) or doublet and sextet superposition (9.0 ± 0.6 mol.% $FeO_{1.5}$). It should be noted that for the specimen containing 6.4 mol.% $FeO_{1.5}$ only doublet components have been commonly observed, while these doublet components are incidental to the atoms of iron in 3+ oxidation rate located in the form of thin layer on the surface of another oxide [44, 45]. With a temperature increase, the sextet appeared again and the doublet share in experimental spectrum has decreased; at a temperature of 1100 °C a share of the magnetically disordered phase was about 23 %. Such an effect was observed in case of increasing of particles sizes [43]. For the specimen, containing 9.0 mol.% $FeO_{1.5}$, the sextet component is common for the whole heat treatment temperature range.

While comparing the data of X-ray phase analysis and Mssbauer spectroscopy, it may be concluded, that at a temperature of 800 °C, transformation of α-Fe_2O_3 begins, which results in its transfer into X-ray amorphous magnetically disordered phase, localized on the surface of zirconium dioxide particles, as shown by the absence of (104) α-Fe_2O_3 peak on the diffractogram, by sextet disappearance and doublet appearance in Mössbauer spectrum of the specimen, containing 6.4 ± 0.3 mol.% $FeO_{1.5}$. With increased thermal treatment temperatures, the sizes of m-ZrO_2 particles are increased (Fig. 3) that causes decrease of their surface area and, therefore, aggregation of the iron oxide surface layer, accompanied with α-Fe_2O_3 bulk phase particles formation. Formation of α-Fe_2O_3 particles is confirmed by the data of X-ray phase analysis and Mössbauer spectroscopy, i.e. (104) α-Fe_2O_3 peak

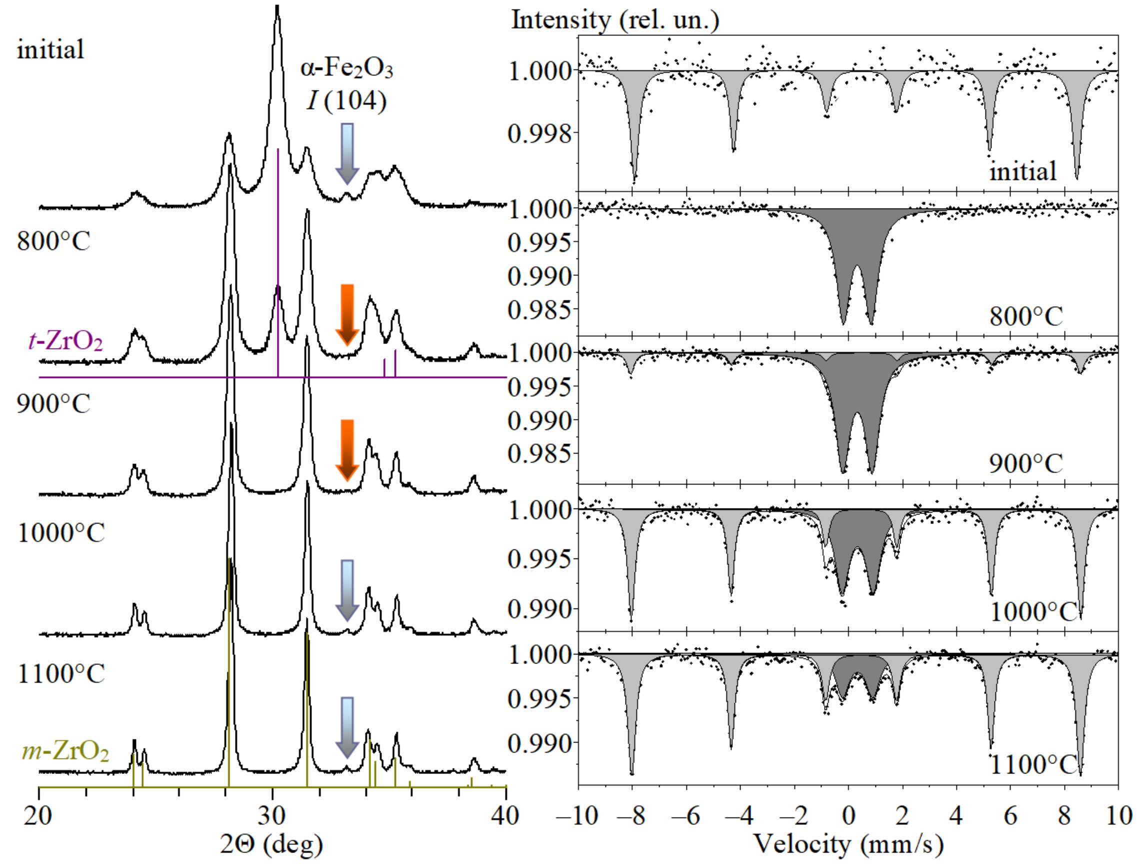

a *b*

FIG. 1. X-ray diffractograms (*a*) and Mössbauer spectra series, measured at 25 °C (*b*) of the specimen, containing 6.4 ± 0.3 mol.% $FeO_{1.5}$, which has been annealed at a temperature of 800, 900, 1000 and 1100 °C during 30 minutes

on the diffractogram appears again, in Mössbauer spectrum for the specimen, containing 6.4 ± 0.3 mol.% $FeO_{1.5}$ sextet corresponding to α-Fe_2O_3, may be revealed against the doublet background.

Apparently, during thermal treatment at a temperature of 800 and 900 °C with exposure for 30 minutes, α-Fe_2O_3 is transformed with the formation of the iron oxide layer on a surface of ZrO_2 nanoparticles. At temperatures of 800 – 900 °C, for α-Fe_2O_3 are corresponding to the melting temperature of the surface (two-dimensional nonautonomous) phase [46]. It appears that transfer of the two-dimensional nonautonomous phase into a liquid (liquid-like) state initiates active mass transfer of the iron-containing component to a surface of ZrO_2 nanoparticles. It should be noted that similar processes were observed earlier in BeO–Fe_2O_3, MgO–Fe_2O_3, Al_2O_3–Fe_2O_3, SiO_2–Fe_2O_3 systems [44, 45]. The transformation pattern, corresponding to the described processes in ZrO_2–Fe_2O_3 system, in which zirconium dioxide is initially represented by m-ZrO_2 and by α-Fe_2O_3 nanoparticles, characterized by the crystallites sizes of 14 ± 2 nm and 43 ± 2 nm, respectively, is presented in Fig. 5.

4. Conclusion

As distinct from the cases, in which compositions are received via codeposition, hydrothermal synthesis, etc., and in which mixing of components is initially possible at the atomic level, in the case of the solid-phase interaction of the nano-scale particles in ZrO_2–Fe_2O_3 system in the range of low contents of the iron-containing component increasing of the treatment temperature up to 800 – 900 °C does not cause stabilization of zirconium dioxide tetragonal modification and the formation of tetragonal solid solution, as well as Fe^{3+} ions are not included into m-ZrO_2 structure.

During the thermal treatment of ZrO_2 and Fe_2O_3 nanoparticles, at definite critical value of temperature in range of 800 – 900 °C, α-Fe_2O_3 transformation occurs with thin layer formation on m-ZrO_2 nanoparticles surface, i.e. formation of the composite nanoparticles of "nucleus (m-ZrO_2 nanoparticles) – shell (amorphous Fe_2O_3)" type takes place.

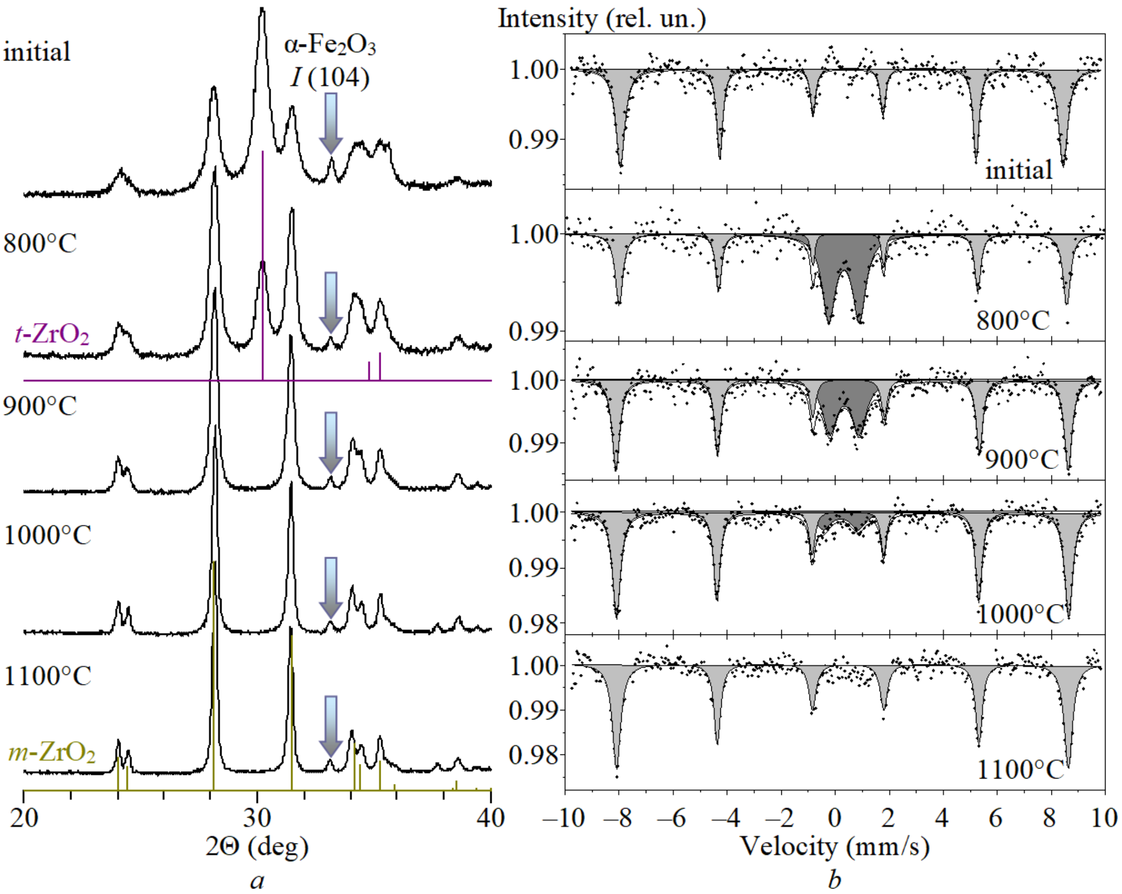

FIG. 2. X-ray diffractograms (*a*) and Mössbauer spectra series, measured at 25 °C (*b*) of the specimen, containing 9.0 ± 0.6 mol.% $FeO_{1.5}$, which has been annealed at a temperature of 800, 900, 1000 and 1100 °C during 30 minutes

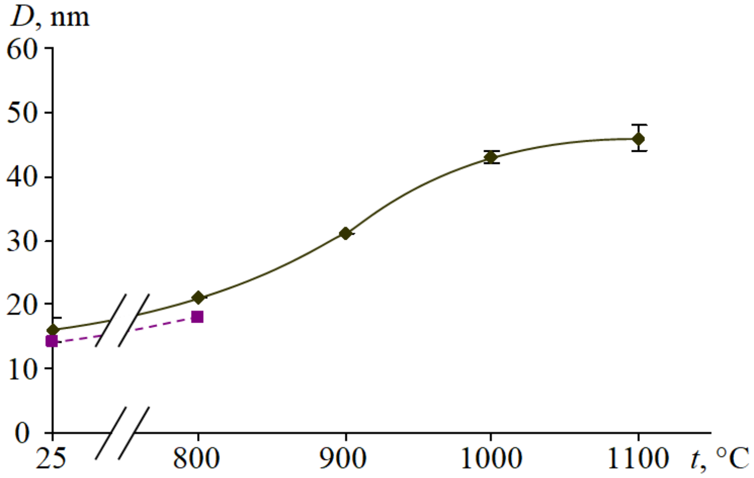

FIG. 3. t-ZrO_2 (■) and m-ZrO_2 (◆) crystallites sizes dependence on the heat treatment temperature for the specimen, containing 6.4 ± 0.3 mol.% $FeO_{1.5}$

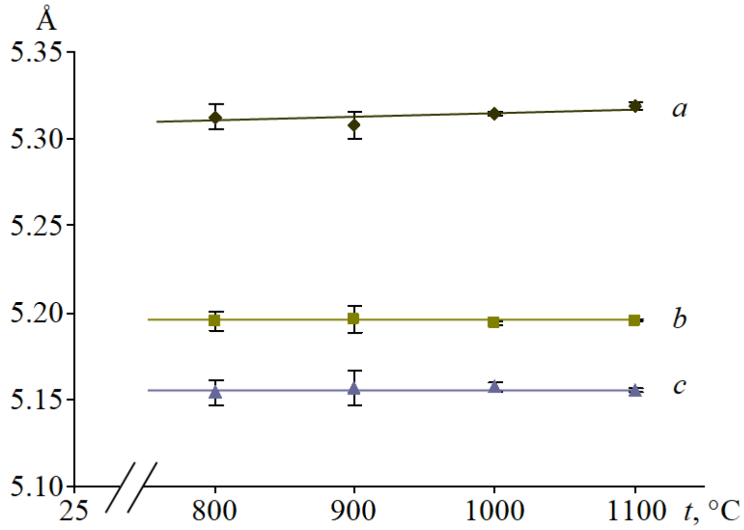

FIG. 4. m-ZrO_2 unit cell parameters dependence on the heat treatment temperature for the specimen, containing 6.4 ± 0.3 mol.% $FeO_{1.5}$

TABLE 1. Mössbauer parameters of spectra, measured for the studied specimens at a temperature of 25 °C

$FeO_{1.5}$ content, mol.%	Annealing temperature, °C	Parameters of Mössbauer spectra					
		sextet			doublet		Paramagnetic component content, %
		Isomer shift, mm/s	Quadrupole splitting, mm/s	Effective field, T	Isomer shift, mm/s	Quadrupole splitting, mm/s	
6.4±0.3	–	0.378±0.013	0.218±0.026	50.871±0.099	–	–	0
	800	–	–	–	0.326±0.000	1.032±0.000	100
	900	0.375±0.018	0.221±0.037	51.734±0.122	0.331±0.000	1.092±0.011	84.85
	1000	0.376±0.005	0.188±0.010	51.693±0.038	0.340±0.014	1.152±0.029	41.51
	1100	0.376±0.004	0.185±0.007	51.594±0.028	0.337±0.021	1.123±0.042	22.62
9.0±0.6	–	0.357±0.005	0.228±0.010	50.905±0.040	–	–	0
	800	0.383±0.016	0.192±0.033	51.458±0.136	0.324±0.042	1.128±0.080	52.54
	900	0.374±0.008	0.240±0.015	51.984±0.060	0.342±0.040	1.093±0.078	35.01
	1000	0.372±0.005	0.193±0.009	51.976±0.037	0.203±0.077	1.292±0.169	14.18
	1100	0.373±0.006	0.211±0.011	51.938±0.044	0.193±0.087	1.282±0.179	∼ 5

Acknowledgements

The authors express their gratitude to V. V. Gusarov for the attention he paid to the work and for his help in the interpretation of the results.

This work was supported by Ministry of education and science of the Russian Federation (Project 3.6522.2017).

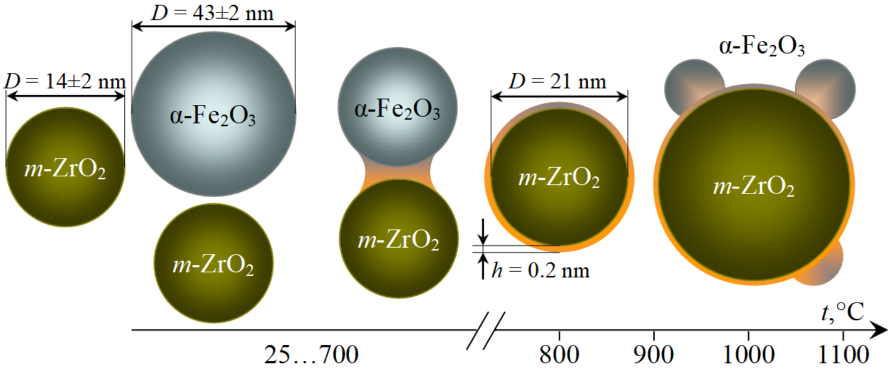

FIG. 5. Transformation pattern in ZrO_2–Fe_2O_3 system

References

[1] Shackelford J.F., Doremus R.H. *Ceramic and Glass Materials. Structure, Properties and Processing*. Springer, Boston, MA, 2008, 209 p.
[2] Almjasheva O.V., Garabadzhiu A.V., Kozina Yu.V., et al. Biological effect of zirconium dioxide-based nanoparticles. *Nanosystems: Phys. Chem. Math.*, 2017, **8** (3), P. 391–396.
[3] Chen K., Dong L., Yan Q., Chen Y. Dispersion of Fe_2O_3 supported on metal oxides studied by Mssbauer spectroscopy and XRD. *J. Chem. Soc., Faraday Trans.*, 1997, **93** (12), P. 2203–2206.
[4] Okamoto Y., Kubota T., Ohto Y., Nasu S. Metal Oxide–Support Interactions in Fe/ZrO_2 Catalysts. *J. Phys. Chem. B*, 2000, **104** (35), P. 8462–8470.
[5] Kuryliszyn-Kudelska I., Arciszewska M., Maolepszy A., et al. Influence of Fe doping on magnetic properties of ZrO_2 nanocrystals. *J. Alloys Compd.*, 2015, **632**, P. 609–616.
[6] de Souza A.O., Ivashita F.F., Biondo V., et al. Structural and magnetic properties of iron doped ZrO_2. *J. Alloys Compd.*, 2016, **680**, P. 701–710.
[7] Belov G.V., Iorish V.S., Yungman V.S. IVTANTHERMO for Windows – database on thermodynamic properties and related software. *Calphad: Comput. Coupling Phase Diagrams Thermochem.*, 1999, **23** (2), P. 173–180.
[8] Srinivasan R., Davis B.H., Burl C.O., Hubbard C.R. Crystallization and phase transformation process in zirconia: an in situ high-temperature X-ray diffraction study. *J. Am. Ceram. Soc.*, 1992, **75** (5), P. 1217–1222.
[9] Oleinikov N.N., Pentin I.V., Murav'eva G.P., Ketsko V.A. Highly disperse metastable ZrO_2-based phases. *Russ. J. Inorg. Chem.*, 2001, **46** (9), P. 1275–1281.
[10] Guo X., Schober T. Water incorporation in tetragonal zirconia. *J. Am. Ceram. Soc.*, 2004, **87** (4), P. 746–748.
[11] Shukla S., Seal S. Mechanisms of room temperature metastable tetragonal phase stabilisation in zirconia. *Int. Mater. Rev.*, 2005, **50** (1), P. 45–64.
[12] Zhang F., Chupas P.J., Lui S.L.A., et al. In situ study of the crystallization from amorphous to cubic zirconium oxide: Rietveld and reverse Monte Carlo analyses. *Chem. Mater.*, 2007, **19** (13), P. 3118–3126.
[13] Lin F.-Q., Dong W.-S., Liu C.-L., et al. In situ source–template-interface reaction route to hollow ZrO_2 microspheres with mesoporous shells. *J. Colloid Interface Sci.*, 2008, **323** (2), P. 365–371.
[14] Almjasheva O.V. Heat-stimulated transformation of zirconium dioxide nanocrystals produced under hydrothermal conditions. *Nanosystems: Phys. Chem. Math.*, 2015, **6** (5), P. 697–703.
[15] Li F., Li Y., Song Z., et al. Evolution of the crystalline structure of zirconia nanoparticles during their hydrothermal synthesis and calcination: Insights into the incorporations of hydroxyls into the lattice. *J. Eur. Ceram. Soc.*, 2015, **35** (8), P. 2361–2367.
[16] Li P., Chen I-W., Penner-Hahn J.E. Effect of dopants on zirconia stabilization – An X-ray Absorption Study: I, Trivalent Dopants. *J. Am. Ceram. Soc.*, 1994, **77** (1), P. 118–128.
[17] Muan A. Phase equilibria at high temperatures in oxide systems involving changes in oxidation states. *Am. Jour. Sci.*, 1958, **256** (3), P. 171–207.
[18] Jones T., Kimura S., Muan A. Phase Relations in the System FeO–Fe_2O_3–ZrO_2–SiO_2. *J. Am. Ceram. Soc.*, 1967, **50** (3), P. 137–142.
[19] Petrov Yu.B., Udalov Yu.P., Slovak J., Morozov Yu.G. Liquid immiscibility phenomena in melts of the ZrO_2–FeO–Fe_2O_3 System. *Glass Phys. Chem.*, 2002, **28** (3), P. 139–146.
[20] Bechta S.V., Krushinov E.V., Al'myashev V.I., et al. Phase relations in the ZrO_2–FeO system. *Russ. J. Inorg. Chem.*, 2006, **51** (2), P. 325–331.
[21] Bechta S.V., Krushinov E.V., Almjashev V.I., et al. Phase diagram of the ZrO_2–FeO system. *J. Nucl. Mater.*, 2006, **348** (1–2), P. 114–121.
[22] Popović S., Gržeta B., Czakó-Nagy I., Musić S. Structural properties of the system m-ZrO_2–α-Fe_2O_3. *J. Alloys Compd.*, 1996, **241** (1–2), P. 10–15.
[23] Kriventsov V.V., Kochubey D.I., Maximov Yu.V., et al. Structural determination of the Fe-modified zirconium oxide. *Nucl. Instrum. Methods Phys. Res., Sect. A*, 2001, **470** (1–2), P. 341–346.
[24] Navo J.A., Hidalgo M.C., Coln G., et al. Preparation and Physicochemical Properties of ZrO_2 and Fe/ZrO_2 Prepared by a Sol-Gel Technique. *Langmuir*, 2001, **17** (1), P. 202–210.
[25] Beck H.P., Kaliba C. On the solubility of Fe, Cr and Nb in ZrO_2 and its effect on thermal dilatation and polymorphic transition. *Mater. Res. Bull.*, 1990, **25** (9), P. 1161–1168.

[26] Ghigna P., Spinolo G., Anselmi-Tamburini U., et al. Fe-Doped Zirconium Oxide Produced by Self-Sustained High-Temperature Synthesis: Evidence for an Fe–Zr Direct Bond. *J. Am. Chem. Soc.*, 1999, **121** (2). P. 301–307.

[27] Davison S., Kershaw R., Dwight K., Wold A. Preparation and characterization of cubic ZrO_2 stabilized by Fe(III) and Fe(II). *J. Solid State Chem.*, 1988, **73** (1), P. 47–51.

[28] Inwang I.B., Chyad F., McColm I.J. Crystallisation of iron(III)-zirconia co-gels. *J. Mater. Chem.*, 1995, **5** (8), P. 1209–1213.

[29] Berry F.J., Loretto M.H., Smith M.R. Iron-zirconium oxides: An investigation of structural transformations by X-ray diffraction, electron diffraction, and iron-57 Mössbauer spectroscopy. *J. Solid State Chem.*, 1989, **83** (1), P. 91–99.

[30] Berry F.J., Jobsen S., Smith M.R. Iron-zirconium oxide catalysts for the hydrogenation of carbon monoxide: In situ studies by iron-57 Mössbauer spectroscopy. *Hyperfine Interact.*, 1989, **46** (1), P. 607–611.

[31] Štefanić G., Musić S., Popović S., Nomura K. A study of the ZrO_2–Fe_2O_3 system by XRD, ^{57}Fe Mössbauer and vibrational spectroscopies. *J. Mol. Struct.*, 1999, **480–481**, P. 627–631.

[32] Štefanić G., Gržeta B., Musić S. Influence of oxygen on the thermal behavior of the ZrO_2–Fe_2O_3 system. *Mater. Chem. Phys.*, 2000, **65** (2), P. 216–221.

[33] Štefanić G., Gržeta B., Nomura K., et al. The influence of thermal treatment on phase development in ZrO_2–Fe_2O_3 and HfO_2–Fe_2O_3 systems. *J. Alloys Compd.*, 2001, **327** (1–2), P. 151–160.

[34] Jiang J.Z., Poulsen F.W., Mrup S. Structure and thermal stability of nanostructured iron-doped zirconia prepared by high-energy ball milling. *J. Mater. Res.*, 1999, **14** (4), P. 1343–1352.

[35] Cao W., Tan O.K., Zhu W., et al. An amorphous-like $x\alpha$-Fe_2O_3–$(1-x)ZrO_2$ solid solution system for low temperature resistive-type oxygen sensing. *Sens. Actuators, B*, 2001, **77** (1–2), P. 421–426.

[36] Kiminami R.H.G. The monoclinic-tetragonal phase transformation of zirconia in the system ZrO_2–Fe_2O_3. *J. Mater. Sci. Lett.*, 1990, **9** (4), P. 373–374.

[37] Bohé A.E., Andrade Gamboa J.J., Pasquevich D.M. Enhancement of the martensitic transformation of tetragonal zirconia powder in the presence of iron oxide. *Mater. Sci. Eng., A*, 1999, **273–275**, P. 218–221.

[38] Maglia F., Anselmi-Tamburini U., Spinolo G., Munir Z.A. Thermal Stability of Combustion-Synthesized Metastable Solid Solutions of Zirconia and Transition Metals. *J. Mater. Synth. Process.*, 1999, **7** (5), P. 327–332.

[39] Garcia F.L., de Resende V.G., De Grave E., et al. Iron-stabilized nanocrystalline ZrO_2 solid solutions: Synthesis by combustion and thermal stability. *Mater. Res. Bull.*, 2009, **44** (6), P. 1301–1311.

[40] Pozhidaeva O.V., Korytkova E.N., Drozdova I.A., Gusarov V.V. Phase state and particle size of ultradispersed zirconium dioxide as influenced by conditions of hydrothermal synthesis. *Russ. J. Gen. Chem.*, 1999, **69** (8), P. 1219–1222.

[41] Patterson A.L. The Scherrer formula for x-ray particle size determination. *Phys. Rev.*, 1939, **56** (10), P. 978–982.

[42] Semenov V.G., Moskvin L.N., Efimov A.A. Analytical potential of Mössbauer spectroscopy. *Russ. Chem. Rev.*, 2006, **75** (4), P. 317–327.

[43] Suzdalev I.P. *Electrical and magnetic transitions in nanoclusters and nanostructures*. KRASAND, Moscow, 2012, 480 p. (in Russian)

[44] Gusarov V.V., Egorov F.K., Ekimov S.P., Suvorov S.A. Mössbauer study of the kinetics of the formation of film states in the interaction of oxides of magnesium and iron. *J. Phys. Chem.*, 1987, **61** (6), P. 1652–1654. (in Russian)

[45] Gusarov V.V., Malkov A.A., Malygin A.A., Suvorov S.A. Thermally activated transformations of 2D nonautonomous phases and contradiction of polycrystalline oxide materials. *Inorg. Mater.*, 1995, **31** (3), P. 320–323.

[46] Gusarov V.V., Suvorov S.A. Melting points of locally equilibrium surface phases in polycrystalline systems based on a single volume phase. *J. Appl. Chem. of the USSR*, 1990, **63** (8), P. 1560–1565.

NANOSYSTEMS: PHYSICS, CHEMISTRY, MATHEMATICS, 2018, 9 (6), P. 770–774

Sensitivity characteristics of germanene

N. N. Konobeeva, M. B. Belonenko

Volgograd State University, 400062, Volgograd, Russia

belonenko@volsu.ru, yana_nn@volsu.ru

PACS 71.20.-b, 73.20. Hb, 73.40. Gk **DOI 10.17586/2220-8054-2018-9-6-770-774**

In this paper, we investigate a sensitivity characteristics of germanene based on the tunneling current in the contact of a germanene with a metal or a superlattice. It is shown, that the sensitivity of the considered system to impurity molecules increases when a constant electric field is applied to it along the germanene plane.

Keywords: germanene, impurities, external electric field.

Received: 8 November 2018

Revised: 26 November 2018

1. Introduction

Recently, the problem of impurity detecting is relevant, since it is important for many practical applications (detection of low and high concentrations of toxic and explosive gases, monitoring the quality of air in a car cabin, automation of ventilation and air conditioning systems, etc.). The main point is to control the sensitivity of the system to the impurity. Many papers are devoted to the development of sensors based on graphene [1–3], including functionalized ones [4, 5].

In this paper, we propose germanene as a basic element for a gas sensor [6]. This material is a relative of graphene with similar properties, but has a stronger spin-orbit interaction as a silicene [7]. In [8], the adsorption of such gas molecules as N_2, CO, CO_2, H_2O, NH_3, NO, NO_2 and O_2 on germanene was investigated within the framework of the density functional theory. In this paper, we propose a method for detecting impurities based on the study of a tunneling current-voltage characteristic (CVC) of a contact of germanene with two types of materials (Me) – a metal and a superlattice (SL).

We have already tested it when study the sensory characteristics of graphene nanostructures (flakes, nanorings, and nanoribbons) [9, 10] and polymers [11]. The advantage of this method is the ability to select the contacting material, which can significantly affect the CVC of the system and enhance its response to the presence of impurities. The choice of these two contact materials due to the fact that the metal is the main material used for the manufacture of elements of electrical circuits. As for superlattices, they attract much attention due to optical, electrical and transport properties [12]. A superlattice is a solid-state structure in which an additional potential acts on the electrons, apart from the periodic potential of the crystal lattice, with a period that is several times higher than the lattice constant. This leads to a significant change in the electron energy spectrum of the system. Therefore, the superlattice acquire a number of characteristic properties which are absent in homogeneous materials.

2. A statement problem

The geometry of the problem is shown in Fig. 1. We consider a fragment of germanene with the size of NxM sites.

Here site A and site B correspond to the different germanene sublattices, d is the bending height (distance between two sublattices), d_1, d_2 are the distance between the A and B sites in the XOY plane, E_z is the constant electric field directed perpendicular to the germanene plane, E_0 is the external constant electric field.

In this paper, we must to take into account the spin-orbit interaction, which in germanene is four orders of magnitude higher than in graphene and introduces significant changes in the electronic structure of this material. The Hamiltonian for the germanene according to Ref. [13, 14] has the following form:

$$H = -t \sum_{\langle ij \rangle s} C_{is}^{+} C_{js} + i \frac{\Delta_{SO}}{3\sqrt{3}} \sum_{\langle\langle ij \rangle\rangle s} s v_{ij} C_{is}^{+} C_{js} - \sum_{is} \mu_i \Delta_z C_{is}^{+} C_{is}, \tag{1}$$

where C_{is}^{+}, C_{is} are birth/annihilation operators of electron, Δ_{SO} is the spin-orbit interaction, $\Delta_z = E_z d$ is the potential at the one lattice site, $\ll ij \gg$ means that the summation goes over all the nearest neighbors, $s = \uparrow\downarrow$

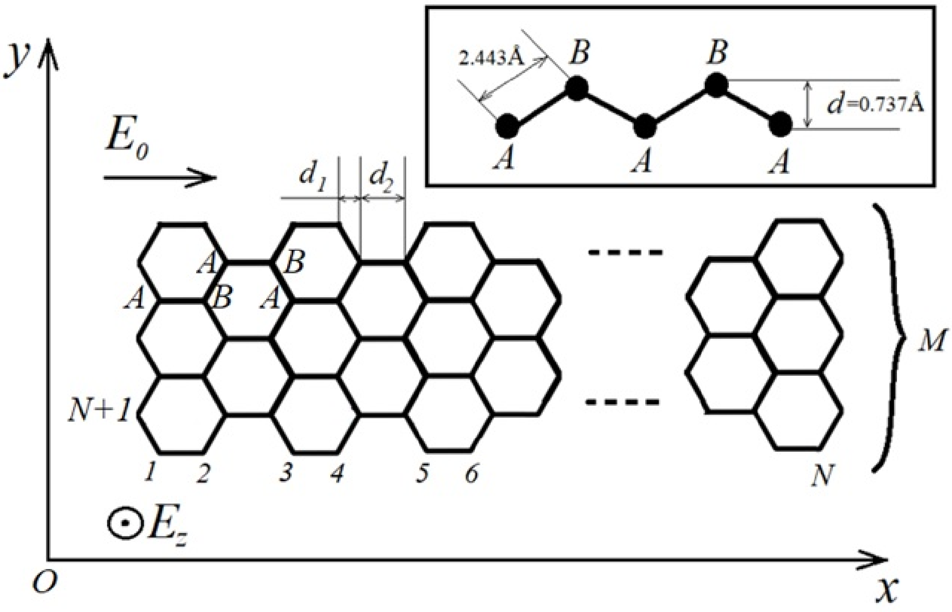

FIG. 1. The geometry of the problem. Side view (parallel to the YOZ plane) is in rectangular area

(if s as an index), $s = \pm$ (if s as a multiplier) [15]. The first term describes the usual electron hopping between the nearest neighboring sites with energy t. The second term is the spin-orbit interaction, where $\upsilon_{ij} = +1$ in the case if jumps between neighbors occur counterclockwise, $\upsilon_{ij} = -1$ in the case if jumps between neighbors occur clockwise [16]. The third term describes the potential of the chess sublattice with $\mu_i = +1$ (-1) for the sites $A(B)$.

A two-dimensional array of carbon atoms is renumbered for the further calculations into a one-dimensional one. The numbering starts from the bottom and goes to the axis OX, then we go up one level vertically and continue the numbering. Thus, we can obtain the Hamiltonian (1) in the matrix form. For example, we write the Hamiltonian for the germanene fragment 4×3:

$$H_{up} = \begin{pmatrix} a_{up} & -t & 0 & 0 & -t & 0 & 0 & 0 & 0 & 0 & 0 & 0 \\ -t & b_{up} & 0 & 0 & 0 & -t & 0 & 0 & 0 & 0 & 0 & 0 \\ 0 & 0 & a_{up} & -t & 0 & 0 & -t & 0 & 0 & 0 & 0 & 0 \\ 0 & 0 & -t & b_{up} & 0 & 0 & 0 & -t & 0 & 0 & 0 & 0 \\ -t & 0 & 0 & 0 & a_{up} & 0 & 0 & 0 & -t & 0 & 0 & 0 \\ 0 & -t & 0 & 0 & 0 & b_{up} & -t & 0 & 0 & -t & 0 & 0 \\ 0 & 0 & -t & 0 & 0 & -t & a_{up} & 0 & 0 & 0 & -t & 0 \\ 0 & 0 & 0 & -t & 0 & 0 & 0 & b_{up} & 0 & 0 & 0 & -t \\ 0 & 0 & 0 & 0 & -t & 0 & 0 & 0 & a_{up} & -t & 0 & 0 \\ 0 & 0 & 0 & 0 & 0 & -t & 0 & 0 & -t & b_{up} & 0 & 0 \\ 0 & 0 & 0 & 0 & 0 & 0 & -t & 0 & 0 & 0 & a_{up} & -t \\ 0 & 0 & 0 & 0 & 0 & 0 & 0 & -t & 0 & 0 & -t & b_{up} \end{pmatrix}, \tag{2}$$

$$a_{up} = \frac{\Delta_z - \Delta_{SO}}{2}, \quad b_{up} = \frac{-\Delta_z - \Delta_{SO}}{2}.$$

Note, the matrix for the spin “down” looks similar with the replacement: of a_{up} by a_{down}, b_{up} by b_{down}:

$$a_{down} = \frac{\Delta_z + \Delta_{SO}}{2}, \quad b_{down} = \frac{-\Delta_z + \Delta_{SO}}{2}. \tag{3}$$

Also, we take into account the external constant electric field E_0. It is important because the application of the external field allows us to control the material properties. The electric field has a great influence on the process of electron tunneling at the contact of the germanene with a metal and a superlattice. The Hamiltonian (2) in this case has the form:

$$H_{up}^{E}=H_{up}+\begin{pmatrix}\Phi_1&0&0&0&0&0&0&0&0&0&0&0\\0&\Phi_2&0&0&0&0&0&0&0&0&0&0\\0&0&\Phi_3&0&0&0&0&0&0&0&0&0\\0&0&0&\Phi_4&0&0&0&0&0&0&0&0\\0&0&0&0&\Phi_5&0&0&0&0&0&0&0\\0&0&0&0&0&\Phi_6&0&0&0&0&0&0\\0&0&0&0&0&0&\Phi_7&0&0&0&0&0\\0&0&0&0&0&0&0&\Phi_8&0&0&0&0\\0&0&0&0&0&0&0&0&\Phi_9&0&0&0\\0&0&0&0&0&0&0&0&0&\Phi_{10}&0&0\\0&0&0&0&0&0&0&0&0&0&\Phi_{11}&0\\0&0&0&0&0&0&0&0&0&0&0&\Phi_{12}\end{pmatrix}, \tag{4}$$

$$\Phi_1=\Phi_9=d_1E_0;\quad \Phi_2=\Phi_{10}=(d_1+d_2)\,E_0;\quad \Phi_3=\Phi_{11}=(3d_1+2d_2)\,E_0;$$
$$\Phi_4=\Phi_{12}=3\,(d_1+d_2)\,E_0;\quad \Phi_5=0;\quad \Phi_6=(2d_1+d_2)\,E_0;$$
$$\Phi_7=2\,(d_1+d_2)\,E_0;\quad \Phi_8=(4d_1+3d_2)\,E_0.$$

where Φ_k describes the potential of the electric field E_0 at the site k.

The current density can be written as [17]:

$$j_{tun}=4\pi e\left|T_{pq}\right|^2\int\limits_{-\infty}^{\infty}d\varepsilon\sum_p\delta\left(\varepsilon+eV-\varepsilon_p^1\right)\sum_q\delta\left(\varepsilon-\varepsilon_q^2\right)\left(n_f\left(\varepsilon\right)-n_f\left(\varepsilon+eV\right)\right), \tag{5}$$

where $\delta(x)$ is the Dirac delta-function, both factors with summation determine the tunneling density of states for each material in contact; $n_f(\varepsilon)$ is the equilibrium number of fermions with the energy ε, V is the voltage applied to material 1, T is the matrix element of the tunneling operator between the states p and q (the germanene plane is perpendicular to the surface of the contact material).

As a material for which we calculate the density of the tunneling current, we choose a metal and a superlattice. Electron spectrum for these substances can be written in the form (6):

$$\begin{array}{l}Me:\ \varepsilon_P^1=\dfrac{p^2}{2m}\,,\\ SL:\ \varepsilon_p^1=\varepsilon_0-\Delta\cdot\cos\left(p\right)\end{array}, \tag{6}$$

here, p is the momentum, m is the effective electron mass, ε_0 is the energy of quantum well electrons, Δ is the overlap integral, which is determined by the overlapping of the electron wave functions in the neighboring “wells” of the superlattice.

3. Results and discussion

The dependence of tunneling current (contact with a metal and a superlattice) on the voltage for the germanene fragment 26×7 with the impurity molecule and without it is shown in Fig. 2.

As can be seen from Fig. 2, the most preferable contact is the germanene with a superlattice. In this case, our method is suitable for detecting impurities. Moreover, the more impurity molecules are adsorbed on the surface of the germanene, the greater the response of the system:

$$\Delta R=\frac{R_1-R_0}{R_0}, \tag{7}$$

here, R_0 is the resistance value without impurity, R_1 is the resistance value with impurity. According to the right Fig. 2, we can conclude that the response decreases with increasing impurity concentration. This result is consistent with the data on the effect of the impurity concentration for graphene obtained, for example, in Ref. [18].

The influence of an external constant electric field E_0 on the tunneling current is shown in Figs. 3, 4.

According to Fig. 3, the introduction of an external constant electric field increases the magnitude of the response (7) and makes it easier to detect an impurity adsorbed on germanene. The applying of an external electric field most significantly affects the shape of the CVC for the contact with a superlattice. Which again speaks in favor of choosing as the second material in the contact of a SL.

The greater the external electric field applied to the system, the more sensitive it is to the presence of impurities.

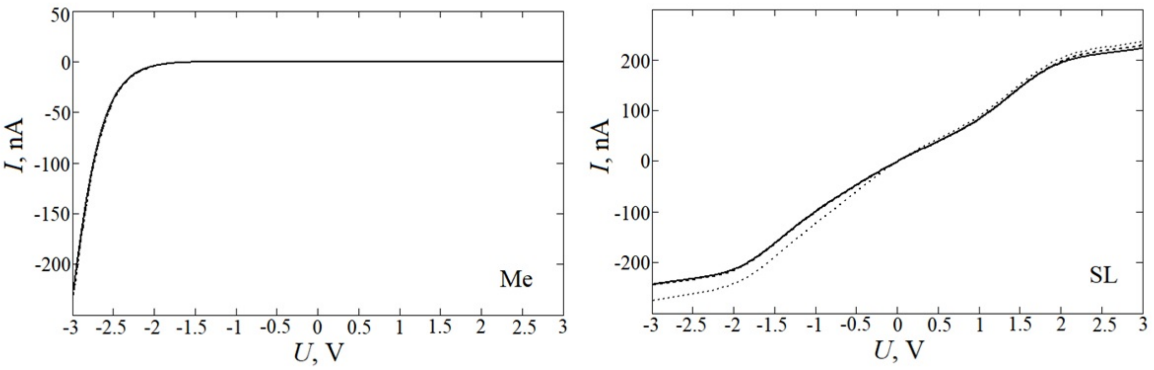

FIG. 2. CVC in the absence of an external field E_0: on the left – contact with a metal; on the right is the contact with a superlattice. The solid line corresponds to the case without impurities, the dotted line – to 1 impurity molecule, the dashed line – to two impurity molecules

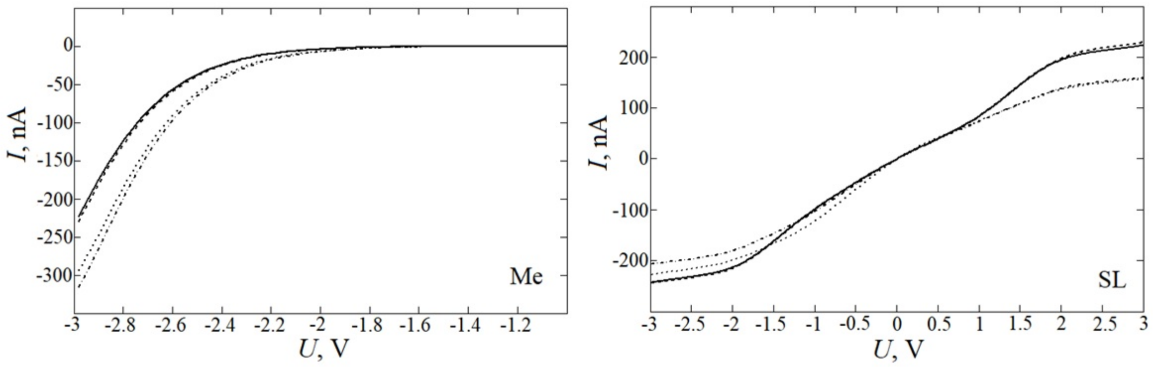

FIG. 3. CVC: on the left – contact with a metal; on the right is the contact with a superlattice. The solid line corresponds to the case without field and impurity, the dashed line – with field and without impurity, the dotted line – without field and with impurity, the dashed point line – with field and impurity

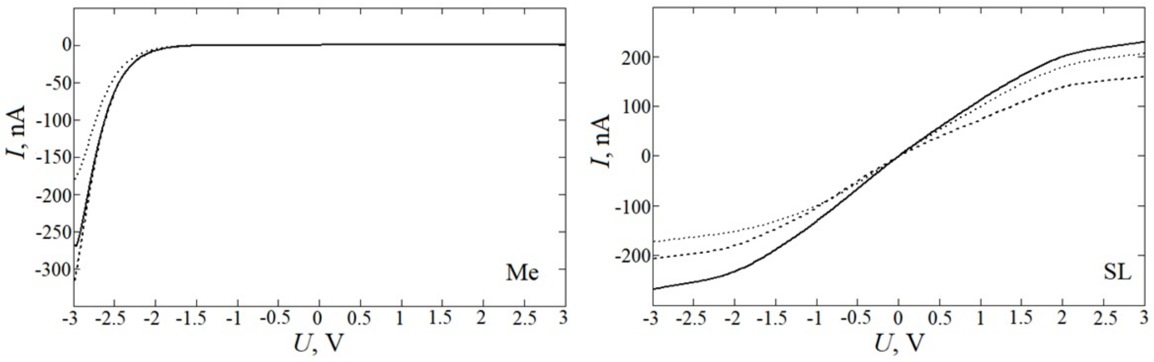

FIG. 4. CVC in the presence of an external field E_0: on the left – contact with a metal; on the right is the contact with a superlattice. The electric field strength: a) $E_0 = 0.5 \cdot 10^7$ V/m; b) $E_0 = 1.0 \cdot 10^7$ V/m; c) $E_0 = 5.0 \cdot 10^7$ V/m

4. Conclusions

In conclusion, we formulate the main outcomes:

1. The method is proposed for calculating the tunneling density of states for the contact of an impurity germanene with a metal and a superlattice with consideration of a strong spin-orbit interaction.

2. The simulation of the interaction of an external electric field with a contact is made.

3. It is shown, that the introduction of an external field increases the response of the system, which makes it more sensitive to the detection of impurities.

Acknowledgement

The reported research was funded by Russian Foundation for Basic Research and the government of Volgograd region, grant No 18-42-343002.

References

[1] Wu B., Zhang X., Huang B., Zhao Y., Cheng C., Chen H. High-performance wireless ammonia gas sensors based on reduced graphene oxide and nano-silver ink hybrid material loaded on a patch antenna. *Sensors*, 2017, **17**, P. 2070.

[2] Li W., Li F., Li H., Su M., Gao M., Li Y., Su D., Zhang X., Song Y. Flexible circuits and soft actuators by printing assembly of graphene. *ACS Appl. Mater. Interfaces*, 2016, **8**, P. 12369–12376.

[3] Lebedev A.A. Growth, study, and device application prospects of graphene on SiC substrates. *Nanosystems: physics chemistry, mathematics*, 2016, **7** (1), P. 30–36.

[4] Karaduman I., Er E., Çelikkan H., Erk N., Acar S. Room-temperature ammonia gas sensor based on reduced graphene oxide nanocomposites decorated by Ag, Au and Pt nanoparticles. *J. Alloys Compd.*, 2017, **722**, P. 569–578.

[5] Su P.G., Yang, L.Y. NH_3 gas sensor based on $Pd/SnO_2/RGO$ ternary composite operated at room-temperature. *Sens. Actuators Chem.*, 2016, **223**, P. 202–208.

[6] Davila M.E., Xian L., Cahangirov S., Rubio A., Le Lay G. Germanene: a novel two-dimensional germanium allotrope akin to graphene and silicene. *New Journal of Physics*, 2014, **16**, P. 095002.

[7] Sheka E.F. Silicene is a phantom material. *Nanosystems: physics, chemistry, mathematics*, 2016, **7**(6), P. 983–1001.

[8] Xia W., Hu W., Liac Z., Yang J. A first-principles study of gas adsorption on germanene. *Phys. Chem. Chem. Phys.*, 2014, **16**, P. 22495.

[9] Konobeeva N.N., Belonenko M.B. Sensitivity of graphene flakes and nanorings to impurities. *Phys. B: Cond. Matter*, 2017, **514**, P. 51–53.

[10] Konobeeva N.N., Belonenko M.B. Conductivity of impurity graphene nanoribbons and gate electric field. *Mod. Phys. Lett. B*, 2017, **31**(2), P. 1750340.

[11] Konobeeva N.N. Modeling of impurity influence on tunneling current in the contact of polymer with quantum dots and metal. *Math. Phys. and Comp. Simul.*, 2017, **20**(5), P. 89–93.

[12] Esaki L. InAs-GaSb superlattices-synthesized narrow- gap semiconductors and semimetals. *Lect. Not. Phys.*, 1980, **133**(2), P. 302–323.

[13] Dohler G.H. Doping superlattices ('n-i-p-i Crystals'). *IEEE J. Quant. Electron.*, 1986, **22**(9), P. 1682–1685.

[14] Ezawa M. A topological insulator and helical zero mode in silicene under an inhomogeneous electric field. *New J. Phys.*, 2012, **14**, P. 033003.

[15] Ezawa M. Monolayer topological insulators: silicene, germanene, and stanene. *J. Phys. Soc. Jpn.*, 2015, **84**, P. 121003.

[16] Kane C.L., Mele E.J. Quantum spin Hall effect in graphene. *Phys. Rev. Lett.*, 2005, **95**, P. 226801.

[17] Levitov L.S. Shitov A.V. Green's functions. Problems and solutions. Fizmatlit, Moscow, 2003, 392 p.

[18] Li H., Gao Zh., Lin W., He W., Li J., Yang Y. Improving the sensitive property of graphene-based gas sensor by illumination and heating. *Sens. Rev.*, 2017, **37**(2), P. 142–146.

NANOSYSTEMS: PHYSICS, CHEMISTRY, MATHEMATICS, 2018, 9 (6), P. 775–782

Anionic redox effect on the electrochemical performance of LLNMC–CeO_2–C nanocomposites

K. A. Kurilenko[1], D. I. Petukhov[1,2,*], A. V. Garshev[1,2], O. A. Shlyakhtin[1]

[1]Department of Chemistry, M.V. Lomonosov Moscow State University, 119991 Moscow, Russia

[2]Department of Materials Sciences, M. V. Lomonosov Moscow State University, 119991 Moscow, Russia

[*]di.petukhov@gmail.com

PACS 61.46+w. 61.72.Ww, 66.10.Ed **DOI 10.17586/2220-8054-2018-9-6-775-782**

$Li[Li_{0.13}Ni_{0.2}Mn_{0.47}Co_{0.2}]O_2$–$CeO_2$ composites have been obtained by coprecipitation with CeO_2 and by coating with ceria followed by coating with carbon film. STEM analysis revealed the formation of 20 – 30 nm ceria particles on the surface of LLNMC grains in all cases. Both carbon-coated LLNMC-CeO_2 composites and carbon-free LLNMC coated with 1 % CeO_2 demonstrated enhanced capacity values that could not be explained by the charge compensation via redox of nickel and cobalt. 5 % CeO_2-coprecipitated sample demonstrated the most intense anomaly in CV at $U = 4.1$ – 4.5 V associated with redox processes in the anionic sublattice of LLNMC and a larger charge transfer resistance compared to other composites. The maximum values of Li^+ diffusion coefficient have been observed for the samples coated with 1 % CeO_2. The different electrochemical behavior of these samples could be explained by the different intensity of anionic redox processes in the samples with different amount of nanocrystalline ceria.

Keywords: Li-ion batteries, cathode materials, coatings, ceria, pyrolytic carbon.

Received: 19 November 2018

1. Introduction

Li(Li,Ni,Co,Mn)O_2 (Li-rich LNMC, LLNMC) is one of the most promising groups of cathode materials for Li-ion batteries. The main advantage of these materials deals with their high specific energy due to the rather high discharge voltage and the enhanced discharge capacity [1,2]. The reasons for the unusually high discharge capacity values have not been fully understood until now. It is proven experimentally that the valence states of Ni, Co and Mn in the hexagonal lattice of LLNMC are 2+, 3+ and 4+, respectively [3]. In order to sustain the electroneutrality, the deintercalation of lithium during charging the battery is accompanied by the increase in valence states of Ni and Co to 4+ while the valence state of Mn remains the same. The highest discharge capacity values that could be achieved in frames of this charge compensation mechanism are 170 – 180 mAh g^{-1} while the experimentally observed values often exceed 200 mAh g^{-1}.

The enhanced capacity of LLNMC compounds with the composition that can be interpreted as $x Li_2MnO_3 \cdot y LiMeO_2$ (Me = Ni,Co,Mn) could be explained in terms of the activation model [4–6]. According to this theory, the deintercalation of lithium at $U > 4.6$ V during the first cycles is accompanied by the electrochemical decomposition of Li_2MnO_3 component and the formation of MnO_2 that attends further cycling. An essential feature of this process, called the activation of cathode materials, is fast decrease of discharge capacity during first several cycles followed by the stabilization of capacity at 220 – 240 mAh g^{-1}. Due to the irreversibility of electrochemical decomposition of Li_2MnO_3, the Coulombic efficiency of first cycles is unusually low. The information on the evolution of gaseous oxygen during the activation process is rather contradictory; several groups did not observe this process during cycling [7]. In order to explain this feature, the alternative model of the activation process was proposed based on the involvement of the anionic sublattice of LLNMC in the redox processes during cycling [8–10]. The formation of the unusual oxygen species in the LLNMC during cycling was recently confirmed experimentally by several spectroscopic methods [7–10].

Recent studies of the LLNMC-based cathode materials with various protecting coatings demonstrated that the better cycling stability of coated materials is often accompanied by the enhancement of these materials' capacity values [11–14]. This enhancement is observed not only at high but also at low discharge rates and after the first cycles. These enhanced capacity values also often exceeded 170 – 180 mAh g^{-1}, which could not be attributed to the increase in valence states of Co and Ni only. Other signs indicating the activation process (fast capacity fade and anomalously low Coulombic efficiency at first cycles) were also not observed in the coated cathode materials. In the case of CeO_2, the capacity enhancement effect was observed not only for the CeO_2-coated LLNMC but also for the CeO_2-doped cathode material when the dopant was introduced during the synthesis of LLNMC [15].

Systematic studies of the relationships between these materials' enhanced electrochemical performance and redox processes in their anionic sublattice have not been performed until now. Taking into account these considerations, the present study deals with the comparative analysis of electrochemical performance of LLNMC-based cathode material doped with CeO_2 by various methods in order to explore the relationships of their enhanced properties with redox processes in the oxygen sublattice of LLNMC. As the amount of CeO_2 that caused the maximum enhancement of electrochemical properties was different for CeO_2-coated and CeO_2-coprecipitated cathode materials, the samples were selected for the analysis that demonstrated the maximum CeO_2 doping effect.

2. Experimental

A synthesis of $Li[Li_{0.13}Ni_{0.2}Mn_{0.47}Co_{0.2}]O_2$ composites with CeO_2 was performed by using $Ni(NO_3)_2\cdot 6H_2O$ (Reachim, analytical grade), $Mn(NO_3)_2\cdot 6H_2O$ ("Alfa Aesar, 98 %+), $Co(NO_3)_2\cdot 6H_2O$ (Reachim, analytical grade), $Ce(NO_3)_3\cdot 6H_2O$ (Reachim, analytical grade), $LiOH\cdot H_2O$ (Acros Organics, extra pure).

In order to obtain $Li[Li_{0.13}Ni_{0.2}Mn_{0.47}Co_{0.2}]O_2$, the mixed hydroxide $Ni_{0.23}Mn_{0.54}Co_{0.23})(OH)_n$ was coprecipitated from 1 M nitrate solution of corresponding salts by 0.2 M LiOH at $T = 50$ °C and pH = 11 under intense stirring. After careful washing by water and acetone, the filtered residue was dried in air at 80 °C overnight. The obtained powder was mixed with corresponding amount of $LiOH\cdot H_2O$ and heated under air at 500 °C (4 hrs) and 850 °C (12 hrs). To introduce 5 wt.% CeO_2 by coprecipitation, corresponding amount of $Ce(NO_3)_3\cdot 6H_2O$ was added to the starting solution. To coat $Li[Li_{0.13}Ni_{0.2}Mn_{0.47}Co_{0.2}]O_2$ with CeO_2 (1 wt.%), LLNMC powder was soaked with cerium nitrate solution in ethyl alcohol, dried and calcined at 600 °C. CeO_2-coated LLNMC was soaked with a polystyrene solution in benzene (polystyrene/LLNMC = 1/6), dried and calcined at 450 °C under argon.

XRD studies were performed by using D/MAX 2500 diffractometer (Rigaku) in the reflection mode with CuKα radiation and Ge monochromator (2Θ range 10 – 90°, step 0.02°, acquisition time 3 s). Analysis of diffraction patterns was performed by using WinXPow software and PDF-2 powder diffraction database.

The morphology and the composition of composite particles were analyzed by the transmission electron microscope Libra 200 MC (Carl Zeiss) (accelerating voltage 200 kV; magnification 30 – 300 kX) equipped with an EDX analysis accessory X-Max 80T detector and Aztec TEM software (Oxford Inc., England). Carbon distribution micrographs have been calculated from the data obtained by means of energy filtered transmission electron microscopy (EFTEM) using three windows method.

The cathode mass containing 85 wt.% of LLNMC–CeO_2–C composite, 10 % of acetylene black and polyvinylidene fluoride (5 wt.%, soluted in N-methyl-2-pyrrolidone) was coated on a stainless steel net (0.05 mm thick), pressed and dried in vacuum ($\sim$1 mbar) at $T = 120$ °C for 8 hrs. The electrochemical measurements were performed in the Teflon 3-electrode cells containing an active electrode, Li counter-electrode and Li reference electrode separated with a porous polypropylene membrane soaked with electrolyte (1 M $LiClO_4$ solution in the mixture of propylene carbonate–dimethoxyethane (7:3 by volume). According to the Fischer titration data by KF 684 (Metrohm, Switserland), the water content in the electrolyte did not exceed 25 ppm.

The galvanostatic curves and cyclic voltammograms (CV) were registered using Potentiostat-Galvanostat 100N Metrohm Autolab (Metrohm, Switzerland) in the potential range 2÷4.6 V at room temperature. The current density during cycling was 20 mAg^{-1}; the potential scan rate during CV measurements was 50 μVs^{-1}.

The data of the electrochemical impedance spectroscopy (EIS) were acquired using Solartron 1255B. The amplitude of the AC signal was 5 mV over a frequency range from 1 MHz to 10 mHz. The obtained hodographs were treated using ZView-Impedance software.

3. Results and discussion

XRD analysis of LLNMC-CeO_2 and LLNMC-CeO_2-C composites obtained by various methods (Fig. 1) revealed the formation of perfectly ordered hexagonal lattice (space group R$\bar{3}$m) in the lack of secondary phases in all cases in study. Significant splitting of 018/110 and 006/012 reflections indicates the low level of ion mixing in all these samples that was not affected by the CeO_2 doping and the interaction with polystyrene pyrolysis byproducts during coating of LLNMC with carbon. The presence of CeO_2 is clearly observed even in the sample with 1 mass% CeO_2.

STEM micrographs demonstrate the formation of 20–30 nm small spherical particles at the surface of 150 – 200 nm sized grains (Fig. 2A-C). STEM-EDX analysis data of these samples show that larger grains consist of LLLNMC while smaller particles at their surface are CeO_2. Several authors observed the formation of thin ceria film during coating [11–16] though in the most cases the coating with CeO_2 by various methods resulted in the formation of individual spherical CeO_2 particles [13–15, 17, 18]. Apart from CeO_2 coating, thin films of pyrolytic

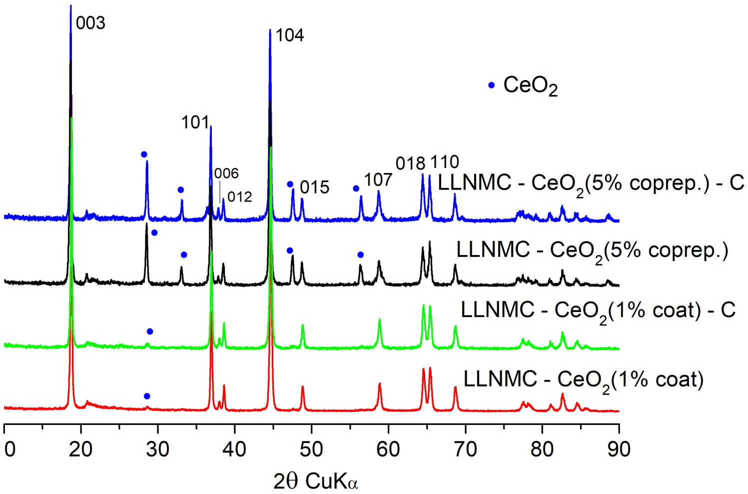

FIG. 1. XRD patterns of $Li[Li_{0.13}Ni_{0.2}Mn_{0.47}Co_{0.2}]O_2$ composites with CeO_2 and carbon

carbon at the surface of LLNMC grains are continuous, as it could be observed in energy filtered TEM (EFTEM) micrographs (Fig. 2D,E).

Analysis of the electrochemical performance of these samples demonstrates that the behavior of the sample doped with 5 % CeO_2 by coprecipitation is different from other ones. First of all, it concerns the absence of peaks at $U = 4.2 - 4.5$ in the anodic branch of cyclic voltammetry curves while these peaks are clearly observed for other samples; however, positions of other peaks corresponding to $Ni^{2+} \leftrightarrow Ni^{4+}$ and $Co^{3+} \leftrightarrow Co^{4+}$ redox processes are almost the same for all these samples (Fig. 3). The introduction of lithium ions into LLNMC lattice during the galvanostatic discharge of 5 %(coprep.) doped sample occurs also at 0.2 – 0.45 V lower potentials than in other samples (Fig. 4). A discharge capacity of this sample (170 mAh g^{-1}) corresponds to the charge compensation mechanism by the change in valence states of nickel and cobalt in the lack of any other anomalies. The characteristic features of CV and galvanostatic curves of LLNMC-based composites are listed in the Table 1.

Instead, discharge capacities of other composites are considerably higher and could not be explained in the framework of this charge compensation model. This discrepancy implies the contribution of alternative redox processes to the charge compensation during lithium intercalation-deintercalation in the course of cycling. Apart from 5 %(coprep.)-doped sample, the CV curves of other three composites display significant anomalies at $U = 4.1 - 4.5$ V both in anodic and cathodic branches of their CV curves (Fig. 3). The most intensive effects are observed for the 5 %(coprep.)-doped sample coated with carbon. According to recent studies, the redox effects in this potential range are associated with the reversible redox processes in the anionic sublattice of LLNMC [2, 19, 20]. In this case, deintercalation of lithium at U > 4.1 V is accompanied by the formation of unusual oxygen species like peroxides O_2^{2-} [7, 8, 10] or the individual holes on the lattice oxygen [9]. The intercalation of lithium back to LLNMC during discharge is accompanied in these cases by the reduction of unusual oxygen species back to the common O^{2-}. Hence, the enhanced capacity values of the both 1 %(coat) and 5 %(coprep.)-C composites could be associated with the switching on the anionic redox processes at $U > 4.1$ during their cycling. The reasons for the oxygen passivation in the 5 %(coprep.) composite sample without carbon coating are not clear now and need more detailed investigation.

The analysis of the electrochemical performance of the composite samples by the electrochemical impe- dance spectroscopy also revealed the difference in their electrochemical behavior (Fig. 5A-D). The equivalent circuit model used to fit the impedance spectra of these samples (Fig. 5E) involved the solution resistance of the cell R_e; the Li^+ migration resistance and the capacity of surface layers R_f and C_f. R_{ct} and C_{ct} are the charge transfer resistance and the double layer capacitance, respectively. Z_w corresponds to the diffusion-controlled Warburg impedance. It is considered that the electric contact between electrochemically-active LLNMC grains is performed by the randomly distributed conducting particles.

The impedance spectra of the samples at $U = 3.5 - 3.8$ V are rather similar and display high and stable charge transfer resistance and surface layer resistance for all samples in study. However, further increase of potential results in the appearance of two separate semicircles for the 5 %(coprep.)-C composite sample that correspond to the charge transfer resistance and the resistance of the surface layer. At $U = 4 - 4.1$ V, this process is accompanied

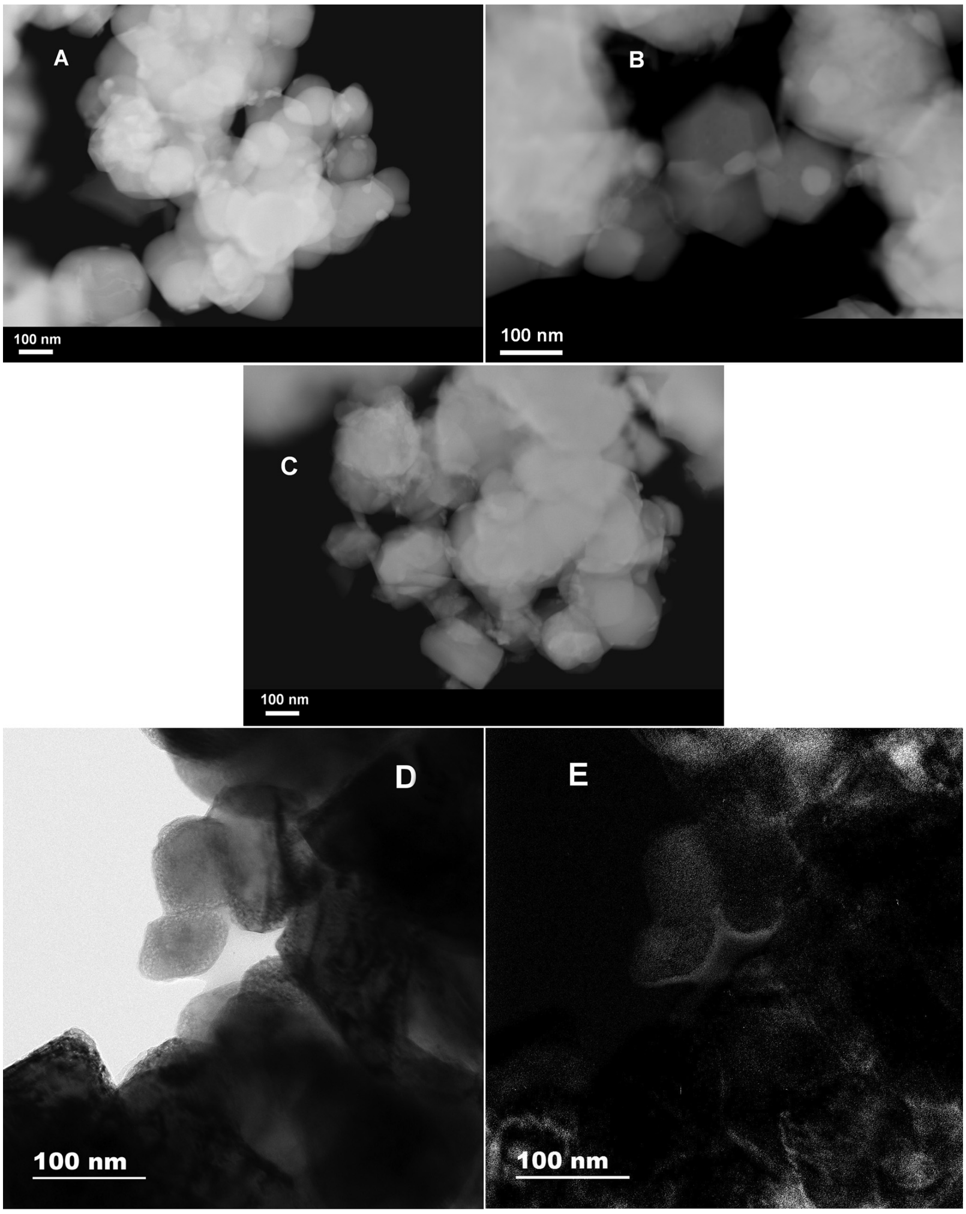

FIG. 2. (A-C) STEM micrographs of various composites: (A) – LLNMC - CeO_2(1 %, coating); (B) –LLNMC –CeO_2 (5 %, coprecipitation); (C) – LLNMC – CeO_2 (1 %, coating) – C; (D, E) – EFTEM micrographs of LLNMC –CeO_2 (5 %, coprecipitation) – C

TABLE 1. Characteristic features of CV and galvanostatic curves of LLNMC-based composites

Sample	Main anodic peak, V	Main cathodic peak, V	Δ (anodic-cathodic), V	Mean discharge potential, V
LLNMC – CeO_2 (1 %, coat)	3.98	3.66	0.32	3.68
LLNMC– CeO_2 (1 %, coat) – C	3.99	3.68	0.31	3.52
LLNMC– CeO_2 (5 %, coprep) – C	4.02	3.71	0.31	3.75
LLNMC – CeO_2 (5 %, coprep)	3.93	3.68	0.25	3.3

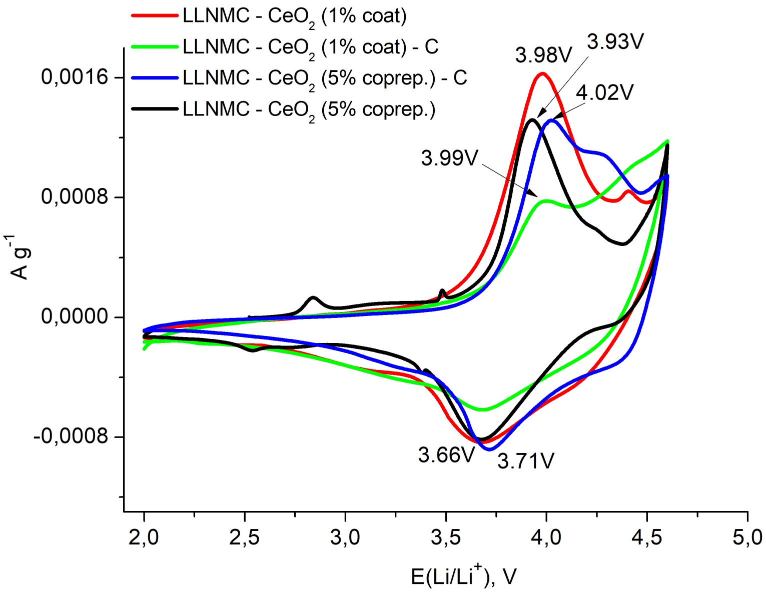

FIG. 3. Cyclic voltammograms at 2-nd cycle of various LLNMC-based composites

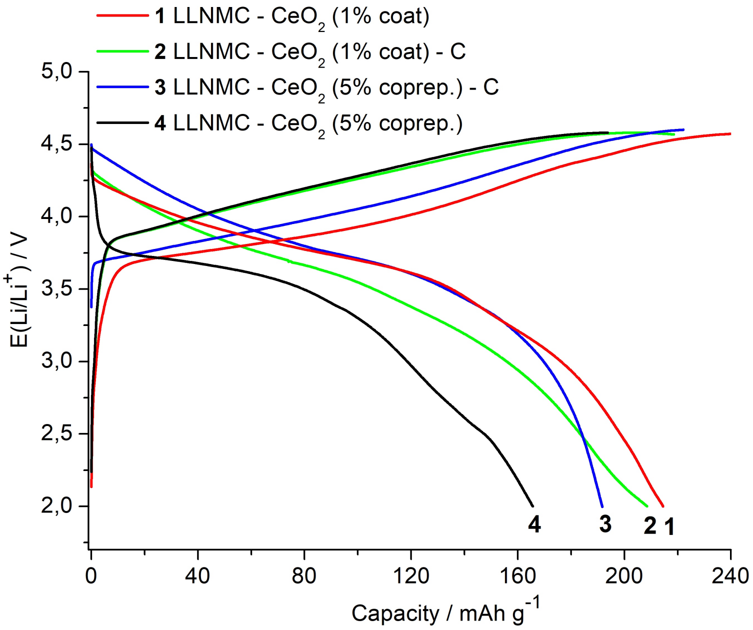

FIG. 4. Galvanostatic charge-discharge curves at 3-rd cycle of various LLNMC-based composites

by a significant increase in the total resistance of charge transfer and the surface layer. These features are absent in the Nyquist plots of other samples. The behavior of samples at $U > 4.1$ V is rather similar; the total charge transfer and surface layer resistance is decreased until $U = 4.3 – 4.4$ V followed by the drastic increase at $U > 4.4$ (4.5) V.

It should be considered, that, according to Fig. 3, the most intense anionic redox processes occurred just in the sample 5 %(coprep.)-C. Taking into account the previous considerations, the unusual increase in resistance of this sample could be also affiliated with anionic redox processes. It was recently found that intense redox processes in the anionic sublattice of LLNMC promote enhanced oxygen mobility during charge-discharge processes. Along with changes in M–O distances due to the changes in the valence state of oxygen, these processes are accompanied also by the reversible and irreversible displacements of transition metals from their permanent positions in the cationic sublattice [2, 21, 22]. These displacements, in turn, result in the complicated lithium transport during

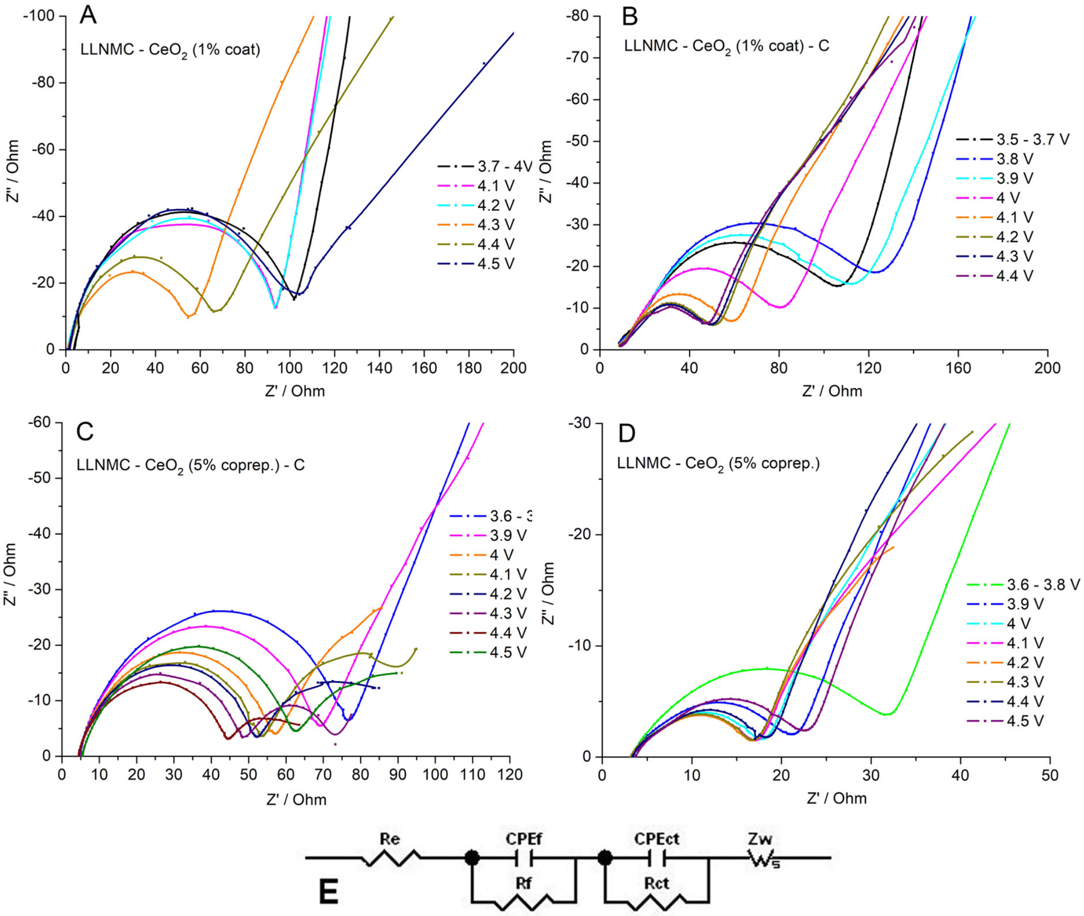

FIG. 5. (A-D) Nyquist plots of LLNMC-CeO$_2$ composites at various charge potentials; (E) The equivalent circuit used for the EI spectra fitting

charge-discharge processes and the additional polarization of electrodes. This polarization makes more difficult the charge transfer, thus increasing the charge transfer resistance. Less intense anionic redox processes in the LLNMC-CeO$_2$ composites obtained by coating and containing smaller amount of ceria could result in the lower cation displacement and, hence, the lower polarization of electrodes caused by this effect.

In order to calculate the apparent Li$^+$ diffusion coefficients from the impedance spectroscopy data, the following relationship was used [21]:

$$D = \left(\frac{V_m}{\sqrt{2} nFs\sigma} \frac{dE}{dx} \right)^2,$$

where σ is Warburg coefficient, Ohm s$^{-0.5}$; F is Faraday constant, 96500 C mol^{-1}; s is the surface of the electrode, cm^2; V_m is specific molar volume and dE/dx is the derivative of the potential versus intercalated/deintercalated lithium content. The Warburg coefficient was calculated from the slope of the effective part of Warburg impedance vs $\omega^{-0.5}$ ($\omega = 2\pi\upsilon$).

As it can be seen (Fig. 6), the lowest values of Li$^+$ diffusion coefficient are observed for the composite LLNMC-5 %(coprep) at almost any potential. It could be affiliated both with the lack of conducting carbon coating, promoting the depolarization of the electrode/electrolyte interface during cycling and with the larger amount of poorly conducting ceria particles among the LLNMC grains. Coating with carbon and the reduction of the amount of ceria result in the significant increase in D for LLNMC-5 %(coprep)-C and, especially, for LLNMC-1 %(coat) and LLNMC-1 %(coat)-composite. However, these enhanced D values are also affiliated with ceria doping, as Li$^+$ diffusion coefficient of the undoped LLNMC obtained at the same synthesis conditions is the lowest in this series [15].

In order to explain this discrepancy, we have to note that the anionic redox could have two different effects on the transport of lithium ions. Along with negative effect briefly described above, the change in the oxygen

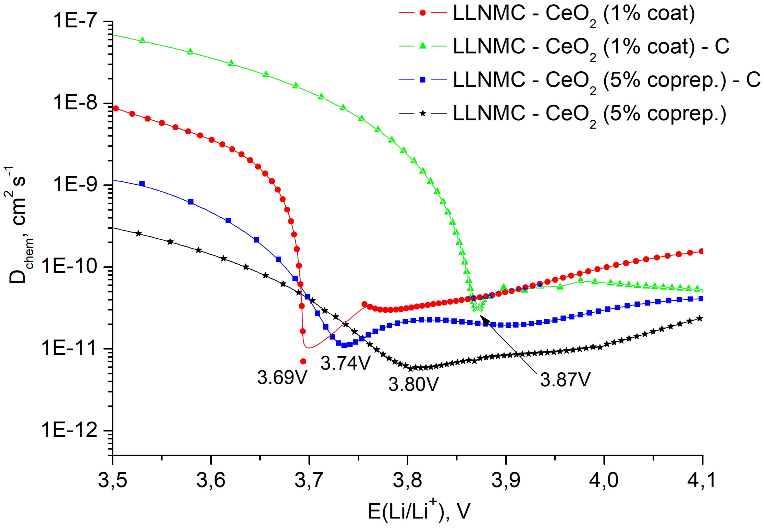

FIG. 6. The variation of Li^+ diffusion coefficients during the charge of various LLNMC-CeO$_2$ composites

valence state at high potentials during cycling and, hence, the appearance of nonbonding O^{n-} species might also promote the faster lithium ion diffusion through the LLNMC lattice [22]. It is known also that ceria is well known catalyst for oxidation processes; this catalytic effect could explain the activation of anionic redox processes in LLNMC by ceria particles even at $U \leq 4.6$ V [14]. Taking into account these features, the higher D values in the coated composites could be explained by the domination of the positive effect of the anionic redox processes on the lithium transport. The higher intensity of these processes at $U = 4.1 - 4.6$ V in LLNMC-5 %(coprep.) than in LLNMC-1 %(coat) samples (Fig. 3) could be accompanied by the more intense cation displacement during cycling and, hence, result in the domination of the negative effect of the anionic redox on the Li^+ transport.

4. Conclusions

Analysis of the LLNMC-CeO$_2$ composites obtained by different methods shows that the synthesis technique has little or no effect on their phase composition and morphology. In all cases in study the composites consisted of 200 nm LLNMC grains covered with 20 – 30 nm ceria particles. Coating of these samples with pyrolytic carbon results in the formation of nanocrystalline carbon film at the surface of composite particles. The electrochemical performance of carbon-free LLNMC doped with 5 % CeO$_2$ by coprecipitation is different from other ones and close to the electrochemical behavior of common undoped LLNMC. Instead, the enhanced values of discharge capacity of other composites could not be explained by the charge compensation via redox processes in the cationic sublattice of LLNMC, as in common LNMC samples. The CV curves of these samples indicate the significant contribution of anionic redox processes at $U = 4.1 - 4.6$ V to the charge compensation mechanism during their cycling.

The higher charge transfer and surface layer resistance of the 5 %(coprep)-C composite demonstrate that the most intense anionic redox-related anomalies in its CV curve could be associated with significant cation displacement observed by several authors during intense oxygen redox processes. However, the intensification of Li diffusion processes in the 1 % ceria-coated samples with smaller but significant contribution of anionic redox during cycling could be also affiliated with anionic redox effects due to the formation of non-bonding oxygen species in the LLNMC lattice. Hence, the majority of ceria-related features of the electrochemical behavior of these composites could be explained by the various effects of redox processes in the anionic sublattice of LLNMC during cycling. The appearance of these phenomena at $U \leq 4.6$ V is unusual for LLNMC and could be affiliated with the catalytic effect of the nanocrystalline ceria particles on the redox processes in the oxygen sublattice of LLNMC.

Acknowledgement

The work is partially supported by the individual grant 16-33-60195 (D. I. Petukhov) of the Russian Foundation for Basic Research. The authors are thankful to the M. V. Lomonosov Moscow State University Program of Development for the partial support of instrumental studies.

References

[1] Li W., Song B., Manthiram A. High-voltage positive electrode materials for lithium-ion batteries. *Chem. Soc. Rev.*, 2017, **46**, P. 3006—3059.

[2] Erickson E.M., Schipper F., Penki T.R., Shin J.Y., Erk C., Chesneau F.F., Markovsky B., Aurbach D. Review—Recent Advances and Remaining Challenges for Lithium Ion Battery Cathodes. II. Lithium-Rich, $xLi_2MnO_3 \cdot (1-x)LiNi_aCo_bMn_cO_2$. *J. Electrochem. Soc.*, 2017, **164**, P. A6341–A6348.

[3] Koga H., Croguennec L., Menetrier M., Mannessiez P., Weill F., Delmas C., Belin S. Operando Xray Absorption Study of the Redox Processes Involved upon Cycling of the Li-Rich Layered Oxide $Li_{1.20}Mn_{0.54}Co_{0.13}Ni_{0.13}O_2$ in Li Ion Batteries, *J. Phys. Chem. C*, 2014, **118**, P. 5700–5709.

[4] Lu Z., Dahn J.R. Understanding the Anomalous Capacity of $Li/Li[Ni_xLi_{(1/3-2x/3)}Mn_{(2/3-x/3)}]O_2$ Cells Using *In Situ* X-Ray Diffraction and Electrochemical Studies, *J. Electrochem. Soc.*, 2002, **149**, P. A815-A822.

[5] Johnson C.S., Kim J-S., Lefief C., Li N., Thackeray M.M. The significance of the Li_2MnO_3 component in 'composite' $xLi_2MnO_3(1-x)LiMn_{0.5}Ni_{0.5}O_2$ electrodes, *Electrochem. Comm.*, 2004, **6**, P. 1085–1091.

[6] Thackeray M.M. Kang S.-H., Johnson C.S. Vaughey J.T., Benedek R., Hackney S.A. Li_2MnO_3-stabilized $LiMO_2$ (M = Mn, Ni, Co) electrodes for lithium-ion batteries. *J. Mater. Chem.*, 2007, **17**, P. 3112–3125.

[7] Sathiya M., Rousse G., Ramesha K., Laisa C.P., Vezin H., Sougrati M.T., Doublet M-L., Foix D., Gonbeau D., Walker W., Prakash A.S., Ben Hassine M., Dupont L., Tarascon J-M. Reversible anionic redox chemistry in high-capacity layered-oxide electrodes. *Nature Mater.*, 2013, **12**, P. 827–835.

[8] Oishi M., Yogi C., Watanabe I., Ohta T., Orikasa Y., Uchimoto Y., Ogumi Z. Direct observation of reversible charge compensation by oxygen ion in Li-rich manganese layered oxide positive electrode material, $Li_{1.16}Ni_{0.15}Co_{0.19}Mn_{0.50}O_2$. *J. Power Sources*, 2015, **276**, P. 89–94.

[9] Luo K., Roberts M. R., Hao R., Guerrini N., Pickup D.M., Liu Y.-S., Edstrom K., Guo J., Chadwick A.V., Duda L.C., Bruce P.G., Charge-compensation in 3d-transition-metaloxide intercalation cathodes through the generation of localized electron holes on oxygen. *Nature Chem.*, 2016, 8, P. 684–691.

[10] Saubanere M., McCalla E., Tarascon J.-M., Doublet M.-L. The Intriguiging Question of Anionic Redox in High-Energy Density Cathodes for Li-ion Batteries. *Energy Environ. Sci.*, 2016, **9**, P. 984–991.

[11] He F., Wang X., Du C., Baker A.P., Wu J, Zhang X. The effect of samaria doped ceria coating on the performance of $Li_{1.2}Ni_{0.13}Co_{0.13}Mn_{0.54}O_2$ cathode material for lithium-ion battery. *Electrochim. Acta*, 2015, **153**, P. 484–491.

[12] Li G.R., Feng X., Ding Y., Ye S.H., Gao X.P. AlF_3-coated $Li(Li_{0.17}Ni_{0.25}Mn_{0.58})O_2$ as cathode material for Li-ion batteries. *Electrochim. Acta*, 2012, **78**, P. 308–315.

[13] Liu K., Yang G-L., Dong Y., Shi T., Chen L. Enhanced cycling stability and rate performance of $Li[Ni_{0.5}Co_{0.2}Mn_{0.3}]O_2$ by CeO_2 coating at high cut-off voltage. *J. Power Sources*, 2015, **281**, P. 370–377.

[14] Kurilenko K.A., Shlyakhtin O.A., Petukhov D.I., Garshev A.V. Catalytic effect of nanostructured CeO_2 coating on the electrochemical performance of $Li(Li,Ni,Mn,Co)O_2$. *Solid State Ionics*, 2018, **324**, P. 59–64.

[15] Kurilenko K.A., Shlyakhtin O.A., Petukhov D.I., Garshev A.V. Effect of CeO_2 coprecipitation on the electrochemical performance of $Li(Li,Ni,Mn,Co)O_2$-CeO_2-C composite cathode materials, *J. Power Sources*, 2017, **354**, P. 189–199.

[16] Wu F., Wang M., Su Y., Bao L., Chen S. Surface of $LiCo_{1/3}Ni_{1/3}Mn_{1/3}O_2$ modified by CeO_2-coating, *Electrochim. Acta*, 2009, **54**, P. 6803–6807.

[17] Yuan W., Zhang H.Z., Liu Q., Li G.R., Gao X.P. Surface modification of $Li(Li_{0.17}Ni_{0.2}Co_{0.05}Mn_{0.58})O_2$ with CeO_2 as cathode material for Li-ion batteries. *Electrochim. Acta*, 2014, **135**, P. 199–207.

[18] Xu Y., Li X., Wang Z., Guo H., Peng W., Pan W. The enhanced high cut-off voltage electrochemical performances of $LiNi_{0.5}Co_{0.2}Mn_{0.3}O_2$ by the CeO_2 modification, *Electrochim. Acta*, 2016, **219**, P. 49–60.

[19] Assat G., Tarascon J.-M. Fundamental understanding and practical challenges of anionic redox activity in Li-ion batteries. *Nature Energy*, 2018, **3**, P. 373–386.

[20] Xu J., Sun M., Qiao R., Renfrew S.E., Ma L., Wu T., Hwang S., Nordlund D., Su D, Amine K., Lu J, McCloskey B.D., Yang W., Tong W., Elucidating anionic oxygen activity in lithium-rich layered oxides, *Nature Comm.*, 2018, **9**, P. 947.

[21] Levi M.D., Salitra G., Markovsky B., Teller H., Aurbach D., Heider U., Heiderb L. Solid-State Electrochemical Kinetics of Li-Ion Intercalation into $Li_{1-2x}CoO_2$: Simultaneous Application of Electroanalytical Techniques SSCV, PITT, and EIS. *J. Electrochem. Soc.*, 1999, **146**, P. 1279–1289.

[22] Zhao S., Sun B., Yan K., Zhang J., Wang C., Wang G. Aegis of Lithium-Rich Cathode Materials via Heterostructured $LiAlF_4$ Coating for High-Performance Lithium-Ion Batteries. *ACS Appl. Mater. Interfaces*, 2018, **10**, P. 33260–33268.

NANOSYSTEMS: PHYSICS, CHEMISTRY, MATHEMATICS, 2018, 9 (6), P. 783–788

Spectral-kinetic properties of LaF_3 nanoparticles doped with Ce^{3+} and Sm^{3+} ions after microwave treatment and in core-shell structure

E. I. Madirov*, E. V. Lukinova, A. S. Nizamutdinov, M. S. Pudovkin, S. L. Korableva, V. V. Semashko

Kazan Federal University, Institute of Physics, 18, Kremlevskaja str., Kazan, 420008, Russia

*ed.madirov@gmail.com

PACS 81.07.Bc, 76.30.Kg **DOI 10.17586/2220-8054-2018-9-6-783-788**

Crystalline LaF_3:Sm^{3+} and LaF_3:Ce^{3+} nanoparticles were fabricated via a co-precipitation method. The obtained nanoparticles were 15 – 20 nm and had good crystallinity. Spectral-kinetic properties of crystalline LaF_3 nanoparticles activated with 5 % Sm^{3+} and 12 % Ce^{3+} ions were studied. Various duration of the microwave treatment as well as core-shell structure were studied as possible ways to control quenching in the nanoparticles. In case of the LaF_3:Sm^{3+} nanoparticles, the additional microwave treatment increased the average luminescence lifetime by 6 % and addition of the LaF_3 shell increased it by 18 %. In case of the LaF_3:Ce^{3+} sample, microwave treatment increased the average lifetime by up to 20 %. The observed effects of varying the synthetic conditions and composite core-shell structure on luminescence properties of nanoparticles provide a means to manage the energy loss in the nanoparticles due to the quenching factors.

Keywords: nanoparticle, rare-earth ions, fluoride, samarium, cerium.

Received: 20 October 2018

Revised: 19 November 2018

1. Introduction

Currently, nanoparticles are the center of attention of the research from completely different fields of science [1, 2]. However, due to the size of nanoparticles their properties can significantly differ from the bulk materials of the same compound. A wide variety of chemical elements are used to produce nanoparticles [3, 4]. The fluoride materials stand out amongst others because of their wide energy gap and low phonon energy usually observed in their crystal lattices. LaF_3 is an interesting example of a fluoride that has been used as a host crystal for lanthanide-doped phosphors. Rare-earth metals are often utilized as activators in fluoride nanoparticles. Having sharp spectral lines, high photochemical stability and long fluorescence decay times, they are convenient material for light-emitting devices. Thus, depending on the excitation and luminescence spectral ranges of action, nanoparticles have a significant potential as up-conversion materials, photosensitizers, etc.

Medicine is another major possibility to utilize the unique properties of nanoparticles [5–7]. Photodynamic therapy (PTD) is a developing method of cancer treatment which has some advantages over conventional methods of cancer treatment like radiotherapy and chemotherapy such as lower impact on healthy organs. However, because dyes used in the PDT require visible range light for excitation, currently it is only possible to apply PDT to surface cancers. However, it can be changed with the combination of PDT agents and scintillator nanoparticles that provide down-conversion from x-ray to visible range [8]. Nanoparticles that could be used in PDT should meet certain requirements such as low size (10s of nm), low toxicity, stable chemical composition and high down-conversion efficiency [9]. The fluoride materials meet most of these requirements and finding the right synthetic conditions might possibly provide desired optical properties [5].

Thus, a detailed study of the processes in nanoparticles, especially research into the energy transfer and decay processes as well as the study of the quenching mechanisms is required. The ability to control the transfer rates from a donor to an acceptor can significantly broaden the possible applications of nanoparticles.

Some work has already been done to understand the energy transfer and quenching of the luminescence mechanisms in the Sm^{3+}-doped fluoride nanoparticles. For example, the role of the core-shell structure has been partially studied in the work by Anees A. Ansari [10]. In this paper, the effect LaF_3 or LaF_3@SiO_2 shell has on the optical properties of the LaF_3:Sm^{3+} nanoparticles was studied using excitation and emission spectra. It was noted that “a remarkable intensity enhancement is recorded in the spectrum of core/shell-NPs in respect to core-NPs” [10]. However, this approach has some drawbacks. An additional layer of the undoped material increases the distance between luminescent ions and photosensitizers on the surface, thus decreasing the possible nonradiative energy transfer between the two. In addition, Juhong Miao et al. also studied the effect that Sm^{3+} concentration has on the luminescent properties of the nanoparticles in the paper [11]. Luminescence excitation, emission spectra as well as luminescence decay kinetics were used to study the concentration effects. It was demonstrated that by changing the percentage of the Sm^{3+} ions, one could significantly alter both luminescence intensity and decay lifetime. The results show both luminescence intensity and luminescence decay time reach a maximum at a Sm^{3+} concentration of $\sim$ 5 mol.%. Further increasing the concentration of Sm^{3+} leads to major concentration quenching with a more than a 2-fold reduction of the luminescence intensity and decay time decreasing from 180 μs to 20 μs.

The nanoparticles doped with Ce^{3+} have also been studied to some extent. Pushpal Ghosh et al. studied the effect of ultrasonication and annealing on the optical properties of Ce^{3+}-doped nanoparticles [12]. Xiaoqing Zhang et al. discussed the influence of the synthetic temperatures and stoichiometry of reactants on the shape of the nanoparticles and decay lifetimes of the Ce^{3+} ions in the fluoride nanoparticles in the work [9]. In addition to this, there are works aimed at implementation of Ce^{3+}-doped nanoparticles with PDT agents [8, 14]. Previously, it was shown that a nonradiative energy transfer between lanthanide – doped fluoride nanoparticles and photosensitizers is possible [8]. It was also demonstrated that the energy transfer from nanoparticles significantly enhances luminescence of the photosensitizers. To do so, the emission of photosensitizer conjugates and doped and undoped nanoparticles was compared under 254 nm excitation. The results showed that the luminescence intensity of the conjugates of photosensitizer and doped nanoparticles was 15 – 20 % higher that the intensity of the undoped ones. In paper [14], the authors have shown that LaF_3:Ce^{3+}/DMSO nanoparticles can be utilized as an intracellular light source for photodynamic activation. Also there is data suggesting that adding these nanoparticles amplifies the effect of the Protoporphyrin IX.

In this paper, we report on attempt to study the following methods of luminescence characteristics manipulation of nanoparticles: the variation of synthesis conditions and composite structure.

2. Experimental details

2.1. Sample preparation

Crystalline LaF_3:Sm^{3+} (C_{Sm} = at. 5 %) and LaF_3:Ce^{3+} (C_{Ce} = at. 12 %) nanoparticles were fabricated via co-precipitation method described earlier [15–19] at neutral pH. The LaF_3:Sm^{3+} samples were used to study the effect of the hydrothermal treatment (60 minutes exposure in the microwave oven) and core-shell composite structure on the spectral-kinetic properties of the nanoparticles. To create undoped LaF_3 shell, LaF_3:Sm^{3+} nanoparticles were dispersed in distilled water by sonication. Then 1.2 mmol of NH_4F was added into suspension and the solution was heated to 50 °C. After stirring for 15 min the 0.4 mmol of $La(NO_3)_3$ was introduced into the solutions. The prepared suspension was placed into the microwave oven for 60 minutes. According to previous work [10] this approach allows to obtain samples with an undoped shell over a doped core nanoparticle.

The LaF_3:Ce^{3+} samples were used to study the effect of the duration of the hydrothermal treatment on the spectral-kinetic properties of the nanoparticles. Three samples were collected: the first one was not exposed to any additional microwave radiation, the second one was exposed for 30 minutes and the third one was exposed for 180 minutes.

After synthesis, every sample was washed with distillate water and separated from the suspension by centrifugation and dried at 60 °C for 12 h.

2.2. Sample characterisation

The TEM images of the obtained nanoparticles are presented in Fig. 1. It can be seen that the nanoparticles are 15-20 nm in average and have elliptical shape. In Fig. 1(b,d), it is explicitly shown that nanoparticles have well-defined atomic layers with distance between them about 0.33 nm that proves that particles have high crystallinity. This result is in good agreement with previous research, where the observed d-spacing was 0.31 nm [10].

To determine optical properties of the obtained nanoparticles, photoluminescence emission spectra and decay kinetics were recorded. A StellarNet EPP2000 spectrometer was used to detect the emission spectra. Decay kinetics were recorded with a MDR-23 monochromator and a FEU-100 photomultiplier tube.

The 405 nm emission of the second harmonic of the LT-2211 Ti:Sapphire laser was used for the excitation of the LaF_3:Sm^{3+} samples, whereas the 266 nm emission of the 4th harmonic of a YAG:Nd solid-state laser was used as an excitation for the LaF_3:Ce^{3+} samples.

3. Results and discussion

The luminescence spectra and decay kinetics of all nanoparticles were recorded. Whereas the luminescence spectra were in line with the spectra of Sm^{3+} or Ce^{3+} ions in single crystals [20, 21] respectively, the decay kinetics differed significantly, showing non-mono exponential behavior.

The normalized luminescence spectra of the studied LaF_3:Sm^{3+} nanoparticles are presented in Fig. 2(a, b, c). These spectra contain well known lines of transitions from $^4G_{5/2}$ state to ^6H_J terms. It should be noted that

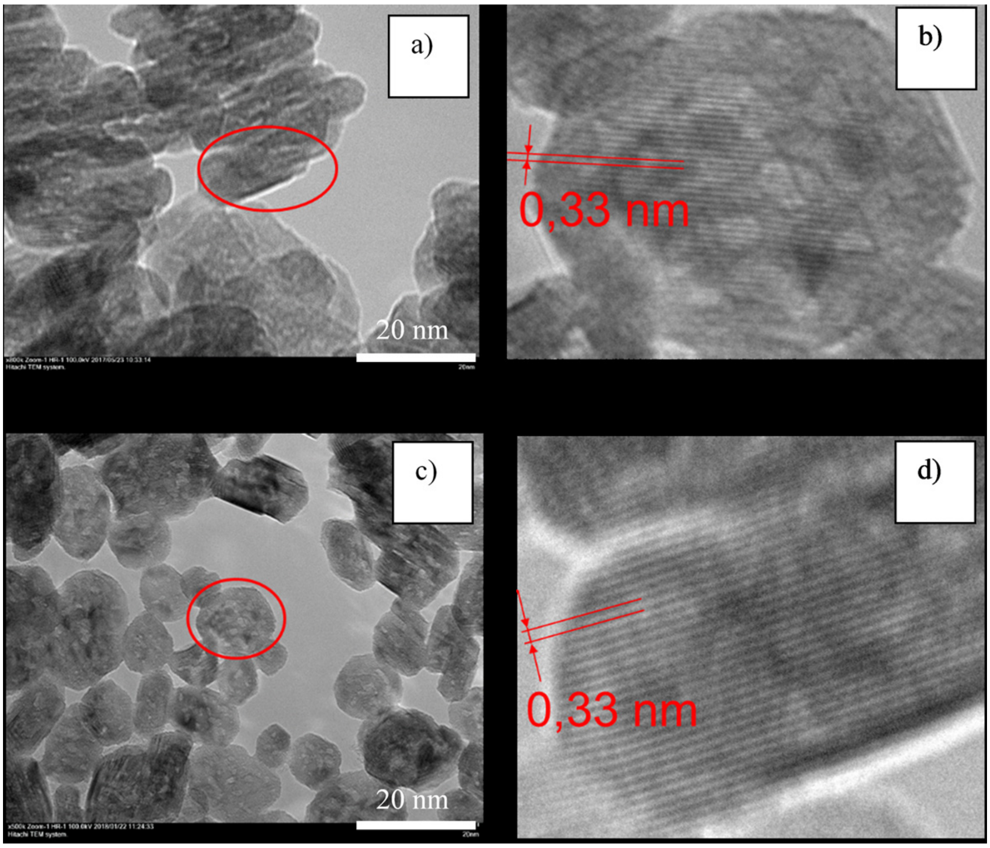

FIG. 1. TEM images of LaF$_3$:Sm^{3+} (5 %) nanoparticles (a), close-up of LaF$_3$:Sm^{3+} (5 %) nanoparticles (b), of LaF$_3$:Ce^{3+} (5 %) nanoparticles (c), close-up of LaF$_3$:Ce^{3+} (5 %) nanoparticles (d)

neither the microwave treatment nor the addition of the LaF$_3$ shell alters the position of the peaks of the emission spectra, which proves that the local environment of the Sm^{3+} ions remains unaltered and there is no change of crystal structure.

The normalized luminescence spectra of the studied LaF$_3$:Ce^{3+} nanoparticles are presented in Fig. 2(d, e, f). These spectra contain the well-known lines of 4f – 5d transitions in Ce^{3+} ions. As in the case of the Sm^{3+}-doped nanoparticles, neither 30 minute nor 180 minute microwave treatment changes the position of the peaks of the emission spectra, thus proving that the local environment of the Ce^{3+} ions is identical in all samples and the crystal structure does not change.

Changes in the preparation method had a tangible effect on luminescence decay of the samples. The decay curves of all samples of LaF$_3$:Sm^{3+} nanoparticles are presented in Fig. 3(a, b, c) and the decay curves of the LaF$_3$:Ce^{3+} nanoparticles can be seen in Fig. 3(d, e, f). All samples have exhibited non-exponential decay, which is common for nanoparticles due to large surface to volume ratio and significant amount of surface perturbed sites [22] in case of LaF$_3$:Sm^{3+}, which empirically can be divided into fast and slow components. In case of LaF$_3$:Ce^{3+} nanoparticles, it is believed that this feature is determined by regular sites and perturbed sites relaxation respectively [23].

To determine the slow and fast components of the luminescence decay time the bi-exponential fitting was used:

$$y = y_0 + A_1 \exp\left(-t/\tau_1\right) + A_2 \exp\left(-t/\tau_2\right). \tag{1}$$

In addition, we have determined the average lifetime of luminescence since bi-exponential fitting is only the assumption and could differ from real picture of the processes in nanoparticles. The average time was found using the following formula [24]:

$$t_{avg} = \frac{\int tI\left(t\right)dt}{\int I\left(t\right)dt}. \tag{2}$$

The results are presented in the Table 1.

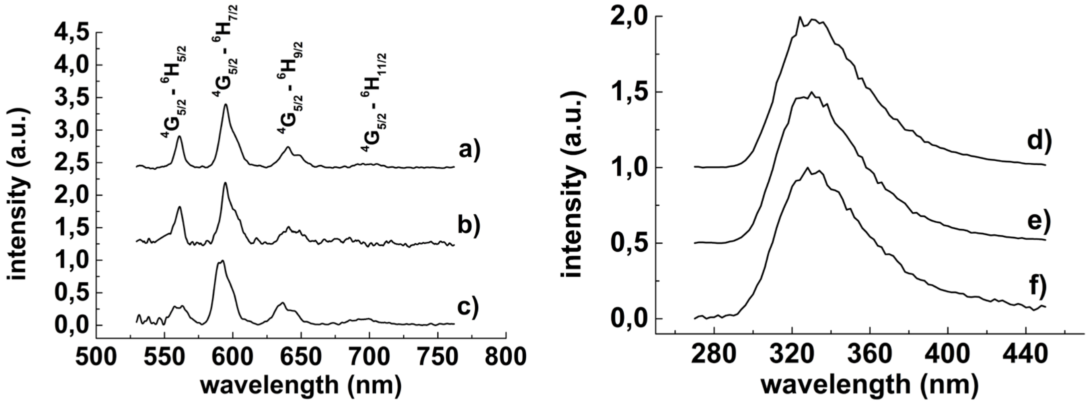

FIG. 2. PL emission spectra of the LaF$_3$:Sm^{3+} 5 % (a); LaF$_3$:Sm^{3+} 5 % with 60 min microwave exposure (b); LaF$_3$:Sm^{3+} 5 % @LaF$_3$ core-shell nanoparticles under 405 nm excitation (c); LaF$_3$:Ce^{3+} + 12 % (d); LaF$_3$:Ce^{3+} 12% with 30 min microwave exposure; f) LaF$_3$:Ce^{3+} 12% with 180 min microwave exposure nanoparticles under 266 nm excitation (e)

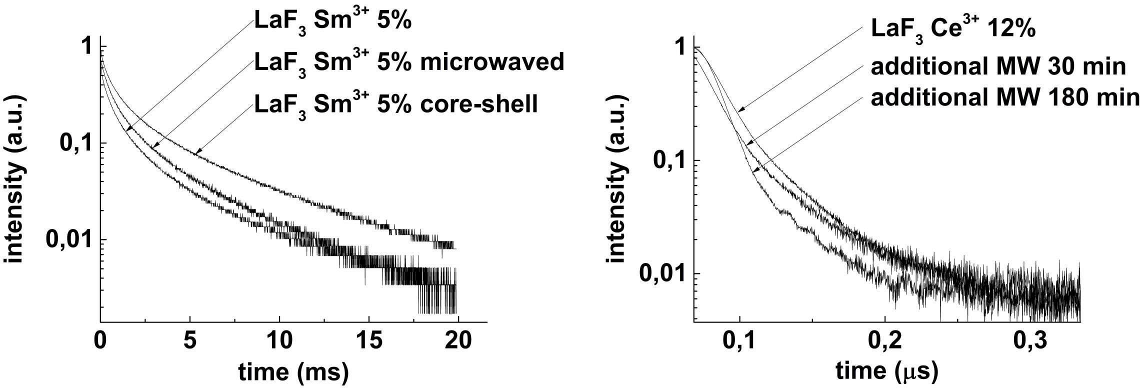

FIG. 3. PL decay kinetics of the 591 nm line of the LaF$_3$:Sm^{3+} nanoparticles under 405 nm excitation (a); 330 nm line of the LaF$_3$:Ce^{3+} nanoparticles under 266 nm excitation (b)

TABLE 1. Luminescence lifetimes of the 591 nm luminescence line of the LaF$_3$:Sm^{3+} nanoparticles under 405 nm excitation

	LaF$_3$ Sm^{3+} 5 %	LaF$_3$ Sm^{3+} 5 % microwaved	LaF$_3$ Sm^{3+} 5 % core-shell
Lifetime of the slow component τ_1, ms	3.3 ± 0.1	3.3 ± 0.1	4.3 ± 0.1
Lifetime of the fast component τ_2, ms	0.4 ± 0.1	0.7 ± 0.1	0.8 ± 0.1
Average lifetime, ms	1.7 ± 0.5	1.8 ± 0.5	2.0 ± 0.5

The results in the Table 1 allow one to draw the following conclusions: 1) the existence of the un-doped LaF$_3$ shell increases the decay times, apparently due to covering impurity sites at the surface thus eliminating surface quenching factors; 2) the microwave treatment of nanoparticles, on the contrary, has not introduced any significant effect in implemented conditions, which can speak for deficient fluorination or exposition during reaction.

Table 2 shows that both fast and slow components of the Ce^{3+} decay curves exhibit changes with synthesis procedure. The decay time of the slow component associated with the perturbed sites increases with the MW exposition time whereas lifetime of the fast component decreases though not that significantly. As well as this, the average lifetime shows general increase with the MW exposure time. The results of the approximations demonstrate that the perturbed sites are somehow more sensitive to the synthesis conditions.

TABLE 2. Luminescence lifetimes of the 330 nm line of the LaF_3:Ce^{3+} nanoparticles under 266 nm excitation

	LaF_3 Ce^{3+} 12 % neutral pH	additional MW 30 min	additional MW 180 min
Lifetime of the slowcomponent τ_1, ns	36.6 ± 0.5	38.2 ± 0.5	43.1 ± 0.5
Lifetime of the fast component τ_2, ns	9.8 ± 0.5	10.1 ± 0.5	7.9 ± 0.5
Average lifetime, ns	29 ± 1	33 ± 1	35 ± 1

4. Conclusion

Series of LaF_3:Sm^{3+} and LaF_3:Ce^{3+} crystalline nanoparticles were synthesized by a co-precipitation method. The size and morphology of the obtained nanoparticles were controlled using transmission electron microscopy. All of the particles were approximately 15 – 20 nm in size and had high crystallinity. The effects of the microwave treatment and additional undoped LaF_3 shell on the luminescent features were studied using LaF_3:Sm^{3+} nanoparticles. Modification of the pH and additional microwave treatment were carried out during the synthesis of the LaF_3:Ce^{3+} nanoparticles. This also caused changes in the luminescence properties of the nanocrystals.

The spectral and kinetic properties of all of the nanoparticles were studied. Luminescence spectra as well as luminescence decay kinetics under 266 nm excitation in case of LaF_3:Ce^{3+} nanoparticles and under 405 nm excitation in case of the LaF_3:Sm^{3+} nanoparticles were recorded and decay times were estimated.

It was determined that the microwave exposure of the nanoparticles and addition of the LaF_3 shell lessens the effect the quenching factors have on the luminescence decay time and increases the luminescence lifetime of the LaF_3 nanoparticles doped with the Ce^{3+} or Sm^{3+} ions. The results of the experiments allowed us to obtain the following quantitative assessments: in case of the LaF_3 nanoparticles doped with Sm^{3+} ions the additional microwave treatment increased the average lifetime by 6 %, whereas addition of the LaF_3 shell increased it by almost 18%; in case of the LaF_3 nanoparticles doped with Ce^{3+} ions, the 30 minute microwave treatment increased the average lifetime by 13 % and 180 minute treatment increased it by 20 %. Thus, we have proposed the approach to lessen the losses of excitation in LaF_3:Ce^{3+} and LaF_3:Sm^{3+} nanoparticles originated from quenching factors characteristic to nanosized crystals.

Acknowledgements

Studies were carried out in the frame of the state assignment in the sphere of scientific activities (Projects No. 3.1156.2017/4.6 and No. 3.5835.2017/6.7). Authors are grateful to specialists of Interdisciplinary Center of Analytical Microscopy of Kazan Federal University for microscopy studies.

References

[1] Kuznetsov S.V., Morozov O.A., et al. $Ca_{1-x-y}Yb_xPr_yF_{2+x+y}$ solid solution powders as a promising materials for crystalline silicon solar energetics. *Nanosystems: Physics, Chemistry, Mathematic*, 2018, **9** (2), P. 259–265.

[2] Fedorov P.P., et al. Nanofluorides. *Journal of Fluorine Chemistry*, 2011, **132** (12), P. 1012–1039.

[3] Shukla N., Saxena A.,et al. Magnetic silica nanoparticles for the removal of Pb^{2+} from water. *Nanosystems: Physics, Chemistry, Mathematics*, 2016, **7** (3), P. 488–491.

[4] Garanina A.S., et al. New superparamagnetic fluorescent Fe@C–$C_5ON_2H_{10}$-Alexa Fluor 647 nanoparticles for biological applications. *Nanosystems: Physics, Chemistry, Mathematics*, 2018, **9** (1), P. 120–122.

[5] Binnemans Koen. Lanthanide-based luminescent hybrid materials. *Chemical reviews*, 2009, **109** (9), P. 4283–4374.

[6] Zhang Q.Y., Huang X.Y. Recent progress in quantum cutting phosphors. *Progress in materials Science*, 2010, **55** (5), P. 353–427.

[7] Kozlov D.A., et al. The microstructure effect on the Au/TiO_2 and Ag/TiO_2 nanocomposites photocatalytic activity. *Nanosystems: Physics, Chemistry, Mathematics*, 2018, **9** (2), P. 266–278.

[8] Bekah, Devesh, et al. Synthesis and characterization of biologically stable, doped LaF_3 nanoparticles co-conjugated to PEG and photosensitizers. *Journal of Photochemistry and Photobiology A: Chemistry*, 2016, **329**, P. 26–34.

[9] Chatterjee, Dev Kumar, Li Shan Fong, Yong Zhang. Nanoparticles in photodynamic therapy: an emerging paradigm. *Advanced drug delivery reviews*, 2008, **60** (15), P. 1627–1637.

[10] Ansari A.A. Effect of Surface Functionalization on Structural and Optical Properties of Luminescent LaF_3: Sm Nanoparticles. *Journal of nanoscience and nanotechnology*, 2018, **18** (2), P. 1043–1050.

[11] Miao Juhong, et al. Preparation, characterization and photoluminescence of Sm^{3+} doped $NaGdF_4$ nanoparticles. *Journal of Alloys and Compounds*, 2015, **636**, P. 8–11.

[12] Ghosh Pushpal, Arik Kar, Amitava Patra. Structural Changes and Spectroscopic Properties of Ce^{3+}-Ion-Doped Sodium Yttrium Fluoride Nanocrystals: Influences of Sonication and Temperature. *The Journal of Physical Chemistry C*, 2009, **114** (2), P. 715–722.

[13] Zhang Xiaoqing, et al. $NaGdF_4$: Ce^{3+} and (Ce, Gd)F_3 nanoparticles: Hydrothermal synthesis and luminescence properties. *Materials Chemistry and Physics*, 2010, **121** (1–2), P. 274–279.

[14] Zou Xiaoju, et al. X-ray-induced nanoparticle-based photodynamic therapy of cancer. *Nanomedicine*, 2014, **9** (15), P. 2339–2351.

[15] Wang Feng, et al. Facile synthesis of water-soluble LaF_3: Ln^{3+} nanocrystals. *Journal of Materials Chemistry*, 2006, **16** (11), P. 1031–1034.

[16] Shao J., Wang Z., et al. Investigation on the preparation and luminescence emission of LaF_3: Eu^{3+}@LaF_3/SiO_2 core-shell nanostructure. *Journal of Solid State Chemistry*, 2017, **249**, P. 199–203.

[17] Pudovkin M.S., Morozov O.A., et al. Physical Background for Luminescence Thermometry Sensors Based on Pr^{3+}:LaF_3 Crystalline Particles. *Journal of Nanomaterials*, 2017, **2017**, 9 pp.

[18] Fedorov P.P., Mayakova M.N., et al. Synthesis of CaF_2–YF_3 nanopowders by co-precipitation from aqueos solutions. *Nanosystems: Physics, Chemistry, Mathematic*, 2017, **8** (4), P. 462–470.

[19] Alakshin E.M., Klochkov A.V., et al. Microwave-assisted hydrothermal synthesis and annealing of DyF_3 nanoparticles. *Journal of Nanomaterials*, 2016, **2016**, 5 pp.

[20] Wang G.Q., et al. Polarized spectral properties of Sm^{3+}: $LiYF_4$ crystal. *Journal of Luminescence*, 2014, **147**, P. 23–26.

[21] Elias L.R., Heaps Wm S., Yen W.M. Excitation of uv Fluorescence in LaF_3 Doped with Trivalent Cerium and Praseodymium. *Physical Review B*, 1973, **8** (11), 4989.

[22] Runowski M., Lis S. Synthesis of lanthanide doped CeF^3: Gd^{3+}, Sm^{3+} nanoparticles, exhibiting altered luminescence after hydrothermal post-treatment. *Journal of Alloys and Compounds*, 2016, **661**, P. 182–189.

[23] Cooper D.R., et al. Photoluminescence of cerium fluoride and cerium-doped lanthanum fluoride nanoparticles and investigation of energy transfer to photosensitizer molecules. *Physical Chemistry Chemical Physics*, 2014, **16** (24), P. 12441–12453.

[24] Rojas-Hernandez, Rocío Estefanía, Santos L.F., Almeida R.M. Tb^{3+}/Yb^{3+} doped aluminosilicate phosphors for near infrared emission and efficient down-conversion. *Journal of Luminescence*, 2018, **197**, P. 180–186.

NANOSYSTEMS: PHYSICS, CHEMISTRY, MATHEMATICS, 2018, 9 (6), P. 789–792

Annealing atmosphere influence on contact resistivity of ohmic Pd/Ge/Au contact to n-GaAs

D. M. Mitin[1], F. Yu. Soldatenkov[1], A. M. Mozharov[2], A. A. Vasil'ev[2], V. V. Neplokh[2], I. S. Mukhin[2,3]

[1]Ioffe Physical Technical Institute of the Russian Academy of Sciences,
Politekhnicheskaya, 26, St. Petersburg, 194021, Russia

[2]Saint Petersburg National Research Academic University of the Russian Academy of Sciences,
Khlopina, 8, building 3, lit. A, St. Petersburg, 194021, Russia

[3]Saint Petersburg National Research University of Information Technologies, Mechanics and Optics,
Kronverkskiy, 49, St. Petersburg, 197101, Russia

mitindm@mail.ru, f.soldatenkov@mail.ioffe.ru, mozharov@spbau.ru, ftf.vasiliev@yandex.ru,
vneplokh@spbau.ru, imukhin@yandex.ru

PACS 81.05.Ea, 73.61.Ey, 73.40.Cg, 81.40.Ef **DOI 10.17586/2220-8054-2018-9-6-789-792**

We report the results of research for the Pd/Ge/Au ohmic contact resistivity to n-GaAs thermally treated in various gas atmospheres at low temperature. The lowest contact resistivity of about $4 \cdot 10^{-6}$ Ω·cm^2 was obtained with annealing under a hydrogen atmosphere. The mechanism of the ohmic contact formation upon annealing under a hydrogen atmosphere has been proposed. The achieved results can be used for development of multi-junction solar cells, power semiconductor devices, lasers, and nanowire-based structures sensible to a high temperature treatment.

Keywords: GaAs, ohmic contact, contact resistivity, thermal annealing, solid-phase regrowth.

Received: 8 November 2018

1. Introduction

Ohmic contact (OC) to n-GaAs is typically achieved with fabrication of multiple cladding Au/Ni/Au:Ge or Au/Ni/Au:Ge/Ni layers during a short time interval (1–3 min). The Au/Ni/Au:Ge contact is remarkable for its low contact resistivity of 10^{-6} Ω·cm^2 and high chemical stability [1,2]. However, this contact has limited applications, mainly due to a non-homogenous redistribution of the contact alloy components in liquid eutectic phase during thermal annealing. This negatively affects the contact morphology, contact resistivity distribution over the sample surface, and reproducibility of the ohmic contact fabrication process. Au-Ge contacts are also reported to lack thermal stability at device operating temperatures [1]. As an alternative solution, Au-Si, Ti/Pt/Au, Ge-Cu$_3$, and other compounds were developed, which partly solve the problems of thermal stability, surface morphology and in some cases allow to avoid use of precious metals in the contact composition [3]. Still, these solutions have a limited application in the GaAs device fabrication technology.

At the end of 20-th century, a solid-phase crystal regrowth method was developed for fabrication of contacts to n- and p-GaAs [4–6]. One of the appropriate solutions for n-GaAs contacts is Pd/Ge/Au, allowing fabrication of planar ohmic contacts with good electrophysical properties [7]. In the years following the appearance of this OC, several papers on solid-phase crystallization mechanism, optimal cladding thicknesses, and corresponding times and maximum temperatures of the thermal annealing processes were published [8, 9]. The highest quality of this OC is attributed to [9], where resistivity as low as 10^{-6} Ω·cm^2 by employing nitrogen atmosphere is reported. Meantime, few publications exist, which address the question of gas atmosphere influence on series resistivity during thermal annealing of Pd/Ge/Au OC, motivating the research reported here.

2. Experimental

To investigate the resistance of the studied alloy, we used 150 nm thick n-GaAs:Si structure with free electron density $N_D = 2 \cdot 10^{18}$ cm^{-3}, grown on semi-insulating GaAs substrate. Each test sample has eight contact pads, located at various distances from each other (from 5 to 100 μm, Fig. 1) used for the resistivity measurements. The contact pads were fabricated with UV lithography using SUSS MicroTec (Germany) MJB4 setup. In order to suppress the current spreading during the measurements, all of the test samples were subjected to H_2SO_4:H_2O_2:H_2O 1:1:20 wet etching solution to remove the doped GaAs layer. 200 nm thick layer was removed from the area surrounding the contact pads at a distance of more than 25 μm (Fig. 1), thus revealing the GaAs substrate.

The contact alloy deposition was performed using Boc Edwards (UK) Auto 500 setup at 5cot10^{-7} mbar vacuum. Before the deposition the samples were treated with HCl:H_2O 1:1 solution for 15 s to remove the naturally oxidized GaAs layer.

10 nm Pd and 50 nm Ge layers were deposited using carbon sources heated with electron beam, 120 nm Au was fabricated with thermal evaporation from a resistively heated molybdenum crucible. After the metal deposition the photoresist was removed with lift-off in dimethyl sulfoxide.

Part of the samples were thermally annealed in N_2 or H_2 atmosphere in Jipelec (France) Jetfirst 100 setup using 500 cm^3/min gas flow. The other part of the samples was annealed in 1 mbar vacuum. All the test samples were annealed during the same time and temperature settings, namely 1 hour and 175 °C. The samples' surface morphology before and after the annealing was controlled using optical microscopy. According to the experimental data, the morphology did not change dramatically after annealing at 175 °C in N_2, H_2 atmospheres or in vacuum, remaining smooth and without scratches or visible grains (Fig. 1a). Meanwhile, higher annealing temperature (360 °C) leads to distortion of the contact surface morphology (Fig. 1b).

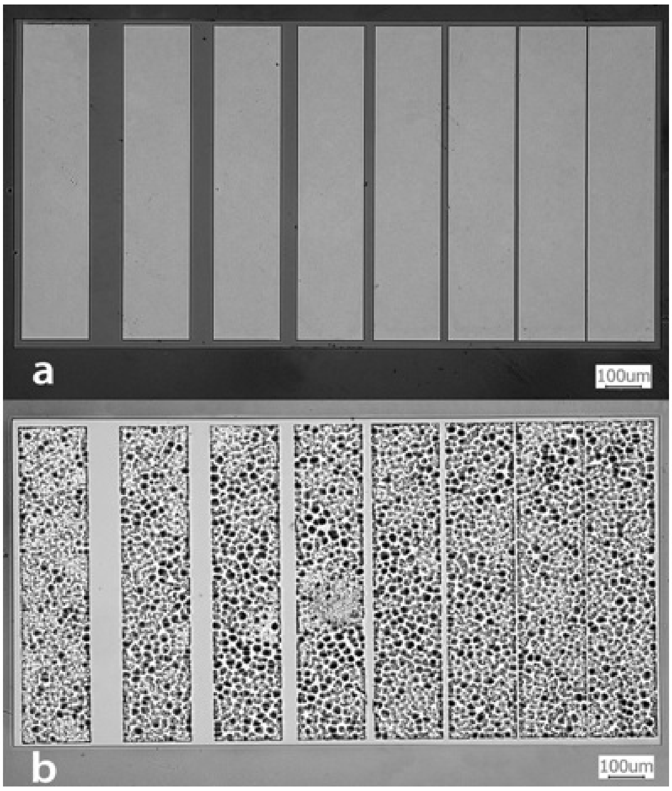

FIG. 1. Optical microscope image of the test sample surface with Pd/Ge/Au OC after annealing at H_2 atmosphere at 175 °C (a) and 360 °C (b)

Contact resistivity ρ_c of the studied Pd/Ge/Au contacts was calculated using transmission line method [10]. It includes measurement of the resistance R_T and distance L between the contact pads to draw $R_T(L)$ curves (Fig. 2). The experimental dots were approximated with a line, which crosses R axis at doubled value of the contact resistance R_c and L axis at double negative value of the current spreading width L_w. The final contact resistivity value was calculated as follows:

$$\rho_c = R_c \cdot L_w \cdot L_c,$$

where L_c is the contact pad length. Deduced R_c, L_w and calculated contact resistivity ρ_c values are presented in Table 1.

3. Results and discussion

The lowest values for the contact resistance, current spreading width and contact resistivity (4.15·10^{-6} Ω·cm^2) were achieved with annealing under H_2. This value corresponds to the previously reported value of 2·10^{-6} Ω·cm^2,

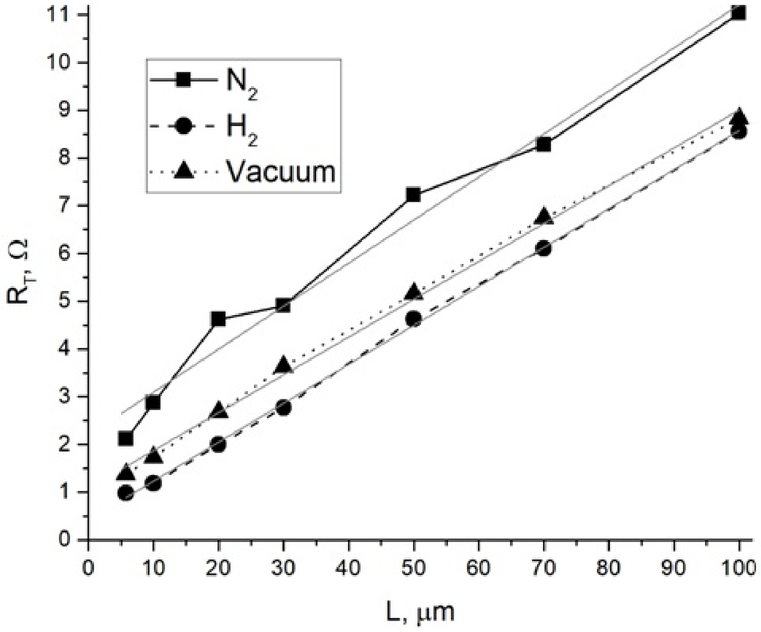

FIG. 2. Experimental dependence (dots) of resistance R_T from the distance L between contact pads. Gray lines represent linear approximations

TABLE 1. n-GaAs/Pd/Ge/Au material system parameters

Gas atmosphere	R_c, Ω	L_w, μ	ρ_c, Ω· cm^2
N_2	1.1	12.2	$1.33\cdot10^{-4}$
H_2	0.19	2.22	$4.15\cdot10^{-6}$
Vacuum	0.54	6.81	$3.68\cdot10^{-5}$

of Pd/Ge/Au OC annealed in N_2+H_2 atmosphere [8]. However, this result was obtained with the contacts deposited under ultra-high vacuum ($5\cdot10^{-8}$ mbar).

Vacuum and nitrogen annealing led to about one and two orders of magnitude higher values of contact resistivity in comparison to hydrogen atmosphere, respectively.

Interpretation of the results requires further investigation of the contact region formation mechanism near the metal-semiconductor interface under different annealing conditions. We propose the following explanation for the observed discrepancy. Ge and Pd layers heating leads to formation of the solid solution. In the presence of hydrogen, the Pd layer absorbs gas molecules (this effect is especially pronounced at temperatures above 160 °C, corresponding to Pd phase transition at atmospheric pressure). The diluted hydrogen molecules dissolve in Pd into atoms. The atomic hydrogen can reduce quantity of Ga_2O_3 formed due to surface oxidation of GaAs near the Pd contact providing crystallization of an epitaxial Ge layer from the Pd–Ge solid solution [6] on the surface of GaAs. The latter effect in turn lowers the electric barrier for the charge carriers near the contact area facilitating low contact resistance.

It is worth noting that before the annealing all of the contacts were non-ohmic. An increase of the annealing temperature to 360 °C led to one order increase of the resistance value. Series resistance increase in this case can be explained with enhanced diffusion of Au and Ge into the GaAs near the interface, so that the solid-phase recrystallization is superseded by eutectic reaction resulting in formation of Au:Ge solution typical for the Au/Ni/Au:Ge contacts [7]. This process is accompanied by surface morphology distortion of the contact pads (Fig. 1b).

4. Conclusion

In this report, we performed a series of experiments aimed at development of a fabrication method for low temperature Pd/Ge/Au ohmic contact to n-GaAs. The measurements have demonstrated that the fabricated contact is characterized with ohmic I–V curve, low contact resistivity value and high conductivity of the contact material after annealing. The best results were achieved with Pd/Ge/Au OC annealed in H_2 atmosphere. This contact composition is suitable for fabrication of OC to semiconductor structures and susceptible to a high temperature annealing. The results are especially promising with respect to multi-junction solar cells [11] and nanowire optical devices [12]. The low values of the Pd/Ge/Au OC series resistance allowed us to increase the efficiency of the devices employing n-GaAs due to the diminishing ohmic losses and enhanced collection of the charge carriers at the interface.

Acknowledgement

Authors thanks V. P. Ulin for helpful discussions of the results.

The work was supported by the Russian Science Foundation (grant No 17-79-30035).

References

[1] Baca A.G., Ren F., Zolper J.C., Briggs R.D., Pearton S.J. A survey of ohmic contacts to III-V compound semiconductors. *Thin Solid Films*, 1997, **309**, P. 599–606.

[2] Kim T., Holloway P.H. Ohmic contacts to GaAs epitaxial layers. *Crit. Rev. Solid State Mater. Sci*, 1997, **22**(3), P. 239–273.

[3] Blank T.V., Gol'dberg Yu.A. Mechanisms of current flow in metal-semiconductor ohmic contacts. *Semiconductors*, 2007, **41**(11), P. 1263–1292.

[4] Sands T., Marshall E.D., Wang L.C. Solid-phase regrowth of compound semiconductors by reaction-driven decomposition of intermediate phases. *J. Mater. Res.*, 1988, **3**(5), P. 914–921.

[5] Wang L.C. The Development of Solid Phase Regrowth on GaAs and its applications. *MRS Proc*, 1993, **319**, P. 93.

[6] Marshall E.D., Zhang B., Wang L.C., Jiao P.F., Chen W.X., Sawada T., Lau S.S., Kavanagh K.L. and Kuech T.F. Nonalloyed ohmic contacts to n-GaAs by solid-phase epitaxy of Ge. *J. Appl. Phys*, 1987, **62**(3), P. 942–947.

[7] Lin C., Lee C.P. Comparison of Au/Ni/Ge, Au/Pd/Ge, and Au/Pt/Ge Ohmic contacts to n-type GaAs. *J. Appl. Phys*, 1990, **67**(1), P. 260–263.

[8] Hao P.H., Wang L.C., Deng F., Lau S.S., Cheng J.Y. On the low resistance Au/Ge/Pd ohmic contact to n-GaAs. *J. Appl. Phys*, 1996, **79**(8), P. 4211–4215.

[9] Wang L.C., Hao P.H., Cheng J.Y., Deng F., Lau S.S. Ohmic contact formation mechanism of the Au/Ge/Pd/n-GaAs system formed below 200 °C. *J. Appl. Phys*, 1996, **79**(8), P. 4216–4220.

[10] Berger H.H. Contact Resistance and Contact Resistivity. *J. Electrochem. Soc*, 1972, **119**(4), P. 507–514.

[11] Pahanov N.A., Andreev V.M., Shvartz M.Z., Phelyakov O.P. Modern Architectures and Technologies of High-efficienct Solar Cells in III–V Heterostructures for Space and Ground Applications. *Autometria*, 2018, **54**(2), P. 93–112.

[12] Orru M., Piazza V., Rubini S., Roddaro S. Rectification and Photoconduction Mapping of Axial Metal-Semiconductor Interfaces Embedded in GaAs Nanowires. *Phys. Rev. Appl*, 2015, **4**, 44010.

NANOSYSTEMS: PHYSICS, CHEMISTRY, MATHEMATICS, 2018, 9 (6), P. 793–797

Resistance of UV-perforated reduced graphene oxide on polystyrene surface

M. N. Nikolaeva[1], A. N. Bugrov[1,2], T. D. Anan'eva[1], A. T. Dideikin[3], M. K. Rabchinskii[3], A. N. Ionov[3]

[1]Institute of macromolecular compounds RAS, Bolshoy pr. 31, 199004 St. Petersburg, Russian Federation

[2]Saint Petersburg Electrotechnical University "LETI",
ul. Professora Popova 5, 197376 St. Petersburg, Russian Federation

[3]Ioffe Institute, Politekhnicheskaya ul. 26, 194021 St. Petersburg, Russian Federation

marianna_n@mail.ru, alexander.n.bugrov@gmail.com, anthracene@hq.macro.ru,
dideikin@mail.ioffe.ru, Rabchinskii@mail.ioffe.ru, ionov@tuch.ioffe.ru

PACS 36.20.-r; 68.65.Pq; 71.20.Rv; 72.80.Tm; 74.78.-w

DOI 10.17586/2220-8054-2018-9-6-793-797

UV-perforated reduced graphene oxide flakes of large areas, some of them up to 500 μm in diameter, have been produced on polystyrene surface. These flakes were formed during precipitation of UV-reduced graphene oxide composites based on polystyrene from benzene solutions by petroleum ether. Two composites based on polystyrene with molecular weights of 9,000 Da and 45,000 Da were synthesized to compare their conductive properties. Conditions of the formation of planar structures from UV-perforated reduced graphene oxide flakes were varied. So, resistances were compared for composites deposited from solutions with different concentrations and at different temperatures. Very low resistances for some flakes precipitated from 5 wt.% solution of composite of 9,000 Da molecular mass at the room temperature were obtained. The absolute values of measured resistances were found to be 1.5 orders of magnitude lower than resistance of copper. At the same time some, regions of graphene inclusions from 12 wt.% solution of latter polystyrene composite demonstrated even lower resistance, almost 3 orders of magnitude lower than copper resistance. This result is explained by existence of superconducting component in the reduced graphene oxide inclusions. In the case of composites with graphene flakes produced from higher molecular weight polystyrene (45,000 Da) resistance was high and varied from semiconducting values to non-conductive state.

Keywords: UV-perforated reduced graphene oxide, polystyrene, composite, resistance, superconductivity.

Received: 2 September 2018

1. Introduction

Graphene-like materials are very attractive for various brenches of practical use due to its unique electronic properties, including possible high-temperature superconductivity [1–7]. It was shown in [8] that some places of graphene oxide reduced at high temperature (RGO) [9] and obtained as planar structures on polystyrene surface have extremely low resistance. Absolute values of experimentally obtained resistance were 2 orders of magnitude lower than copper resistance. In this paper, we investigated the resistance of other graphene structures in the polystyrene composite, namely graphene oxide reduced by UV-perforation (RGO$_p$). Details of its producing can be found in [10, 11]. The mechanism of the holes formation in the graphene oxide film is shown on Fig. 1.

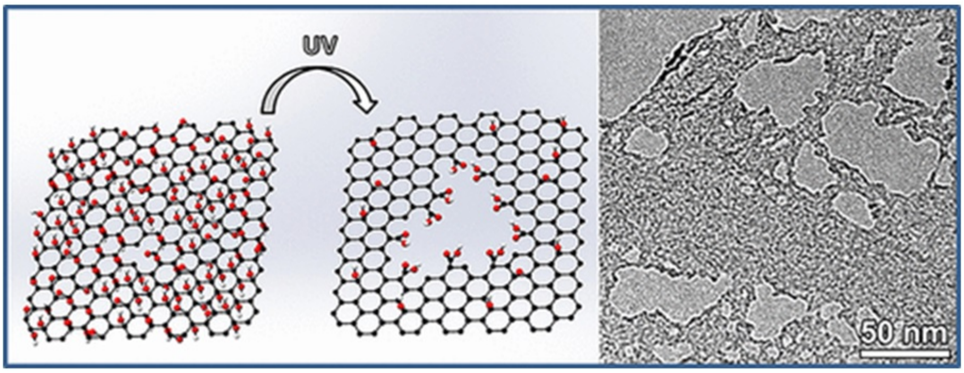

FIG. 1. Reduction scheme of thin graphene oxide (GO) films consisting of flakes with lateral size up to 100 μm through soft ultraviolet irradiation under argon atmosphere [10]

It was found in [10] that reduction leads to a significant decrease in the overall content of the basal-plane functional groups, namely, epoxides and hydroxyls, but with simultaneous increase in the total number of edge-located carboxyl groups and formation of nanoscale holes.

Lateral sizes of individual RGO_p flakes were 10 – 100 μm [10]. As it was previously, the maximum length of reduced graphene oxide flakes produced by heating at 800 °C (RGO) are only up to 8 μm according to the SEM data [12]. Precipitation in [8] led to enlargement of RGO inclusion areas. So this chemical precipitation method of polystyrene composite from benzene can also be used for obtaining planar RGO_p flakes of sufficient size for electrical measurements.

It is important to note that RGO considered in [8, 12–15] was functionalized by 3-(trimethoxysilyl)propyl methacrylate and can participate in radical polymerization with styrene [8], forming covalent bonds between RGO and polystyrene chains, similar to the work [16]. These features of RGO interaction with polystyrene can cause special mutual location of RGO flakes and its further self-organization under precipitation from solvents mixture leading to erasing of superconducting state as in [8]. The occurrence of holes in the RGO sheets after UV-irradiation can change location of (trimethoxysilyl)propyl methacrylate on their surface and affect the mutual self-organization the resulting RGO_p flakes. Thus, the aim of present study was to find out what conditions are needed to obtain the superconducting state for another form of reduced graphene oxide – RGO_p.

2. Experimental

Surface modification technique of RGO_p and its further radical copolymerization with styrene as well as synthesis of RGO composite can be found in [12, 14]. Only the content of the radical initiator, azobisisobutyronitrile (AIBN) was varied during the synthesis of composites in the reaction mixture, 1 wt.% and 0.2 wt.%, correspondingly. Thus, the RGO_p–polystyrene composites differed by molecular mass have been obtained. Molecular masses of composites were evaluated for additionally synthesized pure polystyrene. Polystyrene and composites based on it were synthesized by radical polymerization. The AIBN of 0.2 wt.% and 1 wt.% of the weight of the monomer were taken in the synthesis of pure polystyrene. The molecular weights of synthesized polystyrene using the above-mentioned amounts of initiator were evaluated using an Ubbelohde viscometer and were 9,000 Da and 45,000 Da, respectively. Since the amount of RGO_p introduced into the polystyrene is small and it acts along with styrene as a monomer due to surface modification by vinyl groups we assume that the molecular weights of the composites will be close to their values for unfilled polymer. The composite with molecular mass 9,000 Da further will be named Composite (1), with molecular mass 45,000 Da – Composite (2). The largest areas of graphene inclusions on the polystyrene surface were observed for the benzene/petroleum ether ratio of 1:1 [8]. In this regard, benzene/petroleum ether in ratio of 1:1 was used for RGO_p composite precipitation. This solvents ratio (1:1) was chosen also for production of sufficient RGO_p planar structures. Films of the polymer composite were deposited on glass substrate by casting through the dispenser. We proposed that the sizes of the RGO_p inclusions were dependent on kind of composite, concentration of solvent mixture, and deposition method on the glass substrate. Composite content in the solvents mixture was 5 – 12 wt.%. Deposition was performed at room temperature and at the boiling point of benzene (70°C).

Since areas of obtained RGO_p flakes were not too large to apply 4-probe method their resistance measurements were performed using 2-probe method. Steel needles with curvature radii of 15 μm were used. Resistance values of RGO_p flakes were compared with ones corresponded to macroscopic copper substrate. Pressure on electrodes during measurements did not exceed 0.5 g/μm^2 as in [8].

3. Results and discussion

The RGO_p flake distribution for both composites after deposition was irregular on the polystyrene surface, and their sizes were many fold different from each other in the same way as in [8]. However, special differences in shape and size were observed for the synthesized RGO_p composites. Particularly, for the Composite (1) maximal observed diameters of RGO_p flakes in planar dimensions deposited from 5 wt.% solution were approximately 150 μm without heating and 300 μm when glass substrate was heated up to 70°C. Maximal diameters of RGO_p inclusions in the Composite (2) deposited from 5 wt.% solution reached 300 μm without heating and were up to 500 μm in the opposite case. When concentrated solutions were used, maximal diameters of RGO_p inclusions for both considered composites were even larger. There was one more difference between these two composites: for the Composite (2) RGO_p shapes were close to spherical, for the Composite (1) RGO_p shapes were practically planar, rising above the surface of polystyrene not higher than 100 nm. So, the objects of our investigation had turned out to be the multilayered RGO_p flakes obtained as a result of self-organization during precipitation process.

Since during the precipitation process the polymer coils were tightened, some tensions between the filler and polystyrene led to the release of the RGO$_p$ of each coil from the polymer matrix. In this manner, separate RGO$_p$ particles coalesced into large flakes. Due to the holes in the RGO$_p$ sheets attaching of the 3-(trimethoxysilyl)propyl methacrylate to them will largely depend on the edge groups around cavities. Thus, the molecules of the organosilicon modifier, which are very close to each other at the edges of the hole, can interact between themselves. This process may cause additional tensions between releasing RGO$_p$ sheets and change way of their further self-organization. As a result, new types of RGO$_p$ flakes on the polystyrene surface were formed. So, these RGO$_p$ flakes of different sizes and shapes being deposited from the composites' solutions on glass substrate demonstrated special current-voltage characteristics.

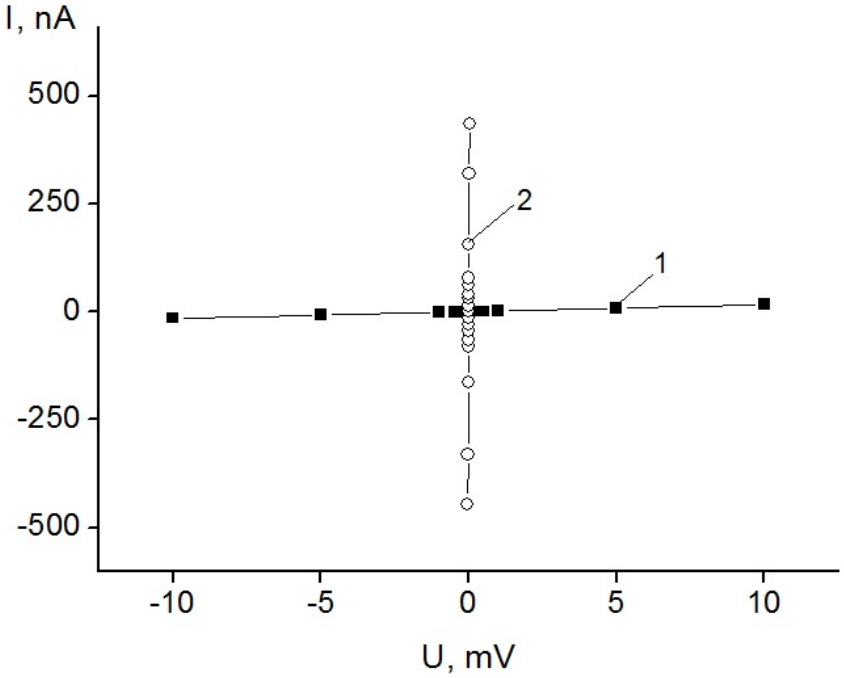

FIG. 2. Current-voltage characteristic of 1 – RGO$_p$ flakes deposited from polystyrene composite of 45,000 Da, distance between electrodes 10 μm, concentration of solution 5 wt.%; 2 – current-voltage characteristic of copper

To measure the resistance, sufficiently large flakes of RGO$_p$ with a diameter of 150 μm or more were used. Resistance was evaluated from current-voltage characteristics (Fig. 2,3). In general, the resistance of RGO$_p$ flakes of Composite (1) obtained without heating lied in the range of 0.6 – 7 Ω for 12 wt.% composite and in interval of 20 – 40 Ω for 5 wt.% composite. Resistance of some RGO$_p$ flakes approached 0.13 Ω for 12 wt.% and 15 Ω for 5 wt.% composites without heating during deposition (Fig. 3, curves 1 and 2). The common resistances for RGO$_p$ flakes of this composite when RGO$_p$ flakes were formed practically immediately being deposited from precipitated composite solution on heated glass substrate were up to 1 order of magnitude lower than copper resistance and were about 5 – 12 Ω. The resistance of copper substrate was approximately 67 Ω (Fig. 2, curve 2; Fig. 3, curve 3). As one can readily see, a temperature increase in the case of low-molecular weight Composite (1) did not significantly affect resistances of deposited RGO$_p$ flakes. Since relatively small polymer coils are divided by the solvent this result would be explained that sufficiently long distances are needed to overcome by separate RGO$_p$ sheets of every polymer molecule for self-organization into larger structures.

The RGO$_p$ flakes in the case of the Composite (2) exhibited both a non-conducting state and a low conducting state in the range of hundreds of kΩ and MΩ. One of the lowest values of resistance obtained for this composite was 670 kΩ (Fig. 2, curve 1). We suppose that fast self-organization of RGO$_p$ inclusions due to the heating in the process of deposition on glass substrate can cause irregular and chaotic interaction of relatively close located RGO$_p$ sheets. In this case, many defects in RGO$_p$ flakes prevent high conductivity.

The resistance of RGO$_p$ flakes was dependent on distance between measuring electrodes. The distance increase in the case of the Composite (1) caused sharp resistance amplification, as was seen in [8]. At the same time, for Composite (2), the distance between measuring electrodes very slightly influenced resistance values. Moreover,

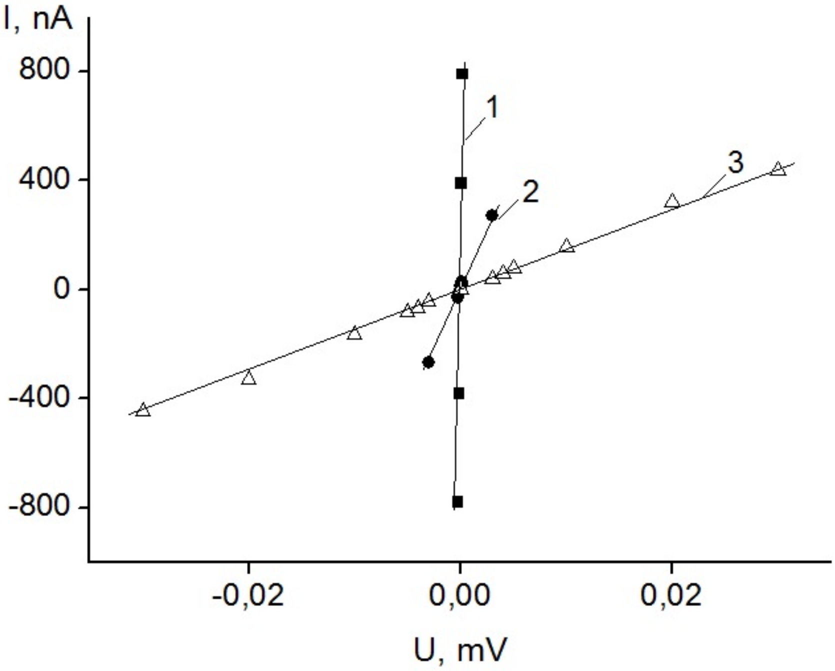

FIG. 3. Current-voltage characteristics of RGO_p flakes deposited from polystyrene composite of 9,000 Da, distance between electrodes 10 μm: 1 – concentration of solution 12 wt.% , 2 – concentration of solution 5 wt.% ; 3 – current-voltage characteristic of copper

the distance between the measuring electrodes for Composite (2) had a very weak effect on the resistance values. These values were almost equal even when the distance between electrodes reached 200–300 μm.

The obtained results of very low resistances for RGO_p flakes from the Composite (1) can be explained by the existence of superconducting phase in the RGO_p flakes at the room temperature. We suppose since there are theoretical papers predicting possibility of superconducting state for graphene at room temperature under special conditions [6, 17–19] the self-organization of separate RGO_p sheets during precipitation and further deposition on the glass substrate possibly can satisfy these conditions. The electric properties of these multilayered RGO_p flakes obtained as a result of self-organization during precipitation process of Composite (1) can be similar to finely dispersed pyrolytic graphite having superconducting inclusions [20]. Obtained resistance values are in consent with our previous work [8] as also with [21] where it was shown for RGO/polysterene composite that Josephson oscillations and Shapiro steps exist at room temperature.

4. Conclusions

Large planar RGO_p structures (hundreds of micrometers in diameter) from two RGO_p/polystyrene composites differing by molecular masses were obtained on polystyrene surface. For this purpose, precipitation of composites with perforated reduced graphene oxide based on the polystyrene from benzene was used. Precipitation of both composites was performed by petroleum ether in ratio 1:1 to benzene. The temperature of further RGO_p deposition on glass substrate strongly influenced on the sizes and resistances of obtained RGO_p flakes. Thus, heating to 70 °C allowed deposit larger, up to 500 μm, structures. At the same time, such enlargement caused decrease of conductivity to non-conductive state. Sizes of RGO_p structures can be enlarged by increasing of composites concentration at the room temperature as well. In this case, the RGO_p flakes' enlargement, otherwise, causes a significant decrease of resistance. The resistance of some rare planar inclusions measured by steel needles was found to be up to 3 orders of magnitude lower than the resistance measured for the copper substrate.

References

[1] Novoselov K.S., Fal'ko V.I., Colombo L., Gellert P.R., Schwab M.G., Kim K.A. Roadmap for Graphene Nature. *Nature*, 2012, **490**, P. 192–200.

[2] Huang X., Yin Z., et al. Graphene-based materials: Synthesis, Characterizations, Properties, and Applications. *Small*, 2011, **7**(14), P. 1876–1902.

[3] Potts J.R., Dreyer D.R., Bielawski C.W., Ruoff R.S. Graphene-Based Polymer Nanocomposites. *Polymer*, 2011, **52**, P. 5–25.

[4] Kostromin S., Saprykina N., Vlasova E. et al. Nanocomposite polyazomethine/reduced graphene oxide with enhanced conductivity. *Journal of Polymer Research*, 2017, **24**(12), P. 211.

[5] Uchoa B., Castro Neto A.H. Superconducting states of pure and doped graphene. *Phys Rev Letters*, 2007, **98** P. 146801-1–146801-4.

[6] Chapman J., Su Y., Howard C.A., et al. Superconductivity in Ca-doped graphene laminates. *Sci. Rep.*, 2016, **6**, P. 23254.

[7] Tonnoir C., Kimouche A., Coraux J., et al. Induced superconductivity in graphene grown on Rhenium. *Phys. Rev. Lett.*, 2013, **111**(24), P. 246805.

[8] Nikolaeva M.N., Bugrov A.N., Anan'eva T.D., et. al. Resistance of reduced graphene oxide on polystyrene surface. *Nanosystems: physics, chemistry, mathematics*, 2018, **9**(4), P. 496–499.

[9] Dideykin A., Aleksenskiy A.E., Kirilenko D., et. al. Monolayer graphene from graphite oxide. *Diam. Relat. Mat.*, 2011, **20**(2), P. 105–108.

[10] Rabchinskii M.K., Shnitov V.V., Dideikin A.T., et.al. Nanoscale Perforation of Graphene Oxide during Photoreduction Process in the Argon Atmosphere. *J. Phys. Chem. C*, 2016, **120**(49), P. 28261–28269.

[11] Aleksenskii A.E., Vul' S.P., Dideikin A.T., et.al. Etching of wrinkled graphene oxide films in noble gas atmosphere under UV irradiation. *Nanosystems: physics, chemistry, mathematics*, 2016, **8**(1), P. 81–86.

[12] Nikolaeva M.N., Bugrov A.N., Anan'eva T.D., et al. Conductive properties of the composite films of graphene oxide based on polystyrene in a metal-polymer-metal structure. *Russ. J. Appl. Chem.*, 2014, **87**(8), P. 1151–1155.

[13] Nikolaeva M.N., Gushchina E.V., Dunaevskii M.S., et al. The influence of substrate material on the resistance of composite films based on reduced graphene oxide and polystyrene. *Nanosystems: physics, chemistry, mathematics*, 2017, **8**(5), P. 665–669.

[14] Khairullin A.R., Nikolaeva M.N., Bugrov A.N. Resistance of the composite films based on polystyrene and graphene oxide. *Nanosystems: physics, chemistry, mathematics*, 2016, **7**(6), P. 1055–1058.

[15] Nikolaeva M.N., Anan'eva T.D., Bugrov A.N., et.al. Correlation between structure and resistance of composites based on polystyrene and multilayered graphene oxide. *Nanosystems: physics, chemistry, mathematics*, 2017, **8**(2), P. 266–271.

[16] Yevlampieva N., Bugrov A., Anan'eva T., et al. Soluble poly (methyl methacrylate) composites containing covalently associated zirconium dioxide nanocrystals. *Am. J. Nano Res. and Appl.*, 2014, **2**(2), P. 1–8.

[17] Esquinazi P., Heikkilä T.T., Lysogorskiy Y.V., et.al. On the superconductivity of graphite interfaces. *JETP Letters*, 2014, **100**(5), P. 336–339.

[18] Scheike T., Bhlmann W., Esquinazi P., et. al. Can doping graphite trigger room temperature superconductivity? Evidence for granular high-temperature superconductivity in water-treated graphite powder. *Advanced Materials*, 2012, **24**(43), P. 5826–5831.

[19] Volovik G.E., Pudalov V.M. Graphite on graphite. *JETP Letters*, 2016, **104**(12), P. 880–882.

[20] Saad M., Gilmutdinov I.F., Kiiamov A.G., et al. Observation of Persistent Currents in Finely Dispersed Pyrolytic Graphite. *JETP Letters*, 2018, **107**(1), P. 37–41.

[21] Ionov A.N. Josephson-Like Behaviour of the Current-Voltage Characteristics of Multi-graphene Flakes Embedded in Polystyrene. *J. Low Temp. Phys.*, 2016, **185**(5-6), P. 515–521.

NANOSYSTEMS: PHYSICS, CHEMISTRY, MATHEMATICS, 2018, 9 (6), P. 798–810

Antioxidant properties of fullerenol-d

D. P. Tyurin[1], F. S. Kolmogorov[1], I. A. Cherepkova[1], N. A. Charykov[1,5], K. N. Semenov[1,2], V. A. Keskinov[1], N. M. Safyannikov[5], Yu. V. Pukharenko[3], D. G. Letenko[3], T. A. Segeda[4], Z. Shaimardanov[4]

[1]St. Petersburg State Technological Institute (Technical University),
Moskovsky prospect, 26, Saint Petersburg, 190013, Russia
[2]St. Petersburg State University, 7/9 Universitetskaya emb., Saint Petersburg, 199034, Russia
[3]St.Petersburg State University of Architecture and Civil Engineering (SPSUACE),
2nd Krasnoarmeiskaya St. 4, 190005, Saint Petersburg, Russia
[4]D. Serikbayev East Kazakhstan state technical university,
A. K. Protozanov Street, 69, Ust-Kamenogorsk city, 070004, The Republic of Kazakhstan
[5]St. Petersburg Electrotechnical University "LETI",
ul. Professora Popova 5, 197376, Saint Petersburg, Russia

keskinov@mail.ru

PACS 61.48.+c **DOI 10.17586/2220-8054-2018-9-6-798-810**

Fullerenol-d $C_{60}(OH)_{22-24}$ was synthesized by the method of direct heterogeneous oxidation of fullerene C_{60}, dissolved in o-xylene, by NaOH, dissolved in water, in the presence of interphase catalyst $\left[t-(C_4H_9)_4\,N\right]OH$. Identification of fullerenol-d was provided by: C–H–N elemental analysis, High performance liquid phase chromatography, IR – and Electronic spectroscopy, Mass-spectrometry. The antioxidant properties of aqueous fullerenol-d solutions were investigated against free radicals, generated by hydrogen peroxide and molecular I_2. Measurement of fullerenol antioxidant activity was based on the potentiometric titration of fullerenol solutions by hydrogen peroxide and molecular I_2 solutions and vice versa with compact Pt as working electrode. As a comparison, the very popular and strong anti-oxidant – ascorbic acid was used. Pourbaix Diagrams ($pH - Eh$) for hydrogen-oxygen and iodine forms were constructed. Fullerenol-d is a weaker antioxidant than ascorbic acid, but in contrast, fullerenols-d molecules are able to undergo multiply reversible absorption-desorption of some free radicals.

Keywords: fullerenol, antioxidant properties, hydrogen peroxide, iodine, Pourbaix Diagrams, platinum electrode.

Received: 19 July 2018

Revised: 12 November 2018

Final revision: 21 November 2018

1. Introduction

This research continues the series of reports, concerning synthesis, identification and investigation of the properties of polyhydroxylated derivatives (also named as fullerenols) of light fullerenes C_{60} and C_{70} (see, for example [1–28]).

Antioxidant properties of fullerenols were previously investigated [7, 9, 17, 42–50]. Several mechanisms for the antioxidant activity of fullerenol nanoparticles have been proposed [42]. The possible mechanism of the antioxidative activity of fullerenol $C_{60}(OH)_{24}$ is the radical-addition reaction of $2n(OH^*)$ (here and further (R^*) – is free radical with one free electron) radicals to the remaining olefinic double bonds of the fullerenol core to yield $[C_{60}\ (OH)_{24}](OH^*)_{2n}$. The other proposed mechanism is the possibility of a hydroxyl radical to abstract a hydrogen from fullerenol, including the formation of a relatively stable fullerenol radical $[C_{60}(OH)_{23}](O^*)$ [46]. In addition, a hydroxyl radical may abstract one electron from fullerenol yielding the radical cation $[C_{60}(OH)_{24}]^+$. One more proposed mechanism is that the polyanion nanoparticles have numerous free electron pairs from oxygen, distributed around the fullerenol molecules, and have a great capacity to form coordinative bonds with prooxidant metal ions [9]. The obtained result demonstrated that fullerenol decreased the reduction of cytochrome-C for 5 – 40 rel. % [7]. The hypothetical mechanism of action of the polyanion fullerenol $C_{60}(OH)_{24}$ with the superoxide radical anion is presented in [50]. Some results suggest that $C_{60}(OH)_{32} \cdot 8H_2O$ scavenges (OH^*) owing to the dehydrogenation of $C_{60}(OH)_{32} \cdot 8H_2O$ and is simultaneously oxidized to a stable fullerenol radical [47]. The antioxidant ability of $C_{60}(OH)_{32} \cdot 8H_2O$ was also confirmed in a beta-carotene bleaching assay [48]. The results suggest that fullerennols possess NO-scavenging activity *in vivo* [7]. The scavenger activity of fullerenol with a smaller or moderate number of hydroxyl groups with (OH^*) radicals can be explained by addition to sp^2 carbon atoms [46, 49].

The phototoxic antioxidant properties of fullerenols have also been reported [42,51,52]. Fullerenol $C_{60}(OH)_{24}$ produces a mixture of reactive oxygen species under both visible and ultraviolet irradiation through two types of photochemical mechanisms [51], with the greatest rates of oxygen consumption at acidic pH $(pH = 5)$. Evidence of both singlet oxygen $(^1O_2)$ and superoxide radical ion production $(O_2^*)^-$ was obtained and when compared to other known sensitizers of reactive oxygen; fullerenol $C_{60}(OH)_{24}$ produced higher quantities of active oxygen species at a rate at least two times that of other sensitizers [52]. Comparing phototoxicity toward HaCaT of $(\gamma\text{-}C_yD)_2/C_{60}$ (c-cyclodextrin bicapped C_{60}) and fullerenol, Zhao et al. concluded that fullerenol was less phototoxic [53].

2. Pourbaix diagram

A Pourbaix diagram (diagram of predominant forms, $Eh - pH$ diagram) is one that illustrates thermodynamically stable forms of existence of elements (ions, molecules, atomic crystals and metals) in solutions at different values of hydrogen indicator – pH and redox electrode potential for compact Pt electrode – Eh [54, 55]. These diagrams were proposed by Marcel Pourbaix [54]. For each element, you can build a separate Pourbaix diagram. Pourbaix diagrams for one element may vary depending on temperature, solvent and presence of ligands in solution. But, as a rule, Pourbaix diagrams are for aqueous solutions at the temperatures near 25 °C. Pourbaix diagrams are constructed on the basis of the Nernst equation and the standard redox potentials.

The Pourbaix diagram is constructed in coordinates of Eh (ordinate) – pH (abscissa). It reflects the species that are thermodynamically stable at a given pH value and the oxidation-reduction potential of the medium – Eh. At a lower potential, the corresponding form can be reduced to the underlying (if any), at a higher – oxidized to the overlying (if any). The boundaries between the existing species of a solution-solid or solution-gas usually depend on the concentration of dissolved forms; the boundaries between the existing species of dissolved forms, as a rule, do not depend on their concentration. Often, the Pourbaix diagram is applied to the boundary of the region of existence of water. The upper of them ($Eh = 1.23 – 0.059\ pH$) corresponds to the release of oxygen (that is, at higher potentials it is possible to oxidize water to oxygen):

$$4H_2O - 4e^- = 4H^+ + O_2 \quad (pH < 7)\,, \tag{1.1}$$

$$4OH^- - 4e^- = 2H_2O + O_2 \quad (pH > 7)\,. \tag{1.2}$$

The lower limit ($Eh = -0.059pH$) corresponds to the release of hydrogen (that is, at lower potentials it is possible to recover water to hydrogen):

$$2H^+ + 2e^- = H_2 \quad (pH < 7)\,, \tag{2.1}$$

$$2H_2O + 2e^- = H_2 + 2OH^- \quad (pH > 7)\,. \tag{2.2}$$

The Pourbaix diagram [53, 54] is one of the most powerful means of predicting the direction of chemical reactions of compounds of this element. From this, it is possible to determine the conditions of most acid-base and redox reactions of compounds of this element without taking into account the interaction with different ions. It is possible to predict the processes of disproportionation and non-proportionally different forms, whether they can contribute hydrogen and oxygen. By comparing the Pourbaix diagrams for the two elements, it is possible to predict the redox reactions between their compounds.

3. Experimental section

3.1. Fullerenol-d synthesis and identification

For synthesis, the authors used fullerene C_{60}, produced by ILIP Corporation (S-Petersburg, Russia) with the purity 99.5 mass. %. All other reactants had qualification “pure for the analysis”.

Fullerenol-d $C_{60}(OH)_{22-24}$ was synthesized by the method of direct heterogeneous oxidation of fullerene C_{60}, dissolved in o-xylene, by NaOH, dissolved in water, in the presence of interphase catalyst $[t-(C_4H_9)_4N]\,OH$ (see, for example [27–29, 42]). The following synthesis reactions were realized:

$$C_{60}|(\text{o-xylene}) + (22-24)NaOH(\text{water}) + [t-(C_4H_9)_4N]\,OH(\text{interphase}) \rightarrow$$

$$C_{60}\,(ONa)_{22-24}\,(\text{water}) + (11-12)H_2;$$

$$C_{60}\,(ONa)_{22-24} + (22-24)HCl \rightarrow C_{60}\,(OH)_{22-24} + (22-24)NaCl(CH_3OH - \text{solution}).$$

Reaction was provided for 7 days; the aqueous phase was separated from the organic phase; product (fullerenol-d) was salting-out by methanol and then purified by triple recrystallization (methanol-water) [27–29, 42]. Identification of fullerenol-d was provided by: C–H–N element analysis, High performance liquid phase chromatography

(HPLC) – device chromatograph “Shimadzu Europa GmbH”, IR – and Electronic spectroscopy, devices: IRAffinity-1S and UV-1280, Mass-spectrometry, device – Bruker MS [27–29]. In particular, with the help of mass-spectrum we determined the number of hydroxyl groups (22-24), purity was determined by HPLC (98.5 mass %).

3.2. Antioxidant properties investigation

To investigate antioxidant properties of ascorbic acid and fullerenol (against oxidants: hydrogen per-oxide and iodine) we determined redox potential Eh at fixed value of hydrogen indicator pH= 4.77, which was set by acetate buffer solution CH_3COOH/CH_3COONa (molar relation 1/1). We used electrochemical cells, containing two electrodes: Pt (compact) is working electrode; Hg, Hg_2Cl_2/KCl (1 mole/dm^3) – reference normal calomel electrode with constant potential and investigated solution in acetate buffer solution. Device pH-meter “ATC pH 200” was used as a Voltmeter during potential-metric titration of anti-oxidants by oxidants and vice-versa.

Titration of comparative “standard” antioxidant – ascorbic acid by hydrogen peroxide and molecular I_2 and vice versa.

3.3. Hydrogen peroxide titration

It is well known, that in an aqueous solution of comparative “standard” antioxidant – ascorbic acid, may realize oxidation-reduction equilibrium between ascorbic acid (reduced form) and dehydroascorbic acid (oxidized form). It is only the first step of oxidation [56,57] by hydrogen peroxide (eq. 3.1) or I_2 in KI water solution (eq. 3.2):

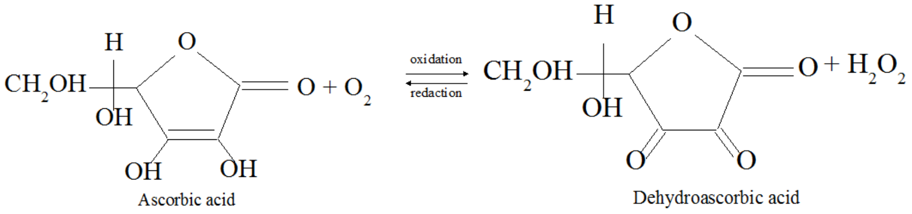

(3.1)

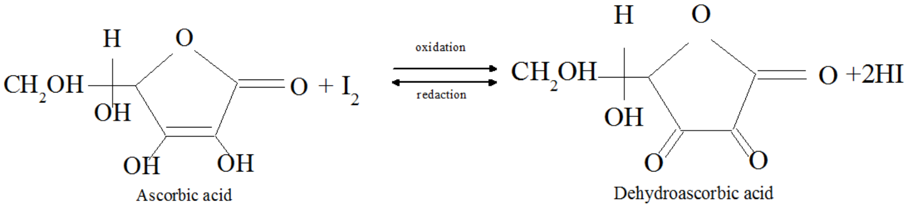

(3.2)

We used following electrochemical cells:

$$\mathrm{Hg, Hg_2Cl_2/KCl} \left(1\ \mathrm{mole/dm^3}\right) /\mathrm{investigated\ solution/Pt\,(compact)}\,, \tag{4}$$

where: Pt (compact) is working electrode; Hg, Hg_2Cl_2/KCl(1 mole/dm^3) – reference normal calomel electrode with constant potential $E^0 = 0.281V$ [58]. Investigated solution in had two compositions:

$$\mathrm{ascorbic\ acid} + \mathrm{dehydroascorbic\ acid} + H_2O_2 + O_2 + H^+\,(\mathrm{acetate\ buffer})\,; \tag{5.1}$$

$$/\mathrm{ascorbic\ acid} + \mathrm{dehydroascorbic\ acid} + I_2 + I^-\,(\mathrm{KI}) + H^+\,(\mathrm{acetate\ buffer})\,. \tag{5.2}$$

The integral and differential curves of the titration of H_2O_2 by ascorbic acid and vice-versa ascorbic acid by H_2O_2 are represented in Fig. 1(a–d).

One can see absolutely equivalent quantities of ascorbic acid and hydrogen peroxide, according to eq. 3.1 and I_2, according to eq. 3.2.

One can also see that upper plateau in two curves $E_1 \approx 0.32V$ (Fig. 1(a,c)) corresponds to the following electrode semi-reaction:

$$O_2 + 2H^{+\cdot} + 2\bar{e} \to H_2O_2(\mathrm{Pt}), \tag{6.1}$$

upper plateau in two curves $E_2 \approx 0.34V$ (Fig. 2(a,c)) corresponds to the following electrode semi-reaction:

$$I_2\,(\mathrm{liquid}) + 2e \to 2I^-\,(\mathrm{Pt}), \tag{6.2}$$

bottom plateau in four curves $E_3 \approx 0.03V$ (Figs. 1(a,c), 2(a,c)) corresponds to the same electrode semi-reaction:

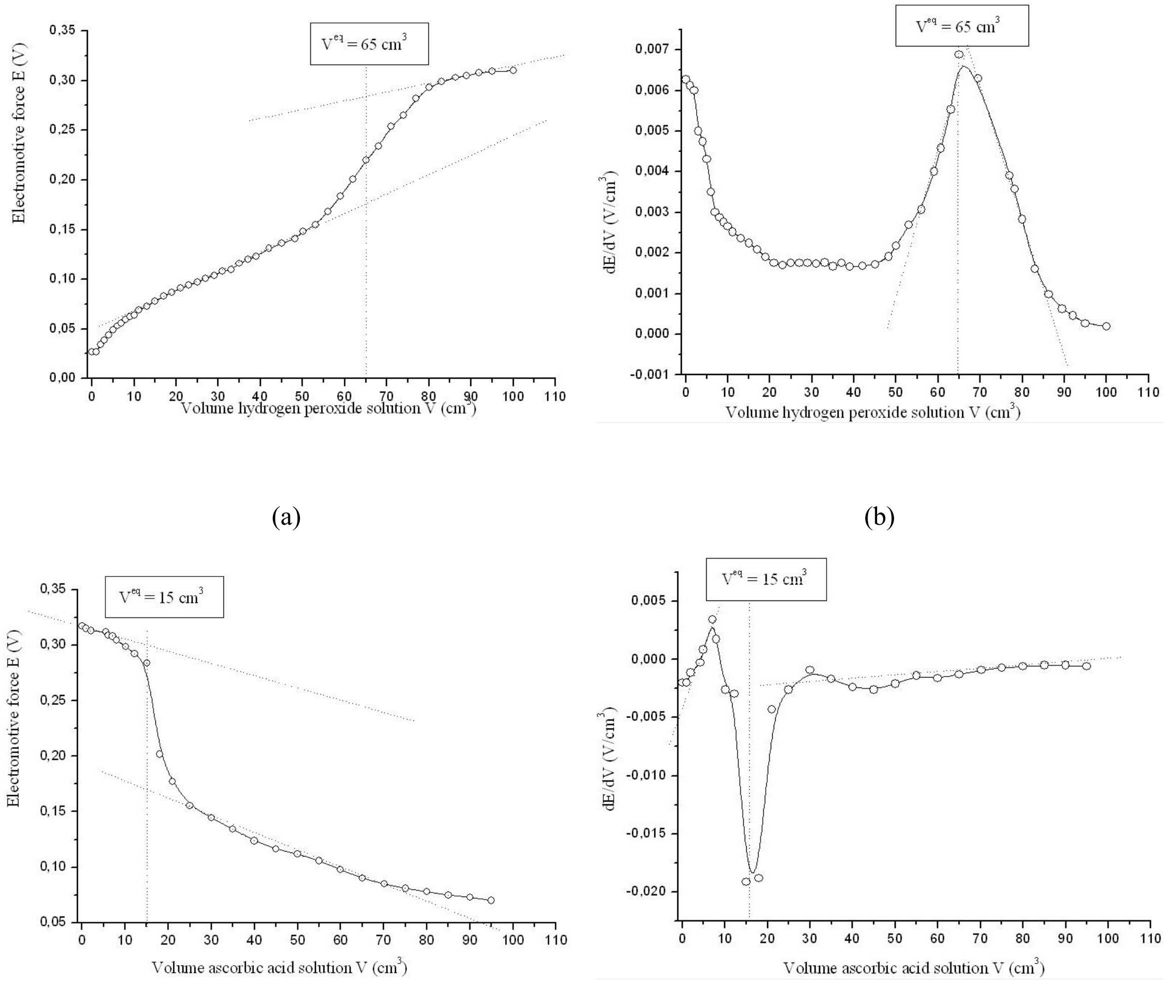

(a) (b)

(c) (d)

FIG. 1. (a,b) – Titration of 30 cm^3 of ascorbic acid solution ($C = 0.05$ mole/dm^3) by the hydrogen peroxide solution ($C = 0.025$ mole/dm^3) in 30 cm^3 of acetic buffer CH_3COOH/CH_3COONa (1/1) – integral (a) and differential (b) curves. (c,d) – Titration of 30 cm^3 of hydrogen peroxide solution ($C = 0.025$ mole/dm^3) by ascorbic acid solution ($C = 0.05$ mole/dm^3) in 20 cm^3 of acetic buffer CH_3COOH/CH_3COONa (1/1) – integral (c) and differential (d) curves. E is potential of Pt electrode relative normal calomel electrode

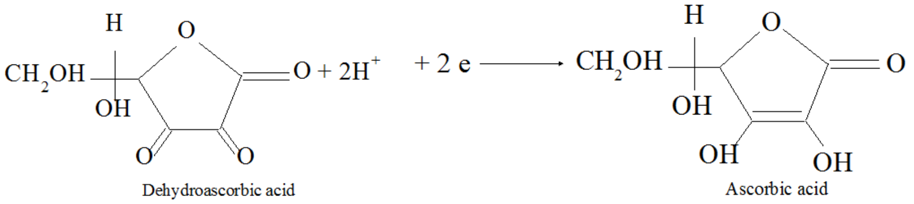

(6.3)

The full oxidation-reduction reaction is given by reaction (3.1). It is the difference between semi-reactions (6.1) and (6.3). Full oxidation-reduction reaction is given by reaction (3.2): I is the difference between semi-reactions (6.2) and (6.3).

Differences of electromotive forces in plateaus in Figs. 1(a,c) and 2(a,c) are, correspondingly:

$$\Delta E_{3.1} \approx 0.32 - 0.03 \approx 0.29V; \quad \Delta E_{3.2} \approx 0.34 - 0.03 \approx 0.31V. \tag{7}$$

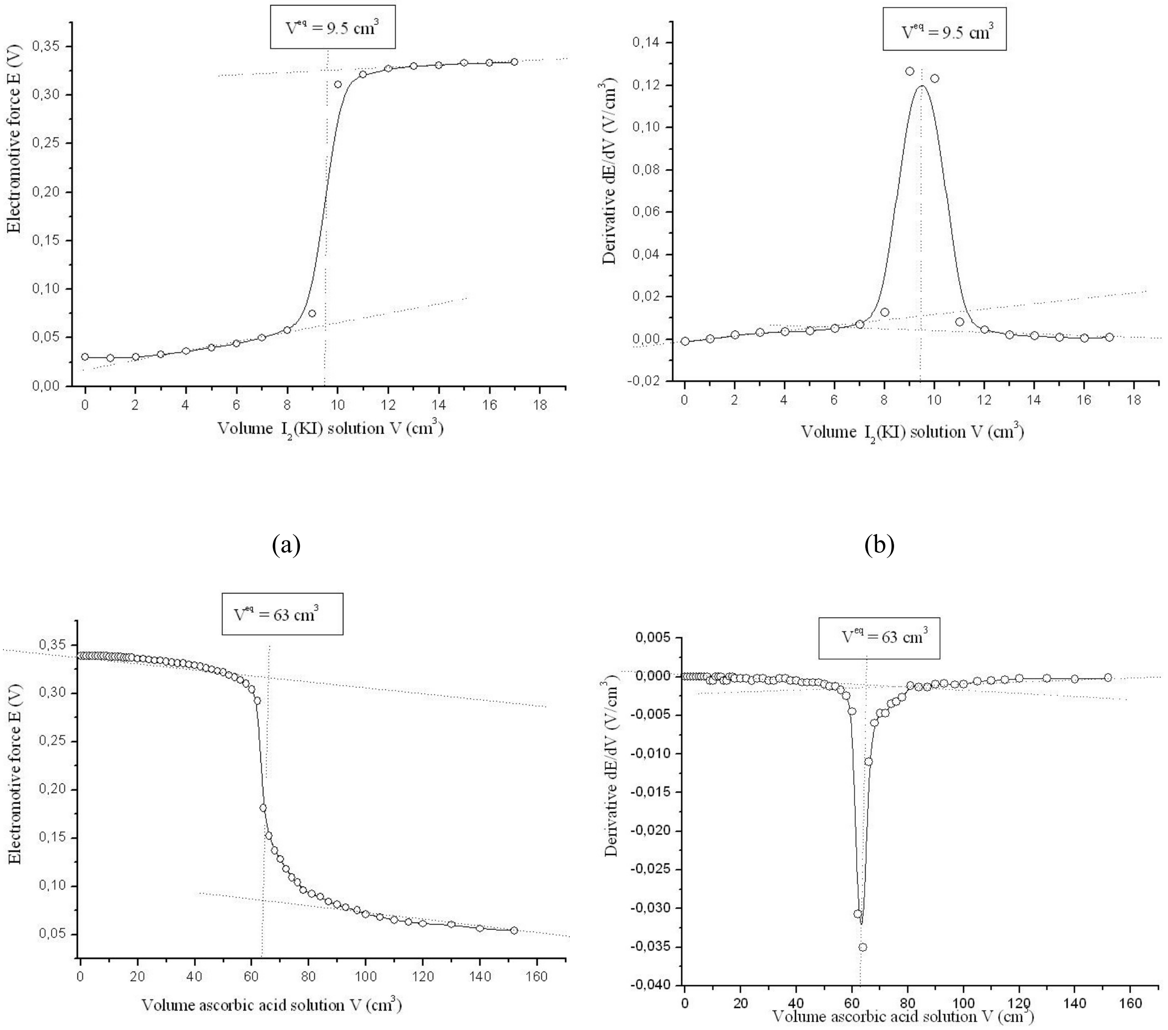

(a) (b)

(c) (d)

FIG. 2. (a,b) – Titration of 25 cm^3 of ascorbic acid solution (C = 0.025 mole/dm^3) by I_2 (in KI) solution (C = 0.05 mole/dm^3) in 20 cm^3 of acetic buffer CH_3COOH/CH_3COONa (1/1) – integral (a) and differential (b) curves. (c,d) – Titration of 30 cm^3 of I_2 (in KI) solution (C = 0.05 mole/dm^3) by ascorbic acid solution (C = 0.025 mole/dm^3) in 20 cm^3 of acetic buffer CH_3COOH/CH_3COONa (1/1) – integral (c) and differential (d) curves. E is potential of Pt electrode relative normal calomel electrode

So, change of Gibbs potential of the oxidation ascorbic acid reactions (3.1) and (3.2), correspondingly in forward directions is:

$$\Delta G_{3.1} \approx -56.0 \text{ kJ/mole}; \quad \Delta G_{3.2} \approx -59.8 \text{ kJ/mole}, \tag{8}$$

and equilibrium constant (K_{eq}) of both these reactions (at normal conditions) are sufficiently large: $\ln[K_{eq}] = 22 - 24$ rel.un.; $K_{eq-3.1} = 3.6 \cdot 10^9$, $K_{eq-3.2} = 2.6 \cdot 10^{10}$, and both reactions are practically irreversible. It is also proved by the form of titration curves Figs. 1(a–d) and 2(a–d).

3.4. Titration of fullerenol-d by hydrogen peroxide and molecular I_2 and vice versa

To investigate antioxidant properties of fullerenol-d acid we determined redox potential Ehat fixed value of hydrogen indicator $pH = 4.77$, which was set by acetate buffer solution CH_3COOH/CH_3COONa (molar relation

1/1). We used following electrochemical cells (see earlier):

$$\mathrm{Hg}, \mathrm{Hg_2Cl_2/KCl}\left(1\ \text{mole/dm}^3\right)/\text{investigated solution/Pt (compact)}, \tag{9}$$

where: Pt(compact) is working electrode; Hg, Hg_2Cl_2/KCl – reference normal calomel electrode with constant potential $E^0 = 0.281V$ [58]. Investigated solution in had two compositions:

$$/\text{fullerenol-d} + \text{oxy} - \text{fullerenol-d} + \mathrm{H_2O_2} + \mathrm{O_2} + \mathrm{H^+}\ (\text{acetate buffer})\ /; \tag{9.1}$$

$$/\text{fullerenol-d} + \text{oxy} - \text{fullerenol-d} + \mathrm{I_2} + \mathrm{I^-}(\mathrm{KI}) + \mathrm{H^+}\ (\text{acetate buffer})\ /. \tag{9.2}$$

The integral and differential curves of the titration of H_2O_2 by fullerenol-d and vice-versa fullerenol-d by H_2O_2 are represented in Fig. 3(a–d).

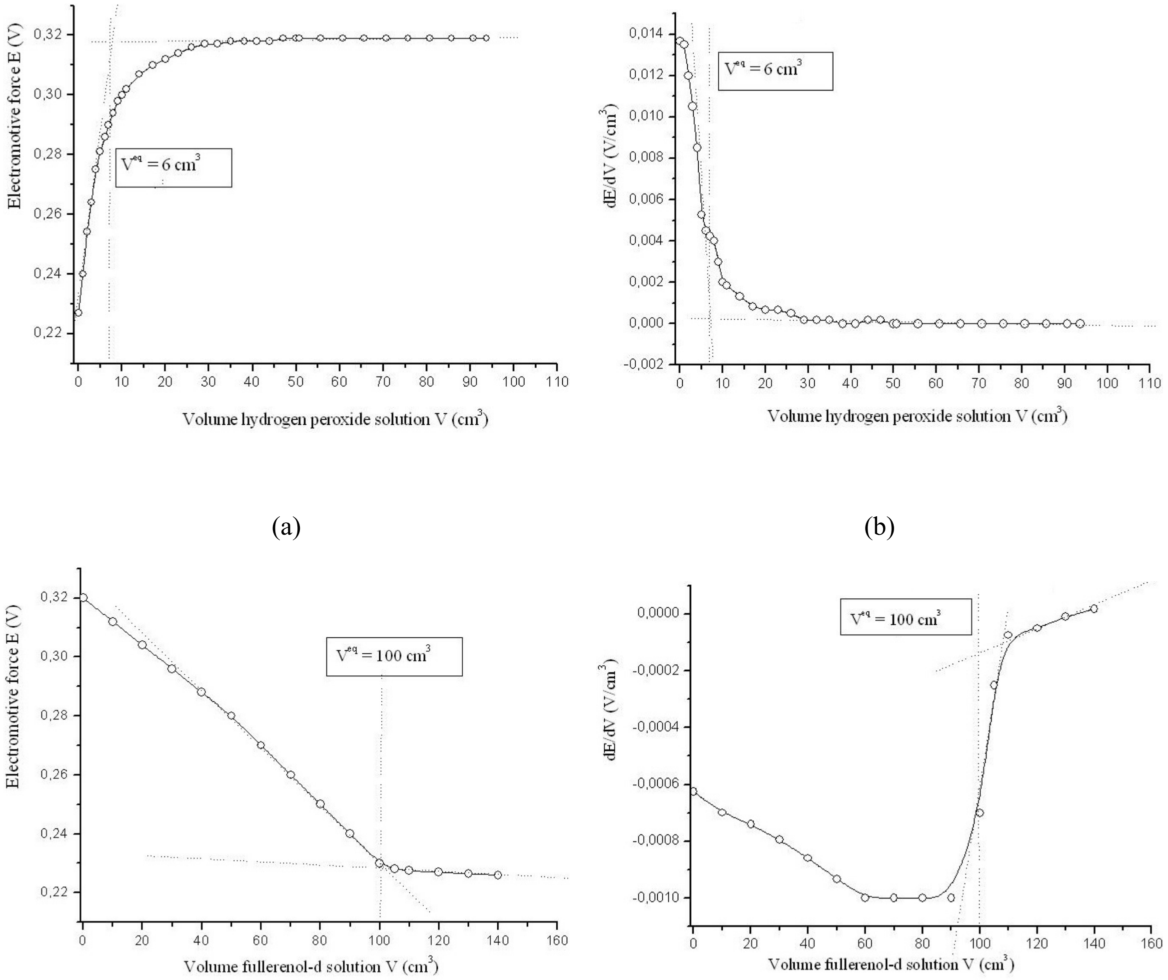

(a) (b)

(c) (d)

FIG. 3. (a,b) – Titration of 25 cm^3 fullerenol-d solution ($C = 0.005$ mole/dm^3) by the hydrogen peroxide solution ($C = 0.020$ mole/dm^3) in 20 cm^3 of acetic buffer CH_3COOH/CH_3COONa (1/1) – integral (a) and differential (b) curves. (c,d) – Titration of 25 cm^3 hydrogen peroxide solution ($C = 0.020$ mole/dm^3) by fullerenol-d solution ($C = 0.005$ mole/dm^3) in 20 cm^3 of acetic buffer CH_3COOH/CH_3COONa (1/1) – integral (c) and differential (d) curves. E is potential of Pt electrode relative normal calomel electrode

The integral and differential curves of the titration of I_2 (in KI) by fullerenol-d and vice-versa fullerenol-d by I_2 (in KI) are represented in Fig. 4(a–d).

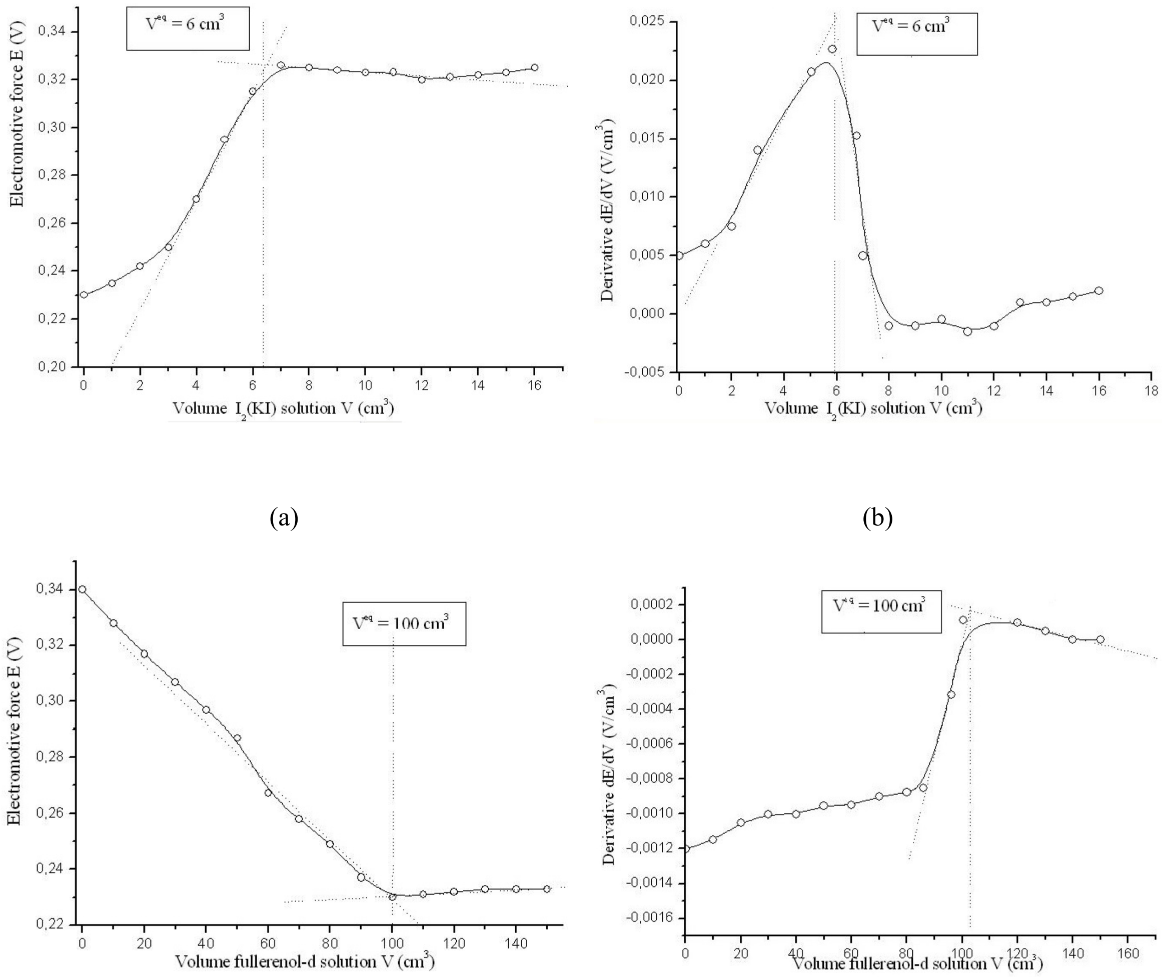

(a) (b)

(c) (d)

FIG. 4. (a,b) – Titration of 25 cm^3 fullerenol-d solution ($C = 0.005$ mole/dm^3) by I_2 (in KI) solution ($C = 0.020$ mole/dm^3) in 20 cm^3 of acetic buffer CH_3COOH/CH_3COONa (1/1) – integral (a) and differential (c) curves. (c,d) – Titration of 25 cm^3 of I_2 (in KI) solution ($C = 0.020$ mole/dm^3) by fullerenol-d solution ($C = 0.005$ mole/dm^3) in 20 cm^3 of acetic buffer CH_3COOH/CH_3COONa (1/1) – integral (c) and differential (d) curves. E is potential of Pt electrode relative normal calomel electrode

One can see nearly equivalent quantities of fullerenol-d and hydrogen peroxide and I_2 (KI), according to eq. (10):

$$C_{60}\,(OH)_{20-22}\,O_2 + 2H^+ + \bar{2}e \rightarrow C_{60}\,(OH)_{22-24}. \tag{10}$$

- Upper plateau $E_1 \approx 0.32V$ (Fig. 3(a)) and initial part of curve (Fig.3(c)) corresponds to the electrode semi-reaction (6.1): O_2 $+2H^{+\cdot}$ $+ 2\bar{e} \rightarrow H_2O_2$ (Pt) as earlier.
- Upper plateau $E_2 \approx 0.34V$ (Fig. 4(a)) and initial part of curve (Fig. 4(c)) corresponds to electrode semi-reaction (6.2): $I_2\,(\text{liquid}) + 2e \rightarrow 2I^-\,(\text{Pt})$.
- Bottom plateau in four curves $E_3 \approx 0.23V$ (Figs. 3(a,c), 4(a,c) corresponds to the same electrode semi-reaction (10).

Full oxidation-reduction reactions in electrochemical cell are:

$$C_{60}(OH)_{22-24} + O_2 = C_{60}(OH)_{20-22}O_2 + H_2O_2, \tag{11.1}$$

$$C_{60}(OH)_{22-24} + I_2 = C_{60}(OH)_{20-22}O_2 + 2HI. \tag{11.2}$$

Reaction (11.1) is the difference between semi-reaction (6.1) and (10), reaction (11.2) is the difference between semi-reaction (6.2) and (10).

Differences of electromotive forces in plateaus in Figs. 3(a,c) and 4(a,c) are, correspondingly:

$$\Delta E_{3.1} \approx 0.32 - 0.23 \approx 0.09V; \quad \Delta E_{3.2} \approx 0.34 - 0.23 \approx 0.11V. \tag{12}$$

So, change of Gibbs potential of the oxidation fullerenol-d reactions (11.1) and (11.2), correspondingly in forward directions is:

$$\Delta G_{3.1} \approx -17.3 \text{ kJ/mole}; \quad \Delta G_{3.2} \approx -21.2 \text{ kJ/mole}, \tag{13}$$

and equilibrium constant (K_{eq}) of both these reactions (at normal conditions) are not so large (as in the case of ascorbic acid): $\ln[K_{eq}] = 7.0 - 8.6$ rel.un.; $K_{eq-3.1} = 1.1 \cdot 10^3$, $K_{eq-3.2} = 5.4 \cdot 10^3$ rel.un. and both reactions are more or less reversible. It is also proved by the form of titration curves Figs. 3(a–d) and 4(a–d). One can see, that integral titration curves (3.1, 3.3, 4.1, 4.3) do not have sigmoid character. Differential curves (3.2, 3.4, 4.2, 4.4) meanwhile sometimes (with I_2 (KI) as oxidant) keep extremal character, but considerably less expressed than in the case of ascorbic acid. The values of the derivatives modules $/dE/dV\ (V/\text{cm}^3)\ /$ in the case of ascorbic acid are considerably higher than in the case of fullerenol-d (compare extremal $/dE/dV/$ values: 0.007, 0.018, 0.12, 0.35 V/cm^3 (Figs. 1(b,d), 2(b,d)) in the first case and $/dE/dV/$ values: absence, absence, 0.02, absence V/cm^3 (Figs. 3(b,d), 4(b,d)).

So, we can state, that:

- Fullerenol-d is more week antioxidant in the comparison with ascorbic acid, at least, in relation to free radicals, generated by hydrogen peroxide and iodine.
- Fullerenol-d, in the contrast with ascorbic acid, is capable to the reversible absorption of free radicals, other words fullerenol-d molecules are able to sorb free radical and then (after change of ox-red potential – Eh or hydrogen indicator – pH) are able to desorb these free radicals and recover. Such process can easily materialize at transition of modified fullerenes from the mouth to the stomach then to the intestines.
- As a consequence fullerenols-d molecules are able to multiply reversible absorption-desorption of some free radicals.

3.5. Pourbaix diagrams hydrogen-oxygen and iodine forms

We calculated Pourbaix Diagrams for hydrogen-oxygen and iodine forms, based on data from Tables 1, 2 [58]. Pourbaix Diagrams for hydroxy species and ascorbic acid are represented in Fig. 5 and for iodine forms and ascorbic acid – in Fig. 6. Green spots symbolize our experimental conditions, red curves – Pt electrode potential formation reactions in our experiment, moving along the spot occurs because the concentrations of oxidized and reduced species are changed in the titration processes.

4. Conclusions

The antioxidant properties of aqueous fullerenol-d solutions were investigated against free radicals, generated by hydrogen peroxide and molecular I_2 (KI). Measurement of fullerenol antioxidant activity was based on potentiometric titration of fullerenol solutions by hydrogen peroxide and molecular I_2 (KI) solutions and vice versa with compact Pt as working electrode. Ascorbic acid, a common and strong antioxidant – was utilized as a comparative agent. Pourbaix Diagrams $(pH - Eh)$ for hydrogen-oxygen and iodine forms were constructed. Fullerenol-d is a weaker antioxidant in comparison to ascorbic acid, but in contrast, fullerenols-d molecules are able to undergo multiply reversible absorption-desorption of some free radicals.

Acknowledgements

This work was supported by Russian Foundation of Basic Research – RFBR (Projects No. 16-08-01206, 18-08-00143) and Russian Found of the Support of Small Business (Project No. 24357).

TABLE 1. Oxygen-hydrogen oxidation-reduction reactions (water solutions, $T = 298$ K)

Reaction (field number of oxidized form// field number of reduced form) in Pourbaix diagrams (Fig. 5)	Nernst Equation	Standard Electro-Motive Force – E^0 (V)
$O^{\cdot}: +2H^+ + 2\bar{e} \rightarrow H_2O$(Pt) I/II	$E = E^0 + RT/2F\ln[a_{O:}a^2_{H^+}/a_{H_2O}] =$ $E^0 - 0.059pH + 0.295\lg[a_{O:}/a_{H_2O}]$	2.422
$O_3^{\cdot} + 2H^+ + 2\bar{e} \rightarrow O_2+H_2O$(Pt) III//IV	$E = E^0 + RT/2F\ln[a_{O_3}a^2_{H^+}/a_{H_2O}P_{O_2}] =$ $E^0 - 0.059pH + 0.295\lg[a_{O_3}/a_{H_2O}P_{O_2}]$	2.070
$OH^{\cdot} + \bar{e} \rightarrow OH^-$(Pt) V//VI	$E = E^0 + RT/F\ln[a_{OH}/a_{OH^-}] =$ $E^0 + 0.059(14 - pH) + 0.059\lg a_{OH} =$ $E^0 + 0.826 - 0.059pH + 0.059\lg a_{OH}$	2.020
$H_2O_2^{\cdot} + 2H^+ + 2\bar{e} \rightarrow 2H_2O$(Pt) VII/II	$E = E^0 + RT/2F\ln[a_{H_2O_2}a^2_{H^+}/a^2_{H_2O}] =$ $E^0 - 0.059pH + 0.0295\lg[a_{H_2O_2}a^2_{H^+}/a^2_{H_2O}]$	1.776
$O_3^{\cdot}+H_2O+2\bar{e} \rightarrow O_2 + 2OH^-$(Pt) VIII//IX	$E = E^0 + RT/2F\ln[a_{O_3}a_{H_2O}/a^2_{OH^-}P_{O_2}] =$ $E^0 + 0.059(14 - pH) + 0.0295\lg[a_{O_3}a_{H_2O}/P_{O_2}] =$ $E^0 + 0.826 - 0.059pH + 0.295\lg[a_{O_3}/a_{H_2O}P_{O_2}]$	1.240
$O_2 + 4H^{+\cdot} + 4\bar{e} \rightarrow 2H_2O$(Pt) X/II	$E = E^0 + RT/4F\ln[P_{O_2}a^4_{H^+}/a^2_{H_2O}] =$ $E^0 - 0.059pH + 0.01475\lg[P_{O_2}/a^2_{H_2O}]$	1.229
$O_2\,(g) + 2H^+$(Pt)$+\bar{2}e \rightarrow H_2O_2\,(g)$ XI//XII	$E = E^0 + RT/2F\ln\left[P_{O_2}/a\left(H^+\right)^2/P_{H_2O_2}\right]$ $E^0 - 0.059pH + 0.0295\lg\left[P_{O_2}/X_{H_2O_2}K^H_{H_2O_2}\right]$	0.839
$C_{60}\,(OH)_{20\div22}O_2 + 2H^+ + 2\bar{e} \rightarrow C_{60}\,(OH)_{22\div24}$ XIII//XIV	$E = E^0 - 0.059pH+$ $0.0295\lg\left(a_{\text{oxy-fullerenol-d}}/a_{\text{fullerenol-d}}\right)$	0.797
$O_2 + 2^{+\cdot} + 2\bar{e} \rightarrow H_2O_2(l)$(Pt) XV/XVI	$E = E^0 + RT/2F\ln[P_{O_2}a^2_{H^+}/a_{H_2O_2}] =$ $E^0 - 0.059pH + 0.0295\lg[P_{O_2}/a_{H_2O_2}]$	0.682
dehydroascorbic(acid) $+2H^++$ $2\bar{e} \rightarrow$ ascorbic(acid) XVII//XVIII	$E = E^0 - 0.059pH+$ $0.0295\lg\left(a_{\text{dehydroascorbic(acid)}}/a_{\text{ascorbic(acid)}}\right)$	0.613
$1/2O_2 + 2H_2O^{\cdot} + 2\bar{e} \rightarrow 2OH^-$(Pt) XIX/VI	$E = E^0 + RT/2F\ln[P^{1/2}_{O_2}a^2_{H_2O}/a^2_{OH^-}] =$ $E^0 + 0.059(14 - pH) + 0.0295\lg[P^{1/2}_{O_2}a^2_{H_2O}] =$ $E^0 + 0.826 - 0.059pH + 0.0295\lg[P^{1/2}_{O_2}a^2_{H_2O}]$	0.401
$H^{+\cdot} + \bar{e} \rightarrow 1/2H_2$(Pt) XX//XXI	$E = E^0 + RT/F\ln[a_{H^+}/P^{1/2}_{H_2}] =$ $E^0 - 0.059pH - 0.0295\lg[P_{H_2}]$	0.000
$2H_2O+2\bar{e} \rightarrow H^{\cdot} + 2OH^-$(Pt) XXII//XXIII	$E = E^0 + RT/2F\ln[a^2_{H_2O}/a_{H^{\cdot}}a^2_{OH^-}] =$ $E^0 + 0.059(14 - pH) + 0.0295\lg[a^2_{H_2O}/a_{H^{\cdot}}] =$ $E^0 + 0.826 - 0.059pH + 0.0295\lg[a^2_{H_2O}/a_{H^{\cdot}}]$	−0.828

Where: $K^H_{H_2O_2}$, $X(H_2O_2)$ – Henry constant and molar fraction of H_2O_2 in liquid phase, (l) and (g) – liquid and gaseous phase states of component; a_i, p_i – activity and partial pressure (atm.) of i-th component.

TABLE 2. Iodine oxidation-reduction reactions (water solutions, $T = 298$ K)

Reaction (field number of oxidized form// field number of reduced form) in Pourbaix diagrams (Fig. 6)	Nernst Equation	Standard Electro-Motive Force – E^0 (V)
$IO_3^- + 6H^+ + 5\bar{e} \rightarrow 1/2I_2 + 3H_2O(Pt)$ I//II	$E = E^0 + RT/5F \ln[a_{IO_3^-} a_{H^+}^6 / a_{I_2}^{1/2} a_{H_2O}^3] =$ $E^0 + 0.0118 \lg[a_{IO_3^-} / a_{I_2}^{1/2} a_{H_2O}^3] - 0.0708pH$	1.195
$C_{60}\,(OH)_{20 \div 22}O_2 + 2H^+ +$ $2\bar{e} \rightarrow C_{60}\,(OH)_{22 \div 24}$ III/IV	$E = E^0 - 0.059pH +$ $0.0295lg\,(a_{\text{oxy-fullerenol-d}} / a_{\text{fullerenol-d}})$	0.797
$1/2I_2(l)^{\cdot\cdot} + \bar{e} \rightarrow I^-(Pt)$ IV/V	$E = E^0 + RT/F \ln[a_{I_2}^{1/2} / a_{I^-}] =$ $E^0 + 0.059 \lg[a_{I_2}^{1/2} / a_{I^-}]$	0.628
dehydroascorbic(acid) $+2H^+ +$ $2\bar{e} \rightarrow$ ascorbic(acid) VI/VII	$E = E^0 - 0.059pH +$ $0.0295 \lg\,(a_{\text{dehydroascorbic(acid)}} / a_{\text{ascorbic(acid)}})$	0.613
$1/2I_2(cr)^{\cdot} + \bar{e} \rightarrow I^-(Pt)$ VIII/V	$E = E^0 + RT/F \ln[1/a_{I^-}] =$ $E^0 - 0.059 \lg a_{I^-}$	0.536
$I_3^{-\cdot} + 2\bar{e} \rightarrow 3I^-(Pt)$ IX/V	$E = E^0 + RT/2F \ln[a_{I_3^-} / a_{I^-}^3] =$ $E^0 + 0.0295 \lg[a_{I_3^-} / a_{I^-}^3]$	0.536

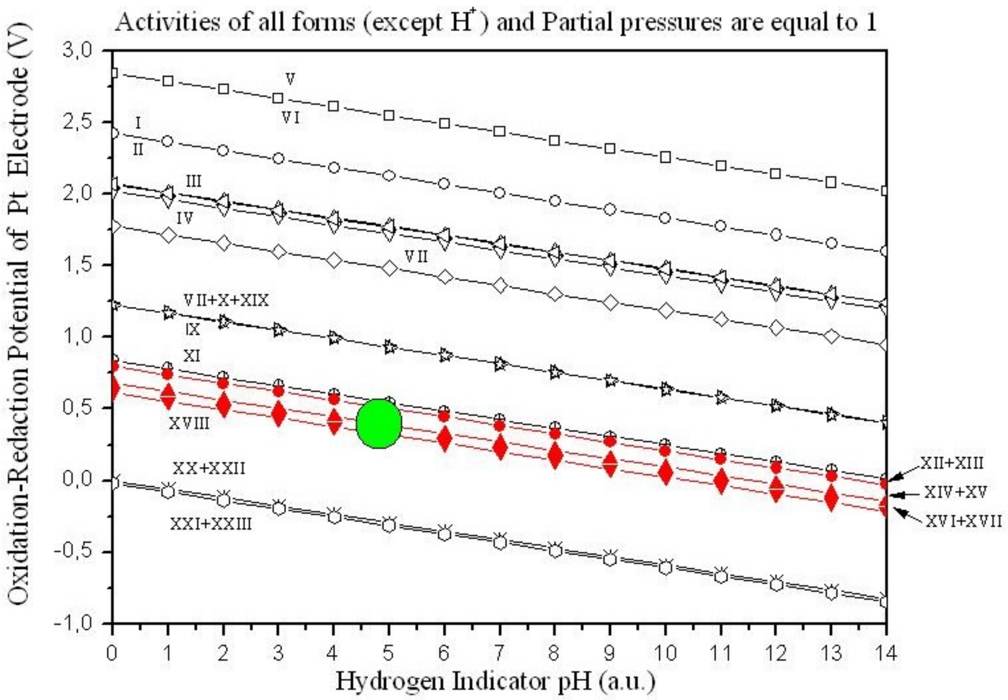

FIG. 5. Pourbaix Diagrams for hydrogen-oxygen forms and ascorbic acid (green spot symbolizes our experimental conditions, red curves – Pt electrode potential formation reactions in our experiment, moving along the spot occurs because oxidized and reduced forms concentrations are changed in the titration)

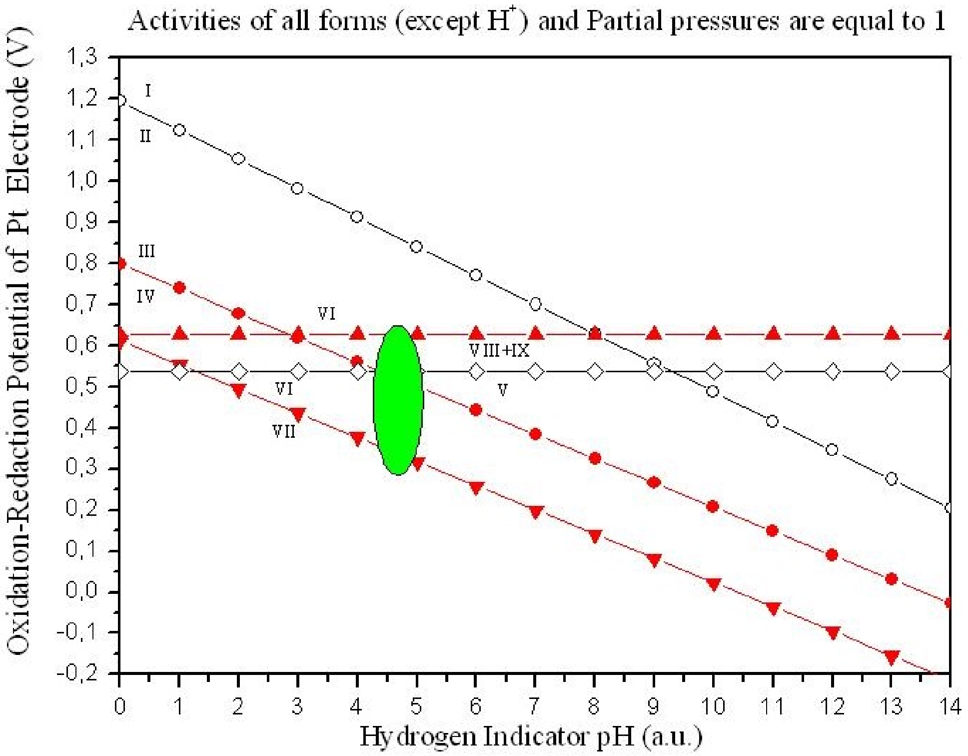

FIG. 6. Pourbaix Diagrams for iodine forms and ascorbic acid (green spot symbolizes our experimental conditions, red curves – Pt electrode potential formation reactions in our experiment, moving along the spot occurs because oxidized and reduced forms concentrations are changed in the titration)

References

[1] Li J., Takeuchi A., Ozawa M., et al. C_{60} Fullerol Formation catalysed by Quaternary Ammonium Hydroxides. *J. Chem. Soc. Commun.*, 1993, **23**, P. 1784–1785.

[2] Pinteala M., Dascalu A., Ungurenasu C. Binding fullerenol $C_{60}(OH)_{24}$ to dsDNA. *Int. J. Nanomedicine*, 2009, **4**, P. 193–199.

[3] Chiang L.Y., Bhonsle J.B., et al. Efficient one-flask synthesis of water-soluble [60] fullerenols. *Tetrahedron*, 1996, **52**, P. 4963–4672.

[4] Chiang L.Y., Upasani R.B., Swirczewski J.W. Versatile nitronium chemistry for C_{60} fullerene functionalization. *J. Am. Chem. Soc.*, 1992, **114**, P. 10154–10157.

[5] Meier M.S., Kiegiel J. Preparation and characterization of thefullerene diols 1,2–$C_{60}(OH)_2$, 1,2–$C_{70}(OH)_2$, and 5,6–$C_{70}(OH)_2$. *Org. Lett.*, 2001, **3**, P. 1717–1719.

[6] Szymanska L., Radecka H., Radecki J., Kikut-Ligaj D. Fullerene modified supported lipid membrane as sensitive element of sensor for odorants. *Biosens. Bioelectron*, 2001, **16**, P. 911–915.

[7] Mirkov S.M., Djordjevic, A.N., et al. Nitric oxidescavenging activity of polyhydroxylated fullerenol, $C_{60}OH_{24}$. *Nitric Oxide*, 2004, **11**, P. 201–207.

[8] Kokubo K., Matsubayashi K., et al. *ACS Nano*, 2008, **2**, P. 327–333.

[9] Anderson R., Barron A.R. Reaction of hydroxyfullerene with metal salts: a route to remediation and immobilization. *J. Am. Chem. Soc.*, 2005, **127** (30), P. 10458–10459.

[10] Kokubo K., Shirakawa S., et al. Facile and scalable synthesis of a highly hydroxylated water-soluble fullerenol as a single nanoparticle. *Nano Research*, 2011, **4** (2), P. 204–215.

[11] Yao L., Kang F., Peng Q., Yang X. An improved method for fullerol preparation based on dialysis. *Chinese Journal of Chemical Engineering*, 2010, **18** (5), P. 876–879.

[12] Huang H.-M., Ou H.-C., Hsieh S.-J., Chiang L.-Y. Blockage of amyloid beta peptide-induced cytosolic free calcium by fullerenol-1, carboxylate C_{60} in PC12 cells. *Life Sciences*, 2000, **66** (16), P. 1525–1533.

[13] Roberts J.E., Wielgus A.R., et al. Phototoxicity and cytotoxicity of fullerol in human lens epithelial cells. *Toxicology and Applied Pharmacology*, 2008, **228** (1), P. 49–58.

[14] Isakovic A., Markovic Z., Todorovic-Marcovic B., et al. Distinct cytotoxic mechanisms of pristine versus hydroxylated fullerene. *Toxicological Sciences*, 2006, **91** (1), P. 173–183.

[15] Johnson-Lyles D.N., Peifley K., Lockett S., et al. Fullerenol cytotoxicity in kidney cells is associated with cytoskeleton disruption, autophagic vacuole accumulation, and mitochondrial dysfunction. *Toxicology and Applied Pharmacology*, 2010, **248** (3), P. 249–258.

[16] Wang S., He P., et al. Novel and efficient synthesis of water-soluble [60]fullerenol by solvent-free reaction. *Synthetic Communications*, 2005, **35** (13), P. 1803–1808.

[17] Piotrovskij L.B., Kiselev O.I. *Fullerenes in biology*. Rostok: Saint Petersburg, 2006.

[18] Semenov K.N., Charykov N.A., Keskinov V.A. Fullerenol-70-d: Synthesis, identification, poly-thermal solubility and density of water solutions. *Nanosystems: physics, chemistry, mathematics*, 2012, **3** (6), P. 146–156.

[19] Assemi S., Tadjiki S., et al. Aggregation of fullerol $C_{60}(OH)_{24}$ nanoparticles as revealed using flow field-flow fractionation and atomic force microscopy. *Langmuir*, 2010, **26** (20), P. 16063–16070.

[20] Vileno B., Marcoux P.R., et al. Spectroscopic and photophysical properties of a highly derivatized C_{60} fullerol. *Advanced Functional Materials*, 2006, **16** (1), P. 120–128.

[21] Schneider N.S., Darwish A.D., et al. Formation of fullerols via hydroboration of fullerene-C_{60}. *Journal of the Chemical Society, Chemical Communications*, 1994, **4**, P. 463–464.

[22] Semenov K.N., Charykov N.A., Letenko D.G., et al. Solubility and Some Properties of Aqueous Solutions of Fullerenol-d and Crystal Hydrates. *Rus. J. of Appl. Chem.*, 2011, **84** (1), P. 44–49.

[23] Semenov K.N., Charykov N.A., Letenko D.G., et al. Electrochemical Properties of Aqueous Solutions of Fullerenol-d. *Rus. J. of Appl. Chem.*, 2011, **84** (1), P. 79–83.

[24] Letenko D.G., Nikitin V.A., et al. Study of Aqueous Solutions of Fullerenol-d by the Dymamic Light Scattering Method. *Rus. J. of Appl. Chem.*, 2011, **84** (1), P. 50–53.

[25] Ioutsi V., Sokolov S.A., Semivrazskhaya O.O., et al. Synthesis and antioxidative properties of some fullerene C_{60} derivatives. *Reports RGMU. Medical biological problems*, 2012, **5**, P. 76–82.

[26] Zhang J.-M., Yang W., He P., Zhu S.-Z. Efficient and convenient preparation of water-soluble fullerenol. *Chinese Journal of Chemistry*, 2004, **22** (9), P. 1008–1011.

[27] Semenov K.N., Charykov N.A., Keskinov V.A. Fullerenol Synthesis and Identification. Properties of Fullerenol Water Solutions. *J. Chem. Eng. Data*, 2011, **56**, P. 230–239.

[28] Semenov K.N., Charykov N.A., et al. The Synthesis and Identification of Mixed Fullerenol Prepared by the Direct One-Stage Oxidation of Fullerene Black. *Rus. J. Phys. Chem.*, 2011, **85** (6), P. 1009–1015.

[29] Semenov K.N., Charykov N.A., Letenko D.G., et al. Synthesis and protecting action of fullerenol-d. II. Modification of water soluble priming enamel. *Phys. Chem. of Surface and Metal Protection*, 2012, **48** (3), P. 286–292.

[30] Letenko D.G., Nikitin V.A., et al. Conductivity of Aqueos Solutions of Fullerol Synthesized by Direct Oxidation. *Rus. J. Phys. Chem.*, 2012, **86** (12), P. 1806–1813.

[31] Semenov K.N., Charykov N.A. Solubility Diagram of a Fullerenol-dNaClH_2O System at 25 C. *Rus. J. Phys. Chem.*, 2012, **86** (10), P. 1636–1639.

[32] Semenov K.N., Charykov N.A., et al. Synthesis of Fullerenol-70-d by Direct Oxidation and Its Identification. *Rus. J. Of Gen. Chem.*, 2013, **83** (4), P. 674–678.

[33] Semenov K.N., Kanterman I.G., et al. SolidLiquid Phase Equilibria in the Fullerenol-dCuCl_2H_2O System at 25 C. *Russian Journal of Physical Chemistry*, 2014, **88** (6), P. 1073–1076.

[34] Semenov K.N., Kanterman I.G., Charykov N.A., et al. Solubility in ternary system fullerenol-d-uranil sulphate–water at 25 . *Radiochemistry*, 2014, **56** (5), P. 421–422. (In Russian)

[35] Zolotarev A.A., Lushin A.I., et al. Impact resistance of cement and gypsum plaster nanomodified by water-soluble fullerenols. *Industrial and engineering chemical research*, 2013, **52**, P. 14583–14591.

[36] Semenov K.N., Keskinov V.A., et al. The fullerenol-d solubility in the fullerenol-d-inorganic salt-water ternary systems at 250C. *Industrial and engineering chemical research*, 2013, **52**, P. 16095–16100.

[37] Semenov K.N., Kanterman I.G., et al. SolidLiquid Phase Equilibria in the Fullerenol-d-CuCl_2-H_2O System at 25 C. *Russian Journal of Physical Chemistry*, 2014, **88** (6), P. 1073–1076.

[38] Semenov K.N., Charykov N.A., Murin I.V., Pukharenko Yu.V. Physico-chemical properties of the fullerenol-70 water solutions. *J. of Molecular Liquids*, 2015, **202**, P. 1–8.

[39] Tyurin D.P., Semenov K.N., et al. Dissociation of Fullerenol-70-d in Aqueous Solutions and Their Electric Conductivity. *Russian Journal of Physical Chemistry A*, 2015, **89** (5), P. 771–775.

[40] Panova G.G., Ktitorova I.N., et al. Impact of polyhydroxy fullerene (fullerol or fullerenol) on growth and biophysical characteristics of barley seedlings in favourable and stressful conditions. Plant Growth Regulation. *An International Journal on Plant Growth and Development*, 2015, **77** 2016, **79** (3), P. 309–318.

[41] Charykov N.A., Semenov K.N., et al. Excess thermodynamic functions in aqueous systems containing soluble fullerene derivatives. *J. of Molecular Liquids*, 2018, **256**, P. 305–311.

[42] Djordjevic A., Srdjenovic B., et al. Review of Synthesis and Antioxidant Potential of Fullerenol Nanoparticles. *Journal of Nanomaterials*, 2015, 567073, 15 pp.

[43] Lao F., Chen L., Li W., et al. Fullerene nanoparticles selectively enter oxidation-damaged cerebral microvessel endothelial cells and inhibit JNK-related apoptosis. *ACS Nano*, 2009, **3** (11), P. 3358–3368.

[44] Yin J.-J., Lao F., Fu P.P., et al. The scavenging of reactive oxygen species and the potential for cell protection by functionalized fullerene materials. *Biomaterials*, 2009, **30** (4), P. 611–621.

[45] Caputo F., De Nicola M., Ghibelli L. Pharmacological potential of bioactive engineered nanomaterials. *Biochemical Pharmacology*, 2014, **92** (1), P. 112–130.

[46] Djordjevic A., Canadanovic-Brunet J.M., Vojinovic-Miloradov M., Bogdanovic G. Antioxidant properties and hypothetic radical mechanism of fullerenol $C_{60}(OH)_{24}$. *Oxidation Communications*, 2004, **27** (4), P. 806–812.

[47] Kokubo K. *Water-Soluble Single-Nano Carbon Particles: Fullerenol and Its Derivatives*, InTech, 2012.

[48] Kato S., Aoshima H., Saitoh Y., Miwa N. Highly hydroxylated or -cyclodextrin-bicapped water-soluble derivative of fullerene: the antioxidant ability assessed by electron spin resonance method and -carotene bleaching assay. *Bioorganic and Medicinal Chemistry Letters*, 2009, **19** (18), P. 5293–5296.

[49] Ueno H., Yamakura S., et al. Systematic evaluation and mechanistic investigation of antioxidant activity of fullerenols using carotene bleaching assay-carotene bleaching assay. *Journal of Nanomaterials*, 2014, **2014**, 802596, 7 pp.

[50] Dordević A., Bogdanović G. Fullerenol: a new nanopharmaceutic? *Archive of Oncology*, 2008, **16** (3–4), P. 42–45.

[51] Pickering K.D., Wiesner M.R. Fullerol-sensitized production of reactive oxygen species in aqueous solution. *Environmental Science and Technology*, 2005, **39** (5), P. 1359–1365.

[52] Zhao B., Bilski P.J., et al. Photo-induced reactive oxygen species generation by different water-soluble fullerenes (C_{60}) and their cytotoxicity in human keratinocytes. *Photochemistry and Photobiology*, 2008, **84** (5), P. 1215–1223.

[53] Zhao B., He Y.-Y., et al. Difference in phototoxicity of cyclodextrin complexed fullerene $[(\gamma\text{-CyD})_2/C_{60}]$ and its aggregated derivatives toward human lens epithelial cells. *Chemical Research in Toxicology*, 2009, **22** (4), P. 660–667.

[54] Pourbaix M. Thermodynamics and corrosion. *Corrosion Science*, 1990, **3** (1), No. 10, P. 963–988.

[55] Remi G. *Course of Inorganic Chemistry, volume 2*. Moscow, Mir, 1955. (In Russian)

[56] Ball E.G. Studies on oxidation reduction. XXIII. Ascorbic acid. *J. Biol. Chem.*, 1939, **118**, P. 219–239.

[57] Borsook H., Davenport H.W., et al. The Oxidation of Ascorbic Acid and Its in Vitro and in Vivo. *J. Biol. Chem.*, 1937, **117**, (1), P. 237–279.

[58] *Brief reference book of physical and chemical quantities*. Ed.: A.A. Ravdel, A.M. Ponomareva. Moscow, OOO TID Az-book, 2009, 237 pp.

NANOSYSTEMS: PHYSICS, CHEMISTRY, MATHEMATICS, 2018, 9 (6), P. 811–822

Influence of cadmium acetate salt concentration on the composition, structure and morphology of $Cd_xPb_{1-x}S$ solid soluton films

I. V. Vaganova[1], L. N. Maskaeva[1,2], V. F. Markov[1,2], V. I. Voronin[3], V. G. Bamburov[4]

[1]Ural Federal University named after the first President of Russia B. N. Yeltsin. Mira St., 19. Yekaterinburg, 620002, Sverdlovsk Region, Russia

[2]Ural State Fire Service Institute of Emergency Ministry of Russia. Mira St., 22, Yekaterinburg, 620022, Sverdlovsk Region, Russia

[3]Institute of Metal Physics URAN named after M. N. Miheev. S. Kovalevsloy St., 18, Yekaterinburg, 620137, Sverdlovsk Region, Russia

[4]Institute of Solid State Chemistry URAN, Pervomaiskaya St. 91, Yekaterinburg, 620990, Sverdlovsk Region, Russia

irina_vaganova@inbox.ru, mln@ural.ru, v.f.markov@urfu.ru, voronin@imp.uran.ru, bam@ihim.uran.ru

DOI 10.17586/2220-8054-2018-9-6-811-822

Films of supersaturated substitutional $Cd_xPb_{1-x}S$ ($0.03 \leq x \leq 0.22$) solutions with a $B1$-type structure based on lead sulfide cubic lattice were produced by chemical bath co-deposition of CdS and PbS with various concentrations of cadmium acetate in the ammonium citrate reaction mixtures. The results of X-ray measurements showed that with increasing cadmium acetate concentration the microstrains increase in the deposited layers and the crystallites have [200] preferred orientation and pronounced volume anisotropy. It is shown that the obtained films are nanostructured. Depending on the solid solution composition, the layers consist of crystallites with average sizes 200 – 1000 nm. These, in turn, are formed from initial nanoparticles with diameter 50 – 70 nm. The conductivity of the films decreases with increasing cadmium-sulfide content. The synthesized films are photosensitive without any special sensitization procedure in the visible and near-infrared spectral ranges. The maximum of spectral characteristic and the long-wave limit of the photo-response of $Cd_xPb_{1-x}S$ films move smoothly toward the short-wave spectral range from 3.1 to 1.6 μm and from 2.5 to 1.2 μm, respectively, with an increase in the substitution level of lead into cadmium in PbS lattice correspondently.

Keywords: chemical bath co-deposition, solid solution films, x-ray diffraction, microstrains, crystallite size.

Received: 2 November 2018

Revised: 7 November 2018

1. Introduction

The contemporary state of the rapidly developing optoelectronics and nanoelectronics, sensor production, and solar power engineering arouses considerable interest in $Cd_xPb_{1-x}S$ substitutional solid solution thin films of varying compositions. The semiconducting properties of these films are promising as functional materials.

Varying the composition of $Cd_xPb_{1-x}S$ substitutional solid solutions allows control of their structure, morphology, and electrophysical properties in a rather wide range, from the wide-bandgap cadmium sulfide ($E_g = 2.42$ eV) to a comparatively narrow-bandgap lead sulfide ($E_g = 0.41$ eV) [1–4]. The unique optical characteristics of these metal sulfides give access to different spectral ranges of photosensitivity: cadmium sulfide is one of the most effective materials in a visible light spectrum (500 – 700 nm) and lead sulfide is characterized by both visible and near-infrared spectral ranges (400 – 3100 nm). The variety of the properties for these metal sulfide-forming solid solutions provides rationale for their usage in the fabrication of different electronic devices.

Both individual metal sulfides are challenging materials for solar power engineering. Cadmium sulfide proved to be a suitable material for use as a window layer in solar radiation converters: CdTe/CdS [7–9] and CIGS/CdS [10]. Lead sulfide is effectively used as an absorbing material [11]. Therefore, recently, there has been observed an increasing interest in creation and investigation of thin film heterostructures with the *p–n* transition in the CdS–PbS system for production of solar cells [11, 12]. It was observed that, a solar cell with the structure ITO/CdS/PbS, covered with a transparent conductive layer of ITO (indium tin oxide), was observed to be more promising conversion efficiency compared with some other similar solar cells [12]. In addition, an enhanced conversion efficiency of 3.10 % was demonstrated for PbS/CdS thin film solar cells without the involvement of quantum dots by focusing on the origin of the enhancement [13].

A thin film solar cell in which chemically deposited layer of cadmium sulfide was doped with silver ITO/CdS-Ag/PbS/graphite operates in a spectral range from visible to near-infrared spectral ranges and is characterized by a short circuit current of 85.2 mA, maximum voltage of 0.6 V, and maximum power of 26.3 μW [14]. The efficiency of ITO/Cu-CdS/PbS/Ag solar cells on the glass substrate increased from 0.52 % to 1.38 % with an increase in the PbS film thickness from 528.3 to 1250.8 nm [15].

It was proved that for the absorbing semiconducting layer in solar cells, the optimum bandgap width is 1.5 eV, which can be achieved by production of solid solutions in the form of ternary $Cd_{1-x}Pb_xS$ compounds [16]. By varying their composition, the optical and semiconducting properties can be optimized, thus providing an efficiency coefficient of conversion of more than 40 %.

It was determined that thin films of pure cadmium sulfide are not stable with respect to the photoconductivity (the experiment was performed over two years) compared to the solid $Pb_xCd_{1-x}S$ solutions [6] and those based on them [17]. In certain conditions, due to limited mutual solubility of CdS and PbS [18], lead ions are displaced on the surface of the film. In this way, the CdS–PbS material was designated which consists of a wide bandgap matrix with a solid solution of PbS into CdS, and narrow bandgap low resistant inclusions of solid solution of CdS into PbS [19]. According to the previous work [20], the lead content in the wide bandgap matrix is not higher than 2 atom %. Generation processes occur predominantly in the wide bandgap matrix, and the recombination is largely related to the narrow bandgap inclusions. In particular, it is confirmed by the data on the film luminescence in the infrared range [21]. Additionally, it is noted that polycrystal layers based on the heterogeneous material CdS–PbS have another useful property such as high photosensitivity [19].

One more characteristic of heterogeneous compounds in the CdS–PbS system is their high irradiation stability [22–24]. Exclusively high irradiation stability (to 108 R) of detectors was observed based on the $Cd_xPb_{1-x}S$ solid solution films [6]. It allows their use in radiation hazardous facilities experiencing both constant and spontaneous radiation loads.

As-deposited $Cd_xPb_{1-x}S$ thin film solid solutions are characterized by anomalously high level of photo response in the visible and near-infrared spectral range without using sensitization methods at relatively low time constant values. This allows employment of these compounds to produce highly-sensitive fast photo detectors [25]. The challenge of using $Cd_xPb_{1-x}S$ nanocrystal as a material for distant earth sounding in the infrared spectral range, and detecting natural or man-made objects radiating at wavelengths of 400 – 3100 nm [5].

Ternary thin film compounds in the PbS–CdS system are polycrystalline and have a limited range of mutual solubility based on both a cubic structure of the sphalerite type (space group $F\bar{4}3m$) and a hexagonal structure of the wurtzite type (space group $P6_{3mc}$) on the side of CdS and a cubic structure of the halite type (modification $B1$) on the side of PbS [26,27].

According to the high temperature phase diagram of the pseudo binary PbS–CdS system [28], the solubility of CdS in the lead sulfide at 873 K is $\sim$ 4.5 mol.% and for the lead sulfide in CdS, less than 0.1 mol.% even at 1203 K. Therefore, it can be suggested that at below 373 K, the solubility of CdS in the galena PbS is negligible and PbS in the sphalerite CdS, practically non-existent.

However, by “soft chemistry” methods it may be possible to obtain supersaturated PbS–CdS substitutional solutions with much wider ranges of compositions than the corresponding results of the high temperature phase diagrams at any temperature. Vesnin reported the possibility of low-temperature formation of supersaturated substitutional solid solutions in view of the low activation energy values for this process [29,30]. Such phases are thermodynamically unstable due to either kinetic obstacles or any other features of the system often are retained for indefinite periods at relatively high temperatures. That is why it may be possible to produce substitutional solid solutions with different compositions, whose formation is impossible under equilibrium conditions.

In particular, according to the literature data, the use of the colloid chemical method of solid solution synthesis $Cd_xPb_{1-x}S$ allows one to produce compounds quite enriched in the substitutional component at a temperature below 373 K. Thus, at 353 K the $Cd_xPb_{1-x}S$ films with the CdS content up to 16 mol.% were produced by the chemical bath deposition [31,32]. Markov *et al.* reported the synthesis of the $Cd_xPb_{1-x}S$ film with the CdS content up to 21 mol.%. [33,34].

Colloid chemical methods for the production of solid solutions (CDB) are quite popular today. Thus, in previous work [35], the authors managed to produce $Cd_xPb_{1-x}S$ solid solution films with the maximum fraction of lead substituting for cadmium in the crystal lattice of PbS, which is equal to 0.15, by chemical deposition from the citrated ethylenediamine system with varying temperature, pH, and reagents. Recently, it was reported that the synthesized $Cd_xPb_{1-x}S$ solid solution films with a value of x of up to 0.21 are highly supersaturated and metastable [31–34, 36, 37]. As a consequence, the continuous contraction of the lattice with increasing cadmium content is shown to be evidence for the formation in nanocrystals of ternary $Cd_xPb_{1-x}S$ compounds, and also the researches considered changes in the properties of the synthesized films [38,39]. Thus, the deposited Pb–Cd–S films, enriched in cadmium, have a high absorption coefficient (10^4 cm^{-1}) and direct type of transition with the bandgap width that is continuously decreasing from 2.47 to 0.49 eV with an increase in the lead content [39].

In most publications, it is noted that in order to provide suitable functional properties (photoluminescence, photosensitivity), their sensitization requires thermal annealing of the as-deposited $\mathrm{Cd}_x\mathrm{Pb}_{1-x}\mathrm{S}$ solid solution layers under aerobic conditions. It was observed that after annealing of chemically deposited $\mathrm{Cd}_{0.5}\mathrm{Pb}_{0.5}\mathrm{S}$ films, the structural, morphological and optical properties were changed. In particular, the bandgap width of the samples decreased from 2.6 to 2.05 eV [40]. With an increase in annealing temperature to 573 K, the decreasing of bandgap width is observed from 1.59 to 1.55 eV and from 1.70 to 1.65 eV for PbS and $\mathrm{Cd}_{0.4}\mathrm{Pb}_{0.6}\mathrm{S}$, respectively [41].

From the literature [42], it was observed that $\mathrm{Cd}_x\mathrm{Pb}_{1-x}\mathrm{S}$ layers ($0 < x \leq 1$) were produced by chemical deposition on glass substrates, in addition, it was also proved that their structural, electrical, and photoelectrical properties depended on the composition. At $x > 0.5$ (high CdS content), the films demonstrate weak crystallinity and low photoconductivity; at $x < 0.5$ (high PbS content), the films have a good crystallinity with an average crystallite size of 100 nm and higher photoconductivity. The increasing cadmium sulphide content leads to the spectra-response displacement into the short-wave region. The experimental results demonstrate the possibility of forming substitution $\mathrm{Cd}_x\mathrm{Pb}_{1-x}\mathrm{S}$ solid solution in the vicinity of compositions of individual PbS and CdS on a certain segments of the layer, whereas the main segment of the deposited film, in authors' opinion, may rather be a mixture of sulfide phases $(\mathrm{CdS})_x(\mathrm{PbS})_{1-x}$.

The chemical bath deposition of enriched $\mathrm{Cd}_x\mathrm{Pb}_{1-x}\mathrm{S}$ solid solution films can be predicted and allows one to formulate clear recommendations for synthetic control [33]. The conditions of metastable structure formation of cadmium content $\mathrm{Cd}_x\mathrm{Pb}_{1-x}\mathrm{S}$ solid solutions at low temperature hydrochemical synthesis is influenced by the following factors: metal salt content in the reaction mixture, complexing agent content, temperature, pH, time of deposition, and a number of other conditions of the process (features of the nucleation, substrate material, and external factors). To evaluate the composition of chemically deposited $\mathrm{Cd}_x\mathrm{Pb}_{1-x}\mathrm{S}$ films on the side of PbS, previous researchers [31] suggested using such an integrated index as the ratio of concentrations of the off-complex ions of lead and cadmium in the reaction mixture: $[\mathrm{CdS}]_{TP}$, mol.% $= f\left([\mathrm{Pb}^{2+}]/[\mathrm{Cd}^{2+}]\right)$. In the reaction mixture, these metal salts were introduced in the form of lead acetate $\mathrm{Pb(OAc)}_2$ and cadmium chloride CdCl_2. For the hydrochemical production of the $\mathrm{Cd}_x\mathrm{Pb}_{1-x}\mathrm{S}$ solid solutions, only metal acetate salts were used in various concentration ratios [3, 40, 41, 43–45]. The influence of anion component of the used lead and cadmium salts on chemical and phase composition, structure, and properties of solid solutions formed was not discussed in these previously reported works. At the same time, in our previous work [33], we observed that the nature of anions of introduced metal salts is an important factor, which influences composition and microstructure of the deposited solid solutions.

The influence of the anion background of the area on the crystallization in films is quite well known; additionally, the impurity nature [46], including the anion nature, significantly influences the composition and morphology of microcrystals. Thus, using spray-pyrolysis, the substitution of cadmium chloride by acetate under equal conditions allows one to double the thickness of CdS films [47]. However, the role of the anion component of the cadmium salt in the crystallization process was not thoroughly studied. In our previous study [33], we showed that the use of the cadmium acetate for the film synthesis under other equal conditions results in an increase in the CdS content to 0.4 – 4.0 mol.% (compared to CdCl_2). This result and the revealed change in the film morphology are connected with the active influence of the anion background of the reaction mixture on the formation of solid solutions. It was suggested that the obtained results depend on the various reaction capacity of thiourea used for the chemical deposition of solid solutions, which forms an intermediate complex due to the anion's nucleophilic addition to carbon atom [33, 48]. It is obvious that the stability of the intermediate complex will depend not only on the strength of the thiourea complex with metal but also on nucleophilic properties of the added anion. The increasing anion nucleophilicity upon transferring from chloride to acetate ions will lead to increasing the reaction capacity of the activated thiourea due to the weakening of the carbon-sulfur bond. The increasing reaction capacity of thiourea will influence mostly the speed of the CdS phase formation due to the high polarization of the carbon-sulfur bond with cadmium. Finally, it will influence the redistribution of the speed of formation of individual sulphides in favor of the latter, and will increase its fraction in the solid solution composition.

In the literature, there are no detailed studies of the influence of concentration of the cadmium acetate salt on composition and structure of the $\mathrm{Cd}_x\mathrm{Pb}_{1-x}\mathrm{S}$ solid solution films deposited from aqueous solutions. Therefore, the purpose of this research is the chemical bath synthesis of $\mathrm{Cd}_x\mathrm{Pb}_{1-x}\mathrm{S}$ films on glass-ceramic substrates, study of their composition, morphological and structural features, and photoelectric properties depending on the cadmium acetate content in the reaction bath.

2. Experimental details

Film deposition in the PbS–CdS system was performed in citrated-ammonium reaction mixture on the preliminary degreased glass-ceramic substrates with a surface of 30 × 30 mm. Cadmium acetate $\mathrm{Cd(OAc)}_2$ was used as the cadmium salt and introduced into the reaction mixture. The concentration of $Cd(OAc)_2$ was varied from 0.01 to 0.1 mol/l, whereas the concentration of the lead acetate ($Pb(OAc)_2$) was constant and equal to 0.02 mol/l in the reaction mixture. Chemical deposition was made in the presence of complex-forming agents: using aqueous ammonia for cadmium and sodium citrate ($Na_3C_6H_7O_8$) for lead. The initial concentration of thiourea (N_2H_4CS) in the reaction mixture was 0.58 mol/l in all experiments. The film synthesis was carried out at 353 K for 120 – 140 minutes in the sealed reactors of molybdenum glass where substrates were fixed in special teflon devices. The reactors were placed into thermostat TS-TB-10 with an accuracy of the temperature control of $\pm 0.1^\circ$.

The thickness of the synthesized layers was estimated using a Linnik interference microscope MII-4.

The crystal structure of the synthesized solid solution $Cd_xPb_{1-x}S$ films was studied by X-ray diffraction method using a diffractometer Dron-4 with copper anode in Bragg-Brentano geometry. The separation of $\mathrm{Cu}K\alpha_{1,2}$-doublet line from the continuous spectrum was made using a monochromator made from pyrolytic graphite with the reflecting plane (002). The experimental XRD patterns were obtained in an angular range from 20 to 100 degrees with a step of 0.02° and exposure of 5 – 10 seconds per point. The samples were rotated in a vertical plane. The analysis of experimental spectra was made by the Rietveld full-profile analysis [49] using software package FullProf [50]. A Pseudo-Voigt function was used to describe reflection profiles. Corrections for errors in the sample setting and deflection of sample plane from the scattering plane were applied for the description of the whole diffraction spectrum. Also, while analyzing the scaling factor, the reflection width and shape, lattice parameters, and atom coordinates were varied. Corrections for the thermal oscillation of atoms and possible deflection of the values of the lattice site occupation were also applied. To calculate the reflection broadening due to the smaller coherent scattering regions (CSR) or internal microstrains, we used the instrumental angular dependence obtained on polycrystalline sample of the cerium oxide, which was preliminary annealed at 1200 °C for 12 hours. The evaluation of grain sizes (CSR) and microstrains was made by the Williamson–Hall method [51, 52] using the dependence of the physical broadening $\beta \cdot (2\theta) = \beta(2\theta)\cos\theta / K_{hkl}\lambda$ on the scattering vector length $s = 2\sin\theta/\lambda$. The same possibility was input in the software package FullProf [50].

The investigation of structural and morphological characteristics and elemental composition of the obtained films was fulfilled by raster electron microscopy using a MIRA3LMV microscope at an accelerating voltage of the electron beam of 10 kV, and a raster electron microscope JEOL JSM-5900 LV with the attachment for the energy-dispersion (EDX) analysis (EDS Inca Energy 250). The error for the elemental composition was about 10 %.

Investigation of optical properties of the solid solution films was carried out on the samples preliminary covered with nickel contacts by the electro-chemical method.

Relative spectral characteristics of photosensitivity were obtained using a double monochromator SPM-2 at a radiation modulation frequency of 400 Hz, whose single-frequency measuring channel was the same as the measuring channel of the UFI-1 device [53]. A halogen incandescent lamp KGM-12-100 was used as the radiation source, while its mode of operation on current was stabilized with an accuracy of ±0.2 %. Spectra were recorded automatically in the wave-length range 0.4 – 3.5 μm with 0.05 μm increments.

3. Results and discussion

Over the whole range of the cadmium acetate concentrations employed in the reaction mixture in the PbS–CdS system, and polycrystalline films with the 0.6 – 1.2 μm thickness were obtained.

In the XRD patterns of the films obtained by co-deposition of PbS and Cd, reflections of two phases are observed – of lead sulfide with the $B1$-type cube structure (space group $Fm\bar{3}m$) and of glass-ceramic substrate (Fig. 1).

Increasing the cadmium content in the reaction solution from 0.01 to 0.10 mol/l was followed by the decreasing of the lattice constant for the PbS phase from 0.59242 (1) to 0.58918 (1) nm (inset in Fig. 1), which exceeds the lattice constant of the cube lead sulfide (0.5932 nm). We ascribed it to substitutional $Cd_xPb_{1-x}S$ solid solutions formed on the side of PbS. The decreasing of the lattice constant upon the solid solution formation results from the substitution of lead ions Pb^{2+} with a radius of 0.120 nm in the PbS lattice by smaller cadmium ions Cd^{2+} with a radius of 0.097 nm. The cadmium sulfide content in the solid-solution films was calculated using Vegard's law. It is valid with rather a high accuracy for chalcogenide systems [54]. The lattice constant of CdS film produced from the ammonium-citrated bath was $a_{\mathrm{CdS}} = 0.5761$ nm. According to the estimation, the maximum content of cadmium sulfide in the solutions with the lattice constants 0.59242 (1), 0.59187 (1), 0.59094 (1), 0.58951 (1), 0.58918 (1) nm was 3.0, 6.0, 12.0, 20.0, and 22.0 mol.%, respectively. The compositions of the solid solutions produced can be defined as $Cd_{0.03}Pb_{0.97}S$, $Cd_{0.06}Pb_{0.94}S$, $Cd_{0.12}Pb_{0.88}S$, $Cd_{0.20}Pb_{0.80}S$, $Cd_{0.22}Pb_{0.78}S$. It means that the cadmium concentration in the supersaturated solid solutions under study is within the range from 3.0 to 22.0 mol.% and gradually increases with the increase in the cadmium acetate concentration in the reaction

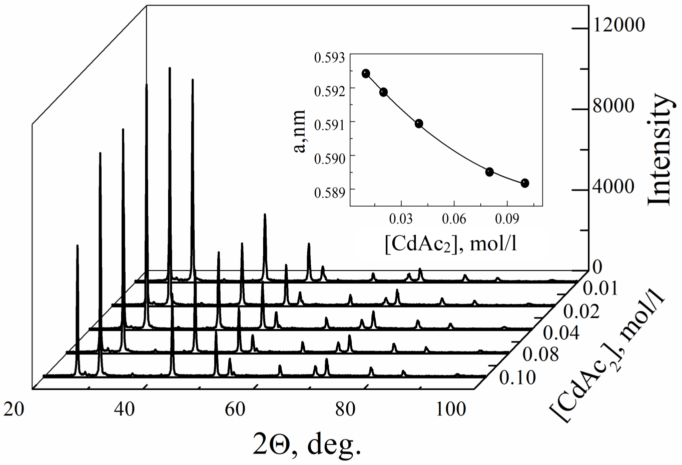

FIG. 1. XRD patterns of $Cd_{0.03}Pb_{0.97}S$, $Cd_{0.06}Pb_{0.94}S$, $Cd_{0.12}Pb_{0.88}S$, $Cd_{0.20}Pb_{0.80}S$, $Cd_{0.22}Pb_{0.78}S$ films, produced by co-deposition of cadmium and lead sulfides at $T = 353$ K for 140 minutes from the reaction mixture containing 0.01, 0.02, 0.04, 0.06, 0.08, 0.10 $CdAc_2$ mol/l. All the XRD patterns contain only reflections of the cubic phase with the $B1$-type structure and solid-solution composition was estimated based on the lattice constant. The change in the lattice constant depending on the cadmium acetate concentration in the reaction mixture is shown in the inset

mixture from 0.01 to 0.10 mol/l. The comparison of the obtained results with the phase diagram of the system PbS–CdS [28] shows a significant supersaturation of the synthesized solid solutions with cadmium.

Figure 2 shows an XRD pattern of the $Cd_xPb_{1-x}S$ film produced by deposition from the reaction mixture containing 0.01 mol/l of cadmium acetate, the composition of solution containing 0.02 mol/l $PbAc_2$, 4.5 mol/l NH_4OH, 0.3 mol/l $Na_3C_6H_5O_7$ and 0.58 mol/l N_2H_4CS. The analysis showed that the basic reflections refer to the cube phase with the potential symmetry groups $Fm\bar{3}m$ or $F\bar{4}3m$. Along with these reflections, additional reflections were also observed which refer to the tetragonal phase TiO_2. It is associated with the fact that the solid-solution film $Cd_xPb_{1-x}S$ was condensed on the substrate made of glass-ceramic, which contains the titanium oxide TiO_2. The sulphide PbS crystallizes in the NaCl type structure ($B1$-phase), but also, under certain conditions, it can have the wurtzite-type structure ($B3$-phase) [55]. As the CdS phase has a cube structure of the wurtzite-type, we verified both models for the solid solutions obtained. The calculations showed that the obtained sample has the $B1$-type structure. However, at the same time, we found that the experimental intensity of reflection (200) is slightly higher than the calculated one. This can be associated with the formation upon deposition of a bulk polycrystalline state in which a certain ordering (texture) of grains perpendicular to the substrate surface is prevailed.

Figure 3 shows the segments of the XRD patterns (reflections (111) and (200)) of $Cd_xPb_{1-x}S$ solid-solution films produced from the reaction bath containing 0.01, 0.02, 0.04, 0.08, 0.1 mol/l of cadmium acetate. The difference in the ratio of intensities of diffraction peaks (111) and (200) in the XRD patterns, which clearly manifests itself upon increasing the cadmium acetate concentration, is associated with the preferable orientation of grains along the crystallographic direction (200), which is perpendicular to the substrate surface in the films under study.

Introduction in the analysis of experimental data of texture provides an adequate description of the experimental profile in the XRD pattern of the $Cd_{0.20}Pb_{0.80}S$ solid-solution film. The same method was used for the description of other XRD patterns in which a good correlation with the experiment was also obtained (Fig. 3(a–e)). Fig. 3(f) shows the dependence of volume of the randomly orientated material P1 on the cadmium acetate concentration in the solution. It has been seen that, in general, the texture degree decreases with the increase in the cadmium salt content $Cd(OAc)_2$ in the reaction mixture, except for the last point 0.1.

The structure refinement for the solid solutions with the correction of selected reflections (111) and (200) by the software package FullProf [50] is provided on the $Cd_{0.20}Pb_{0.80}S$ solid-solution film produced from the reactor containing 0.08 mol/l of cadmium acetate within two models, without and with account for the preferable orientation (Fig. 4).

There is a shift to the range of the reflections observed in the XRD patterns of all the studied $Cd_xPb_{1-x}S$ solid-solution films (Fig. 1), as well as their broadening due to either decrease in the grain size or appearance of

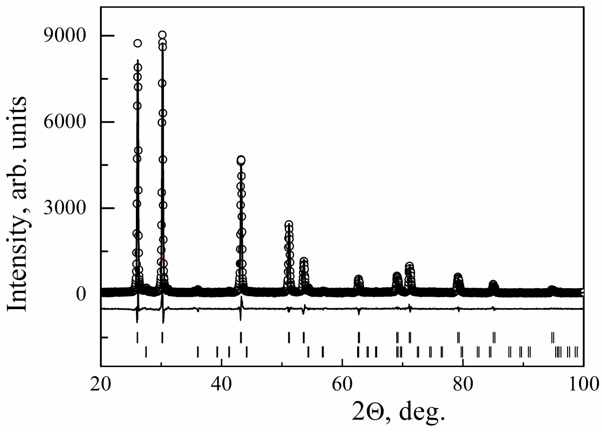

FIG. 2. XRD pattern of $Cd_xPb_{1-x}S$ film produced by chemical deposition from the reaction mixture containing 0.01 mol/l of cadmium acetate in a composition of 0.02 mol/l $PbAc_2$ 4.5 mol/l NH_4OH, 0.3 mol/l $Na_3C_6H_5O_7$, 0.58 mol/l N_2H_4CS. Points – experimental, envelope line – calculated, low line – difference between the calculated and experimental values. Dashes – peak positions, upper ones correspond to crystal structure *B*1-type, lower ones, to TiO_2, which enters in the glass-ceramic composition

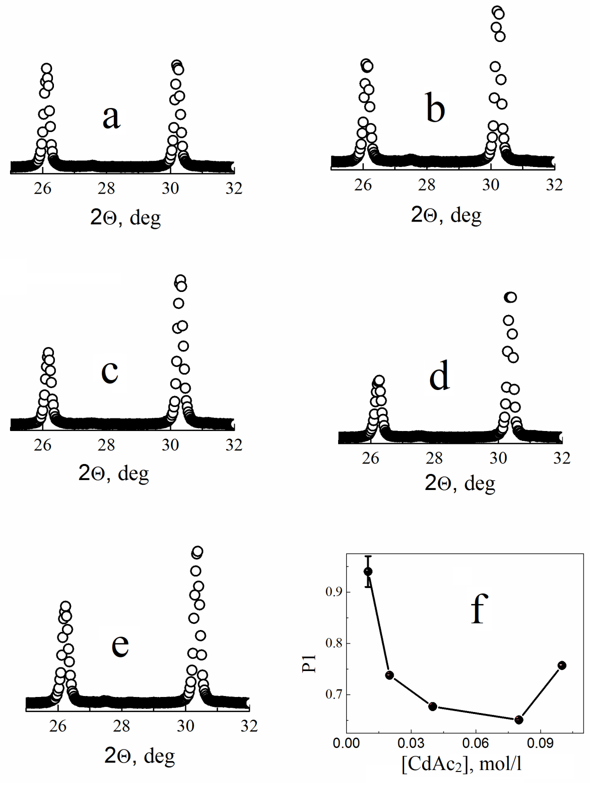

FIG. 3. Reflections (111) and (200) of $Cd_xPb_{1-x}S$ solid-solution films deposited on glass-ceramic substrate from the ammonium-citrated reaction bath with various cadmium acetate content: 0.01 (a), 0.02 (b), 0.04 (c), 0.08 (d), 0.1 (e) mol/l volume of random-orientated material (f)

microdeformations in the films. Fig. 5 shows reflections (220) of the $Cd_xPb_{1-x}S$ solid-solution films deposited from the reaction mixtures containing different cadmium acetate concentrations in the range from 0.01 to 0.10 mol/l.

The shift of the angular position of reflections (220) with changing the cadmium acetate concentration corresponds to the change in the crystal lattice parameter of the $Cd_xPb_{1-x}S$ solid solution films. The value of broadening was calculated by $\beta(2\theta) = [(\mathrm{FWHM}_{exp})^2 - (\mathrm{FWHM}_R)^2]^{1/2}$, where FWHM_{exp} is the experimental

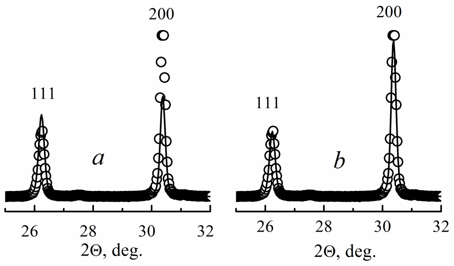

FIG. 4. XRD pattern segment of solid-solution film. Experimental (points) and calculated (solid lines) diffraction peaks (111) and (200) without account (a) and with account for preferable orientation (b)

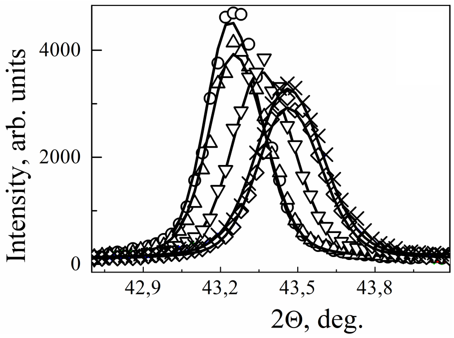

FIG. 5. Reflections (220) of $Cd_{0.03}Pb_{0.97}S$ (circle), $Cd_{0.06}Pb_{0.94}S$ (triangle up), $Cd_{0.12}Pb_{0.88}S$ (triangle down), $Cd_{0.20}Pb_{0.80}S$ (rhombus), $Cd_{0.22}Pb_{0.78}S$ (cross) solid-solution films produced by deposition from reaction mixtures containing 0.01, 0.02, 0.04, 0.08, 0.10 mol/l of cadmium acetate $CdAc_2$

full-width of reflection at its half- height. The separation of dimensional and deformation contributions into the reflection broadening and the estimation of the average size of the coherent scattering region, which is considered as the average grain size (L), were made by the Williamson–Hall extrapolation method [51, 52] according to the dependence of the resulting broadening $\beta(\theta)\cos\theta = f(\sin\theta)$.

The reflection broadening connected with the small grain size is proportional to $\sec\theta$, whereas the broadening connected with microstrains is proportional to $\tan\theta$ [56], i.e. they have different angular dependence (here θ is the diffraction angle). In the dependence $\beta(\theta)\cos\theta = f(\sin\theta)$ (Fig. 6), given for the solid solution film $Cd_{0.20}Pb_{0.80}S$, the line slope characterizes the amount of microstrains, while the intercept on the $\beta(\theta)\cos\theta$ axis upon extrapolation on the $\sin\theta$ axis gives the grain size (L), which can be calculated using the Selyakov–Sherrer formula $L = k\lambda/\beta(\theta)\cos\theta$, where the coefficient k is close to 1 and depends on the grain shape.

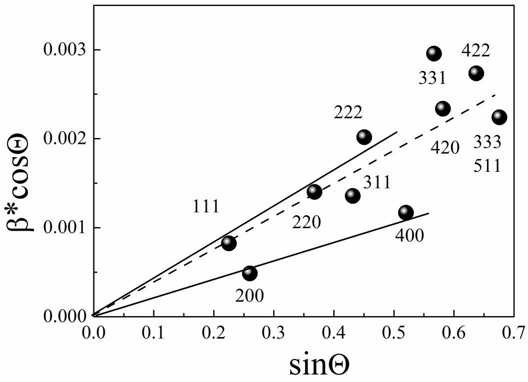

FIG. 6. Experimental $\beta(\theta)\cos\theta$ versus $\sin\theta$ dependence for the $Cd_{0.20}Pb_{0.80}S$ solid-solution film

According to the estimation of the experimental dependence $\beta(\theta)\cos\theta = f(\sin\theta)$ for the $Cd_{0.20}Pb_{0.80}S$ solid-solution film, it can be concluded that the average values of $\beta(\theta)\cos\theta$ are close to 0 at $\sin\theta$ tending to zero. This indicates that the reflection broadening is mainly connected with the appearance of microstrains $\Delta d/d$ in the solid-solution film $Cd_{0.20}Pb_{0.80}S$ in the course of chemical deposition. Moreover, irregularity in the localization of points in the figure testifies to the anisotropy of microstrains along different crystallographic directions. Actually, if we connect the points for dimensional crystallographic directions $[hhh]$ and $[h00]$ with the straight line in Fig. 6, it can be seen that the slope angle differs indicating various values of microstrains along these directions. Similar studies were performed for all synthesized $Cd_xPb_{1-x}S$ solid solution films. We can conclude that there is anisotropy of microstrains in the synthesized films. Taking into account this fact the analysis of all experimental XRD patterns for the $Cd_xPb_{1-x}S$ solid-solution films was made by Rietveld method [50] using software package FullProf [50] (Fig. 7).

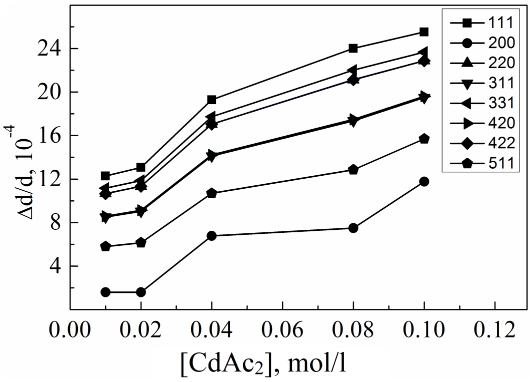

FIG. 7. Dependence the microstrains value Δd/d in $Cd_xPb_{1-x}S$ solid solution films as a function of the cadmium acetate concentration in the reaction mixture

The results for the estimation of microstrains $\Delta d/d$ in the $Cd_xPb_{1-x}S$ solid-solution films show that the increasing the cadmium acetate concentration in the reaction mixture leads to an increase in microdeformations with approximately equal speed and anisotropy keeping in the microdeformation distribution in all studied thin film samples.

Thus, in the $Cd_xPb_{1-x}S$ ($0.03 \leq x \leq 0.22$) solid-solution films synthesized by chemical deposition from the ammonium-citrated reaction bath, is a crystal state with the NaCl ($B1$) type lattice and a relatively large size of microcrystals is realized. The crystals have the preferable orientation [200] that is perpendicular to the substrate surface and are characterized by anisotropy of microstrains in the volume. As it was estimated above, the broadening of diffraction reflextions in the $Cd_xPb_{1-x}S$ solid-solution films are associated only with the appearance of microstrains in the sample bulk and can evidence the fact that the films were formed from grains with a size of 300 – 400 nm or more.

The microstructure investigation of the synthesized $Cd_xPb_{1-x}S$ films carried out upon varying the cadmium acetate content in the reaction mixture in the range 0.01 – 0.10 mol/l and at fixed concentration 0.02 mol/l of the lead salt showed that with an increase in the cadmium salt concentration in the solution both sizes and the microcrystal habit change (Fig. 8).

Herewith the morphology of the deposited films largely depends on the solid solution composition. Thus, the films based on $Cd_{0.03}Pb_{0.97}S$ and $Cd_{0.06}Pb_{0.94}S$ with the average size of crystallites 200 – 300 nm have a relatively high granular inhomogeneity. There are quite a number of nano-sized particles in their composition: less than 70 – 100 nm. The increasing of the enrichment of solid solution in the substitutional component in the line $Cd_{0.09}Pb_{0.91}S$, $Cd_{0.12}Pb_{0.88}S$, $Cd_{0.20}Pb_{0.80}S$ leads to the formation of well-bounded crystals with the average gross-sizes of 500 – 1000 nm. However, the X-ray investigation of the diffraction peak width using Scherrer formula showed that the films are nanostructured with 50 – 70 nm particles. It is the result of the intercluster growth mechanism proved by us, which occurs at the bath deposition of metal chalcogenide films [33]. The proof of the nanostructural character of the deposited layers is also the film based on $Cd_{0.22}Pb_{0.78}S$ solid solution shown in Fig. 8f. It is clearly seen that the film preliminary consists of 200 – 300 nm globules, which in turn are formed from 50 – 60 nm particles. It should be noted that nanostructural character of precursory layers of hydrochemically deposited sulfides is also mentioned in [57].

The smallest size of crystal grain (200 – 400 nm) was observed in the $Cd_{0.03}Pb_{0.97}S$ solid-solution film formed from the initial particles with a size of $\sim$ 100 nm. With increasing the cadmium acetate concentration

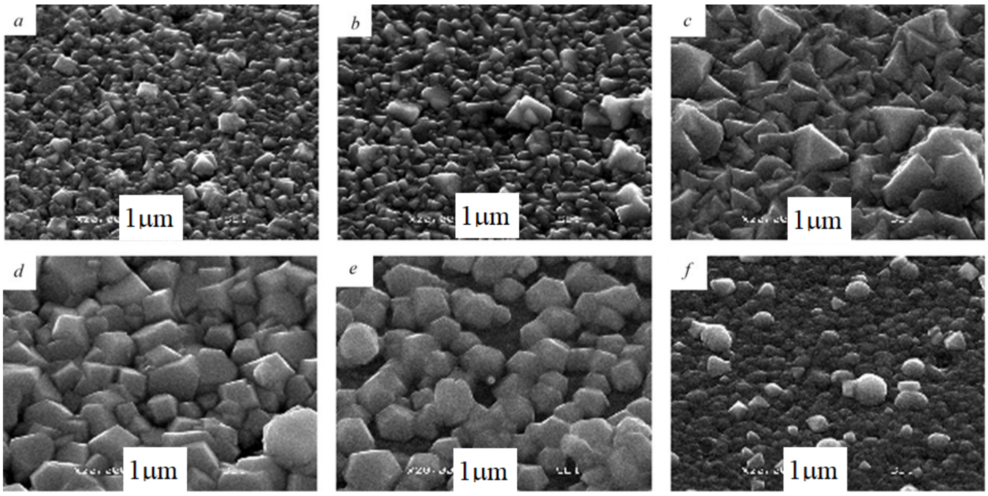

FIG. 8. Electron micrographs of $Cd_{0.03}Pb_{0.97}S$ (a), $Cd_{0.06}Pb_{0.94}S$ (b), $Cd_{0.09}Pb_{0.91}S$ (c), $Cd_{0.12}Pb_{0.88}S$ (d), $Cd_{0.20}Pb_{0.80}S$ (e), $Cd_{0.22}Pb_{0.78}S$ (f) solid solution films produced by chemical deposition from reaction mixtures containing: $[PbAc_2]$ = 0.02 M, $[Na_3C_6H_5O_7]$ = 0.3 M, $[NH_4OH]$ = 4.5 M, $[N_2H_4CS]$ = 0.58 M. Cadmium acetate content ($CdAc_2$) is 0.01 M (a), 0.02 M (b), 0.04 M (c), 0.06 M (d), 0.08 M (e), 0.10 M (f). The synthesis was carried out at 353 °C for 140 minutes

in the reaction bath from 0.02 to 0.08 mol/l, the average size of well-bounded crystals increased from 300 – 500 nm for the $Cd_{0.06}Pb_{0.94}S$ films to 500 – 1000 nm for the layers based on $Cd_{0.09}Pb_{0.91}S$, $Cd_{0.12}Pb_{0.88}S$, and $Cd_{0.20}Pb_{0.80}S$.

The $Cd_xPb_{1-x}S$ $(0.03 \leq x \leq 0.09)$ solid-solution films have a clear texture: at the concentration of cadmium fraction of 0.03 – 0.09, the crystals have the cube habit and grow on by the plane [111]. Agglomerates, from which the solid solution films $Cd_{0.12}Pb_{0.88}S$ and $Cd_{0.20}Pb_{0.80}S$ were formed, in the course of growing transformed into hexahedrons.

In general, the results of the average size estimation of crystallites that form the $Cd_xPb_{1-x}S$ solid-solution films by X-ray diffraction method and electron microscopy method are in a very good agreement with each other.

Keeping in mind the semiconductive character of the deposited $Cd_xPb_{1-x}S$ films, we can receive important information on their composition from the study of their conductivity. The investigation of film the conductivity performed upon varying the cadmium acetate concentration in the reaction bath in coordinates $\ln\sigma - f([\mathrm{CdAc_2}])$ indirectly confirmed the formation of substitutional solid solutions $Cd_xPb_{1-x}S$ upon co-deposition of the lead and cadmium sulfides from the ammonium-citrated reaction mixture. With the formation of solid solutions, the semiconductivity of films will decrease due to the increase in the bandgap width upon the substitution of lead in the PbS structure by cadmium ions. Actually, Fig. 9 shows that the conductivity of the $Cd_xPb_{1-x}S$ films is essentially lower than the conductivity of PbS and continues to decrease with increasing cadmium content in the solid-solution structure of $Cd_{0.03}Pb_{0.97}S$, $Cd_{0.09}Pb_{0.91}S$, and $Cd_{0.12}Pb_{0.88}S$.

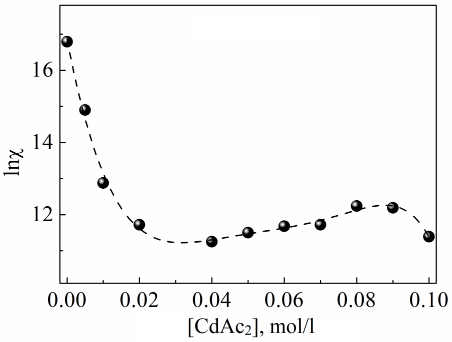

FIG. 9. Dependence of conductivity χ of $Cd_xPb_{1-x}S$ solid-solution films versus cadmium acetate concentration in the reaction mixture in coordinates "$\ln\chi - [\mathrm{CdAc_2}]$"

Such a situation is realized in semiconductors with the prevailing covalent bond and with preferable scattering of carriers on the lattice sound vibration, which is characteristic of both lead and cadmium sulfides [58,59].

The $Cd_xPb_{1-x}S$ solid-solution films of various compositions are photosensitive in the visible and near-infrared spectral range. It does not require sensabilization after their removal from the reaction mixture and are ready for practical use. The range of spectral sensitivity of the substitutional $Cd_xPb_{1-x}S$ alloys depends on their composition.

Figure 10 shows typical spectral characteristics of the $Cd_xPb_{1-x}S$ films with different cadmium sulfide content. It is clear that with increasing cadmium content (x) in the solid-solution structure, a gradual shift occurs for the spectral characteristics toward the short-wave region. As shown in Fig. 10, with an increase in the cadmium fractional concentration in the $Cd_xPb_{1-x}S$ solid solution from 0.03 to 0.22, the critical frequency and the photo response maximum moves to the short-wave range from 3.1 to 1.6 μm and from 2.5 to 1.2 μm, respectively.

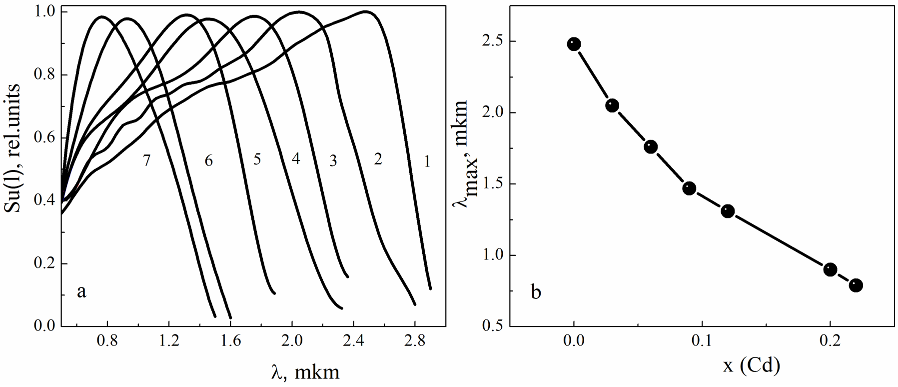

FIG. 10. (a) – Plots of relative spectral photosensitivity of films based on PbS (1) and $Cd_xPb_{1-x}S$ solid solutions of various composition: $Cd_{0.03}Pb_{0.97}S$ (2), $Cd_{0.06}Pb_{0.94}S$ (3), $Cd_{0.09}Pb_{0.91}S$ (4), $Cd_{0.12}Pb_{0.88}S$ (5), $Cd_{0.20}Pb_{0.80}S$ (6), $Cd_{0.22}Pb_{0.78}S$ (7). (b) – Change of the maximum position of photo response for the $Cd_xPb_{1-x}S$ solid-solution films depending on x

In general, the means of synthesizing $Cd_xPb_{1-x}S$ solid-solution films with various compositions and specific properties provides an opportunity to produce photosensitive semiconductive materials with the controlled maximum position and threshold of spectral sensitivity over the whole near-infrared range. The $Cd_{0.06}Pb_{0.94}S$ solid solution has attracted special attention because its spectral characteristic practically similar to single-crystalline germanium but with higher ohmic resistance, thus providing easy compatibility in electron circuits.

4. Conclusions

Substitutional $Cd_xPb_{1-x}S$ solid solution films based on the cubic lattice of PbS with the thickness 0.6 – 1.2 μm were produced by chemical bath co-deposition of lead and cadmium sulfides in the ammonium citrate reaction mixture on glass-ceramic substrates. With an increase in the concentration of cadmium acetate from 0.01 to 0.10 mol/l, the monotonous increase in the CdS content in the solid solutions obtained from 3.0 to 22.0 mol.%. Comparison of the determined $Cd_{0.03}Pb_{0.97}S$, $Cd_{0.06}Pb_{0.94}S$, $Cd_{0.09}Pb_{0.91}S$, $Cd_{0.12}Pb_{0.88}S$, $Cd_{0.20}Pb_{0.80}S$, $Cd_{0.22}Pb_{0.78}S$ compositions with the phase diagram for the PbS–CdS system testifies to a significant supersaturation level of the cadmium content in the synthesized solid solutions. The films were formed from crystallites with the preferable orientation [200] perpendicular to the substrate surface and are characterized by a clear anisotropy in distribution of microdeformations over the bulk of all researched samples. With an increase in the cadmium acetate concentration in the reaction mixture, an increase in the microstrains $\Delta d/d$ was observed in the films of the deposited $Cd_xPb_{1-x}S$ solid solutions. Both sizes and crystal habit changed. The smallest crystal sizes (200 – 400 nm) are characteristic of the $Cd_{0.03}Pb_{0.97}S$, $Cd_{0.06}Pb_{0.94}S$ solid solution formed from the initial particles $\sim$ 100 nm in size. There are quite a number of nanometer-scaled particles in their composition: less than 70 – 100 nm. Increasing the enrichment of solid solution in the substitutional component in the line $Cd_{0.09}Pb_{0.91}S$, $Cd_{0.12}Pb_{0.88}S$, $Cd_{0.20}Pb_{0.80}S$ leads to the film formation of well-bounded crystals with the average gross-sizes of 500 – 1000 nm. According to the X-ray research, they are nanostructured with an average size for the initial particles of 50 – 70 nm. Films based on $Cd_{0.22}Pb_{0.78}S$ primarily consist of 200 – 300 nm globules, which in turn are formed from 50 – 60 nm particles.

With an increase in the cadmium acetate concentration in the reaction bath, the average size of the well-bounded crystals increases from 300 – 500 nm for $Cd_{0.06}Pb_{0.94}S$ to 500 – 1000 nm for the layers based on $Cd_{0.09}Pb_{0.91}S$, $Cd_{0.12}Pb_{0.88}S$, and $Cd_{0.20}Pb_{0.80}S$. Results from estimating the crystal size from XRD and microscopic examination are similar. The data from conductivity measurements of the synthesized layers indirectly confirm the formation of substitutional $\mathrm{Cd}_x\mathrm{Pb}_{1-x}\mathrm{S}$ solid solutions. The synthesized $\mathrm{Cd}_x\mathrm{Pb}_{1-x}\mathrm{S}$ solid-solution films have photosensitivity in the visible and near-infrared spectral ranges, the ranges of their spectral sensitivity corresponding to their compositions. With an increase in the level of the lead substitution in the PbS lattice by cadmium, it was determined that the maximum of the spectral characteristic and the long-wave limit of photo response of the $\mathrm{Cd}_x\mathrm{Pb}_{1-x}\mathrm{S}$ films gradually moved toward the short-wave spectral range from 3.1 to 1.6 μm and from 2.5 to 1.2 μm, respectively. The obtained results create a basis for the purposeful synthesis via chemical bath deposition of the $\mathrm{Cd}_x\mathrm{Pb}_{1-x}\mathrm{S}$ solid-solution films with a specified composition in order to make semiconducting materials which have photosensitivity in the visible and near-infrared spectral ranges with variable spectral characteristics.

Acknowledgements

The work was supported by Act 211 Government of the Russian Federation, contract No. 02.A03.21.0006. The research was carried out in part at IMP Neutron Material Science Complex within the state assignment of FASO of Russia (theme "Flux" No. AAAA-A18-118020190112-8).

References

[1] Kumar S., Bhattacharya B. Variation of band gap in CdPbS with composition prepared by a precipitation technique. *Indian J. Pure Appl. Phys.*, 2005, **43**, P. 609–611.

[2] Barote M.A., Yadav A.A., Masumdar E.U. Effect of deposition parameters on growth and characterization of chemically deposited $\mathrm{Cd}_{1x}\mathrm{Pb}_x\mathrm{S}$ thin films. *Chalcogenide Letters*, 2011, **8**, P. 129–138.

[3] Kamruzzman M., Dutta R., Podder J. Synthesis and characterization of the as-deposited $\mathrm{Cd}_{1x}\mathrm{Pb}_x\mathrm{S}$ thin films prepared by spray pyrolysis technique. *Semiconductors*, 2012, **46**, P. 957–961.

[4] Al-Jumaili H.S. Structural and optical properties of nanocrystalline $\mathrm{Pb}_{1x}\mathrm{Cd}_x\mathrm{S}$ thin films prepared by chemical bath deposition. *Appl. Phys. Research*, 2012, **4**, P. 75–82.

[5] Tan G.-L., Liu L., Wu W. Mid-IR band gap engineering of $\mathrm{Cd}_x\mathrm{Pb}_{1-x}\mathrm{S}$ nanocrystals by mechanochemical reaction. *AIP Advances*, 2014, **4**, 067107.

[6] Maskaeva L.N., Markov V.F., Porkhachev M.Yu., Mokrousova O.A. Thermal and radiation stability IR-detectors based on films of solid solutions $\mathrm{CdPb}_{1-}\mathrm{S}$. *Fire and Explosion Safety*, 2015, **9**, P. 67–73.

[7] Chu T.L., Chu S.S., et al. High efficiency thin film CdS/CdTe heterojunction solar cells. *J. Cryst. Growth*, 1992, **117**, P. 1073–1076.

[8] Ferekides C., Britt J. CdTe solar cells with efficiencies over 15%. *Sol. Energy Mater. Sol. Cells*, 1994, **35**, P. 255–262.

[9] Uda H., Ikegami S., Sonomura H. Effect of substrate temperature on the photovoltaic properties of a CdS/CdTe solar cell. *Japanese J. Appl. Phys.*, 1990, **29**, P. 2003–2007.

[10] Bairamov B.Kh., Nikolaev Yu.A., et al. Effect of electron irradiation on the photopleochroism of ZnO/CdS/Cu(In,Ga)Se_2 solar cells. *Tech. Phys. Lett.*, 2005, **31**, P. 698–701.

[11] Hernadez-Borja J., Vorobiev Y.V., Ramirez-Bon R. Thin films solar cells of CdS/PbS chemically deposited by an ammonia – free process. *Solar Energy Materials & Solar Cells*, 2011, **95**, P. 1882–1888.

[12] Obaid A.S., Mahdi M.A., Hassan Z., Bououdina M. Preparation of chemically deposited thin films of CdS/PbS solar cell. *Superlattices and Microstructures*, 2012, **52**, P. 816–823.

[13] Yeon D.H., Lee S.M., et al. Origin of the enhanced photovoltaic characteristics of PbS thin film solar cells processed at near room temperature. *J. Mater. Chem. A*, 2014, **2**, P. 20112–20117.

[14] Peña-Cabrera L., Arizmendi-Morquecho A., Vorobiev P. Thin film CdS/PbS solar cell by low temperature chemical bath deposition and silver doping of the window layer. *J. of Non-Oxide Glasses*, 2016, **8**, P. 59–66.

[15] Saikia D., Phukan P., Das M.R. Influence of thickness of active layer on the performance of CBD grown Cu-CdS/PbS hetero-junction. *Adv. Mater. Lett.*, 2017, **8**, P. 65–69.

[16] Caselli D.A., Ning C.Z., High-performance laterally-arranged multiple-bandgap solar cells using spatially composition-graded $\mathrm{Cd}_x\mathrm{Pb}_{1-x}\mathrm{S}$ nanowires on a single substrate: a design study. *Optics Express A*, 2011, **19**, P. 686–694.

[17] Rokakh A.G., Stetsyura S.V., Trofimova N.B., Elagina N.V. Stabilizing effect of doping with PbS on properties of $\mathrm{CdS}_x\mathrm{Se}_{1-x}$ wide-gap photoconductors. *Inorg. Mater.*, 1999, **35**, P. 452–454.

[18] Bethke P.M., Barton P.B. Sub-solidus relations in the system PbS–CdS. *American Mineralogist*, 1971, **56**, P. 2034–2039.

[19] Rokakh A.G., Stetsyura S.V., Serdobintsev A.A. Heterophase semiconductors under action of radiations. *Izvestiya of Saratov University. New Series. Series: Physics*, 2005, **5**, P. 98–101.

[20] Bukharov V.E., Rokakh A.G., Stetsyura S.V. Diffusion degradation model for a heterogeneous photoconducting system. *Tech. Phys.*, 2003, **48**, P. 225–230.

[21] Rokakh A.G., Trofimova N.B. On luminescence enhancement in narrow-gap phase of PbS–CdS heterogeneous semiconductor. *Tech. Phys.*, 2001, **46**, P. 926–928.

[22] Bukharov V.E., Rokakh A.G., Stetsyura S.V. Influence of electron bombardment on recombination and attachment in II-VI - IV-VI film photoconductors. *Tech. Phys. Lett.*, 1999, **25**, P. 111–113.

[23] Bukharov V.E., Rokakh A.G. Influence of defect diffusion on radiation resistance of the heterogeneous photoconductor CdS–PbS. *Tech. Phys. Lett.*, 1999, **25**, P. 994–996.

[24] Malyar I.V., Stetsyura S.V. The effect of morphology and surface composition on radiation resistance of heterogeneous material CdS–PbS. *Semiconductors*, 2011, **45**, P. 888–893.

[25] Markov V.F., Kitaev G.A., Ujmin S.N., Maskaeva L.N. Chemical technique of thin film synthesis of photosensitive materials. Photo resistors of visible and IR-range. *Innovation*, 1998, **1**, P. 55–56.

[26] Barote M.A., Yadav A.A., Chavan T.V., Masumdarb E.U. Characterization and photoelectrochemical properties of chemical bath deposited n-PbS thin films. *Digest Journal of Nanomaterials and Biostructures*, 2011, **6**, P. 979–990.

[27] Mohammed M.A., Mousa A.M., Ponpon J.P. Optical and optoelectric properties of PbCdS ternary thin films deposited by CBD. *J. of Semiconductor Technology and Science*, 2009, **9**, P. 117–123.

[28] Shelimova L.E., Tomashik V.N., Gricyv V.I. *Phase diagrams in semiconducting material science (systems based on Si, Ge, Sn, Pb)*. Nauka, Moscow, 1991.

[29] Vesnin Yu.I. On threshold temperature of solid substitutional solution formation. *Izvestiya of SB AS USSR. Series Chem. Sc.*, 1987, **17**, P. 145–149.

[30] Vesnin Yu. I. On formation mechanism of substitutional solid solutions. Izvestiya of SB AS USSR. Series Chem. Sc., 1985, **15**, P. 7–10.

[31] Markov V.F., Maskaeva L.N., Kitaev G.A. Predicting the composition of $Cd_xPb_{1x}S$ films deposited from aqueous solutions. *Inorg. Mater.*, 2000, **36**, P. 1194–1196.

[32] Markov V.F., Maskaeva L.N., Polikarpova Yu.S. Films of supersaturated $Cd_xPb_{1-x}S$ solid solutions deposited on porous glass, their structure and properties. *Butlerov Communications*, 2006, **8**, P. 54–61.

[33] Markov V.F., Maskaeva L.N., Ivanov P.N. *Chemical bath deposition of metal sulfide films: modeling and experiment*. UB RAS, Yekaterinburg, 2006.

[34] Kirsanov A.Yu., Markov V.F., Maskaeva L.N. Solid solution CdxPb1-xS forecasting by simulating of sulphides lead and cadmium co-precipitation process. *Bulletin of the South-Ural State University. Series "Chemistry"*, 2013, **5**, P. 35–39.

[35] Rabinovich E., Wachtel E., Hodes G. Chemical bath deposition of single-phase (Pb,Cd)S solid solutions. *Thin solid films*, 2008, **517**, P. 737–744.

[36] Markov V.F., Maskaeva L.N. Calculating the boundary conditions of the formation of solid-phase metal sulfides and selenides by deposition with thio- and selenourea. *Russian J. of Phys. Chem. A*, 2010, **84**, P. 1288–1293.

[37] Nichols P.L., Liu Z., et al. $Cd_xPb_{1-x}S$ alloy nanowires and heterostructures with simultaneous emission in mid-infrared and visible wavelengths. *Nano Lett.*, 2015, **15**, P. 909–916.

[38] Suryavanshi K.E., Dhake R.B., Patil A.M. Optical properties of PbxCd1xS thin films prepared by chemical bath deposition method. *Int. J. of Advanced Scientific and Technical Research*, 2014, **2**, P. 858–861.

[39] Osuwa J.C., Oriaku C.I., Ezema F.I. Impurity effects of cadmium salt on the absorption edge and structure of chemically prepared PbS films. *Chalcogenide Lett.*, 2009, **6**, P. 385–391.

[40] Deo S.R., Singh A.K., et al. Studies on structural, morphological and optical behavior of chemically deposited $Cd_{0.5}Pb_{0.5}S$ thin films. *Int. J. for Light and Electron Optics*, 2015, **126**, P. 2311–2317.

[41] Ahmad S.M., Kasim S.J., Latif L.A. Effects of thermal annealing on structural and optical properties of nanocrystalline $Cd_xPb_{1-x}S$ thin films prepared by CBD. *Jordan J. of Physics*, 2016, **9**, P. 113–122.

[42] Pentia E., Draghici V., et al. Structural, electrical, and photoelectrical properties of $Cd_xPb_{1-x}S$ thin films prepared by chemical bath deposition. *J. of the Electrochemical Society G*, 2004, **151**, P. 729–733.

[43] Nayak B.B., Acharya H.N. Characterization of chemically deposited $Pb_{1-x}Cd_xS$ films by scanning electron microscopy. *J. of Materials Science Lett.*, 1985, **4**, P. 651–652.

[44] Bhushan S., Mukherjee M., Bose P. Electro-optical studies in chemically deposited La/Nd doped (Cd–Pb) S films. *J. of Material Science Materials in Electronics*, 2002, **13**, P. 581–584.

[45] Omotoso E., Adegboyega G.A., et al. Synthesis and some properties of MOCVD lead sulphide and lead cadmium sulphide thin films. *J. Non-Oxide Glasses*, 2013, **5**, P. 9–19.

[46] Belov N.V. *Processes of grain formation*. Nauka, Moscow, 1977.

[47] Chavez H., Jordan M., et al. Physical and electrical characterization of CdS deposited by vacuum evaporation, solution growth and spray pyrolysis. *J. Mater. Sci.: Mater. Electronics*, 1997, **8**, P. 151–154.

[48] Makurin Yu.N., Pletnev R.N., Kleshchev D.G., Zhelonkin N.A. *Intermediate complex in chemical reactions*. UB AS USSR, Sverdlovsk, 1990.

[49] Rietveld H.M. A profile refinement method for nuclear and magnetic structures. *J. Appl. Crystallogr.*, 1969, **2**, P. 65–71.

[50] Rodriguez-Carvajal J. Recent advances in magnetic structure determination by neutron powder diffraction. *Physica B: Condensed Matter*, 1993, **192**, P. 55–69.

[51] Hall W.H., Williamson G.K. The diffraction pattern of cold worked metals: I the nature of extinction. *Proceedings of the Physical Society. Section B*, 1951, **64**, P. 937–946.

[52] Williamson G.K., Hall W.H. X-ray line broadening from filed aluminium and wolfram. *Acta metallurgica*, 1953, **1**, P. 22–31.

[53] Muhamedyarov R D., Stuk V.I., Blinov O.Yu. Device for measuring threshold parameters of photo detectors. *Instruments and Experimental Techniques*, 1976, **6**, P. 234.

[54] Chichagov A.V., Sipavina L.V. *Parametaers of solid solution cells*. Nauka, Moscow, 1982.

[55] Qadri S.B., Singh A., Yousuf M. Structural stability of PbS films as a function of temperature. *Thin Solid Films*, 2003, **431**, P. 506–510.

[56] Kitajgorodskij A.I. *X-ray structure analysis of fine-crystalline and amorphous materials*. GITTL, Leningrad, 1952.

[57] Kozhevnikova N.S., Vorokh A.S., et al. Synthetic path way of a Cu_2ZnSnS_4 powder using low temperature annealing of nanostructured binary sulfides. *Nanosystems: Phys., Chem., Math.*, 2017, **8** (6), P. 787–792.

[58] Abrikosov N.Kh., Bankina V.F., et al. *Semiconducting chalcogenides and their alloys*. Nauka, Moscow, 1982.

[59] Blakemore J.S. *Solid State Physics*. Second ed., Cambridge University Press, Cambridge, 1985, 506 pp.

NANOSYSTEMS:

PHYSICS, CHEMISTRY, MATHEMATICS

INFORMATION FOR AUTHORS

The journal publishes research articles and reviews, and also short scientific papers (letters) which are unpublished and have not been accepted for publication in other magazines. Articles should be submitted in English. All articles are reviewed, then if necessary come back to the author to completion.

The journal is indexed in Web of Science Core Collection (Emerging Sources Citation Index), Chemical Abstract Service of the American Chemical Society, Zentralblatt MATH and in Russian Scientific Citation Index.

Author should submit the following materials:

1. Article file in English, containing article title, the initials and the surname of the authors, Institute (University), postal address, the electronic address, the summary, keywords, MSC or PACS index, article text, the list of references.
2. Files with illustrations, files with tables.
3. The covering letter in English containing the article information (article name, MSC or PACS index, keywords, the summary, the literature) and about all authors (the surname, names, the full name of places of work, the mailing address with the postal code, contact phone number with a city code, the electronic address).
4. The expert judgement on possibility of publication of the article in open press (for authors from Russia).

Authors can submit a paper and the corresponding files to the following addresses: nanojournal.ifmo@gmail.com, popov1955@gmail.com.

Text requirements

Articles should be prepared with using of text editors MS Word or LaTex (preferable). It is necessary to submit source file (LaTex) and a pdf copy. In the name of files the English alphabet is used. The recommended size of short communications (letters) is 4-6 pages, research articles– 6-15 pages, reviews – 30 pages.

Recommendations for text in MS Word:

Formulas should be written using Math Type. Figures and tables with captions should be inserted in the text. Additionally, authors present separate files for all figures and Word files of tables.

Recommendations for text in LaTex:

Please, use standard LaTex without macros and additional style files. The list of references should be included in the main LaTex file. Source LaTex file of the paper with the corresponding pdf file and files of figures should be submitted.

References in the article text are given in square brackets. The list of references should be prepared in accordance with the following samples:

[1] Surname N. *Book Title*. Nauka Publishing House, Saint Petersburg, 2000, 281 pp.
[2] Surname N., Surname N. Paper title. *Journal Name*, 2010, **1** (5), P. 17-23.
[3] Surname N., Surname N. Lecture title. In: Abstracts/Proceedings of the Conference, Place and Date, 2000, P. 17-23.
[4] Surname N., Surname N. Paper title, 2000, URL: http://books.ifmo.ru/ntv.
[5] Surname N., Surname N. Patent Name. Patent No. 11111, 2010, Bul. No. 33, 5 pp.
[6] Surname N., Surname N. Thesis Title. Thesis for full doctor degree in math. and physics, Saint Petersburg, 2000, 105 pp.

Requirements to illustrations

Illustrations should be submitted as separate black-and-white files. Formats of files – jpeg, eps, tiff.

NANOSYSTEMS:

PHYSICS, CHEMISTRY, MATHEMATICS

Журнал зарегистрирован
Федеральной службой по надзору в сфере связи, информационных технологий и массовых коммуникаций
(свидетельство ПИ № ФС 77 - 49048 от 22.03.2012 г.)
ISSN 2220-8054

Учредитель: федеральное государственное автономное образовательное учреждение высшего образования
«Санкт-Петербургский национальный исследовательский университет информационных технологий, механики и оптики»

Издатель: федеральное государственное автономное образовательное учреждение высшего образования
«Санкт-Петербургский национальный исследовательский университет информационных технологий, механики и оптики»

Отпечатано в Учреждении «Университетские телекоммуникации»
Адрес: 197101, Санкт-Петербург, Кронверкский пр., 49

Подписка на журнал НФХМ
На второе полугодие 2019 года подписка осуществляется через
ОАО Агентство «Роспечать»
Подписной индекс 57385 в каталоге «Издания органов научно-технической информации»